

**Insights into Ligand-centered Redox Mechanisms in Li-rich Metal Oxides during Battery
Reactions**

BY

Haifeng Li

B.S., Qingdao University of Science & Technology, 2011

THESIS

Submitted in partial fulfillment of the requirements
for the degree of Doctor of Philosophy in Chemistry
in the Graduate College of the
University of Illinois at Chicago, 2020

Chicago, Illinois

Defense Committee:

Jordi Cabana, Chair and Advisor

Donald J. Wink

Neal P. Mankad

Andy I. Nguyen

Teak D. Boyko, Canadian Light Source

Acknowledgements

First and foremost, I would like to thank my advisor, Dr. Jordi Cabana, for his mentorship, advice, insight, motivation, and generous financial support throughout the Ph.D. process. His contribution to this work has been both instrumental and inspirational. I am sincerely honored to meet and work with him and shall never forget his endless advice and help. I am also grateful for his aid in preparing for post-graduate work. I would also like to express my deepest gratitude to my committee members: Dr. Donald J. Wink, Dr. Neal P. Mankad, Dr. Andy I. Nguyen, and Dr. Teak D. Boyko for their time and guidance.

I would also like to acknowledge the help and support of all my past and present fellow members in Cabana group, who have provided invaluable aid by being friends off whom I could bounce ideas, from whom I learn experimental techniques, and on whom I could rely. I am also grateful to the staff in the Department of Chemistry, who has also provided administrative aid throughout my graduate period.

Moreover, I would also like to extend my special thanks to my co-authors and collaborators, Dr. Bryan D. McCloskey, Dr. Srinivasan Ramakrishnan at University of California, Berkeley, Dr. John W. Freeland and Dr. Maria K. Chan and Dr. Liang Li at Argonne National Laboratory, Dr. Jean-Marie Tarascon and Dr. Arnaud J. Perez at Collège de France, Chimie du Solide et de l'Energie, Dr. Marie-Liesse Doublet and Beata Taudul at Institut Charles Gerhardt, Univ. Montpellier, Dr. Teak D. Boyko at Canadian Light Source, and Dr. Bohang Song and Dr. Jue Liu at Oak Ridge National Laboratory for their invaluable help throughout my projects. I also extend a heartfelt thank you to the numerous brilliant beamline scientists without whom this thesis would have been impossible.

I would also like to acknowledge the financial support from the National Science Foundation under Grant No. DMR-1809372. This research also used resources of the Advanced Photon Source, a U.S. Department of Energy (DOE) Office of Science User Facility operated for the DOE Office of Science by Argonne National Laboratory under Contract DE-AC02-06CH11357. In addition, part or all of the research described in this thesis was performed at the Canadian Light Source, a national research facility of the

University of Saskatchewan, which is supported by the Canada Foundation for Innovation (CFI), the Natural Sciences and Engineering Research Council (NSERC), the National Research Council (NRC), the Canadian Institutes of Health Research (CIHR), the Government of Saskatchewan, and the University of Saskatchewan. Moreover, the research was also aided by UIC Research Resources Center.

Last but not least, I am especially grateful for my loving family. I cannot thank enough to my grandmother, my parents and brother. They have influenced, inspired, and shown me the true meaning of hard work and dedication! I am the person I am today because of them. I would like to thank my beloved wife, Wenjuan Huai, whose patience, endless support, understanding, encouragement, and love made this possible.

Contribution of authors:

Chapter 1 is a background introduction, briefly reviewing the literatures pertaining to the lattice oxygen redox in Li-rich transition metal oxides during the electrochemical reactions.

Chapter 2 is a theoretical overview of the experimental techniques employed to study the ligand involvement in charge compensation and includes specific experimental protocols utilized to generate the data contained in this thesis.

Chapter 3 is currently being prepared for submission for publication of the material “Elucidation of Spectroscopic Features of Oxygen Redox upon Lithium Intercalation in Li_2RuO_3 ”. The dissertation author would be the primary author of this paper. Bohang Song and Jue Liu performed the crystal structure analysis and solved crystal structures at certain different states of charge. Xue Rui assisted me in the TEM measurements. John Freeland assisted in conducting x-ray absorption measurements. Jordi Cabana, my research advisor, assisted in reviewing the manuscript.

Chapter 4, in full, is a reprint of the material “Definition of Redox Centers in Reactions of Lithium Intercalation in Li_3RuO_4 Polymorphs” published in Journal of the American Chemical Society, H. Li, S. Ramakrishnan, J. W. Freeland, B. D. McCloskey, J. Cabana. **2020**, 142, 8160–8173. The dissertation author is the primary author of this paper. Srinivasan Ramakrishnan and Bryan D. McCloskey conducted the

DEMS measurement. John Freeland assisted in conducting x-ray absorption measurements. Jordi Cabana assisted in reviewing the manuscript.

Chapter 5 is the reprint of the material “Elucidation of Active Oxygen Sites upon Delithiation of Li_3IrO_4 ”, which has been submitted for peer review, and also contains the unpublished work from a manuscript in progress. The dissertation author is the primary author of this paper. Arnaud Perez and Jean-Marie Tarascon performed the magnetic measurement. Arnaud Perez and Marie-Liesse Doublet conducted the computational calculation. Teak Boyko assisted in the X-ray emission and absorption measurements and analysis. John Freeland assisted in conducting x-ray absorption measurements. Jordi Cabana assisted in reviewing the manuscript.

Chapter 6 is currently being prepared for submission for publication of the material “Definition of Redox Centers in Reactions of Lithium Intercalation in Li_7RuO_6 ”. The dissertation author is the primary author of the paper. Grant Alexander performed the crystal structure analysis and deduced the structure of Li_8RuO_8 . John Freeland assisted in conducting x-ray absorption measurements. Jordi Cabana assisted in reviewing the manuscript.

Table of contents

Chapter 1 Introduction	1
1.1 Motivation	1
1.2 Fundamental principle of rechargeable Li-ion batteries	2
1.3 Li-rich transition-metal oxides	7
1.3.1 Li_2MnO_3 and derivatives	10
1.3.2 Li_2MO_3 ($\text{M} = 4\text{d}/5\text{d}$)	12
1.3.3 Disordered rock-salt compounds	13
1.6.4 Li_3MO_4	15
1.4 Fundamental principle of redox chemistry	16
1.5 Possible mechanism of anionic redox reactions Li-rich oxides.....	22
1.7 Research goals	34
Chapter 2 Experimental methods.....	36
2.1 Synthetic procedures.....	36
2.2 Electrochemical characterization.....	36
2.2.1 Theoretical concepts of galvanostatic experiments	36
2.2.2 Experimental details	39
2.3 Synchrotron light source.....	40
2.4 Neutron source.....	41
2.5 Characterization of crystal structure.....	41
2.5.1 Theory of diffraction	42
2.5.2 Diffraction data analysis.....	44
2.5.3 <i>Ex situ</i> X-ray and neutron diffraction	44
2.5.4 <i>Operando</i> synchrotron X-ray diffraction.....	45
2.5.5 Experimental setups for <i>operando</i> synchrotron X-ray diffraction	47
2.6 Electronic structure analysis of electrode materials	48
2.6.1 X-ray absorption spectroscopy	49
2.6.1.1 Overview of X-ray absorption spectroscopy	49
2.6.1.2 Experimental setups for X-ray absorption spectroscopy	53
2.6.2 X-ray emission spectroscopy.....	54
2.6.2.1 Overview of X-ray emission spectroscopy	54
2.6.2.2 Experimental setups for X-ray emission spectroscopy	54
2.6.3 Resonant inelastic X-ray scattering	55

2.6.3.1 Overview of resonant inelastic X-ray scattering.....	55
2.6.3.1 Experimental setups for resonant inelastic X-ray scattering.....	56
2.7 Differential electrochemical mass spectroscopy.....	56
2.7.1 Overview of differential electrochemical mass spectroscopy	56
2.7.2 Experimental setups for differential electrochemical mass spectroscopy	57
2.8 Density functional theory	57
2.8.1 Structural relaxation and electronic structures	58
2.8.2 XAS simulation	58
Chapter 3 Elucidation of spectroscopic features of oxygen redox upon lithium intercalation in Li_2RuO_3 .	60
3.1 Introduction	60
3.2 Experimental methods	60
3.3 Structural characterization of Li_2RuO_3	61
3.4 Electrochemical properties of Li_2RuO_3	64
3.5 Structural evolution upon cycling.....	66
3.6 <i>Ex situ</i> Ru K-edge XAS.....	75
3.7 <i>Ex situ</i> O K-edge XAS.....	78
3.8 <i>Ex situ</i> O $\text{K}\alpha$ XES.....	82
3.9 <i>Ex situ</i> O K-edge RIXS	84
3.10 Conclusion	85
Chapter 4 Definition of redox centers in reactions of lithium intercalation in Li_3RuO_4 polymorphs.....	87
4.1 Introduction	87
4.2 Experimental methods	88
4.3 Structural Characterization of Li_3RuO_4	88
4.4 Voltage cutoff window of 2.5-3.9 V.....	93
4.4.1 Electrochemical properties of Li_3RuO_4	94
4.4.2 Structural evolution of Li_3RuO_4	96
4.4.3 <i>Ex situ</i> Ru K-edge XAS of Li_3RuO_4	104
4.4.4 <i>Ex situ</i> O K-edge XAS of Li_3RuO_4	107
4.4.5 <i>Operando</i> analysis of gas evolution	111
4.5 Voltage cutoff window of 1.5-2.5 V.....	113
4.5.1 Electrochemical properties of Li_3RuO_4	113
4.5.2 Structural variation of Li_3RuO_4	115
4.5.3 <i>Ex situ</i> Ru K-edge XAS of Li_3RuO_4	121
4.5.4 <i>Ex situ</i> O K-edge XAS of Li_3RuO_4	122

4.6 Discussion.....	123
4.7 Conclusion.....	134
Chapter 5 Resolving oxygen contribution to charge Compensation in lithiation reactions of Li_3IrO_4	136
5.1 Introduction	136
5.2 Experimental methods	137
5.3 Results	137
5.3.1 Electronic structure and electrochemistry of Li_3IrO_4	137
5.3.2 Changes at O states upon delithiation	146
5.3.3 Chemical reversibility of the process of LOR.....	151
5.3.4 Implications for the existence and mechanism of LOR	155
5.4 Conclusion.....	158
Chapter 6 Definition of redox centers in reactions of lithium intercalation in Li_7RuO_6	160
6.1 Introduction	160
6.2 Experimental methods	160
6.3 Structural Characterization of Li_7RuO_6	161
6.3 Voltage cutoff window of 2.6-3.68 V.....	164
6.4 Voltage cutoff window of 1.5-2.6 V.....	173
6.5. Conclusion.....	179
Chapter 7 Summary and future work.....	180
Bibliography	182
VITA.....	198
Appendix.....	201

List of tables

Table 3-1. Crystallographic parameters and reliability factors deduced from the joint Rietveld refinement of SXRD and NPD patterns for Li_2RuO_3 under the space group of $\text{P2}_1/\text{m}$	63
Table 3-2. Crystallographic parameters and reliability factors deduced from the joint Rietveld refinement of SXRD and NPD patterns for Li_2RuO_3 charged to 3.6 V.	69
Table 3-3. Crystallographic parameters and reliability factors extracted from the joint Rietveld refinement of SXRD and NPD patterns for Li_2RuO_3 charged to 3.9 V.	71
Table 3-4. Crystallographic parameters and reliability factors extracted from the joint Rietveld refinement of SXRD and NPD patterns for Li_2RuO_3 charged to 4.6 V.	72
Table 3-5. Crystallographic parameters and reliability factors extracted from the joint Rietveld refinement of SXRD and NPD patterns for Li_2RuO_3 discharged to 3.2 V.	73
Table 4-1. Crystallographic parameters and reliability factors extracted from the joint Rietveld refinement of SXRD and NPD for (a) D- and (b) O- Li_3RuO_4	92
Table 4-2. Selected bond lengths (Å) O- Li_3RuO_4 at 298 K	93
Table 4-3. Calculated Unit Cell Parameters via Pawley refinement of the data in Figure 4-6.	100
Table 4-4. Calculated Unit Cell Parameters via Pawley refinement of the data in Figure 10.....	103
Table 4-5. Delivered capacities and the corresponding O_2 and CO_2 evolution during the <i>operando</i> DEMS measurement.	112
Table 4-6. Calculated Unit Cell Parameters from SXRD patterns through Pawley refinement.....	117
Table 4-7. Crystallographic parameters and reliability factors extracted from Rietveld refinement of SXRD of $\text{Li}_{4.6}\text{RuO}_4$	119
Table 4-8. Calculated Unit Cell Parameters from SXRD patterns through Pawley refinement.....	120
Table 4-9. Delivered capacities and the corresponding O_2 and CO_2 evolution during the <i>operando</i> DEMS measurement.	132
Table 5-1. Number of $\text{O}_{3\text{LP}}$ and $\text{O}_{2\text{LP}}$ in the non-equivalent IrO_6 octahedra occurring in the Li/Ir ordered and disordered phases considered in the calculations.....	144
Table 6-1. Crystallographic parameters and reliability factors extracted from the combined Rietveld refinement of SXRD and NPD for Li_7RuO_6	163
Table 6-2. Crystallographic parameters and reliability factors extracted from the combined Rietveld refinement of SXRD for Li_7RuO_6 after reduction to 1.5 V.	176

List of figures

- Figure 1-1.** Comparison of different rechargeable battery technologies in terms of energy density and specific energy. Reprinted with permission from “Issues and challenges facing rechargeable lithium batteries”.³ Copyright © 2001 Springer Nature. 2
- Figure 1-2.** Schematic illustration of typical electrochemical cell in a commercial Li-ion battery comprised of the first-generation layered oxide LiCoO_2 as cathode and graphite as anode. Reprinted with permission from “The Li-Ion Rechargeable Battery: A perspective”.⁹ Copyright © 2013 American Chemical Society. 3
- Figure 1-3.** Relationship of the cell voltage with the specific capacity for electrodes intensively studied today, in conventional electrolyte, 1M LiPF_6 dissolved in diethyl carbonate (DEC) and ethylene carbonate (EC) with the volume ratio of 1:1. Reprinted with permission from “Cathode materials for next generation lithium ion batteries”.¹⁶ Copyright © 2013 Elsevier Ltd. 7
- Figure 1-4.** Crystal structure of (a) LiM_2O_4 , (b) LiMPO_4 and (c) LiMO_2 in which Li^+ ions migrate via 3D, 1D and 2D frameworks, respectively. Adapted with permission from “Comparative Issues of Cathode Materials for Li-Ion Batteries”.¹⁷ Copyright© 2014 MDPI. 8
- Figure 1-5.** (a) Crystal structure of Li_2MnO_3 . (b) Local coordination environment around O in Li_2MnO_3 . (c) First three cycling profile of $\text{Li}_{1.2}\text{Ni}_{0.13}\text{Co}_{0.13}\text{Mn}_{0.54}\text{O}_2$. Adapted with permission from “Molecular Orbital Principles of Oxygen-Redox Battery Electrodes”.⁷² Copyright © 2017 American Chemical Society. 11
- Figure 1-6.** (a) First three voltage-capacity curves of Li_2RuO_3 . (b) Voltage-composition cycling profile of $\alpha\text{-Li}_2\text{IrO}_3$. Reprinted with permission from “Visualization of O-O peroxo-like dimers in high-capacity layered oxides for Li-ion batteries”.⁷⁴ Copyright © 2015, American Association for the Advancement of Science. (c) Crystal structure of $\beta\text{-Li}_2\text{IrO}_3$. (d) Local coordination environment around O in $\beta\text{-Li}_2\text{IrO}_3$. (e) First three voltage-composition profiles of $\beta\text{-Li}_2\text{IrO}_3$. Reprinted with permission from “Molecular Orbital Principles of Oxygen-Redox Battery Electrodes”.⁷² Copyright © 2017 American Chemical Society. 12
- Figure 1-7.** (a) Possible ways of an *o-t-o* Li diffusion in rock-salt-like transition metal oxides. (A) *o-t-o* diffusion: two tetrahedral sites connect each pair of neighboring octahedral sites. (B to D) The intermediate activated state can share faces with no octahedral transition metals (O-M channel) (B), one transition metal (1-M channel) (C), or two transition metals (2-M channel) (D). (b) Calculated migration barriers of Li^+ ions along 1-M (Mo^{4+}) channels (red squares), 1-M (Cr^{3+}) channels (blue triangles), and O-M (Li^+) channels (black circles) as a function of the average tetrahedral height of mode disordered Li_2MoO_3 and LiCrO_2 . Reprinted with permission from “Unlocking the Potential of Cation-Disordered Oxides for Rechargeable Lithium Batteries”.⁸² Copyright © 2014 American Association for the Advancement of Science. 14
- Figure 1-8.** (a) First three voltage-capacity curves of $\text{Li}_{1.3}\text{Nb}_{0.3}\text{Mn}_{0.4}\text{O}_2$. (b) Local coordination environment around O in $\text{Li}_{1.3}\text{Nb}_{0.3}\text{Mn}_{0.4}\text{O}_2$. (c) Voltage-composition cycling profile of $\text{Li}_{1.2}\text{Ti}_{0.4}\text{Mn}_{0.4}\text{O}_2$. Reprinted with permission from “Molecular Orbital Principles of Oxygen-Redox Battery Electrodes”.⁷² Copyright © 2017 American Chemical Society. 15
- Figure 1-9.** (a) Zig-zag chains in Li_3RuO_4 . (b) Layered Li_3IrO_4 with cation disorder in metal layer. Reprinted with permission from “Approaching the limits of cationic and anionic

- electrochemical activity with the Li-rich layered rock-salt Li_3IrO_4 ".⁹⁸ Copyright © 2017 Springer Nature. 16
- Figure 1-10.** (a) Local coordination environment around oxygen composed of three Li-O-M configuration in layered LiMO_2 . (b) Schematic of the band structure for LiMO_2 . (c) Local atomic coordination around oxygen comprising of one two Li-O-M and one Li-O-Li configuration in layered or cation-disordered Li-rich oxides Li_2MO_3 . (d) Schematic of the band structure for Li-rich Li_2MO_3 . Reprinted with permission from "The structural and chemical origin of the oxygen redox activity in layered and cation-disordered Li-excess cathode materials".⁸⁴ Copyright © with permission from Springer Nature. 19
- Figure 1-11.** Crystal structures (focusing on slabs of MO_2 and $\text{Li}_{1/3}\text{M}_{2/3}\text{O}_2$) and the relevant parts of the band structures of LiMO_2 (a) and Li-rich Li_2MO_3 . (c-e) Qualitative representation of the Li_2MO_3 band structure by taking Mott-Hubbard splitting into account. Reprinted with permission from "Fundamental understanding and practical challenges of anionic redox activity in Li-ion batteries".¹¹⁴ Copyright © 2018 Springer Nature. 21
- Figure 1-12.** (a) and (b) Difference spectra of O K-edge XAS of Li_2MnO_3 at different states of charge and (a) the reference XAS spectra of Li_2O_2 and KO_2 . Reprinted with permission from "Direct observation of reversible oxygen anion redox reaction in Li-rich manganese oxide, Li_2MnO_3 studied by soft X-ray absorption spectroscopy". Copyright © 2016 Royal Society of Chemistry.¹³¹ 23
- Figure 1-13.** Schematics of the proposed mechanisms accounting for the bulk and surface reactions in $\text{Li}_x\text{Ni}_{0.13}\text{Co}_{0.13}\text{Mn}_{0.54}\text{O}_{2.8}$. Reprinted with permission from "Detailed Studies of a High-Capacity Electrode Material for Rechargeable Batteries, $\text{Li}_2\text{Mn}_2\text{O}_3$ - $\text{LiCo}_{1/3}\text{Ni}_{1/3}\text{Mn}_{1/3}\text{O}_2$ ".¹⁴⁰ Copyright © 2011 American Chemical Society. 25
- Figure 1-14.** (a) Reaction mechanism of the localized electron holes at ligand oxygen anions. Reprinted with permission from "Charge-compensation in 3d-transition-metal oxide intercalation cathodes through the generation of localized electron holes on oxygen".¹¹⁷ Copyright © 2016 Springer Nature. (b) Schematic of the reorganization of the electronic structure of $\text{Li}_{1.17}[\text{Ni}_{0.21}\text{Co}_{0.08}\text{Mn}_{0.54}]\text{O}_2$ due to M migration. Reprinted with permission from "Coupling between oxygen redox and cation migration explains unusual electrochemistry in lithium-rich layered oxides".¹⁴⁹ Copyright © 2017 Springer Nature. 27
- Figure 1-15.** (a) O 1s XPS spectra of $\text{Li}_2\text{Ru}_{0.5}\text{Sn}_{0.5}\text{O}_3$ samples in the pristine state, charged to 4.0 V, charged to 4.6 V and discharged to 2.0 V, respectively (from top to bottom). (b) X-band EPR spectra collected on the same series at room temperature (top) and 4 K (bottom). (c) Reductive coupling mechanism stabilizing the oxidized oxygen by forming peroxo-like species (O_2)ⁿ⁻. Reprinted with permission from "Reversible anionic redox chemistry in high-capacity layered-oxide electrodes".⁷³ Copyright © 2013 Springer Nature. 29
- Figure 1-16.** (a) Evolution of the Ir L_{III}-edge white line energy of α - Li_2IrO_3 during the first cycle. The raw XANES data for charging and discharging are shown in the left and right insets, respectively. (b) Mechanism of cation migration and LMCT-mediated anionic redox in $\text{Li}_2\text{Ir}_{1-y}\text{Sn}_y\text{O}_3$. Reprinted with permission from "Metal-oxygen decoordination stabilizes anion redox in Li-rich oxides".¹²² Copyright © 2019 Springer Nature. 31
- Figure 1-17.** (a) Comparison of the crystal structure and the transition metal migration path for O3- $\text{Li}(\text{Li}_{0.2}\text{Ni}_{0.2}\text{Mn}_{0.6})\text{O}_2$ -type structure (b) and O2- $\text{Li}_x(\text{Li}_{0.2}\text{Ni}_{0.2}\text{Mn}_{0.6})\text{O}_2$ -type structure (c). Reprinted from "Voltage decay and redox asymmetry mitigation by reversible cation migration

in Li-rich layered oxide electrode” with permission from Springer Nature. ¹⁵⁵ Copyright © 2020 Springer Nature. (b) Comparison of electrochemistry and structure of honeycomb- and ribbon-ordered cathode materials. Reprinted with permission from “Superstructure control of first-cycle voltage hysteresis in oxygen-redox cathodes”. ¹⁵⁶ Copyright © 2020 Springer Nature..	33
Figure 2-1. Charge-discharge cell voltages of NMC cells under C/25 rate galvanostatic operation and OCVs of a fresh NMC cell. The inset demonstrates how the overpotential and voltage hysteresis are obtained. Reprinted with permission from “Effects of cycling on lithium-ion battery hysteresis and overvoltage”. ¹⁵⁹ Copyright © 2019 Springer Nature.	38
Figure 2-2. The geometry derivation of Bragg’s Law for X-ray diffraction from a set of crystal plans (<i>hkl</i>) with interplanar spacing, <i>dhkl</i> . Reprinted with permission from “Crystals and Crystal Structures”. ¹⁶² Copyright © 2006 John Wiley and Sons.	43
Figure 2-3. (a) Schematic of the AMPIX cell with principle components, (b) schematic of interaction between the assembled AMPIX cell with x-ray, (c) a typical battery stack, and photographs of (d) an assembled AMPIX cell and (e) a six-cell multicell holder used for <i>operando</i> experiment. Reprinted with the permission from “The AMPIX electrochemical cell: a versatile apparatus for in situ X-ray scattering and spectroscopic measurements”. ¹⁶⁶ Copyright © 2012 the International Union of Crystallography.....	47
Figure 2-4. Schematic of an XAS spectrum with the main regions and their sources.	51
Figure 2-5. Nomenclature rule used to describe electronic transitions that contribute to XAS edges.....	52
Figure 2-6. (a) Mn L-edge RIXS map of $\text{LiNi}_{1/3}\text{Mn}_{1/3}\text{Co}_{1/3}\text{O}_2$ with the excitation energy as the vertical axis and the emission energy as the horizontal axis. (b) Integration of RIXS intensity along the horizontal direction leads to different types of XAS spectra. Reprinted with permission from “Anionic and cationic redox and interfaces in batteries: Advances from soft X-ray absorption spectroscopy to resonant inelastic scattering”. ¹⁷⁷ Copyright © 2018 Elsevier B.V.	56
Figure 3-1. Rietveld refinement of SXRD (a) and NPD (b) patterns of pristine Li_2RuO_3 under space group of C2/c. Panels (b) and (d) show a zoom of a small angular region of (a) and (c), respectively. At around $Q = 1.33 \text{ \AA}^{-1}$, there is no corresponding Bragg reflection. Black crosses, red solid line and tick bars represent experimental data, calculated patterns, and Bragg reflects, respectively. Blue solid line stands for the difference between observed data and calculated one.	62
Figure 3-2. Rietveld refinement of SXRD (a) and NPD (b) patterns of pristine Li_2RuO_3 under space group of P2 ₁ /m. (b) is the magnified part of (a) and (d) is the magnified part of (c). At $Q = 1.33 \text{ \AA}^{-1}$, there exists a corresponding Bragg reflection denoted by the asterisk symbol. Black crosses, red solid line and tick bars represent experimental data, calculated patterns, and Bragg reflects, respectively. Blue solid line stands for the difference between observed data and calculated one.	63
Figure 3-3. High-magnification HAADF-STEM image of pristine Li_2RuO_3 and the inset shows the diffraction pattern.	64
Figure 3-4. (a) Voltage-composition profiles of Li_2RuO_3 under the galvanostatic cycling, compared to the corresponding capacity in the first cycle (a) and upon extensive cycling (c). (b) Differential capacity (<i>dQ/dV</i>) analysis of Li_2RuO_3 in the first cycle. (d) Discharge capacity (black circles) and coulombic efficiency (red squares) as a function of cycle number.	66

Figure 3-5. Voltage-composition profile of Li_2RuO_3 cycled galvanostatically between 2 and 3.9 V, compared to the corresponding capacity.	66
Figure 3-6. <i>Operando</i> synchrotron XRD of Li_2RuO_3 during the first charge-discharge process. The left panel displays the contour plot of synchrotron XRD patterns between 2.85° and 3.25° . The right panel demonstrates the representative diffraction patterns extracted from the <i>operando</i> data and the pure phase at certain state of charge are signified by different color line which is pertinent to the point in the corresponding electrochemical profile depicted in the middle part. Given the permitted experimental error, the profile is reasonable.	69
Figure 3-7. Rietveld refinement of SXR (a) and NPD (b) patterns of Li_2RuO_3 charged to 3.6 V using space group $\text{P2}_1/\text{m}$	69
Figure 3-8. XRD patterns of Li_2RuO_3 during charged to 3.7 V collected under <i>ex situ</i> mode (black line) and <i>operando</i> mode (red line). The asterisk symbols represent the existence of peaks that could not be indexed and that were not observed under <i>operando</i> conditions.	70
Figure 3-9. Rietveld refinement of SXR (a) and NPD (b) patterns of Li_2RuO_3 charged to 3.9 V using space group $\text{R}\bar{3}$	71
Figure 3-10. Rietveld refinement of SXR (a) and NPD (b) patterns of Li_2RuO_3 charged to 4.6 V using space group $\text{R}\bar{3}$	72
Figure 3-11. Rietveld refinement of SXR (a) and NPD (b) patterns of Li_2RuO_3 discharged to 3.2 V using two phases with space group $\text{R}\bar{3}$	73
Figure 3-12. (a) SXR of state discharged to 3.3 V (Dch 3.3 V) and state discharged to 2.0 V (Dch 2.0 V) extracted from <i>operando</i> data. The inset elucidates the asymmetric broadening of the first peak from Dch 3.3 V to Dch 2.0 V. (b) SXR of the pristine state and state discharged to 2.0 V (Dch 2.0 V) extracted from <i>operando</i> data. The inset elucidates the lower position of the first peak after reduction to 2.0 V.	74
Figure 3-13. High resolution SXR of Li_2RuO_3 of samples harvested after electrochemical cycling. 1C, 1D, 2C, and 2D represent the first charge and discharge, and the second charge and second discharge, respectively.	75
Figure 3-14. (a) <i>Ex situ</i> Ru K-edge XANES spectra of Li_2RuO_3 at different states of charge and (b) the corresponding first derivative plots for locating the position of the rising edge. RuO_2 was used as a standard reference for Ru^{4+}	76
Figure 3-15. (a) <i>Ex situ</i> Ru K-edge XAS spectra of Li_2RuO_3 at different states of charge and pristine Li_3RuO_4 . (b) Zoom of the pre-edge region of Li_2RuO_3 at different states of charge.	77
Figure 3-16. (a) <i>Ex situ</i> Ru K-edge XANES spectra of Li_2RuO_3 at different states of charge and (b) the corresponding first derivative plots.	78
Figure 3-17. <i>Ex situ</i> O K edge XAS spectra of Li_2RuO_3 at different states of charge measured in TFY (a) and PFY modes (b), along with the difference spectra between the points indicated.	81
Figure 3-18. First derivative plots of the O K-edge XAS spectra measured in TFY and PFY modes.	81
Figure 3-19. (a) <i>Ex situ</i> O K-edge XAS of Li_2RuO_3 at different states of charge measured in TEY mode. (b) O K-pre-edge part of Li_2RuO_3 at different states of charge measured in PFY mode.	81

- Figure 3-20.** (a) *Ex situ* O K edge XAS spectra of Li_2RuO_3 at different states of charge under total fluorescence yield (TFY) mode and (b) the corresponding first derivative plots of O K-edge XAS spectra..... 82
- Figure 3-21.** (a) Stacked and (b) overlaid *ex situ* non-resonant O K α XES spectra of Li_2RuO_3 at different states of charge. 84
- Figure 3-22.** *Ex situ* RIXS map of Li_2RuO_3 at different states of charge through the first cycle. The red rectangles represent the pre-edge feature due to the transition of O 1s core electron to the Ru 4d-O 2p hybridization states. The white rectangle stands for the elastic peak enhancement. . 85
- Figure 4-1.** Structural characterization of disordered and ordered Li_3RuO_4 . Combined Rietveld refinement of SXRD and NPD patterns of (a) D- Li_3RuO_4 and (b) O- Li_3RuO_4 . Black crosses: experimental patterns, red solid line: calculated patterns, blue solid line: difference and green bars: Bragg reflections. 90
- Figure 4-2.** Structure of (a) D- and (B) O- Li_3RuO_4 . Oxide ions (red) stack in a cubic close-packed arrangement while both Li (green) and Ru (purple) occupy octahedral sites for both polymorphs. D- Li_3RuO_4 has mixed Li and Ru arrangement in the metallic layers. O- Li_3RuO_4 has a long-range distribution of zig-zag chains (c). Schematic arrangement of various bonds in (d) D- and (e) O- Li_3RuO_4 . (f) Individual coordination environment for each cation in O- Li_3RuO_4 91
- Figure 4-3.** SEM images of (a) D- and (b) O- Li_3RuO_4 92
- Figure 4-4.** Voltage-composition profiles of D- Li_3RuO_4 between 2.5-3.9 V upon (a) the first five cycling and (c) extensive cycling. (b) Differential capacity analysis (dQ/dV) of D- Li_3RuO_4 . (d) Discharge capacity and coulombic efficiency as a function of the cycle number. 95
- Figure 4-5.** Voltage-composition profiles of O- Li_3RuO_4 between 2.5-3.9 V upon (a) the first 24th cycling and (c) extensive cycling. The profiles in (a) were re-scaled back to x=3 (0 mAhg⁻¹) for clarity. (b) Differential capacity analysis (dQ/dV) of O- Li_3RuO_4 . (d) Discharge capacity and coulombic efficiency as a function of the cycle number. 96
- Figure 4-6.** SXRD patterns of D- Li_3RuO_4 at selected points during the first cycle within a potential range of 2.5-3.9 V, collected *operando*. The complete evolution of the data is found in Figure S7. The black arrows denote Bragg reflections that could not be indexed by the parent rock-salt lattice, which also did not change with cycling. The stars represent the newly formed peaks concurrent with Li (de)intercalation. 98
- Figure 4-7.** *Operando* SXRD patterns in the first cycle of a D- Li_3RuO_4 /Li half-cell at a rate of C/20. The left panel shows the corresponding galvanostatic curve between 2.5 and 3.9 V. Colored lines indicate key points in the experiment, discussed in the text. 99
- Figure 4-8.** Pawley refinements of SXRD patterns of D- Li_3RuO_4 at different electrochemical states between 2.5 V and 3.9 V. 100
- Figure 4-9.** (a) *Ex situ* SXRD patterns of ordered Li_3RuO_4 after the first cycling; (b) *Ex situ* Laboratory XRD patterns when the capacity reached maximum. The black dots represent the Bragg reflections from Al foil. “Max Cap” in (b) is the abbreviation of “Maximum Capacity”. (c) Enlarged and (d) overlaid SXRD patterns of O- Li_3RuO_4 during the first cycle. There was no obvious peak shift upon cycling. The intensity experienced substantial decrease after oxidation

- to 3.9 V, while the subsequent reduction did not bring about remarkable change in the intensity in relative to that of the previous oxidation. 102
- Figure 4-10.** Pawley refinements of XRD patterns of O-Li₃RuO₄ at different electrochemical states. Panel a shows the SXRD patterns. Panel b portraits the XRD results collected by the Cu K α irradiation. 103
- Figure 4-11.** (a) *Ex situ* Ru K-edge XANES spectra and (b) the corresponding derivative curves of RuO₂, disordered Li₃RuO₄ and ordered Li₃RuO₄. 105
- Figure 4-12.** (a) *Ex situ* Ru K-edge XANES spectra of D-Li₃RuO₄ at different electrochemical states and (b) zoom of the pre-edge region. The inset in (a) presents the corresponding derivative curves, used to define the position of the absorption edge. RuO₂ was used as reference for Ru⁴⁺. 106
- Figure 4-13.** (a) *Ex situ* Ru K-edge XANES spectra of O-Li₃RuO₄ at different electrochemical states and (b) zoom of the pre-edge region. The inset in (a) presents the corresponding derivative curves, used to define the position of the absorption edge. RuO₂ was used as reference for Ru⁴⁺. “Max Cap” here denotes data at cycles with maximum capacity (see text). 107
- Figure 4-14.** *Ex situ* O K-edge XAS spectra of (a) D- and (b) O-Li₃RuO₄ measured at different electrochemical states between 2.5-3.9 V. “Max Cap” in (b) is the abbreviation of “Maximum Capacity”. The peak at ~533.8 eV is ascribed to the existence of Li₂CO₃ in both (a) and (b). 110
- Figure 4-15.** *Ex situ* O K-edge XAS spectra of (a) disordered Li₃RuO₄ and (b) ordered Li₃RuO₄ at different states collected under TEY (dot line) and TFY (solid line) detection modes. 110
- Figure 4-16.** *Operando* gas evolution of D- (a) and O- (b) Li₃RuO₄, as measured by DEMS for the first cycle. 112
- Figure 4-17.** Voltage-composition profiles of D-Li₃RuO₄ between 1.5 and 2.5 V upon (a) the first 20th cycling and (c) extensive cycling. (b) Differential capacity analysis (dQ/dV) of D-Li₃RuO₄. (d) Discharge capacity and coulombic efficiency as a function of the cycle number. 114
- Figure 4-18.** Voltage-composition profiles of O-Li₃RuO₄ between 1.5 and 2.5 V upon (a) the first 20th cycling and (c) extensive cycling. (b) Differential capacity analysis (dQ/dV) of O-Li₃RuO₄. (d) Discharge capacity and coulombic efficiency as a function of the cycle number. 115
- Figure 4-19.** SXRD patterns of D-Li₃RuO₄ at selected points during the first cycle within a potential range of 1.5-2.5 V, collected *operando*. The complete evolution of the data is found in Figure 4-22. The black arrows denote the invariant Bragg reflections from the background only. 116
- Figure 4-20.** *Operando* SXRD patterns in the first cycle of a D-Li₃RuO₄/Li half-cell at a rate of C/20. The left and middle panels show the contour plot and the corresponding galvanostatic curve between 1.5 V and 2.5 V. Black, red and blue patterns represent the pristine, the fully discharged and the fully charged state, respectively. 117
- Figure 4-21.** Pawley refinements of SXRD patterns of D-Li₃RuO₄ at different electrochemical states within 1.5 and 2.5 V. 117
- Figure 4-22.** (a) *Ex situ* SXRD patterns of O-Li₃RuO₄ at different electrochemical state within the range of 1.5-2.5 V. (b) Rietveld refinement of SXRD pattern of Li_{4.6}RuO₄. The black crosses and red solid line represent the observed and calculated patterns. The green vertical tick bars denote

the Bragg reflections. The blue continuous line is the difference between calculation and observation.	119
Figure 4-23. Pawley refinements of SXRD patterns of O-Li ₃ RuO ₄ at different electrochemical states between 1.5 and 2.5 V.	120
Figure 4-24. <i>Ex situ</i> Ru K-edge XANES spectra of (a) D-Li ₃ RuO ₄ and (b) O-Li ₃ RuO ₄ at different electrochemical states in the 1.5-2.5 V window, and (b) zoom of the pre-edge region. The insets in (a) and (c) present the corresponding derivative curves, used to define the position of the absorption edge. RuO ₂ was used as reference for Ru ⁴⁺	122
Figure 4-25. <i>Ex situ</i> O K-edge XAS spectra of (a) D- and (b) O-Li ₃ RuO ₄ measured at different electrochemical states between 1.5 and 2.5 V.	123
Figure 4-26. Schematic summary of the electrochemical reactions of Li ₃ RuO ₄ systems observed in this study.	124
Figure 4-27. Image of a coin cell after the removal of 0.5 mol Li from per mol O-Li ₃ RuO ₄ . Clear black color can be observed on the otherwise white separator.	126
Figure 4-28. Voltage-composition profiles of (a-c) D-Li ₃ RuO ₄ and (d-f) O-Li ₃ RuO ₄ at different states of charge. (a) and (d) directly discharged to 1.5 V, (b) charged to 3.81 V and discharged to 1.5 V, (e) charged to 3.9 V and discharged to 1.5 V, (c) and (f) cycled between 1.5-2.5 V and then charged to 3.9 V and discharged to 1.5.	128
Figure 4-29. <i>Ex situ</i> Ru K-edge XANES spectra of (a) D-Li ₃ RuO ₄ and (c) O-Li ₃ RuO ₄ electrodes in Figure 4-27, compared to the pristine state, with the corresponding 1 st derivative curves in (b) and (d).	129
Figure 4-30. Comparison of <i>ex situ</i> Ru K-edge XANES spectra of D-Li ₃ RuO ₄ in different electrochemical state and (b) corresponding derivative curves.	130
Figure 4-31. Comparison of <i>ex situ</i> Ru K-edge XANES spectra of O-Li ₃ RuO ₄ in different electrochemical states and (b) corresponding derivative curves.	130
Figure 4-32. Overlaid <i>ex situ</i> O K-edge XAS spectra of (a) D- and (b) O-Li ₃ RuO ₄ measured at different electrochemical states. See text for discussion.	131
Figure 4-33. Gas evolution during the first two cycles of D- (black line) and O- (red line) Li ₃ RuO ₄ measured by <i>operando</i> DEMS. The voltage profiles are shown in the bottom panels.	132
Figure 4-34. (a) Evolution of the voltage-composition profile upon cycling of a D-Li ₃ RuO ₄ electrode, when the first charge capacity was limited to 1.25 mol Li extracted; (b) Discharge capacity and coulombic efficiency as a function of the cycle number.	134
Figure 5-1. (a) Voltage-composition profile of Li ₃ IrO ₄ collected electrochemically. The states of interest for <i>ex situ</i> analysis are marked. (b) <i>Ex situ</i> O K α XES spectra of Li ₃ IrO ₄ with the specific excitation energy set to the respective arrows on the right. The excitation energy is displayed to the left of the O K α emission spectra. (c) <i>Ex situ</i> O K-edge XAS spectra of Li ₃ IrO ₄ at difference electrochemical states of charge measured under PFY mode. (d) Differential XAS spectra between states of charge indicated. Integrated intensity under the pre-edge region between 525 and 530 eV (t _{2g} region in an undistorted ligand field) (e) and between 530 and 535 eV (e _g) (f) for PFY O K-edge XAS at states indicated.	139

- Figure 5-2.** (a) Voltage-composition profile of Li_3IrO_4 collected electrochemically. The states of interest for *ex situ* analysis are marked. Magnetization measurement of Li_xIrO_4 with different Li contents at $x = 3$ (b), $x = 2$ (c), $x = 1$ (d), $x = 4$ (e) and $x = 4.7$ (f). The black circles are zero-field cooled magnetic susceptibility measurements, the red line is obtained from fitting the data with a modified Curie-Weiss law, with the fitting parameters indicated, and the blue circles are the inverse magnetic susceptibility after removing the temperature independent contribution χ_0 140
- Figure 5-3.** O K-edge XAS spectra of Li_3IrO_4 at different electrochemical states measured under (a) TFY (solid) and TEY (short dot) and (b) TFY (solid) and PFY (dot) modes. The intense peak at approximate 533.7 eV dictated by the vertical dot line in TEY implied a predominant presence of Li_2CO_3 in the surface. The corresponding small peak in TFY showed Li_2CO_3 was present at thickness significant enough to be visible in a measurement probing ~ 100 nm into the material. PFY spectra of samples handled in Ar-filled glovebox immediately after the synthesis showed the absence of this peak from Li_2CO_3 141
- Figure 5-4.** *Ex situ* O $K\alpha$ X-ray emission spectra of pristine Li_3IrO_4 at an excitation energy of 527.85 and 529.05 eV. 141
- Figure 5-5.** (a) Electron localization Function (ELF), as computed within the DFT framework for the pristine Li_3IrO_4 phase showing 2 and 3 lone-pairs around $\text{O}_{2\text{LP}}$ (red) and $\text{O}_{3\text{LP}}$ (orange), respectively, in agreement with their different local environments. The Lewis structures of the two different oxygen sites obey the octet rule stating that O^{2-} is stable with four electron-pairs distributed into n bonding-pairs (involved in Ir-O) and $4 - n$ lone-pairs (un-hybridized to Ir). (b) Atom-projected density of states (pDOS) showing a shift in energy of $\text{O}_{3\text{LP}}$ lone-pair states with respect to $\text{O}_{2\text{LP}}$ due to a lower Madelung potential (\mathcal{M}_O). A Mott insulator electronic ground-state is obtained for Li_3IrO_4 , with a small energy gap for the Li/Ir ordered structure that cancels out when disorder is introduced in the model. (c) Simulated XAS spectra of the ordered and disordered Li_3IrO_4 structures (see Supplementary Information for details) with or without including core-level shift (CLS) in the calculations. The XAS projected on the $\text{O}_{3\text{LP}}$ and $\text{O}_{2\text{LP}}$ absorbing species showing that the splitting of the first excitation peak arises from the different oxygen electronic structures, the $\text{O}_{3\text{LP}}$ 1s core-level having a lower binding energy than $\text{O}_{2\text{LP}}$ 1s. 143
- Figure 5-6.** Crystal structure of the Li_3IrO_4 pristine phase and its associated Electron Localization Function (ELF), as considered in DFT calculations with (right) and without (left) Li/Ir disorder. The ordered structure displays regular zig-zag chains of edge-shared octahedra with red oxygens connected to 2 Ir atoms and orange oxygens connected to only 1 Ir atom. The disordered structures are obtained by exchanging one Li and one Ir atoms, leading in the present case to three different IrO_6 octahedra occurring in the unit cell (instead of one only in the ordered structure) with different number of red and orange oxygens (see Table S1). Electron Localization Functions (ELF) invariably show that all oxygens connected to 1 and 2 Ir atoms display 3 and 2 lone pairs (yellow volumes), respectively, in perfect accord with the octet rule and with the Li^+ , O^{2-} and Ir^{5+} formal oxidation states..... 144
- Figure 5-7.** Voltage-composition profiles of Li_3IrO_4 at different cutoff voltage window. The electrochemical states of interest are represented with labels of different colors. Samples were harvested from the representative states. 146
- Figure 5-8.** First (a) and second derivative (b) plots of O K-edge XAS spectra of Li_3IrO_4 at different states of charge indicated in the electrocheical profiles (Figures 5-1a). 147

- Figure 5-9.** (left) Simulated vs. experimental XAS spectra for Li_3IrO_4 , Li_2IrO_4 and LiIrO_4 showing that the evolution of the excitation peaks are due to the progressive participation of the two oxygen sites in the oxidation process of the pristine material. (right) Electron localization functions (right) computed for each structure and confirming the main oxidation of $\text{O}_{3\text{LP}}$ (orange) from $x=3$ to $x=2$ and a mixed oxidation of $\text{O}_{2\text{LP}}$ (orange) and $\text{O}_{2\text{LP}}$ (red) from $x=2$ to $x=1$. Other results with different Li/Ir disorder are shown in Figure 5-9. 149
- Figure 5-10.** (a) ELF and atom-projected Density of States (pDOS) for the partially delithiated Li_2IrO_4 phase showing that $\text{O}_{3\text{LP}}$ becomes redox-active when Li/Ir disorder is introduced in the calculation. It is labelled $\text{O}_3 \rightarrow 2\text{LP}$ (orange), the color and the subscript referring to the connection to 1 Ir atom and the involvement of one lone pairs in the electrochemical process, respectively. (b) ELF and pDOS for the ordered and disordered Li_1IrO_4 phases showing now the involvement of both orange ($\text{O}_3 \rightarrow 2\text{LP}$) and red ($\text{O}_2 \rightarrow 1\text{LP}$) oxygens in the process, with a relative participation depending on the Li/Ir distribution..... 150
- Figure 5-11.** (a) and (b) Voltage-composition profiles of Li_3IrO_4 collected under the galvanostatic mode. The electrochemical states of interest are marked. D is the state after the sample was reduced to 2.6 V followed by 1 mol Li removal. E is the state after the sample was reduced to 1.8 V followed by 1 mol Li removal. F is the state after the sample was reduced to 1.3 V followed by 1 mol Li removal. G is the state after the sample was re-oxidized to 3.0 V followed by 1 mol Li removal. I is the state after the sample was initially reduced to 1.3 V. (c) *Ex situ* O 1s XAS spectra of Li_xIrO_4 at difference electrochemical states of charge measured under PFY mode (D, and G) and TFY mode (E, F and I). The peak at around 533.7 eV (denoted by the asterisk symbol) for samples E, F and I is related to carbonate-related peak due to the transitions to π^* (C=O) orbitals, which has little influence on the spectral interpretation..... 153
- Figure 5-12.** Simulated XAS spectra of different electrochemical states and the corresponding experimental ones..... 154
- Figure 5-13.** The first (a) and second derivative (b) plots of O K-edge XAS spectra of Li_3IrO_4 at different states of charge indicated in the electrochemical profile..... 155
- Figure 5-14.** *Ex situ* O K-edge RIXS maps of Li_3IrO_4 at the different electrochemical states indicated. The white rectangular regions represent the elastic peak. 158
- Figure 6-1.** Joint Rietveld refinement of SXRD and NPD patterns of Li_7RuO_6 pristine. Black crosses: experimental patterns, red solid line: calculated patterns, blue solid line: difference and green bars: Bragg reflections..... 162
- Figure 6-2.** SXRD patterns of Li_7RuO_6 pristine sample and the Bragg diffractions of references. The down triangles signify the unknown phase. 162
- Figure 6-3.** Crystal structure of pristine Li_7RuO_6 . Red sphere represents oxygen atom, and green sphere represent lithium atom, and purple sphere represents ruthenium atom. 163
- Figure 6-4.** Voltage-composition profile of Li_7RuO_6 in the voltage window of 2.6-3.68 V upon the first cycling (a) and (c) upon extensive cycling. The dQ-dV plots of the first charge-discharge process (b) and the extensive cycling processes (d). 165
- Figure 6-5.** (a) Voltage-capacity profiles of Li_7RuO_6 between 1.5 and 4.3 V. (b) Voltage-composition profiles of Li_7RuO_6 under a constrained voltage window between 2.6 V and 3.5 V upon extensive cycling. 166

- Figure 6-6.** *Ex situ* SXRD patterns of Li_7RuO_6 upon (a) the first and (b) the second charge and discharge in the voltage window of 2.6-3.68 V. 167
- Figure 6-7.** (a) *Ex situ* Ru K-edge XANES spectra of RuO_2 reference, Li_7RuO_6 pristine, and Li_3RuO_4 pristine and (b) the corresponding first derivative. 168
- Figure 6-8.** (a) *Ex situ* Ru K-edge XANES spectra of Li_7RuO_6 at different states of charge in the voltage window of 2.6-3.68 V as well as RuO_2 reference, and (b) the corresponding first derivative. 169
- Figure 6-9.** (a) *Ex situ* O K-edge XAS spectra of Li_7RuO_6 at different states of charge in the voltage window of 2.6-3.68 V measured under TFY mode. (b) Differential XAS spectra between states of charge indicated. (c) The integrated pre-edge area below 530 eV as a function of x in Li_xRuO_6 . (d) The dependence of the integrated pre-edge above 530 eV on x in Li_xRuO_6 171
- Figure 6-10.** (a) *Ex situ* O K-edge XAS spectra of Li_7RuO_6 pristine state measured the total electron yield (TEY) mode and the total fluorescence yield (TFY) mode. The asterisk denotes a peak associated with the presence of Li_2CO_3 on the surface of the material. (b) *Ex situ* O K-edge XAS spectra of Li_7RuO_6 at different states of charge, measured in TEY mode. The green dot line denotes the preservation of the 535-eV feature in both modes. The purple short-dash line represents the feature associated with the carbonate-related species. 172
- Figure 6-11.** First derivative of the TFY O K-edge XAS spectra of Li_7RuO_6 at different states of charge in the voltage window of 2.6-3.68 V. The black dot line represents the reservation of the position of the inflection point. 173
- Figure 6-12.** Voltage-composition profiles of Li_7RuO_6 in the voltage window between 1.5 and 2.6 V upon the first cycle (a) and upon extensive cycling processes (b). The dQ-dV plots of the first charge-discharge process (b) and the extensive cycling processes (d). 174
- Figure 6-13.** *Ex situ* SXRD patterns of Li_7RuO_6 upon (a) the first and (b) the second cycling between 1.5 V and 2.6 V. 174
- Figure 6-14.** Rietveld refinement of SXRD patterns of Li_7RuO_6 after reduction to 1.5 V. Black crosses: experimental patterns, red solid line: calculated patterns, blue solid line: difference and green bars: Bragg reflections. 175
- Figure 6-15.** Crystal structure of pristine Li_8RuO_6 . Red sphere represents oxygen atom, and green sphere represent lithium atom, and purple sphere represents ruthenium atom. 176
- Figure 6-16.** *Ex situ* Ru K-edge XANES spectra of Li_7RuO_6 at different states of charge in the 1.5-2.6 voltage window as well as the reference RuO_2 177
- Figure 6-17.** (a) *Ex situ* O K-edge XAS spectra of Li_7RuO_6 at different states of charge in the voltage window of 1.5-2.6 V V measured under TFY mode. (b) Differential XAS spectra between states of charge indicated. (c) The integrated pre-edge area below 530 eV as a function of x in Li_xRuO_6 . (d) The dependence of the integrated pre-edge above 530 eV on x in Li_xRuO_6 178
- Figure 6-18.** (a) *Ex situ* O K-edge XAS spectra of Li_7RuO_6 at different states of charge under the total electron yield (TEY) mode. The green dot line betokens the preservation of the 535-eV feature under both modes. The purple dot line represents the feature associated with the carbonate-related species. (b) The first derivative plots of the TFY O K-edge XAS spectra of Li_7RuO_6 at different states of charge in the voltage window of 1.5-2.6 V. The black dash line represents the remaining of the position of the inflection point. 178

List of abbreviations

APS	Advanced Photon Source
ANL	Argonne National Laboratory
SNS	Spallation Neutron Source
ORNL	Oak Ridge National Laboratory
ALS	Advanced Light Source
BNL	Berkeley National Laboratory
CLS	Canadian Light Source
EC	Ethylene carbonate
HAADF-STEM	High-angle annular dark field scanning tunneling electron microscope
NMP	N-methyl-2-pyrrolidone
PVDF	Polyvinylidene fluoride
SEM	Scanning electron microscopy
TEY	Total electron yield
TFY	Total fluorescence yield
PFY	Partial fluorescence yield
XAS	X-ray absorption spectroscopy
XRD	X-ray diffraction
TOF	Time of flight
ND	Neutron diffraction
XES	X-ray emission spectroscopy
RIXS	Resonant inelastic X-ray scattering
DFT	Density functional theory
VASP	Vienna ab initio simulation package
LDA	local-density approximation

Summary

High-energy-density batteries have been a long-standing target toward achieving a sustainable society featuring electric transport and grid-scale utilization. However, the energy density of state-of-the-art Li-ion batteries is limited in part by the small capacity of the cathode materials associated with the transition metal redox reactions only. Tapping the lattice oxygen redox in Li-rich transition metal oxides could cross the current barriers of the capacity by providing additional capacities. However, the associated voltage fade and structural reorganization have prevented their commercialization. These technological disadvantages are mainly underpinned by the unclear mechanisms whereby the lattice oxygen redox reactions are activated and stabilized. Building a thorough picture of the mechanisms of lattice oxygen redox is a critical to design next-generation cathode materials with high energy density.

This thesis begins with an overview of common Li-rich transition metal oxides and associated oxygen redox reactions, focusing on the activation and stabilization of oxygen redox reactions under different circumstances, leading to diverse and ambiguous viewpoints of chemistry in initiating and stabilizing the oxygen redox. This complexity of the lattice oxygen redox revealed that comprehensive analytical techniques, described in Chapter 2, should be needed to study the lattice oxygen redox by probing the variation in both crystal and electronic structure. Galvanostatical electrochemical cycling could provide insights into the macroscopic battery performance, whereas diffraction and spectroscopy unravel changes in electrode crystallographic and electronic structures, all of which could provide unique insights into the electrode materials.

In order to clearly understand the chemistry of the lattice oxygen redox reaction, a series of Li-rich 4d/5d transition metals oxides are investigated in this thesis. Li_2RuO_3 , firstly studied as a canonical model of Li-rich oxides, displayed typical electrochemical performance of Li-rich cathodes with the staircase profile upon the first charge and sloping profiles upon the reverse discharge, reflecting a large hysteresis, and relatively reversible subsequent cycling with less hysteresis. The *operando* synchrotron X-ray

diffraction demonstrated that the structure of Li_2RuO_3 evolved from monoclinic to trigonal arrangement upon the initial delithiation to 4.6 V and into a much more disordered structure than the pristine state upon re-lithiation to 2.0 V. X-ray spectroscopy of both Ru and O revealed a conventional cationic redox reaction involving $\text{Ru}^{4+}/\text{Ru}^{5+}$ couple upon Li extraction to 3.9 V. Further oxidation was accompanied by Ru reduction and O participation. The re-lithiation is associated with a mechanism where the formal oxidation state of Ru was reduced, even beyond the pristine state. Clearly, the changes in both crystal and electronic structure upon first oxidation were not mirrored upon reverse reduction, providing an explanation to the electrochemical hysteresis. Study of samples upon extensive cycling showed that the electrochemical reactions were accompanied by changes at both Ru and O consistent with a conventional model of redox via changes in the formal Ru state.

In comparison with the stoichiometry of Li_2RuO_3 , the amount of non-bonding O 2p states is predicted to increase with the increase of O/TM ratio, which is the initial motivation to utilize another compound Li_3RuO_4 to explore the lattice oxygen redox. Two polymorphs of Li_3RuO_4 were obtained with different Ru/Li ordering by varying the synthetic temperature. Both polymorphs displayed highly reversible Li intercalation within the voltage window between 1.5 and 2.5 V, with a conventional cationic redox with $\text{Ru}^{5+}/\text{Ru}^{4+}$ couple. However, both polymorphs could undergo anionic Li extraction to 3.9 V, which was accompanied by a predominant O activity. The following re-intercalation unlocks a different yet conventional pathway also involving the formal $\text{Ru}^{5+}/\text{Ru}^{4+}$ couple despite operating above 2.5 V. This new pathway is both chemically and electrochemical reversible in subsequent cycles.

Although Li_3RuO_4 unraveled an explicit evidence of oxygen activity upon the initial delithiation, the O activity was not remained for the subsequent Li re-intercalation which was not a mirror to the previous process. In contrast, Li_3IrO_4 exhibits reversible cycling of 2 mol Li per mol TM, which enables it an ideal compound to investigate the oxygen redox. Via a combination of experiments and computations, the existence of non-equivalent O sites with different number of non-bonding O 2p states in the pristine state was confirmed due to the disordered Li/Ir arrangement. Upon oxidation of Li removal, the O site with 3

electron lone pairs was mainly involved in the oxygen redox for the charge compensation, which was fully reversible for the subsequent reduction of Li re-intercalation process. In spite of the pronounced oxygen redox, the commonly reported RIXS signatures were absent, indicating multiple possible pathways of the oxygen redox may exist, with different electronic and structural implications. In addition, further lithiation to $\text{Li}_{4.7}\text{IrO}_4$ is highly reversible in both electrochemistry and chemistry, which is a typical conventional intercalation process accompanied by changes in the formal oxidation state of Ir as a proxy for the Ir-O covalent bond.

In order to further study the effect of O/TM ratio on the lattice oxygen activity, Li_7RuO_6 with higher O/TM ratio of 6 was employed as another model to investigate the charge compensation mechanism. Li_7RuO_6 exhibited highly reversible Li intercalation to Li_8RuO_6 within the voltage window range of 1.5-2.6 V, following a conventional cationic redox reaction via the formal $\text{Ru}^{5+}/\text{Ru}^{4+}$ couple. In contrast, the electrochemical performance between 2.6 and 3.68 V behaved quite distinct and complicated. Constricting the oxidation to 3.5 V led to reversible (de)lithiation, without any hysteresis, accompanied by the formal $\text{Ru}^{5+}/\text{Ru}^{6+}$ redox reaction. The associated O participation was through Ru-O covalent interaction and did not involve tapping any existing lone pairs. In contrast, further oxidation to 3.68 V brought about additional capacity, which was associated with the lattice oxygen redox and little involvement of Ru redox. The reverse reduction was irreversible and resulted in a noticeable hysteresis, reflecting a different pathway from the oxidation, with a dominant contribution from Ru.

Chapter 1 Introduction

1.1 Motivation

Since the commercial lithium ion (Li-ion) battery was first introduced by Sony Corporation in 1991 using a LiCoO_2 cathode and a C_6Li anode,¹ the rechargeable Li-ion battery technology has dominated the consumer electronic market and power a series of portable electronic devices including cell phones, laptops and many others. This dominance is due to the high stored volumetric and gravimetric energy density compared with other battery technologies as shown in Figure 1-1, enabling the realization of a wireless revolution in our society.² With the increased concerns of the climate change due to the vast greenhouse gas emission from the burning of fossil fuels and biomass, there is a strong push to enable renewable energy sources, such as solar radiation, wind and waves, as environmentally friendly alternatives. However, due to the intrinsic issue of the intermittency arising from variable atmospheric conditions, energy storage devices used to safely and efficiently store the generated energy are required, especially to transfer it to light duty vehicles. Among the energy carriers, portable chemical energy in the form of Li-ion battery is the most convenient and efficient form of energy storage. These technologies lead to the ever increasing demand for leaps in energy density from current levels.

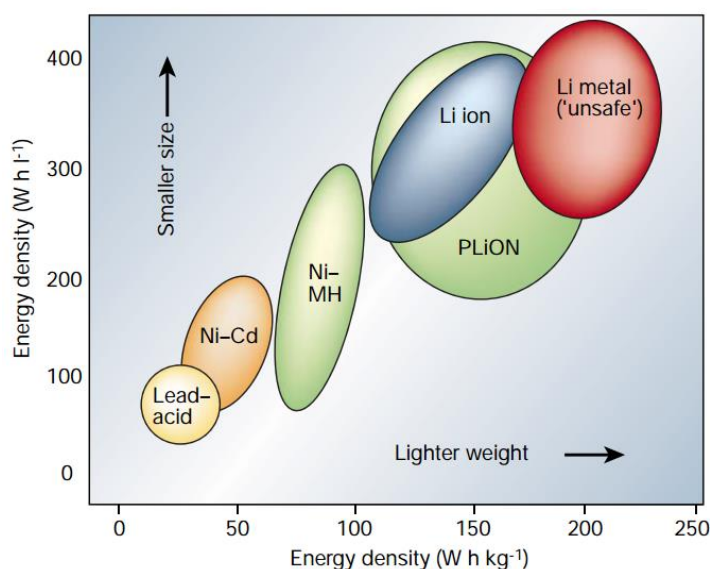


Figure 1-1. Comparison of different rechargeable battery technologies in terms of energy density and specific energy. Reprinted with permission from “Issues and challenges facing rechargeable lithium batteries”.³ Copyright © 2001 Springer Nature.

1.2 Fundamental principle of rechargeable Li-ion batteries

In the 1970s, Whittingham reported the first lithium battery based on the lithium (de)intercalation process by employing the cathode TiS_2 , anode pure lithium metal and electrolyte lithium perchlorate dissolved in dioxolane.^{4, 5} Although TiS_2 was considered the best layered compound then, favoring a reversible lithiation/delithiation process, the inhomogeneous deposition of Li on the surface of the lithium metal gave rise to the formation of dendrites (Figure 1-2a), which may penetrate the separator and therefore result in the short circuit, leading to fire and even explosion. To circumvent the safety issues induced by the use of the lithium metal, Armand *et al.* first proposed to use a second insertion material as an alternative to substitute metallic lithium.⁶ This concept was first proved realistically by Murphy *et al.*⁷ and then Scrosati *et al.*⁸, which finally led to what we called Li-ion batteries in early 1990s (Figure 1-2b).³

Li-ion batteries are electrochemical energy storage devices that manifests the conversion of chemical energy into electrical energy via the electrochemical oxidation-reduction (redox) reaction at the electrodes (anode and cathode) concurrent with Li (de)intercalation. In contrast to the primary battery, which is supplied fully charged and discarded after use, the rechargeable (or secondary) battery could be charged and discharged for multiple times. In general, a Li-ion battery consists of a stack of electrochemical cells that are connected in series or in parallel to provide the voltage and capacity as required, where the overall voltage is dependent on the potentials of the individual electrochemical cell. Each electrochemical cell consists of two electrochemically active couples (the positive electrode or cathode, and the negative electrode or anode) of chemical reactions, the electrodes being separated by an ion conductive but electronically insulating medium (electrolyte). The basic principle of the normal Li-ion battery operation is described as follows: upon discharging, the Li ions de-intercalate out of the anode and intercalated into the cathode by crossing the electrolyte, while simultaneously electrons flow from the anode to the cathode via

the external electrically conductive circuit to maintain the electric neutrality, and also do the useful work; upon the subsequent charging, the process reverses (Figure 1-2). In a rechargeable battery, the discharge-charge process must be highly reversible, with the integrity of the electrolyte and electrodes maintained for multiple discharge-charge process.

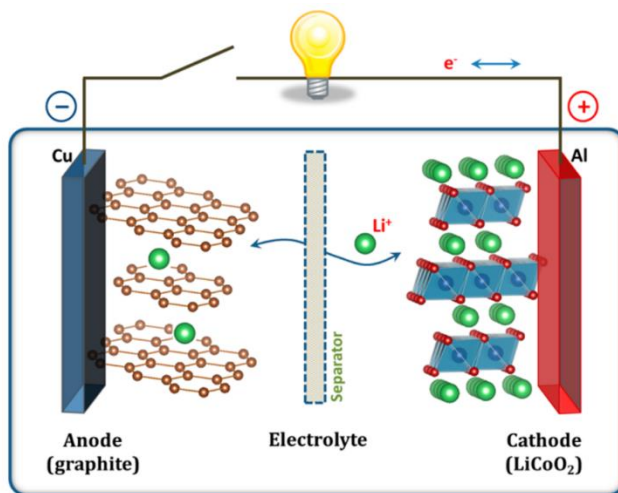


Figure 1-2. Schematic illustration of typical electrochemical cell in a commercial Li-ion battery comprised of the first-generation layered oxide LiCoO₂ as cathode and graphite as anode. Reprinted with permission from “The Li-Ion Rechargeable Battery: A perspective”.⁹ Copyright © 2013 American Chemical Society.

The theoretical electrochemical reactions involved in the operation of the above described Li-ion battery in Figure 1-2 are demonstrated as follows:



Where equation 1.1 represents the half reaction at the cathode side, and equation 1.2 stands for the counterpart at the anode side, and equation 1.3 is the overall electrochemical reaction.

One of the greatest goals in the Li-ion battery research is to develop devices with high energy density. The energy density of a battery, defined in Whl⁻¹, or its equivalent specific energy, in Whkg⁻¹, are equal to

the product of the specific capacity and cell voltage.¹⁰ The specific capacity is determined by the total amount of electric charge (q) per mass or volume that is reversibly transferred between electrodes during the electrochemical cycling.¹¹ The number of electrons involved in an ideal electrochemical cell is theoretically equal to the number of Li⁺ ions that are reversibly extracted out of (inserted into) the electrodes. The corresponding specific capacity could be calculated using the following equation:

$$\text{Specific capacity} = \frac{n \times F}{M} \times \frac{1000}{3600} \quad (1.4)$$

Where n is the number of moles of Li⁺ ions that can be reversibly intercalated into (de-intercalated out of) the electrode within a designated voltage window, and M is the molecular mass of the electrode host, and F is the Faraday constant with a value of 96485 Cmol⁻¹. According to equation 1.4, a high specific capacity of an electrode requires a light electrode material (small M) that can reversibly store and release a large amount of Li⁺ ions (large n).

Cell voltage is the second factor that determines the energy a battery can store, which is defined by the electrochemical potential difference between cathode electrode and anode electrode, as described in the following equation:

$$E_{\text{cell}} = E_{\text{cathode}} - E_{\text{anode}} \quad (1.5)$$

where E_{cathode} and E_{anode} represent the potential of cathode and anode vs Li⁺/Li⁰, respectively.

This difference is the work that is needed when an elementary electrical charge is moved from one point to the other. The larger the difference in potential between two points, the stronger the force is exerted on a charged particle transferred between two points. When electric charges (q) are moved across a potential difference (E), the work that is required is as follows:

$$\text{Work} = E \times q \quad (1.6)$$

Based on the laws of thermodynamics, the change of the Gibbs free energy, ΔG , in an electrochemical cell operated at constant temperature and pressure, equals the maximum electrical work that can be attained by the electrochemical reaction with the following equation:

$$Work = -\Delta G \quad (1.7)$$

The negative sign dictates the Gibbs free energy decreases with the output work.

The fundamental principle used to relate the potential difference (E) to the electronic charge (q) via the variation of the Gibbs free energy is described in equation 1.8:

$$\Delta G = \int_0^Q E(q) dq \quad (1.8)$$

where the potential difference E is not a constant value and varies with the electronic charge. In practice, often, the potential difference is constant during the entire electrochemical cycling process, which, hence, could simplify equation 1.8 to the commonly used:

$$\Delta G = -nFE_{cell} \quad (1.9)$$

where n represents the amount of electronic charges involved in the electrochemical reaction in terms of moles. F is the Faraday constant with a value of 96485 Cmol⁻¹. The product of n and F is the total amount of electric charges q.

Based on equation 1.9, therefore, in order to increase the capability of the energy storage of a battery, that is to increase the magnitude of ΔG , one can increase the specific capacity of cathodes and anodes and/or increase the reaction potential.

Aside from the energy density, power (current) density, also expressed as rate capability, is another factor to evaluate the performance of the Li-ion battery.^{12, 13} The power density is the product of the current and cell voltage, normalized per unit of volume.¹² High power density is of significant importance for applications such as electric vehicles because of the desire of the consumer to charge the battery (i.e. “re-fuel”) fast. The power density depends on the cell resistances (impedances) originating from various factors such as charge transfer at the electrode/electrolyte interface, mass transfer related to the Li diffusion within electrodes, and electric resistance of the electrolyte associated with its ionic conductance.² A battery with large impedances has a poor rate capability and severe energy loss due to the conversion of a large portion of the stored electrical energy into heat upon cycling.

In addition, battery life, cost and safety should also be required to satisfy requirements of Li-ion batteries.² Battery life is a measure of battery performance and longevity, which can be defined as the total number of reversible charge-discharge cycles before the specific capacity of the battery reduces to a cut-off limit. During the operation of the battery, the occurrence of various parasitic reactions and the continuous degradation of electrodes could deteriorate the performance of the battery. Low cost is also crucial for a wide application of Li-ion batteries, especially for large scale applications with large upfront costs. Like cost, safety is a critical requirement for large scale power batteries due to the potential fire and explosion and release of hazardous materials.

The electrochemical performance of Li-ion batteries is largely dependent on the behavior of battery electrodes.^{2, 14, 15} In order to meet the demand of high performance Li-ion batteries, hence, it is imperative to develop electrode cathodes/anodes with better electrochemical properties. The key requirements for a high performance electrode material are listed as follows:

- (1) The material should reversibly store and release a large amount of Li^+ ions while preserving the structural integrity upon extensive charge-discharge processes. This feature would ensure high capacity with good reversibility.
- (2) The material should react with Li^+ ions within a reasonable voltage window of the electrolyte. Within the safe voltage window, a high (low) potential is preferred for a cathode (anode) material, which could result in a high cell voltage and contribute to the increase of the energy density.
- (3) The material should be a good electronic conductor and react with Li^+ ions very rapidly both on insertion and removal. This could enable high diffusion of Li^+ ions and reduce the hysteresis and thus lead to the high power density.
- (4) The material should be thermally stable without oxygen evolution and heat release at high temperature. Oxygen release is an exothermic reaction, which could significantly elevate the temperature inside the battery. The coexistence of oxygen gas and a flammable organic electrolyte under the high temperature

condition could cause the battery to catch fire. This scenario, which is the common source of publicized battery fires, must be inhibited.

(5) The material's mass and dense should be light such that the specific energy and energy density would be high.

(6) The material should be low cost and environmentally benign.

So far extensive research has been devoted to a variety of cathode and anode electrodes for the potential application in Li-ion batteries. Figure 1-3 displays commonly studied materials as a function of their specific capacity and battery operational potential.

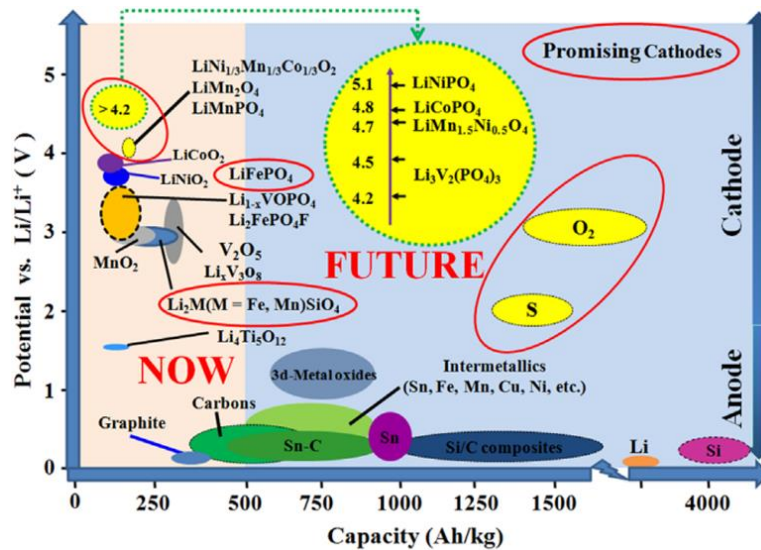


Figure 1-3. Relationship of the cell voltage with the specific capacity for electrodes intensively studied today, in conventional electrolyte, 1M LiPF₆ dissolved in diethyl carbonate (DEC) and ethylene carbonate (EC) with the volume ratio of 1:1. Reprinted with permission from “Cathode materials for next generation lithium ion batteries”.¹⁶ Copyright © 2013 Elsevier Ltd.

1.3 Li-rich transition-metal oxides

While all components in the Li-ion battery are very important, the cathodes are the component limiting performance, especially energy density and cost.² It is therefore critical to design cathodes with high electrochemical performance.

Although there exist multiple choices of compounds for cathodes, none of them are perfect. So far three common structural families have been employed for practical applications (Figure 1-4): lithium transition-metal oxides LiM_2O_4 ($\text{M} = \text{Mn}$ etc.) with a spinel structure (Figure 1-4a), lithium transition-metal orthophosphates LiMPO_4 ($\text{M} = \text{Mn}, \text{Fe}, \text{Co}, \text{Ni}$, etc.) with an olivine structure (Figure 1-4b), and layered lithium transition-metal oxides LiMO_2 ($\text{M} = \text{Co}, \text{Ni}$, etc.) with an ordered rock-salt structure (Figure 1-4c).

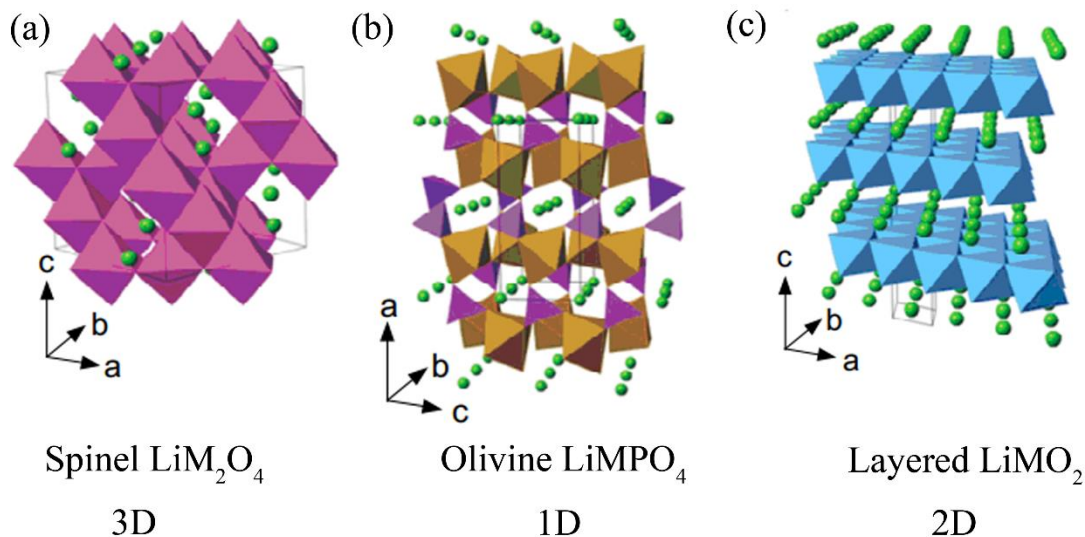


Figure 1-4. Crystal structure of (a) LiM_2O_4 , (b) LiMPO_4 and (c) LiMO_2 in which Li^+ ions migrate via 3D, 1D and 2D frameworks, respectively. Adapted with permission from “Comparative Issues of Cathode Materials for Li-Ion Batteries”.¹⁷ Copyright© 2014 MDPI.

Each of them has its own advantages and disadvantages. Spinel-type LiMn_2O_4 , proposed first by Thackeray et al. in 1983 displays an excellent rate capability but with a low practical discharge capacity ($\sim 110\text{--}120$ mAh/g), low energy density, poor cycle life at elevated temperature, as well as unacceptable capacity loss due to both structural effects associated with the Jahn-Teller distortion of Mn^{3+} and interfacial effects due to the propensity of Mn to dissolve into the electrolyte.¹⁸⁻²⁴ Olivine-type LiFePO_4 is made of inexpensive and environmentally friendly elements, and it has long cycle life and high stability. But it must be engineered as a carbon-coated nanomaterial²⁵⁻²⁷ due to a combination of low diffusion coefficient of Li^+

ions ($\tilde{D} \approx 10^{-14} \text{ cm}^2/\text{s}$) and poor electronic conductivity ($\sigma_e < 10^{-9} \text{ S/cm}$), and, most importantly, an inherently low energy density ($\sim 2000 \text{ Wh/l}$) and specific energy ($\sim 590 \text{ Wh/kg}$) because of the relative low working potential ($\sim 3.5 \text{ V}$) and the low mass density ($\sim 3.4 \text{ kg/l}$).²⁸⁻³⁴

The layered rock-salt lithium transition metal oxides with a general formula of LiMO_2 are the most popular class of cathodes, displaying high capacities, high gravimetric and volumetric energy densities, and long life span. Layered LiMO_2 oxides are isostructural with layered $\alpha\text{-NaFeO}_2$, with space group $\bar{R}3m$, in which the oxygen ions form a cubic close-packed arrangement and lithium and transition metal ions occupy the octahedral sites and stack alternatively with an ABCABC sequence, called “O3-type” stacking. Due to the layered structure, Li^+ ions diffuse through a 2D plane perpendicular to the $(00l)$ axis (Figure 1-7c), enabling high diffusion coefficient of Li^+ ions upon cycling. LiCoO_2 initially reported in 1980,³⁵ was the first commercialized cathode material for Li-ion battery in 1991.¹ It now also dominates the Li-ion battery market. LiCoO_2 could reversibly deliver a practical capacity of $\sim 160 \text{ mAh/g}$ with a high energy density and specific energy being $\sim 3000 \text{ Wh/l}$ and $\sim 1000 \text{ Wh/kg}$, respectively, due to the high voltage ($\sim 4.0 \text{ V}$ vs. Li^+/Li^0) and high density (5 kg/l).³⁶ Nevertheless, LiCoO_2 also exhibits a few drawbacks, such as the high price of cobalt associated with its limited availability in nature, poor thermal safety issue, and oxygen loss upon overcharge. These drawbacks greatly restrict its application and further encourage scientists to continue to search for other layered oxides with better electrochemical properties. Although LiNiO_2 , isostructural to LiCoO_2 , displays favorable specific capacity (ca. 200 mAh/g) and better environmental compatibility in comparison to LiCoO_2 ,^{37, 38} a lower thermal stability of delithiated phase in the electrolyte, such as a lower temperature of decomposition and a greater released energy,³⁹⁻⁴² cripples its applicability. Similar to LiNiO_2 , LiMnO_2 cannot compete with LiCoO_2 due to the poor electrochemical performances derived from the progressive structural transition upon cycling into a more stable LiMnO_2 spinel arrangement, a transformation that is kinetically impeded and induces severe fatigue due to mechanical strain.⁴³⁻⁴⁵

Given the rich chemistry of layered oxides, elemental substitution at the metal site has been extensively explored to design materials that outperform LiCoO₂. As such, binary Li[M, M']O₂ and ternary Li[M, M', M'']O₂ have been realized by various combinations of either two or three 3d transition metals. Binary oxides like Li[Ni_{1-y}Co_y]O₂,⁴⁶ Li[Mn_{1-y}Co_y]O₂,^{47, 48} and Li[Ni_{1-y}Mn_y]O₂⁴⁹ deliver enhanced electrochemical behavior and structural stability relative to single-metal LiMO₂. Furthermore, the dual substitution led to the appearance of oxides like Li[Ni_{1-y-z}Co_yAl_z]O₂ (coined NCA)^{50, 51} and Li[Ni_{1-y-z}Mn_yCo_z]O₂ (termed as NMC)^{52, 53} with Ni accounting for the capacity, Co enforcing ordered layers to maximize rate capabilities, Al and Mn providing thermal stability. Specifically, Li[Ni_{0.8}Co_{0.15}Al_{0.05}]O₂^{54, 55} and Li[Ni_{1/3}Mn_{1/3}Co_{1/3}]O₂⁵⁶ have been most intensively investigated, and now are widely employed in the Li-ion batteries in the market today.

In order to further boost the energy density of Li-ion batteries compounds with an over-stoichiometry of Li were sought by substitution of Li into the transition metal layer to form Li[Li_xM_{1-x}]O₂, also denoted as “Li-rich oxides”. These compounds were first reported with a general formula of Li[Li_xNi_yMn_zCo_{1-x-y-z}]O₂ (Li-rich NMC) by Thackeray and Dahn groups independently, and found to deliver a high capacity exceeding 260 mAh/g.⁵⁷⁻⁵⁹ The extraordinary electrochemical performance makes the category of Li-rich oxides promising for the next-generation positive electrode materials and stimulates further study. The most common sub-families of Li-rich transition metal oxides will be discussed next.

1.3.1 Li₂MnO₃ and derivatives

Li₂MnO₃ is a seminal compound among Li-rich oxide cathodes. It crystallizes in a layered structure with alternative stacking of [Li_{1/3}Mn_{2/3}] and Li layers, resulting into Li[Li_{1/3}Mn_{2/3}]O₂ with Li excess in the transition metal layer relative to the conventional layered LiMO₂ (Figure 1-4a). In the structure, octahedral sites are occupied by cations, and [Li_{1/3}Mn_{2/3}] layers have a LiMn₂ honeycomb-type cationic arrangement, where each oxygen atom is coordinated by four Li and two Mn to form OLi₄Mn₂ octahedra (Figure 1-4b).⁶⁰

⁶¹ Although Mn⁴⁺ is generally considered electrochemically inactive, Kalyani et al. first reported in 1999 Li

can be extracted from Li_2MnO_3 upon charging.⁶² This electrochemical activity was further confirmed by the later reports, which revealed that Mn^{4+} did not participate in the charge compensation.^{63, 64} This observation suggested an underlying mechanism centered at oxygen ligands as explanation for this abnormal electrochemical behavior, which will be further discussed below. Subsequently, a series of solid solution $\text{Li}_2\text{MnO}_3\text{-LiCoO}_2$ phases were synthesized because they are isostructural with $\alpha\text{-NaFeO}_2$.^{65, 66} Those solid solution compounds essentially have the same layered structure as that of Li_2MnO_3 however with honeycomb $[\text{LiMnCo}]$ layers where oxygen atom is coordinated either by four Li and two transition metals to form OLi_4M_2 octahedra or three Li and three transition metals to with the formation of OLi_4M_2 octahedra. Further compositional extensions came through solid solutions of the formula $\text{Li}_2\text{MnO}_3\text{-LiMO}_2$ (e.g. $\text{M} = \text{Ni}_{1/2}\text{Mn}_{1/2}$ or $\text{Ni}_{1/3}\text{Co}_{1/3}\text{Mn}_{1/3}$). They were found to deliver a high capacity up to 260 mAh/g with unique electrochemical behavior, involving a large voltage plateau at ~ 4.5 V vs Li^+/Li^0 upon the first charge providing capacity beyond the expected formal changes in M, a large irreversible capacity during the first cycle, and sloping charge/discharge curves without a voltage plateau in subsequent cycles (Figure 1-4c).^{57, 67-71} Other intrinsic drawbacks included voltage hysteresis and fade, as well as sluggish kinetics (Figure 1-4c).

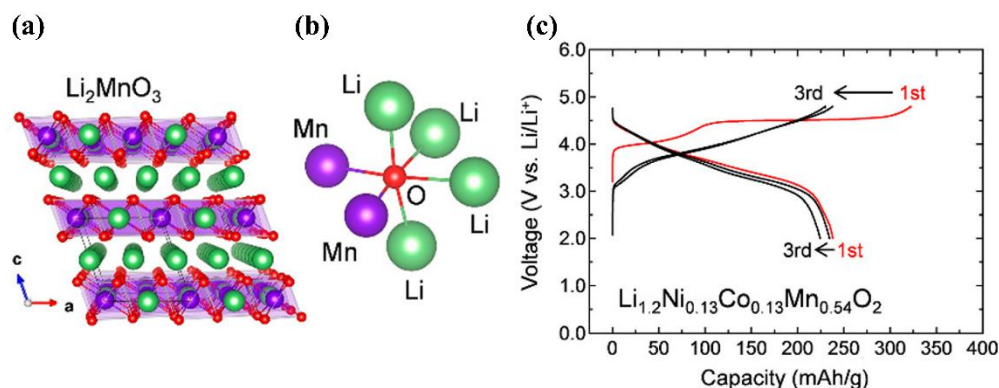


Figure 1-5. (a) Crystal structure of Li_2MnO_3 . (b) Local coordination environment around O in Li_2MnO_3 . (c) First three cycling profile of $\text{Li}_{1.2}\text{Ni}_{0.13}\text{Co}_{0.13}\text{Mn}_{0.54}\text{O}_2$. Adapted with permission from “Molecular Orbital Principles of Oxygen-Redox Battery Electrodes”.⁷² Copyright © 2017 American Chemical Society.

1.3.2 Li_2MO_3 ($\text{M} = 4\text{d}/5\text{d}$)

In order to deeply understand the underlying mechanism of the high voltage plateau of Li_2MnO_3 - LiMO_2 , canonical compounds $\text{Li}_2\text{RuO}_3/\alpha\text{-Li}_2\text{IrO}_3$, isostructural with Li_2MnO_3 , were studied by the research group led by Tarascon.^{73, 74} A reversible oxygen-centered redox reaction was proposed with a formation of peroxo-like species $(\text{O}_2)^{n-}$ (Figures 1-6a and 1-6b). In addition, the solid solution $\text{Li}_2\text{RuO}_3\text{-Li}_2\text{MO}_3$ ($\text{M} = \text{Mn}$, and Sn) demonstrates similar electrochemical behaviors to those of $\text{Li}_2\text{MnO}_3\text{-LiMO}_2$ system.^{73, 75}

Different from the typical two-dimensional (2D) layered compounds, $\beta\text{-Li}_2\text{IrO}_3$ is a three-dimensional (3D) framework, where Li and Ir occupy octahedral sites in an ABCABC close-packed O3 array. The edge-sharing IrO_6 octahedra forms a 3D matrix (Figure 1-6c), and oxygen is coordinated by four Li and two Ir to form an OLi_4Ir_2 octahedron (Figure 1-6d).^{76, 77} $\beta\text{-Li}_2\text{IrO}_3$ illustrates high reversible electrochemical properties with capacities suggesting joint cation- (M^{n+}) and anion-centered $(\text{O}_2)^{n-}$ redox processes under the absence of the cationic migration and shearing of atomic layers.⁷⁸

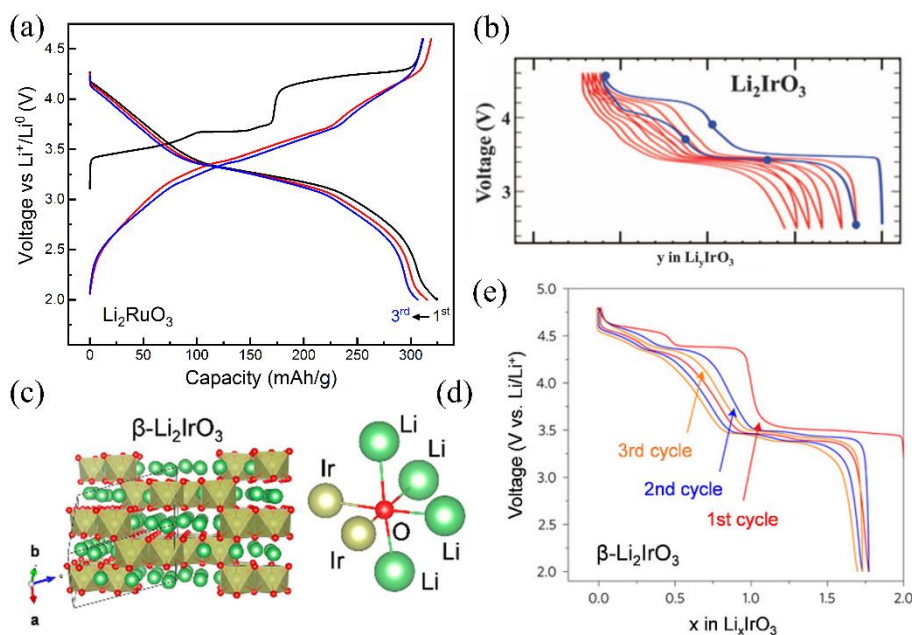


Figure 1-6. (a) First three voltage-capacity curves of Li_2RuO_3 . (b) Voltage-composition cycling profile of $\alpha\text{-Li}_2\text{IrO}_3$. Reprinted with permission from “Visualization of O-O peroxo-like dimers in high-capacity layered oxides for Li-ion batteries”.⁷⁴ Copyright © 2015, American Association for the Advancement of Science. (c) Crystal structure of $\beta\text{-Li}_2\text{IrO}_3$. (d) Local coordination environment around O in $\beta\text{-Li}_2\text{IrO}_3$. (e)

First three voltage-composition profiles of β - Li_2IrO_3 . Reprinted with permission from “Molecular Orbital Principles of Oxygen-Redox Battery Electrodes”.⁷² Copyright © 2017 American Chemical Society.

1.3.3 Disordered rock-salt compounds

Different from the layered Li-excess oxides where Li and M layers stack alternatively, the disordered Li-rich oxides have a rock-salt structure with a space group of $\text{Fm}\bar{3}\text{m}$ where Li and M arrange randomly in the octahedral 4a site while O atoms occupy 4b site. As a result, the coordination environment of oxygen varies from OLi_6 to OM_6 due to the disordered arrangement of cations. Their current interest was triggered by the discovery that Li diffusion could be enhanced via tailoring its stoichiometry to introduce percolation of diffusion pathways where Li is never surrounded by face-sharing transition metal MO_6 octahedra (O-M channels) in the intermediate tetrahedral site (Figure 1-7), minimizing electrostatic repulsion.⁷⁹⁻⁸³ With the rise of Li-excess level, the percolation network of O-M channels becomes more extensive, enabling a higher fraction of Li^+ ions to cycle via the network.^{81, 82} This theory was first supported by the discovery of the cation-disordered rock-salt Li-rich oxide $\text{Li}_{1.211}\text{Mo}_{0.467}\text{Cr}_{0.32}\text{O}_2$, which delivers a large capacity due to the existence of a percolation network of Li-ion diffusion channels.⁸² In addition to the increased percolating diffusion channels, DFT calculations illustrated that the cation disorder could promote the occurrence of the Li-O-Li linear clusters, which brings about the existence of labile oxygen electrons giving rise to the possibility of anionic redox and, consequently, high capacity.⁸⁴ Later, the reported Li-rich random rock-salt $\text{Li}_{1.3}\text{Nb}_{0.3}\text{Mn}_{0.4}\text{O}_2$ was shown to deliver a large capacity due to the addition of contributions from oxygen activity (Figures 1-8a and 1-8b),⁸⁵ revealing that the combination of the percolation strategy with oxygen redox chemistry could highly enhance electrochemical behavior. Later on, another disordered rock-salt compound $\text{Li}_{1.2}\text{Ti}_{0.4}\text{Mn}_{0.4}\text{O}_2$ was reported to deliver a large capacity of 300 mAh/g with a stable voltage plateau upon extensive cycling (Figure 1-8c), further supporting this joint approach.⁸⁶ Other rock-salt oxides $\text{Li}_{1.2}\text{Ni}_{1/3}\text{Ti}_{1/3}\text{Mo}_{2/3}\text{O}_2$ ⁸⁷, $\text{Li}_{1.25}\text{Nb}_{0.25}\text{Mn}_{0.5}\text{O}_2$ ⁸⁸, Li_2VO_3 ,⁸⁹ $\text{Li}_4\text{Mn}_2\text{O}_5$,⁹⁰ and $\text{Li}_{1.3}\text{Nb}_{0.3}\text{V}_{0.4}\text{O}_2$ ⁹¹ have also been reported as oxygen-redox electrode materials. Given those successes in disordered rock-salt Li-

excess compounds, the combination of the structural cation disorder and the anionic redox is now considered a promising approach to design electrode materials with high capacity.

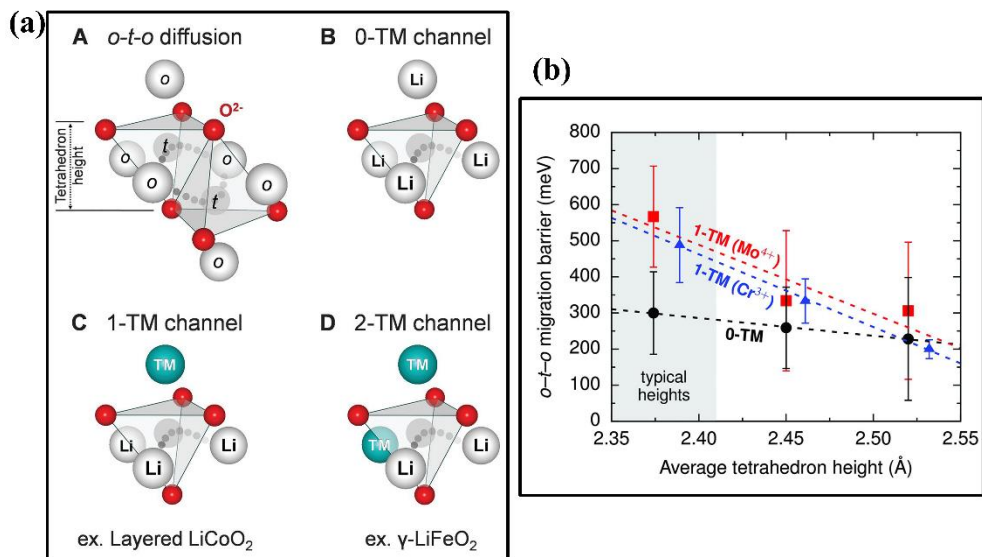


Figure 1-7. (a) Possible ways of an *o-t-o* Li diffusion in rock-salt-like transition metal oxides. (A) *o-t-o* diffusion: two tetrahedral sites connect each pair of neighboring octahedral sites. (B to D) The intermediate activated state can share faces with no octahedral transition metals (O-M channel) (B), one transition metal (1-M channel) (C), or two transition metals (2-M channel) (D). (b) Calculated migration barriers of Li^+ ions along 1-M (Mo^{4+}) channels (red squares), 1-M (Cr^{3+}) channels (blue triangles), and O-M (Li^+) channels (black circles) as a function of the average tetrahedral height of mode disordered Li_2MoO_3 and LiCrO_2 . Reprinted with permission from “Unlocking the Potential of Cation-Disordered Oxides for Rechargeable Lithium Batteries”.⁸² Copyright © 2014 American Association for the Advancement of Science.

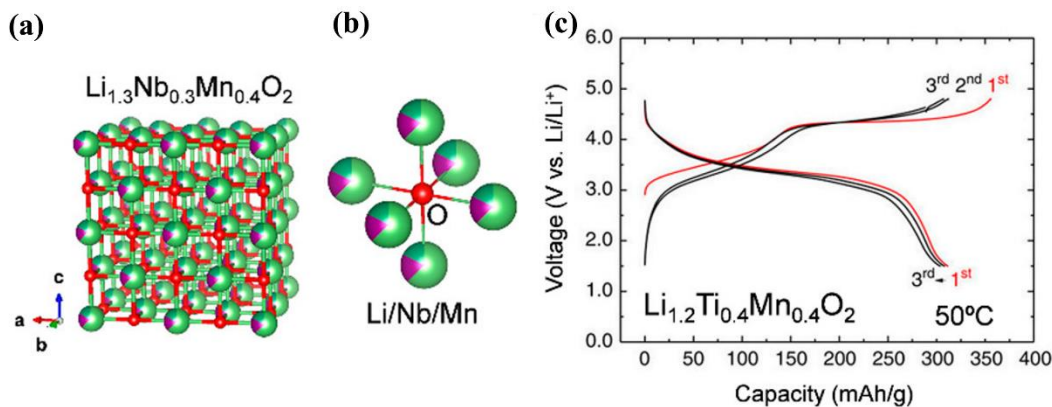


Figure 1-8. (a) First three voltage-capacity curves of $\text{Li}_{1.3}\text{Nb}_{0.3}\text{Mn}_{0.4}\text{O}_2$. (b) Local coordination environment around O in $\text{Li}_{1.3}\text{Nb}_{0.3}\text{Mn}_{0.4}\text{O}_2$. (c) Voltage-composition cycling profile of $\text{Li}_{1.2}\text{Ti}_{0.4}\text{Mn}_{0.4}\text{O}_2$. Reprinted with permission from “Molecular Orbital Principles of Oxygen-Redox Battery Electrodes”.⁷² Copyright © 2017 American Chemical Society.

1.6.4 Li_3MO_4

As discussed in more detail below, oxygen-centered redox is predicted to depend on the existence of non-bonding O 2p states in the Li-rich oxides.⁸⁴ Computational calculations uncovered that the amount of the non-bonding O 2p states increases with the O/M ratio, and reaches attractively high levels for Li_3MO_4 compounds.⁹² Li_3NbO_4 is a cation-ordered rock-salt structure and consists of four edge-shared NbO_6 octahedra forming a Nb_4O_{16} tetramer.⁹³ Within the structure, Li ions are accommodated in a body-centered cubic lattice of the Nb_4O_{16} tetramers. In spite of the Li-rich rock-salt structure, it is electrochemically inactive since Nb^{5+} cannot be further oxidized due to the absence of electrons in the conduction band. In contrast, Li_3RuO_4 synthesized at high temperature is also an ordered rock-salt framework where Li only and Li/Ru layers stack alternatively.^{94, 95} In the Li/Ru layers, Li and Ru are also ordered through a formation of long range of zig-zag chains of $[\text{RuO}_6]$ and $[\text{LiO}_6]$ octahedral (Figure 1-9a). Almost all Li can be removed from Li_3RuO_4 upon charging to 4.2 V, which is accompanied by a severe structural amorphization, followed by a drastic degradation in the electrochemical performance for reverse discharging. However, the Ru oxidation cannot account for the charges equivalent to the extracted Li, suggesting the proactive role of alternate mechanisms, such as ligand involvement, in the charge compensation.^{96, 97} To further increase covalence, Li_3IrO_4 was investigated. It crystallizes in a specific layered rock-salt frame with oxygen atoms arranging in a cubic close-packed form, and Li/Ir occupying all octahedral sites. The cations are ordered into Li layers sandwiched by the Li/Ir layers where Li and Ir are arranged randomly (Figure 1-9b). All Li can be removed from Li_3IrO_4 upon charging to 4.5 V but with minor Ir participation, strongly indicating the existence of the dominant oxygen-centered redox activity. By restraining the first oxidation to LiIrO_4 ,

Li_3IrO_4 shows a reversible capacity of nearly 3.5 mol Li removal per mol transition metal with a good cyclability over extensive cycles.⁹⁸

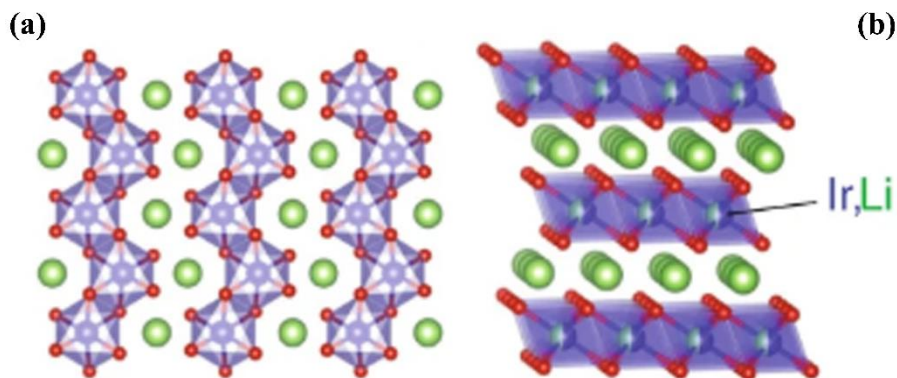


Figure 1-9. (a) Zig-zag chains in Li_3RuO_4 . (b) Layered Li_3IrO_4 with cation disorder in metal layer. Reprinted with permission from “Approaching the limits of cationic and anionic electrochemical activity with the Li-rich layered rock-salt Li_3IrO_4 ”.⁹⁸ Copyright © 2017 Springer Nature.

To enable the discovery of Li-rich oxides that represent further leaps from current performance, the detailed role of the oxygen redox and its activation and stabilization mechanism should be established. This knowledge could guide the design of phases rich in base metals, rather than precious metals like Ru or Ir.

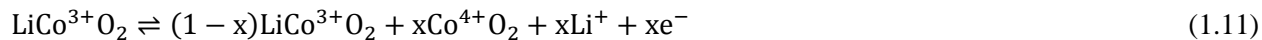
1.4 Fundamental principle of redox chemistry

The band structure of a compound fundamentally determines its redox processes. The Fermi level (E_F) in the band structure can be correlated with the electrochemical redox potential such that electrons below E_F and holes above E_F form a redox couple.⁹⁹ The overlap between transition-metal d orbitals and ligand oxygen p orbitals results in M-O covalent interaction varying with the transition metals and the crystal structure. The band structure can be extrapolated from the molecular orbital energy diagrams which are constructed based on the symmetry theory. Herein, the studied compounds adopt a rock-salt-type structure with the transition metal coordinated by six oxygen, forming an octahedral symmetry with the format of MO_6 . On the basis of the Oh point group of MO_6 coordination environment, an approximation to the band

structure can be drawn by extension of the molecular orbitals, as shown in Figure 1-10a. During the molecular-orbital formation, the atomic orbitals of Li can be neglected since the energy level of its frontier orbitals 2s/3s is much higher relative to that of O 2p. The nd, (n+1)s, and (n+1)p orbitals of M and 2p orbitals of O are ordered in the energy-level sequence as follows: $E(2p) < E(nd) < E((n+1)s) < E((n+1)p)$. The proximity of the energy of O 2p and M nd enhances the hybridization between M nd and O 2p. Whereas, the overlap integral between M (n+1)s/(n+1)p and O 2p is larger than that of O 2p-M nd interaction due to much more diffusive of the radial distributions of (n+1)s and (n+1)p with respect to nd. As such, the hybridization between O 2p and M (n+1)s/(n+1)p leads to the most bonding a_{1g}/t_{1u} and the antibonding a_{1g}^*/t_{1u}^* molecular orbitals. For the transition metal atom, its five nd orbitals are classified as d_{z^2} , $d_{x^2-y^2}$, d_{xy} , d_{xz} , d_{yz} . It is worth noting that ligand O here is a π donor having a π interaction with metal involving electron transfer from filled O p orbitals to the metal center. Among those, the $d_{z^2}/d_{x^2-y^2}$ (e_g) orbitals are directed toward ligand oxygen σ -orbitals to form strong σ bonds comprising bonding e_g orbital with lower energy and antibonding e_g^* orbital with comparatively higher energy. In contrast, the interaction of $d_{xy}/d_{xz}/d_{yz}$ (t_{2g}) orbitals with ligand O π -orbitals, which are filled and lie above, but relatively very close to oxygen σ -orbitals, leads to bonding t_{2g} and antibonding t_{2g}^* orbitals. Due to the higher electronegativity of the ligand oxygen compared with transition metal M, the a_{1g} , t_{1u} , e_g and t_{2g} orbitals usually have a greater contribution in their wavefunction from O 2p orbitals, demonstrating a O-dominant character leading to the common term “anion p band” (Figure 1-10b) in the band structure.

In general, upon (de)intercalation, the charges used to compensate electrons equivalent to the amount of the extracted Li ions, are derived from the occupied states below the Fermi level. In compounds with d occupancy, these states are at the top of the valence band. For the conventional (de)intercalation process occurred in the classical LiMO_2 , these d states have a greater contribution from the transition-metals and they are well separated from states rich in O p states, due to the lower electronegativity of d electrons with respect to anion p electrons.^{99, 100} Therefore, this reaction is conventionally associated with the variation of

the formal oxidation state of M ions, and termed as the conventional cationic redox. An example with LiCoO₂ involve Co 3d states changing electron occupancy, associated with the formal Co³⁺/Co⁴⁺ couple:³⁵



For cationic redox, the amount of the depleted electrons depends on the number of electrons in the d states and the relative gap between the transition metal d states and the anion p states.¹⁰¹ Therefore, the compounds that contain metal ions without electrons in d states, like LiAlO₂ are electrochemically inactive toward this process.¹⁰⁰

However, upon delithiation, the energy level of the transition metal-rich d band downshifts, which reflects an increased overlap between transition metal d and the ligand p states. It is proposed that this process leads to the pinning of the redox couple at the top of the ligand p band. As such, further deintercalation would depopulate states with a high contribution from the ligand p states, leaving behind holes which can only be stabilized via certain anion-cation interactions proposed for heavy chalcogenides proposed by Rouxel as early as 1990s.¹⁰² This process involving more ligand participation than transition metals is usually referred to as anionic redox to differentiate from cationic redox. The phenomenon was first identified in 3d transition-metal chalcogenides, such as TiS₂ or Ti²⁺(Ti₂)²⁻ and TiS₃ or Ti⁴⁺S₂²⁻(S₂)²⁻ and FeS₂ or Fe²⁺(S₂)²⁻, with the possibility of S being oxidized due to the high covalent interaction between transition metal and sulfur.¹⁰³ However, anionic redox in oxides was not initially envisaged due to its lower covalence than sulfides. This viewpoint was then overturned by the later experimental and theoretical phenomena observed in Co-containing oxides like LiCoO₂, where the oxidation state of Co in the most delithiated state was found to be less than (4+),^{104, 105} with a significant charge redistribution at O^{100, 106} through an evolution in its electronic structure¹⁰⁷⁻¹¹¹ and a slight reduction of O-O inter-planar distance in Li_xCoO₂.¹¹² However, the resulting holes in the oxygen p states would result in the oxygen evolution with the molecular O₂ release, detrimental to the compound and the battery performance.

However, the situation is different for Li-rich compounds $\text{Li}[\text{Li}_x\text{M}_{1-x}]\text{O}_2$ (often represented as $\text{Li}_{1+x}\text{MO}_{\frac{2}{1-x}}$). Seo et al. revealed the structural and chemical origin of the oxygen redox activity in layered and cation-disordered Li-excess oxides via density functional theory (DFT).⁸⁴ In comparison with the coordination environment of O (OM_3Li_3) in traditional LiMO_2 , they demonstrated that the local structural environment of O (OM_4Li_2) in layered and/or disordered Li-rich oxides contributes to the formation of a linear Li-O-Li configuration, as illustrated in Figure 1-9. Because of the electrostatic interaction with Li, the O 2p orbitals along this Li-O-Li cluster do not hybridize well with M orbitals, resulting in non-bonding O 2p states near the Fermi level, which can be tapped with appropriate chemical design. This feature stands in contrast with conventional LiMO_2 where all O 2p orbitals hybridize with M nd orbitals. It is predicted that the density of these non-bonding O 2p states is proportional to the O/M ratio in the compound.⁹²

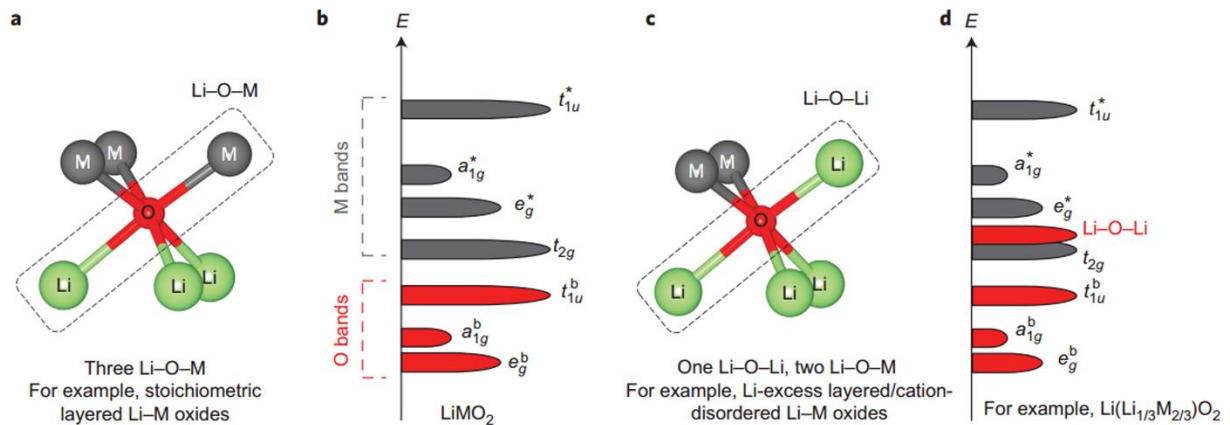


Figure 1-10. (a) Local coordination environment around oxygen composed of three Li-O-M configuration in layered LiMO_2 . (b) Schematic of the band structure for LiMO_2 . (c) Local atomic coordination around oxygen comprising of one two Li-O-M and one Li-O-Li configuration in layered or cation-disordered Li-rich oxides Li_2MO_3 . (d) Schematic of the band structure for Li-rich Li_2MO_3 . Reprinted with permission from “The structural and chemical origin of the oxygen redox activity in layered and cation-disordered Li-excess cathode materials”.⁸⁴ Copyright © with permission from Springer Nature.

A complication from the picture by Seo et al. is introduced by the existence of electron correlation in condensed phases, which further split partially occupied d bands in addition to the splitting induced by the

extent of M-O overlap, into bonding and anti-bonding M nd-O 2p states. To clarify oxides according to their extent of correlation, the qualitative Zaanen-Sawatzky-Allen picture is used. In it, oxides are classified as Mott-Hubbard vs charge transfer insulators based on the U/Δ ratio where U and Δ stand for the on-site electron Coulomb interaction within the d orbitals and the charge transfer derived from the energy difference between (M-O) bonding and (M-O)* anti-bonding, respectively.¹¹³ Specifically, U defines the degree of split of the partially filled (M-O)* anti-bonding states (termed Mott-Hubbard splitting), leading to filled lower- and empty upper-Hubbard bands (LHB and UHB, respectively, Figure 1-11). Intuitively, Δ term depends on the difference in electronegativity $\Delta\chi$ between O and M, reflecting the ionic-covalent character of M-O bonds. The U/Δ ratio in one compound determines the relative position of between LHB and the O 2p non-bonding band, giving rise to three different scenarios,^{92, 114} which have different implications for the possibility of inducing O redox.

First, for $U \ll \Delta$, a situation of a predicated Mott-Hubbard regime that is widely applied to oxides with high ionic M-O bonds, electrons are removed from the filled LHB located at the Fermi level (Figure 1-11c), suggesting a classical one-band cationic redox scenario. Turning to a situation of highly correlated systems, where a charge transfer regime is predicted, with $U \gg \Delta$, the one-band redox process still remains, but with electronic states at the Fermi level having a heavy O 2p character because they are located above the filled LHB (Figure 1-11e). If those electrons can be extracted, highly unstable holes are predicted on localized states, which corresponds to the picture of formation of peroxo-like states. These states are very unstable and may de-coordinate from the metallic network by reductive elimination or attacking the electrolyte, leading to a progressive material decomposition upon extensive cycling. This scenario is ascribed to compounds like Li_2MnO_3 ^{64, 115} and the related Li-rich NMCs¹¹⁶⁻¹¹⁸. Lastly, an interesting scenario arises from the intermediate situation with $U/2 \approx \Delta$ when both the LHB and non-bonding O 2p band overlap with each other and lie at the Fermi level (Figure 1-11d). In this case, both bands can be simultaneously accessed for electrochemical activity.^{78, 119} or conjointly ($\text{Li}_{2-x}\text{Ir}_{1-y}\text{Sn}_y\text{O}_3$). The electron depopulation associated with the Li removal is stabilized via a collective distortion of the transition metal sphere through formation of

short O-O distances, which induces lowering of the symmetry and promotes the emergence of the stabilizing $M-(O_2)^n$ interactions and rehybridization between M and O.⁹² Such stabilization of the oxidized oxygen via the covalent interaction from the transition metal is referred to as “reductive coupling mechanism”.^{73, 120} This principle is proposed to occur for the experimentally observed distortion of MO_6 octahedra upon charge in Li_2RuO_3 ^{119, 121}, Li_2IrO_3 ^{74, 78}, Li_3RuO_4 ⁹⁷, Li_3IrO_4 ⁹⁸, and $Li_2Ir_{1-y}Sn_yO_3$ ¹²².

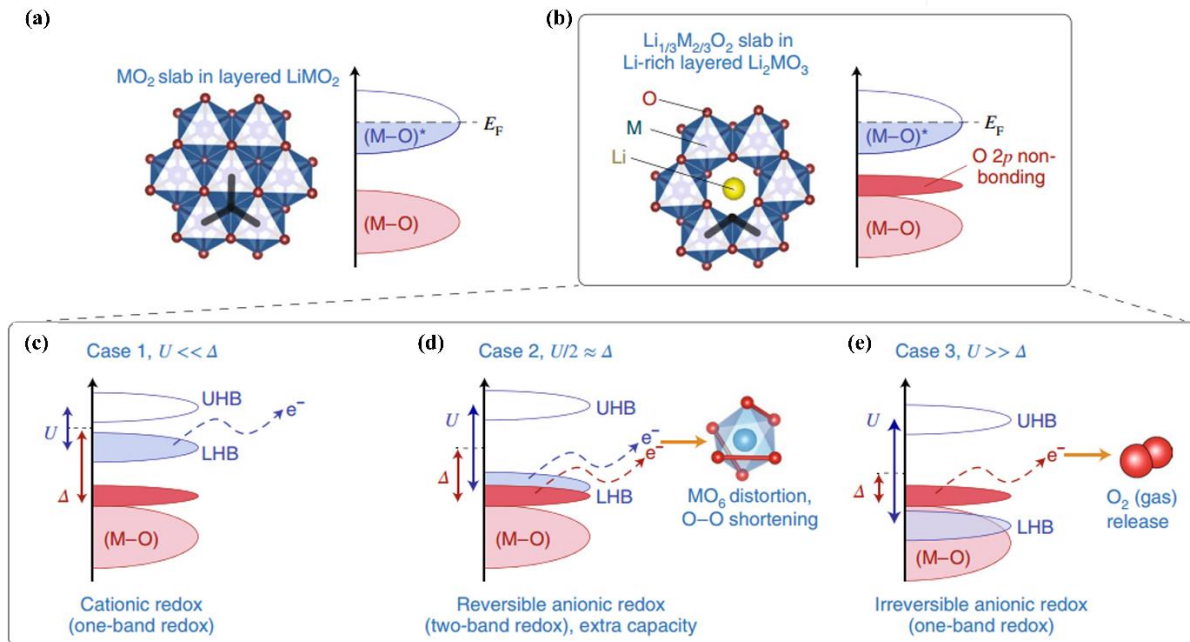


Figure 1-11. Crystal structures (focusing on slabs of MO_2 and $Li_{1/3}M_{2/3}O_2$) and the relevant parts of the band structures of $LiMO_2$ (a) and Li-rich Li_2MO_3 . (c-e) Qualitative representation of the Li_2MO_3 band structure by taking Mott-Hubbard splitting into account. Reprinted with permission from “Fundamental understanding and practical challenges of anionic redox activity in Li-ion batteries”.¹¹⁴ Copyright © 2018 Springer Nature.

Altogether, the band structure, largely relying on the local coordination environment, plays a fundamental role in activating the anionic redox. However, due to the different chemical environment and the interaction between transition metal and oxygen, the oxygen activity can significantly vary. The knowledge of the possible mechanisms of anionic redox for different Li-rich oxides will be discussed next.

1.5 Possible mechanism of anionic redox reactions Li-rich oxides

Li_2MnO_3 is generally considered as a prototypical model of Li-overstoichiometry oxides. Since the formal oxidation state of octahedral Mn ions in Li_2MnO_3 is (4+), further oxidation of Mn ions is believed to be inaccessible, resulting in the plausible fact that Li_2MnO_3 is electrochemically inactive.⁴⁴ However, an anomalous electrochemical activity of Li_2MnO_3 was probed upon charge to above 4.5 V, which is beyond the expectation, followed by a feasible subsequent lithiation but with a large capacity loss and low efficiency.^{62, 123, 124} This unexpected observation brought about extensive research on the underlying charge compensation mechanism, which remains highly controversial.

The first proposed mechanism by Rossouw et al. involved Li^+/H^+ ion exchange.¹²⁴ The existence of exchange was later supported by a suite of the experimental data.^{63, 64, 125} During the electrochemical experiments, the oxidation of the non-aqueous electrolyte at high voltage oxidation not only generated H^+ ions used for exchanging with Li^+ ions, but provided electrons for the external circuit. However, this process would be limited to interfaces between the electrode particle and the electrolyte, and could not account for the existence of delithiation from the particle bulk. Recently, NMR study confirmed the existence of proton-containing species on the surface of the charged electrode but no proton-bearing species within the bulk, ruling out the insertion of protons into the Li_2MnO_3 lattice.¹²⁶ Hence, the simple Li^+/H^+ ion exchange cannot solely account for the high capacity of Li_2MnO_3 upon charge.

Robertson et al. found that the Li removal is accompanied with the oxidation of O^{2-} with subsequent O loss from the lattice concurrent with the Li^+/H^+ exchange, with the former being the dominant one upon oxidation to 4.5 V.^{64, 127-129} Building up from these studies, Yu et al. proposed that the initial oxidation capacity exhibited by Li_2MnO_3 could be primarily attributed to the evolution of species like molecular O_2 and other forms, resulting in the formation of vacancies in the bulk lattice that induced a subsequent phase transformation to spinel-like framework.¹¹⁵ The formation of O vacancies was later computed to be thermodynamically favorable when the Li content is lower than $x \approx 1$ in Li_xMnO_3 , suggesting that O_2 gas evolves upon oxidation when x is lower than 1, which led to the hypothesis that e^- O^{2-}/O^- could still be the

redox center as $1 < x < 2$.¹³⁰ The possibility of $\text{O}_2^{2-}/\text{O}_2^-$ species was proposed to be supported by comparing the O K-edge XAS of these states with Li_2O_2 and KO_2 (Figure 1-12).¹³¹ However, more recent quantitative measurements of gas evolution indicate that the first charge capacity originates primarily from O_2 release, with much smaller contributions from reversible lattice oxygen redox and decomposition of surface carbonates.¹³²

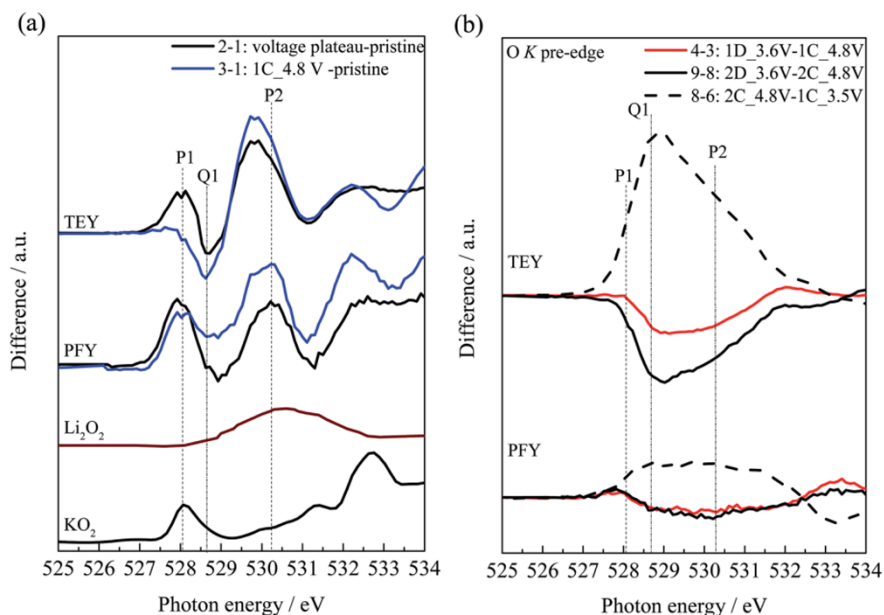


Figure 1-12. (a) and (b) Difference spectra of O K-edge XAS of Li_2MnO_3 at different states of charge and (a) the reference XAS spectra of Li_2O_2 and KO_2 . Reprinted with permission from “Direct observation of reversible oxygen anion redox reaction in Li-rich manganese oxide, Li_2MnO_3 studied by soft X-ray absorption spectroscopy”. Copyright © 2016 Royal Society of Chemistry.¹³¹

A third proposed mechanism centers on the possibility of Mn over-oxidation, which has persisted from the early stages of discovery of the electrochemical activity of Li_2MnO_3 .⁶² Recently, first-principle calculations indicated that the electrochemical behavior could be thermodynamically consistent with the formation of Mn^{7+} redox and its concomitant migration to tetrahedral sites.¹³³ However, there is no experimental verification for this model so far. Indeed, *operando* Mn K-edge XANES data of Li_2MnO_3 demonstrates little energy shift of the main absorption edge beyond that of the pristine state even at a voltage

up to 5.0 V, which is inconsistent with the existence of oxidation of Mn^{4+} and indirectly consolidates the contribution of the oxygen to the redox.¹³²

In spite of its limited electrochemical performance and complicated mechanism, Li_2MnO_3 has the merit of allowing various chemical substitutions aiming toward enhancing its properties. The substitution leads to numerous derivatives, especially the representative $\text{Li}[\text{Li}_x\text{Ni}_y\text{Mn}_z\text{Co}_{1-x-y-z}]\text{O}_2$ (so-called Li-rich NMC), which show high capacities of over 260 mAh/g.⁷⁰ Li-rich NMC cathode materials demonstrate a peculiar two-step charge profile upon the first charge followed by a sloped S-shaped curve for the subsequent discharge. Afterwards, the S-shape voltage profile is preserved on subsequent cycling. In spite of the intriguing capacity, this evolution of the electrochemical profile highlights one of the inherent drawbacks of these materials: the decay of the reaction potential upon cycling, leading to energy inefficiency.

The capacities measured for these materials are well beyond what could be predicted by a conventional cationic redox activity. The origin of both the intrinsic shortcomings and extra capacity has been the source of a prolific but still inconclusive literatures. Analogous to the situation of Li_2MnO_3 , several scenarios accounting for the oxygen participation in Li-rich NMC are the object of intense debate, such as Li^+/H^+ ion exchange,^{134, 135} irreversible oxygen loss with surface densification,^{116, 136, 137} Li_2O removal with “ MnO_2 -like” activation,^{70, 138} oxygen release/re-accommodation,¹³⁹ oxygen redox at the interphase,¹⁴⁰ and finally, reversible lattice oxygen redox^{117, 141-149}. Among all these sometimes conflicting hypotheses, it is widely accepted that the oxygen participation contributes to the extra capacity delivered in Li-rich NMC but with different mechanisms of reaction between the surface and the bulk (Figure 1-13).¹⁴⁰ At the surface, the introduction of oxidized species would induce reaction with the electrolyte with the formation of CO_2 and the carbonate,¹⁵⁰ conflated with release of molecular O_2 enabled by the migration of Mn to sub-surface layers which induces a phase transformation to spinel-like domains. The gas evolution and phase transformation result in the degradation of the electrode, detrimental to the electrochemical performance.

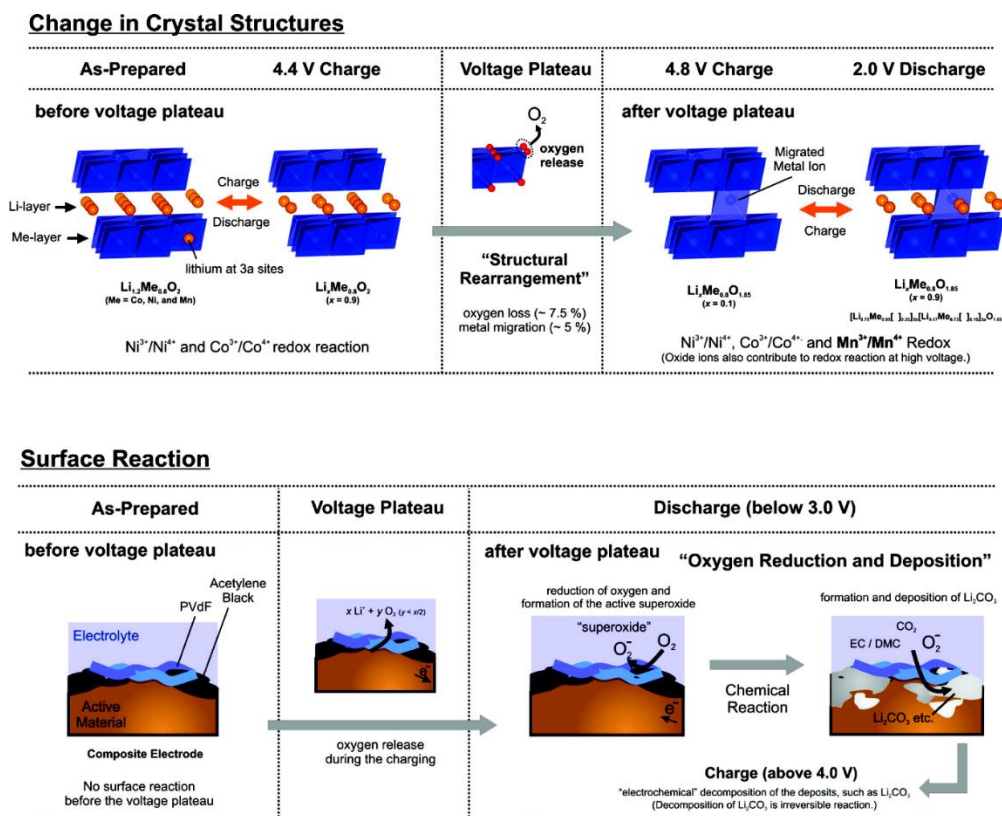


Figure 1-13. Schematics of the proposed mechanisms accounting for the bulk and surface reactions in $\text{Li}_x\text{Ni}_{0.13}\text{Co}_{0.13}\text{Mn}_{0.54}\text{O}_{2-\delta}$. Reprinted with permission from "Detailed Studies of a High-Capacity Electrode Material for Rechargeable Batteries, $\text{Li}_2\text{Mn}_2\text{O}_3\text{-LiCo}_{1/3}\text{Ni}_{1/3}\text{Mn}_{1/3}\text{O}_2$ ".¹⁴⁰ Copyright © 2011 American Chemical Society.

In the bulk, however, Luo et al. proposed that a reversible anionic redox was possible thanks to the formation of localized electron holes on O ions coordinated by Mn^{4+} and Li^+ upon Li removal (Figure 1-14a).^{117, 142} within this proposal, the oxygen redox was attributed to generation of the localized holes on oxygen coordinated by $\text{Mn}^{4+}/\text{Li}^+$ in $\text{Li}_{1.2}[\text{Ni}_{0.13}\text{Co}_{0.13}\text{Mn}_{0.54}]\text{O}_2$.¹¹⁷ Upon oxidation to 4.5 V, the less covalent interaction of O^{2-} with the surrounding Mn^{4+} and Li^+ leads to relatively localized states near the top of the O^{2-} valence band with respect to those interacting with only Co^{4+} and Ni^{4+} . Localized oxygen holes would be then generated on those less covalent O^{2-} anion. This mechanism also recognizes the significance of Mn, within the Li-rich NMC series, in promoting the localization of electron-holes on O and determining the

fine balance between oxygen evolution and lattice oxygen redox and, consequently, the crucial challenge in favoring the latter by suppressing the former.

Pushing forward, A dynamic $[O^{2-} + M] \rightarrow [O^{\cdot} + M_{\text{mig}}] + e^{-}$ process of defect evolution was proposed by Gent et al. through the investigation of $\text{Li}_{1.17}[\text{Ni}_{0.21}\text{Co}_{0.08}\text{Mn}_{0.54}]\text{O}_2$ to explain the change in the electrochemical profile after the first oxidation process (Figure 1-14b).¹⁴⁹ During this dynamic process, oxygen redox is proposed to be coupled with a reversible migration of M out of its original octahedral site (out-of-plane). The authors proposed that the result is reorganization of the electronic structure and a shift of non-bonding O 2p states to higher energy relative to the M-O hybridization states. This coupling is proposed to stabilize the oxygen redox couple and explain the persistence of the oxygen redox for 500 cycles. This insight sheds light on the interplay between anionic and cationic redox unravels that the anionic redox as the root of the intricate shortcomings of the materials such as hysteresis, poor kinetics and voltage fade.¹⁵¹ Despite the persistent degree of controversy, there is also consensus that the extraordinary capacity delivered by Li-rich NMC is ascribed to the cumulative contribution of both anomalous anionic and conventional cationic reversible redox processes in the bulk.

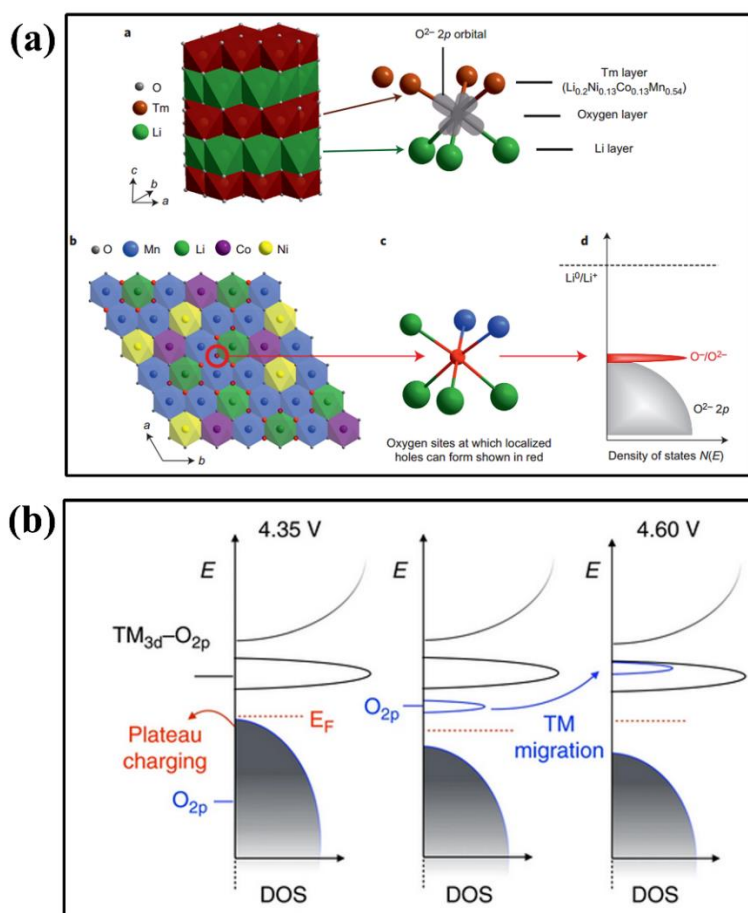


Figure 1-14. (a) Reaction mechanism of the localized electron holes at ligand oxygen anions. Reprinted with permission from “Charge-compensation in 3d-transition-metal oxide intercalation cathodes through the generation of localized electron holes on oxygen”.¹¹⁷ Copyright © 2016 Springer Nature. (b) Schematic of the reorganization of the electronic structure of $Li_{1.17}[Ni_{0.21}Co_{0.08}Mn_{0.54}]O_2$ due to M migration. Reprinted with permission from “Coupling between oxygen redox and cation migration explains unusual electrochemistry in lithium-rich layered oxides”.¹⁴⁹ Copyright © 2017 Springer Nature.

During the anionic redox process, oxidized oxygen could condensate to evolve in the form of molecular O_2 being released from the material, giving rise to a progressive structural degradation and subsequently a decay of the electrochemical performance. This irreversible structural evolution and capacity deterioration have been demonstrated in $LiCoO_2$ and Li_2MnO_3 and the derived Li-rich NMC upon high voltage oxidation when the oxygen redox is triggered but without stabilization. Despite the intriguing properties of the Li-rich NMC compounds, therefore, their practical utilization is largely impeded by the issues of voltage

stability and cycle life, which have not been fully alleviated. There is also a persistent hysteresis in potential in all these compounds, especially in the first cycle, which demands attention for practically important reactions, as it undermines energy efficiency and thermal management. Based on the understanding that the covalent interaction between transition metal and ligand oxygen has a profound effect on the participation of the oxygen in the redox, researchers turned to 4d/5d-based Li-rich oxides to continue to turn the knob covalency and ascertain its role. Although 4d/5d transition metals such as Ru and Ir are not suitable for the practical application due to the high cost, their distinct characteristics could establish new fundamental principles of oxygen redox.

Li_2RuO_3 was first designated as a canonical model for lattice oxygen redox. It has similar electrochemistry and structure to Li-rich NMC phases but a simpler redox chemistry since Ru is the only redox-active cation, in comparison with Li-rich NMC which contains up to three different redox-active centers (Ni, Co and Mn). Upon delithiation $\text{Li}_2\text{Ru}_{1-y}\text{Sn}_y\text{O}_3$, a combination of XPS and EPR results was assigned to the existence of formally oxidized O^{n-} ($n < 2$) species (Figures 1-15a and 1-15b).^{73, 152} The individual contribution of the cationic and anionic redox was decoupled based on *operando* Ru K-edge XAS spectra data, demonstrating that changes at the Ru states were not sufficient to account for electrochemical activity, indicating oxidation of the lattice oxygen.¹¹⁹ Computational analysis indicated that the oxidation is stabilized by the formation of short O-O distances (termed as “peroxo-like species”) while remaining coordinated to the transition metals. This process would induce re-hybridization with the transition metal that enhances electronic donation from the ligands via a reductive coupling mechanism.⁷³ The unstable oxidized O created in the anionic process could trigger the oxygen network reorganization by adopting different coordination modes to the transition metal (here Ru) from a η^1 - to η^2 -type model of either $\text{Ru}^{5+}\text{-(O}_2\text{)}^{2-}$ or $\text{Ru}^{4+}\text{-(O}_2\text{)}^-$ (Figure 1-14c), leading to the formation of peroxo/superoxo-like species with short O-O bonds to restabilize the oxygen network and simultaneously the reduction of transition metal by means of the ligand metal ($\text{O} \rightarrow \text{M}$) charge transfer due to the high covalent interaction between Ru and O. This proposal was further verified by the variation of the atomic charges through the atomic charge Bader

analysis, reflecting the anionic redox should be reversible once the peroxo-like species $(O_2)^n$ are covalently stabilized to the transition metal through powerful M-O covalent interactions.¹²⁰ Further studies also demonstrated that this form of activity also occurs in $Li_2Ru_{1-y}Ti_yO_3$ and $Li_2Ru_{1-y}Mn_yO_3$.^{75, 153} This reductive coupling mechanism was claimed to also account for the activity in other highly covalent oxides, such as α - and β - Li_2IrO_3 ^{74, 78}. Although the detailed mechanism accounting for the approached limits of the cationic and anionic electrochemical activity of Li_3IrO_4 is still not clear, this reductive coupling mechanism may apply as well.⁹⁸

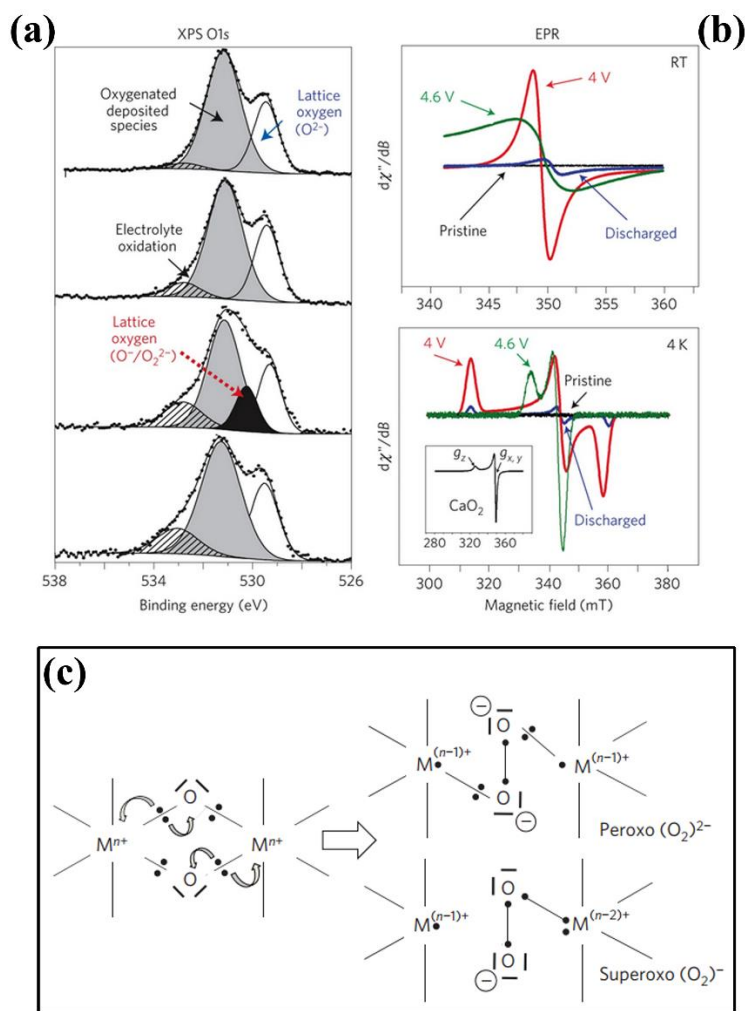


Figure 1-15. (a) O 1s XPS spectra of $Li_2Ru_{0.5}Sn_{0.5}O_3$ samples in the pristine state, charged to 4.0 V, charged to 4.6 V and discharged to 2.0 V, respectively (from top to bottom). (b) X-band EPR spectra collected on the same series at room temperature (top) and 4 K (bottom). (c) Reductive coupling mechanism stabilizing the

oxidized oxygen by forming peroxo-like species (O_2)ⁿ⁻. Reprinted with permission from “Reversible anionic redox chemistry in high-capacity layered-oxide electrodes”.⁷³ Copyright © 2013 Springer Nature.

The first visualization of the shortening of O-O distances was achieved in $\alpha\text{-Li}_2\text{IrO}_3$ using scanning transmission electron microscopy (STEM) and neutron diffraction.⁷⁴ This evidence is of great significance since it provides structural clues for the existence of the signatures of anionic redox and also establishes a fundamental relationship between the evolution of the O-O bonding and anionic redox process in layered oxides. However, subsequent analysis of the activity with *operando* Ir L-edge XAS revealed that the transition metal remained active throughout delithiation (Figure 1-16a), indicating that the shortening of O-O distances may not be sufficient condition for oxygen redox.¹²² Instead, it was proposed that cation migration was needed to activate oxygen redox in $\text{Li}_2\text{Ir}_{1-y}\text{Sn}_y\text{O}_3$ by Hong et al (Figure 1-16b).¹²² Whereas they proposed that Ir oxidation to an average state of 5.5+ could explain all the activity at $y = 0$, oxidation beyond the capacity of Ir was observed for $y > 0$ due to the existence of out-of-plane migration of the cations into a Li layer site, leading to the creation of a cation vacancy V_M and neighboring single-coordinate (dangling) oxygen atoms. The subsequent formation of $\text{Sn}_{\text{Li}}\text{-}V_M$ and $\text{Ir}_{\text{Li}}\text{-}V_M$ (antisite cation-vacancy) defect pairs stabilize the delithiated structure. When M is Ir, the substantial bond contraction is accompanied by a splitting of the previously unhybridized O 2p states with some moving above the Fermi level and being oxidized as oxygen redox. Meanwhile, the bond contraction results in charge donation from the dangling oxygens to the Ir bonding partners (called ligand metal charge transfer, LMCT), leading to the formation of very short Ir-O bonds, reminiscent of bond order greater than 1. On the other side, when M is Sn, the single-coordinate oxygens are proposed to pair up to form short O-O dimers with a bond distance of ~ 1.44 Å that straddle the V_M , resulting in a shift of the previously buried non-bonding O 2p states from below to above the Fermi level along with donation of electron from O to a neighboring Ir via LMCT. This LMCT would be achieved either by the increased covalency due to the short Ir-O bond in $\text{Ir}=\text{O}$ or via the direct electron transfer from the O-O σ^* antibonding to neighbouring Ir ions. All together, the dangling oxygen

derived from the cation migration simultaneously stabilize both the low valence electron count in oxidized state through LMCT and the resulting oxygen species in the form of either terminal oxo ligands or O-O dimers. Not limited to typical two-dimensional (2D) layered oxides, unconventional processes were also proposed for 3D β - Li_2IrO_3 with high electrochemical reversibility, enriching the structural chemistry of the electrodes that display this unconventional reactivity.⁷⁸ In this case, Ir L-edge XAS seemed to be consistent with the existence of electronic changes centered beyond Ir.

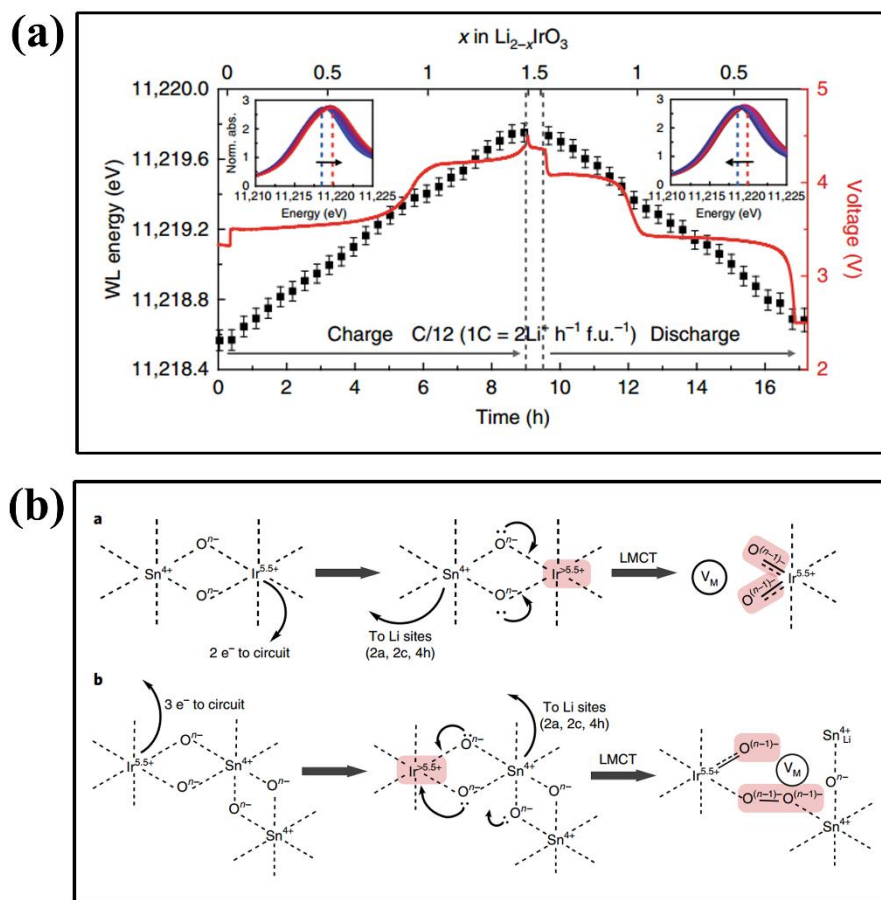


Figure 1-16. (a) Evolution of the Ir L_{III}-edge white line energy of α - Li_2IrO_3 during the first cycle. The raw XANES data for charging and discharging are shown in the left and right insets, respectively. (b) Mechanism of cation migration and LMCT-mediated anionic redox in $\text{Li}_2\text{Ir}_{1-y}\text{Sn}_y\text{O}_3$. Reprinted with permission from “Metal-oxygen decoordination stabilizes anion redox in Li-rich oxides”.¹²² Copyright © 2019 Springer Nature.

By comparing the electrochemical performance delivered by Li_2RuO_3 , $\text{Li}_2\text{Ru}_{1-y}\text{Sn}_y\text{O}_3$ and $\text{Li}_2\text{Ru}_{1-y}\text{Ti}_y\text{O}_3$, the voltage decay is ascribed to the trapping of the cations in the interstitial tetrahedral sites, thus establishing a robust correlation between the voltage decay and the amount of cations that remain locked in tetrahedral sites.¹⁵⁴ In these compounds, hysteresis was proposed to result from the interplay between the cationic-anionic redox processes, which may follow different paths between oxidation and reduction.¹¹⁹ The processes ascribed to anionic redox in these phases have also been associated with a severe distortion of the coordination sphere around transition metal atoms, especially compared to conventional cationic redox processes, which introduces energy inefficiency and demands enough atomic movement to compromise the kinetics of the overall reaction.

While the measured capacities associated with oxygen redox-cation migration are highly reversible, this process is, in many aspects, irreversible precisely because it is accompanied by the evolution of the redox potential after the first charge and the associated migrated transition metals are not fully restored to their original positions at any time upon cycling. These issues were overcome to suppress hysteresis in potential by adopting a different layer stacking in $\text{O2-Li}_x(\text{Li}_{0.2}\text{Ni}_{0.2}\text{Mn}_{0.6})\text{O}_2$. The structure of this compound alters the topology of the pathway of M migration compared to a conventional O3 stacking of the majority of layered oxides known, rendering it reversible.¹⁵⁵ The local coordination environment of Li sites in the O3 and O2 structures substantially differ: LiO_6 octahedra only share edge with MO_6 octahedra in the former, while they share faces with MO_6 octahedra in the latter (Figure 1-17a). In the O2-type layered oxides, the M migration from the octahedral/tetrahedral intermediate sites to the adjacent Li vacant tetrahedral/octahedral sites is thermodynamically unfavorable due to the large electrostatic repulsion between face-shared cations. This electrostatic barrier of face-shared sites enables the facilitation of the recovery of M ions upon reduction by streamlining the return path. Anionic redox with a high electrochemical, chemical and structural reversibility was further demonstrated in $\text{Na}_{0.6}[\text{Li}_{0.2}\text{Mn}_{0.8}]\text{O}_2$ (Figure 1-17b), whose intralayer ordering through a ribbon superstructure largely suppress Mn migration

while maintaining O states accessible to ligand-centered redox. This feature prevent O₂ formation and stabilize electron holes on O²⁻ by preserving the degeneracy of the O 2p states.¹⁵⁶

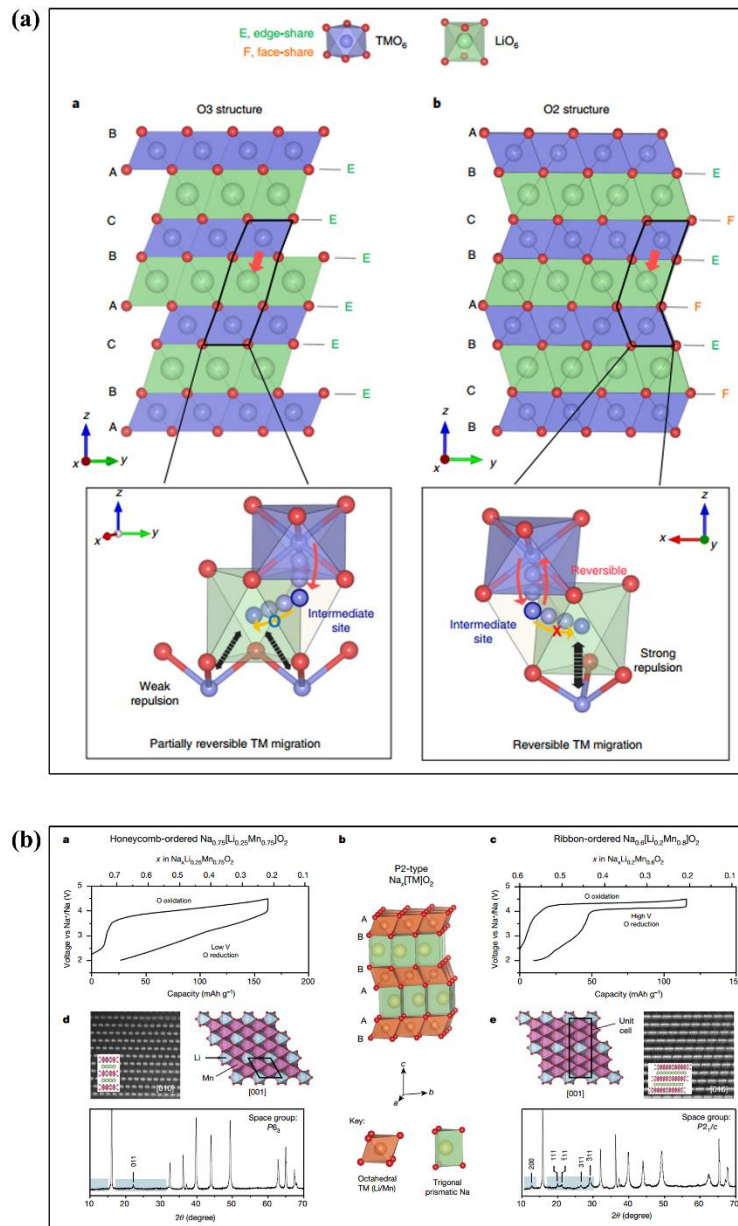


Figure 1-17. (a) Comparison of the crystal structure and the transition metal migration path for O3-Li(Li_{0.2}Ni_{0.2}Mn_{0.6})O₂-type structure (b) and O2-Li_x(Li_{0.2}Ni_{0.2}Mn_{0.6})O₂-type structure (c). Reprinted from “Voltage decay and redox asymmetry mitigation by reversible cation migration in Li-rich layered oxide electrode” with permission from Springer Nature.¹⁵⁵ Copyright © 2020 Springer Nature. (b) Comparison of electrochemistry and structure of honeycomb- and ribbon-ordered cathode materials. Reprinted with

Altogether, the above description demonstrates that the anionic redox is appealing and could be an alternative for the design of advanced electrode materials. But, clearly, pushing oxygen redox brings about complications since highly oxidized oxides become increasingly unstable towards O₂ release and other detrimental reactions. In order to rationalize this intriguing oxygen activity and overcome the disadvantage aspects, a complete picture of the fundamentals of the oxygen involvement in the charge compensation process is imperatively required.

1.7 Research goals

Exploiting lattice oxygen redox could significantly enhance the capacity of the Li-rich cathode electrodes. In spite of such advantage, unsolved associated drawbacks, such as hysteresis and sluggish kinetics, largely impede practical application of this concept to design phases that truly break through the existing barriers of energy density of Li-ion batteries. In this introduction, many arguments have been made of the signatures that enable oxygen redox, but mechanistic insight into the evolution of O states has strongly depended on theoretical models with scant direct experimental validation of which exact species are involved in charge compensation. The research presented in this thesis helps further our understanding the process of the ligand-centered redox occurred in 4d/5d-based Li-rich model oxides by systematically investigating the variation of both the crystal and electronic structure associated with Li (de)intercalation. The established picture of the ligand-centered redox could then be applied for the design of high-energy-density Li-ion battery electrodes. In Chapter 2, the methods including a series of analytical techniques and computational approaches utilized to analyze the redox in these compounds are discussed in greater detail. In Chapter 3, a comprehensive study was carried out to elucidate the spectroscopic signatures of oxygen redox in Li₂RuO₃. In Chapter 4, the redox centers associated with Li intercalation were defined in the model

compound Li_3RuO_4 with two polymorphs by systematically exploring the variation of crystallographic and electronic structure upon cycling. In Chapter 5, the role of O states in the solid state electrochemistry of Li_3RuO_4 is comprehensively evaluated, validating the existence of the non-bonding O 2p bands and the reversible evolution of the O electronic structure by combining X-ray spectroscopy and computational techniques. Finally, in the direction of increasing O/TM ratio, Chapter 6 discussed the electrochemical behavior of Li_7RuO_6 and detailed the charge compensation mechanism and the associated activity of ligand oxygen concurrent with Li intercalation.

Chapter 2 Experimental methods

2.1 Synthetic procedures

A conventional solid-state method of synthesis at high temperature was used throughout this thesis. The reactants for the target products were weighted under the stoichiometric ratio and then mixed in an agate mortar and pestle before grinding in a planetary ball mill using a zirconia set for 1 h at 500 rpm and finally the homogeneous mixture was compacted into pellets. The pellets were reacted at varied synthetic conditions including the temperature, the calcination time and the gas atmosphere in an alumina crucible. After cooling to room temperature naturally, the obtained samples were ground into fine powders for characterization.

2.2 Electrochemical characterization

For battery applications, electrochemical evaluation is critical to understand the functionality of cathode materials. This evaluation is also indispensable to define the redox chemistry of solid materials. These experiments reveal unique insights into the delithiation mechanism and the long-term electrochemical reversibility of batteries can.¹⁵⁷ Among the various modes of electrochemical experimentation, controlled current methods (termed galvanostatic) were used in this work.

2.2.1 Theoretical concepts of galvanostatic experiments

Galvanostatic techniques, also called chronopotentiometric techniques, involve passing a controlled current between a working and reference electrode in an electrochemical cell followed by the recorded potential response as a function of time.¹⁵⁷ During the experiment, the current is imposed by a high-voltage power supply (e.g., several 90-V batteries or a 400-V power supply) and a large resistor. Under galvanostatic options, the amount of charge transferred in the electrochemical cell can be precisely calculated via a coulometry based on the applied current and the elapsed time as follows:

$$Q = I \times t \quad (2-1)$$

where Q is the quantity of the transferred charge, I is the controlled current in amperes, and t is the time elapsed in seconds.

In the Li-ion battery field, the quantity of the transferred charge, Q , theoretically equates to the amount of Li shuttled between the working and counter electrodes with an underlying assumption being that the faradaic efficiency is 100%, that is, all of the transferred charge comes from electrode redox reactions of interest, and not from parasitic reactions occurring concurrently such as electrolyte decomposition at the electrode-electrolyte interface. In this work, a constant-current chronopotentiometry was used where the applied current was calculated by “ C/x ” (i.e. $C/10$) where C is the total charge required to achieve 100% delithiation in x hours.

The obtained voltage profile from galvanostatic testing could provide chemical insight into the underlying reactions during electrochemical cycling. To understand the voltage profile, the first parameter to consider is the coulombic efficiency, which describes the charge efficiency by which electrons are transferred in batteries. It has been widely utilized in battery community as a quantifiable signal of the electrochemical reversibility of batteries. By definition, coulombic efficiency is the ratio of the discharge capacity over charge capacity of a specific electrode in a cell. Since capacity is usually measured by the total charge flow into/out of the electrode, coulombic efficiency could also be expressed as the ratio between the amount of electrons or Li^+ ions returning to the cathode and that of electrons or Li^+ ions departing from the cathode during a full cycling process, as described in equation 2-1,¹⁵⁸

$$\text{Coulombic efficiency} = \frac{\text{Discharge capacity}}{\text{Charge capacity}} = \frac{\text{Total number of } \text{Li}^+ \text{ ions back to cathode}}{\text{Total number of } \text{Li}^+ \text{ ions departing from cathode}} = \frac{\text{Total number of } e^- \text{ back to cathode}}{\text{Total number of } e^- \text{ departing from cathode}} \quad (2-2)$$

In an ideal cell where there are no side reactions on the electrode, the flow of Li^+ ions or electrons should be completely from reversible electrochemical reactions, and subsequently, coulombic efficiency equals to 100%. In realistic cells, however, side reactions between electrodes and electrolytes are ubiquitous and can be either electrochemical or chemical. In the former case, electron loss and acceptance still occur

on the current collectors but are irreversible. The electrons there can be acquired by the current collector and subsequently counted into the coulombic calculation, which complicates the meaning of the obtained coulombic efficiency. In the latter case, electrons generated from side reactions may or may not be collected by current collectors, depending on pathways of the reactions. In this thesis, the electrochemical reactions are considered ideally and the electrons all come from the electrochemical reactions of interest.

Another consideration to evaluate the electrochemical curves is overpotential. Overpotential is defined as the difference between a thermodynamic potential of a redox reaction (open circuit voltage, OCV) and the potential at which the redox chemistry is experimentally observed.¹⁵⁷ Overpotential is correlated with the coulombic efficiency of an electrochemical cell with a rule of thumb that the smaller overpotential, the higher efficiency. Overpotential is also the most common source of voltage hysteresis, measured as the difference between the experimental value of redox potential during oxidation (cathode charging) and reduction (cathode discharging). Although a unique thermodynamic potential for an electrochemically redox reaction can be obtained based on the Nernst equation, in reality, a small hysteresis due to thermodynamic effects has been proposed to exist (Figure 2-1). While still an emerging concept, this “thermodynamic hysteresis” (V_{HYS} in Figure 2-1) has been ascribed to entropic effects, mechanical stress and microscopic distortions within the active material particles.¹⁵⁹

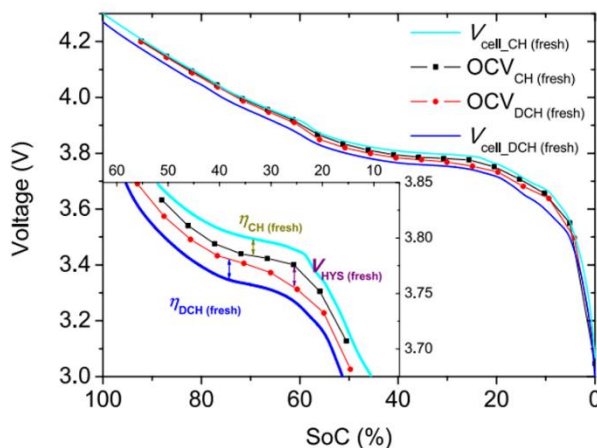


Figure 2-1. Charge-discharge cell voltages of NMC cells under C/25 rate galvanostatic operation and OCVs of a fresh NMC cell. The inset demonstrates how the overpotential and voltage hysteresis are obtained.

Rigorously, overpotential is due to the existence of kinetic barriers that can substantially influence the electrode response during the forward and backward reaction. These barriers can be grouped into two effects: mass transfer and charge transfer. Mass-transfer effect results from limited chemical diffusion in both electrolyte and electrode, but, in intercalation reactions, it is most dominant in the latter because transport in the solid phase is generally slower than in liquids. The charge-transfer effect is due to the need to exchange charged species involved in the redox reaction at the electrode-electrolyte interface. Under both circumstances, the overpotential will increase with the rise of the applied current. Hence, a balance between the applied current and the kinetic barrier is sought to realize practical reversibility.

2.2.2 Experimental details

Galvanostatic experiments were carried out in two-electrode 2032 coin-type cells. The active materials were homogeneously mixed with 10 wt% carbon black (Denka) under Argon atmosphere. Working electrodes were prepared from the uniformly ballmilled mixtures, and 10 wt% polyvinylidene fluoride (PVDF) (Kynar) in 1-methyl-2-pyrrolidone (NMP, Sigma–Aldrich). The slurries were cast on an electrochemical grade aluminum foil using a doctor blade, followed by drying under vacuum at 110°C overnight. Dried electrodes with typical active material loadings of 3-5 mg/cm² were punched into pieces with a diameter of ½ inch for further cell assembling. All the cells were fabricated in an argon-filled glovebox in which moisture and oxygen levels were lower than 0.1 ppm. Within the cells, a high-purity lithium foil (Alfa Aesar) was employed as the counter/reference electrode, and a 25-μm-thick polypropylene membrane (Celgard 2400) was used as the separator, and a solution of 1 M LiPF₆ in a mixture of ethylene carbonate (EC)/dimethyl carbonate (DMC) (1:1, V/V, Novolyte Technologies) was employed as the electrolyte. The galvanostatic charge–discharge cycling was performed at room temperature using a BT-Lab tester with a current rate of C/10 with different voltage-cutoff windows. All

potentials quoted in this thesis were referenced to Li^+/Li^0 unless otherwise mentioned. For *ex situ* experiments, when the state of the cell reached a point of chemical interest, it was stopped and immediately disassembled in an Ar-filled glovebox to avoid self-discharging under open-circuit conditions. The working electrode was washed with DMC three times to remove excess electrolyte followed by drying under vacuum inside the glove box antechamber for 5 mins. The harvested electrodes were then stored in the glovebox. Before they were transferred to different experimental stations, they were enclosed in an Ar-filled metal sleeve rated for vacuum applications in order to minimize the exposure to air.

2.3 Synchrotron light source

The best quality diffraction and spectroscopic data, a target in this work, requires the measurements to be conducted at synchrotron facilities supplying X-rays with the tunable energy and high brilliance.

Brilliance measures the quality of the light. It takes into consideration the angular divergence of photons, the amount of photons produced per second, the cross-section area of the beam, and the photons falling within a bandwidth (BW) of 0.1% of the central frequency. The relationship is described as follows:

$$\text{brilliance} = \frac{\text{photons}}{\text{second} \cdot \text{mrad}^2 \cdot \text{mm}^2 \cdot 0.1\% \text{BW}} \quad (2-3)$$

The greater the brilliance, the more photons of a given wavelength are concentrated on a spot per unit of time.¹⁶⁰

Charged particles, typically electrons, are used to generate X-ray radiation in the storage ring. First, the electrons are accelerated to high relativistic speeds, where they are subject to an acceleration perpendicular to their velocity due to the existence of the Lorentz force exerted by the strong magnetic field from bending magnets or insertion devices (undulators or wigglers). Synchrotron radiation is formed by converting high energy electrons into photons with the energy proportional to the fourth power of the electron and inversely proportional to the square of the radius of the path. The brightness of the radiation from insertion devices can be orders of magnitudes brighter than bending magnets, due to the coherence of the radiation. The functionality of a certain beamline determines which device would be used to generate the radiation. The

energy of the generated radiation will then be tuned by monochromators for specific experimental application. As of 2018, over 60 synchrotron facilities exist in the world, or under various stages of development.

To explore the ligand-centered redox in Li-rich transition metal oxides, experiments were carried out at two different light sources: the Advanced Photon Source (APS) at Argonne National Laboratory (Lemont, IL) and the Canadian Light Source (CLS) in Saskatoon, Canada.

2.4 Neutron source

Although many processes like the nuclear fission and nuclear fusion can be used to emit neutrons, nuclear spallation is currently the primary choice due to advantages in energy cost, pulsed beams and high safety from the absence of the chain reaction.

Usually the neutron production at a spallation source starts with a high-power proton accelerator. Then the intense beam of protons is focused onto a heavy-metal target, such as tantalum, tungsten and mercury, to generate neutrons with very high energies through the spallation process. The generated neutrons are then decelerated in moderators filled with liquid methane or liquid hydrogen. The neutrons with proper energy will be guided through beamlines to areas containing highly specialized scattering instruments. There, neutrons of different energies are used in a wide variety of experiments on materials.

To determine the crystal structure and locate the precise Li position in the oxides with heavy transition metals, high resolution neutron diffraction was performed at the beamline POWGEN (BL-11A) at the Spallation Neutron Source (SNS) at Oak Ridge National Laboratory (ORNL).

2.5 Characterization of crystal structure

The crystal structure of an electrode material determines its electrochemical performance since it not only has a significant influence on the electrochemical redox potential but also the long-term reversibility. Obtaining knowledge of the structural variation with the Li (de)intercalation could help identify reaction bottlenecks and kinetic factors that underpin the performance and coulombic efficiency of the battery. The combination of X-ray diffraction, sensitive to heavy atoms, and time-of-flight neutron diffraction, sensitive

to light atoms like Li, could unveil the (de)lithiation mechanism and identify the crystallographic phases present in the electrode during the electrochemical process.

2.5.1 Theory of diffraction

The interaction of incident radiation with matter causes it to be coherently scattered, or diffracted. In a solid, each atom can be treated as a coherent point scatterer, and the strength with which the radiation is scattered by an atom is a function of its electron count, i.e. its atomic number. When atoms are arranged periodically, as in a crystal, the scattered radiation from the lattice atoms produces interference patterns as the waves combine constructively or destructively based on the wave paths. The interferences, or diffraction patterns contain structural information about the periodic atomic arrangement and the thermal vibrations within a crystal. Due to the similar magnitude of their wavelength and atomic spacings, X-rays are the ideal candidate for analyzing solids. But because X-rays interact with the electron clouds of an atom, they are not very sensitive to light atoms. Furthermore, X-rays are insensitive to the electron spin and, therefore, is not capable of characterizing unpaired electrons giving rise to magnetic properties in solids.¹⁶¹

Thermal neutrons can be generated at a wavelength of 1-2 Å, which is also in the same order of magnitude as interplanar spacings in ordinary crystalline substances. The corresponding neutron diffraction offers advantages over X-ray diffraction. The most important one in the context of this thesis is that the neutron scattering length is not dependent on atomic number, rather on nuclear composition, which leads to sensitivity of light atoms such as Li. Therefore, the combination of X-ray diffraction and neutron diffraction is a powerful method for the determination of the crystal structure of cathode materials of interest in this work.

Both X-ray diffraction and neutron diffraction follow Bragg's law shown in equation 2-4:

$$2d_{hkl} \sin \theta = n\lambda \quad (2-4)$$

where θ is the diffraction angle or Bragg angle, d is the interplanar spacing of the lattice planes defined by the Miller indices (hkl), n is an integer that corresponds to the order of diffraction, and λ is the wavelength of incident X-ray.

The Bragg's law states that diffraction will happen when constructive interference occurs between two scattered waves from crystallographic planes separated by the distance, d_{hkl} .

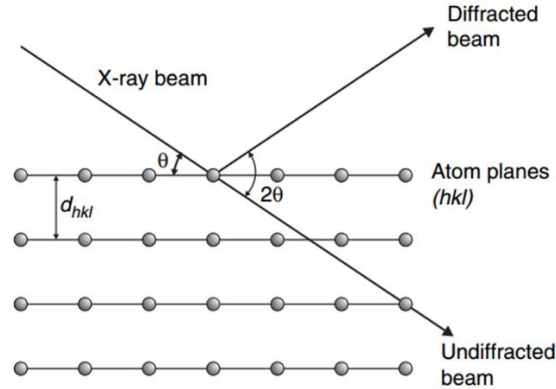


Figure 2-2. The geometry derivation of Bragg's Law for X-ray diffraction from a set of crystal plans (hkl) with interplanar spacing, d_{hkl} . Reprinted with permission from "Crystals and Crystal Structures".¹⁶² Copyright © 2006 John Wiley and Sons.

Theoretically, the diffracted intensity at certain Bragg reflection (hkl) could be calculated based on the structure factor F_{hkl} as it is proportional to $|F_{hkl}|^2$. The structure factor is described in equation 2-5:

$$F_{hkl} = \sum_j f_j \exp[2\pi i(hx_j + ky_j + lz_j)] \quad (2-5)$$

Where j refers to the number of atoms in the unit cell, f_j is the atomic form factor, (x_j, y_j, z_j) stands for the position of the atom j in the unit cell and (hkl) is the Miller index.

The physical and geometrical factors that modify the diffraction intensity need to be considered. Any atomic displacement parameters away from the perfect arrangement of the crystal structure would result in the diminishment of the intensity. The *Lorentz* factor is a measure of the amount of time that a point in the reciprocal lattice remains on the sphere of the reflection, which could affect the diffraction position and intensity. Multiplicity factor refers to the number of types of plane in the set (hkl), which directly affects the intensity. The last term to be considered is the absorption (attenuation), which also influences diffracted intensity.¹⁶³ Therefore, all those factors need to be taken into account to obtain a satisfactory result during the simulation of the diffraction patterns.

2.5.2 Diffraction data analysis

Qualitative analysis of diffraction patterns can be performed by comparing the experimental with the reference data, which identify the phases present in the sample. However, such analysis cannot extract the detailed quantitative information such as phase ratios or defect chemistry. In the case of powder samples, this quantitative analysis is realized by performing structural refinements of the diffraction data. Using refinements, one can determine phase composition, lattice parameters, atomic positions and site occupancies, atomic displacement parameters, crystallite size, microstrain, and preferred orientation,

Diffraction data can be refined by three methods: Le Bail, Pawley and Rietveld refinements. During the refinement, the theoretical diffraction patterns would be calculated based on input variables including instrumental parameters, signal background and hypothesized lattice structure. Then the calculated diffraction would be compared with the experimental data. Following this procedure, the input variables would be adjusted iteratively so that the calculated data would match the experimental one within acceptable parameters of least-squares minimization. Le Bail and Pawley refinements are faster with an only difference being that Pawley fit considers the individual intensity. At the atomic scale, both methods only provide information on the symmetry and size of the unit cell lattice. In contrast, Rietveld refinements extract additional information such as atomic positions, thermal parameters and site occupancy by implementing a more sophisticated algorithm that better accounts for the structure factor, but it needs high-quality diffraction data. In this work, both Pawley and Rietveld refinements were employed to obtain the crystallographic information of the electrode materials at different states of charge. Pawley refinements were mainly performed on patterns with low resolution. GSAS-II was used to conduct the refinements.¹⁶⁴

2.5.3 *Ex situ* X-ray and neutron diffraction

Laboratory powder X-ray diffraction (pXRD) profiles were collected by scanning from 10° to 90° (2 θ), using a step size of 0.019°, at a rate of 2.6x10⁻⁵ °/min 2 θ , in a custom air-free sample holder, in a Bruker D8 Advance diffractometer operating at 40 kV and 40 mA with Cu K α radiation (λ = 1.5418 Å). The XRD

patterns of samples were aligned by shifting them linearly on the basis of the position of the (220) peak of aluminum foil (JCPDS card number: 04–0787) used as an internal standard.¹⁶⁵

In order to obtain high-quality diffraction data for the structural analysis, high-resolution synchrotron X-ray diffraction measurements (SXR) were performed at 11-BM beamline of APS at Argonne National Laboratory with an average wavelength of 0.41 Å. For samples with high X-ray absorption coefficient, an appropriate amount of amorphous silicon dioxide was introduced and mixed homogeneously with sample powders to reduce X-ray absorption and subsequently to increase the ratio of intensity to background. The powders were sealed in Kapton capillaries with a diameter of 0.8 mm mounted on bases provided. Air-sensitive samples were loaded and sealed under Ar in a glove box to minimize the exposure to ambient O₂ and H₂O. The data points were recorded at room temperature with a scan speed of 0.01°/s and step size of 0.001° 2θ and the general data collection time was 2 hours.

Time of flight neutron powder diffraction (TOF-NPD) data were collected at room temperature at the beamline 11A (POWGEN) of the Spallation Neutron Source (SNS) at Oak Ridge National Laboratory (ORNL) with the center wavelength of neutrons of 1.5 Å. An appropriate amount of samples were sealed in airtight vanadium sample cans with the inner diameter of 6 mm under argon and transferred to the beamline station for data collection.

2.5.4 Operando synchrotron X-ray diffraction

During an electrochemical reaction, the system is not at thermodynamic equilibrium, due to the passage of electrical current. As a result, kinetic constraints can impose the formation of metastable states during battery reactions. These states can easily undergo relaxation in the absence of electrical stimuli. As a result, *ex situ* approaches, where electrode materials of interest are harvested from a cell at a desired state of charge for analysis, introduce confounding variables into the analysis, whereby it is difficult to verify if the states being measured are actually the predominant phases under actual operating conditions. In addition, *ex situ* measurements could also allow detrimental exposure of highly reactive species, short circuits during the cell disassembly, and contamination with atmospheric species (O₂, N₂ and H₂O) even in the glovebox.

In contrast, *operando/in-situ* measurements, where the experiment can be conducted during the electrochemical reaction, can circumvent spontaneous relaxation so that the real electrochemical state can be reliably identified. However, performing *operando* measurements requires a special electrochemical cell device that both satisfies requirements for uncompromised measurement and reliable electrochemical behavior, which is much more challenging than *ex situ* experiments.¹⁶⁶ In order to minimize the X-ray absorption to ensure the successful spectroscopic measurement, X-ray transmissive windows ideally made from amorphous and low Z materials should be employed. Besides, they should be nonpermeable to H₂O, O₂ and N₂, and have sufficient electrical conductivity. Today, reliable electrochemical performance can be accomplished with a number of delicately designed cells with excellent stability, a hermetic seal and uniform pressure.

In this work, Argonne's multi-purpose *in situ* X-ray (AMPIX) cell (Figure 2-3) was employed to carry out the *operando* synchrotron X-ray diffraction.¹⁶⁶ The cell delivers reliable electrochemical performance over extended cycling period comparable with that of the coin cell, due to the high-fidelity hermetic seal and uniform pressure from the rigid X-ray transparent windows. The cell body is electrically insulating, containing a cylindrical cavity with an aperture along the body axis for the transmission of incident/outgoing X-rays. The two electrodes are comprised of 316-series stainless steel with corrosion and chemical resistance and suitable electrical conductivity. X-ray windows, made from an electrically conductive dense glassy carbon Sigradur-(G) protected by a thin polyimide film from directly contacting Li, are attached to the electrodes by using an electrically conductive adhesive.

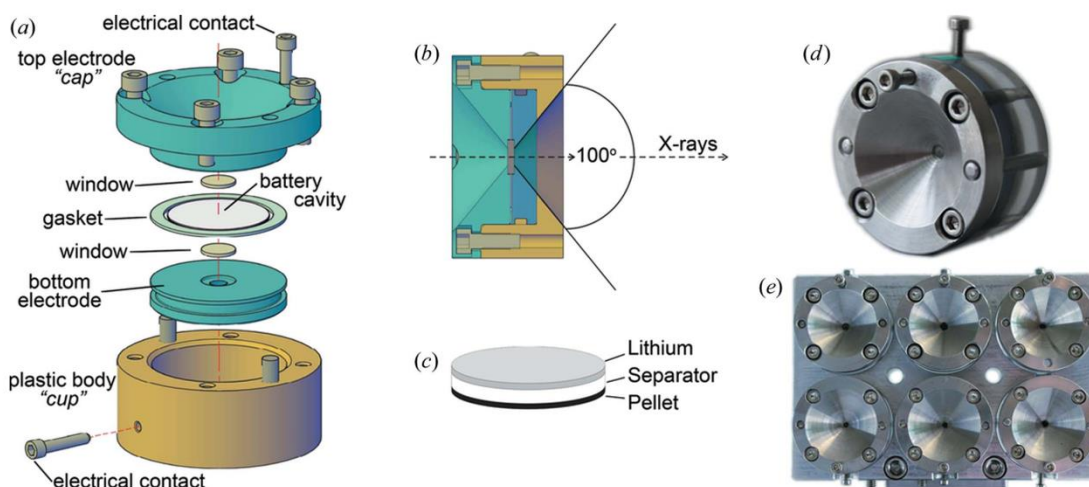


Figure 2-3. (a) Schematic of the AMPIX cell with principle components, (b) schematic of interaction between the assembled AMPIX cell with x-ray, (c) a typical battery stack, and photographs of (d) an assembled AMPIX cell and (e) a six-cell multicell holder used for *operando* experiment. Reprinted with the permission from “The AMPIX electrochemical cell: a versatile apparatus for in situ X-ray scattering and spectroscopic measurements”.¹⁶⁶ Copyright © 2012 the International Union of Crystallography.

2.5.5 Experimental setups for *operando* synchrotron X-ray diffraction

Pellet electrodes were used for the *operando* synchrotron X-ray diffraction. Firstly, the electrode was prepared by mixing 60wt% active material, 10wt% carbon black (Vulcan XC-72, Cabot Corporation), 10 wt% “Super P” carbon (Alfa Aesar), 20 wt% polytetrafluoroethylene (PTFE) (Sigma-Aldrich) in a mortar and pestle in an argon-filled glovebox. The homogeneous mixture powder was then pressed into an ~11 mm diameter pellet with a thickness of ~150 μm and a mass of ~20 mg. The AMPIX cell was assembled in the argon-filled glovebox using Li metal as the counter electrode, a Whatman GF/B borosilicate microfiber filter as the separator, and 1 M solution of LiPF_6 in a 1:1 mixture of ethylene carbonate (EC)/dimethyl carbonate (DMC) as the electrolyte (Tomiya Pure Chemical Industries). The assembled AMPIX cells were then put in the cell holder and then galvanostatically cycled at room temperature with a rate of C/10 by using the 8-channel MACCOR® battery cycler (Maccor model 4300).

Operando SXRD experiments were performed at high-energy beamlines 17-BM ($\lambda = 0.25463 \text{ \AA}$) and 11-ID-B ($\lambda = 0.2113 \text{ \AA}$) of the Advance Photon Source (APS) at Argonne National Laboratory to collect

data of electrode materials of interest within the setup voltage window. Diffraction images were recorded in a Debye–Scherrer geometry using an amorphous silicon-based area detector with time interval of 10 mins at 17-BM-B and 30 mins at 11-ID-B. The background calibration of the AMPIX cell was collected by utilizing an assembled AMPIX cell containing all the components except for a cathode. The data were calibrated using GSAS-II software via LaB₆ calibrant (SRM660a) for 17-BM-B data and using a CeO₂ standard (SRM674b) for 11-ID-B data and integrated within GSAS-II.¹⁶⁴

2.6 Electronic structure analysis of electrode materials

The charges associated with Li (de)intercalation are compensated by the concurrent redox reactions, inevitably leading to variations in the electronic structure. The evaluation of changes in the electronic structure could help to understand the detailed charge compensation mechanism of (de)lithiation. Core-level spectroscopies provide element-specific information of the electronic structure around a given atomic site due to the localized core level and no contribution from other atoms in the system. Thereby core-level spectroscopies are ideal probes to study the chemical state, nature of chemical bonding, and local geometric structure. The obtained information is critical to understand and improve the function of electrode materials.

In this type of spectroscopy, a core is created by the ejection of an electron in a core level through the absorption of an X-ray photon with appropriately tuned energy.¹⁶⁷ The ejected core electron can be excited to a bound, empty state below the continuum or above the continuum where it becomes ionized. The creation of the core hole leads to a highly excited state, which is unstable and easily relaxes via a radiant or non-radiant decay process. The resulting excitations and relaxations form the basis of the various core-level spectroscopies. The creation of a core hole by ionization forms the basis of X-ray photoelectron spectroscopy (XPS) while the creation of a core hole by excitation to different intermediate levels before ionization is investigated in X-ray absorption spectroscopy (XAS), which, as a result, probes the unoccupied density of states of a compound. The radiant decay of the core hole filled by the valence electron forms the basis for X-ray emission spectroscopy (XES) while non-radiant decay is studied in Auger emission spectroscopy (AES), both of which are used to probe the occupied electronic structure of a system. In this

work, XAS and XES were used to evaluate the variation of the electronic structure associated with Li (de)intercalation upon cycling of electrode materials.

2.6.1 X-ray absorption spectroscopy

2.6.1.1 Overview of X-ray absorption spectroscopy

Upon irradiation of X-rays with finite energy, they selectively get absorbed by the atoms in the sample. The figure of merit is the absorption coefficient, μ , which emerges from Beer's law¹⁶⁸:

$$I = I_0 e^{-\mu t} \quad (2-6)$$

Where I is the intensity transmitted through the sample, I_0 is the intensity incident on the sample, t is the sample thickness. The absorption coefficient μ is also a smooth function of energy, with a value that relies on the atomic number Z , atomic mass A , sample density ρ and X-ray energy E . The relationship is described as follows,

$$\mu \approx \frac{\rho Z^4}{AE^3} \quad (2-7)$$

The strong dependence of μ on both Z and E is an essence of X-rays, and is the essential to the distinctive advantage of elemental specificity. Due to the Z^4 dependence, the absorption coefficient for different elements could span several orders of magnitude, which leads to a good contrast between different elements for nearly any sample by tuning X-ray energy alone.

As the energy of the incident is equal to the binding energy of a core-level electron during the X-ray absorption process, a sharp rise in the absorption occurs: an absorption edge corresponding to the promotion of the core electron to the empty states at higher energy level and ultimately, to the continuum. This phenomenon is what renders XAS a technique to probe the unoccupied partial density of states (pDOS) of matter. An XAS measurement is actually a measure of μ at and above the binding energy of a certain core level of a known atomic species. The dependence of the absorption coefficient $\mu(E)$ can be measured either under transmission or indirectly via X-ray fluorescence or electron emission modes, as described in equations (2-6) and (2-7), respectively,

$$\mu(E) = \log(I_0/I) \quad (2-8)$$

$$\mu(E) \propto I_f/I_0 \quad (2-9)$$

where I_f is the intensity of X-ray fluorescence or Auger electron emission counted by the amount of fluorescence photons or Auger electrons.

Following the absorption event, the absorbing atom is in the excited state, with one core hole formation and one photo-electron emission, and would relax to the ground state either through the radiative X-ray fluorescence emission or the non-radiative Auger electron emission. When the photoelectron leaves the absorbing atom, its wave will be backscattered by the neighboring atoms and returned back to the absorbing atom. The constructive and destructive interference between the photoelectron wave and the backscattered wave then generate oscillations, resulting in maxima and minima after the edge. In general, a complete XAS spectrum can be divided three regions (Figure 2-4): (1) pre-edge region with the energy of the incident X-ray lower than the absorption edge energy; (2) X-ray absorption near edge structure (XANES) ranging from approximately 0 to 50 eV with respect to the absorption edge energy; (3) extended X-ray absorption fine structure (EXAFS) locating from 50 to 1000 eV or higher above the absorption edge. The features in the pre-edge region are usually ascribed to electron transitions from the core level state to the unoccupied or half-unoccupied orbitals, such as $s \rightarrow p$, or $p \rightarrow d$, which can be used to evaluate the ligand-field effect, spin state and centrosymmetry. The main absorption edge in XANES region is ascribed to the transition to the electric dipole-allowed transition, such as from $1s$ to p states, which is very sensitive to the geometric structure, metal-ligand overlap via shake-down transitions, ligand arrangement, and charges on the metal center. In the EXAFS region, the single scattering by the nearest neighboring atoms could be used to probe local bonding environments of elements and deduce information about types and numbers of atoms coordinating with absorbing atoms, their interatomic distances, and the degree of local molecular bonding disorder.

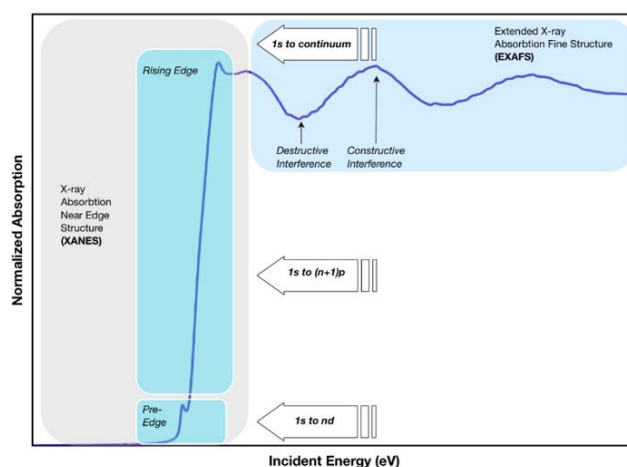


Figure 2-4. Schematic of an XAS spectrum with the main regions and their sources.

Electronic transitions triggered by X-ray absorption obey the dipole selection rule so that the angular momentum is preserved. Within this rule, transitions can only occur between energy states that differ in the angular quantum number (l) by ± 1 . For example, transitions between an s orbital ($l = 0$) and a p orbital ($l = 1$) and vice-versa are allowed, while transitions between an s orbital ($l = 0$) and a d orbital ($l = 2$) are forbidden. The probability of observing the allowed dipole electronic transition is one hundred times higher than that of the forbidden quadrupole transition based on the Fermi Golden Rule, leading to a larger absorption intensity for the allowed transition.¹⁶⁹

Electrons may be excited from different core levels depending on the incident energy of the X-ray. A specific nomenclature is employed to denote the original core orbitals. Promotion from $n = 1$ is called K-edge and excitations from $n = 2$ core levels are coined L-edges, and this approach proceeds alphabetically. With respect to the electronic transition involving the principal quantum numbers of $n \geq 2$ to higher states, spin-orbital coupling effect should be considered, which results into a split in energy between states that have different total angular momentums. As an example, for a transition from a 2p state ($l = 1$), the electron can step from the $2p_{1/2}$ or $2p_{3/2}$, terms as L_{2-} or L_{3-} -edge. Figure 2-5 demonstrates the nomenclature rule used to describe electronic transitions that contribute to XAS edges.

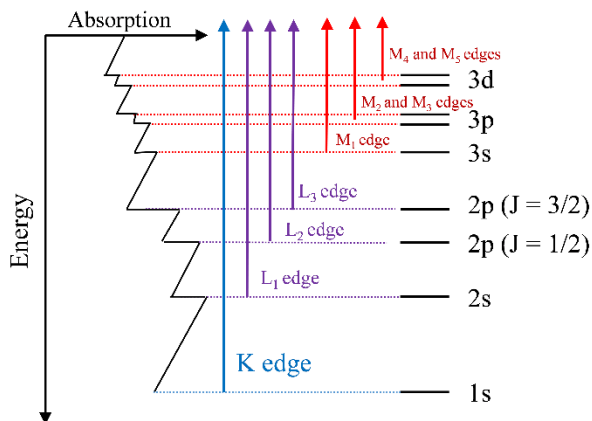


Figure 2-5. Nomenclature rule used to describe electronic transitions that contribute to XAS edges.

As described above, the dependence of $\mu(E)$ on the energy of the incident X-ray could be assessed by three approaches. In practical, one or two detection modes can be employed to measure X-ray absorption spectroscopy. For the transmission mode, the X-ray transmitted through the sample is measured so that it is a bulk sensitive probe. During the measurement, the sample prepared should be thin and homogeneous so that sufficient transmission signal could be obtained. An ion chamber is used to detect the transmitted X-rays. Alternatively, the total quantity of ejected Auger electrons can be summed into the total electron yield (TEY). Due to the escape depth of the electron being less than 10 nm, TEY mode produces surface sensitive signals. It is performed via devices like pico-amperometers and channeltrons to amplify the emitted electrons to a detectable level. With respect to the X-ray fluorescence mode, the escape depth of emitted X-ray photons is similar to X-ray attenuation length, or ~ 100 nm from inside the sample. The fluorescence spectra can be measured either in total fluorescence yield (TFY), partial fluorescence yield (PFY) or inverse partial fluorescence yield (IPFY) modes. The TFY mode is carried out by integrating all of the emitted photons using a non-energy dispersive detector such as a channel electron multiplier. The PFY measurements are taken by only integrating photons with the emission energy of the resonant core electron excitation. The detector for PFY must have energy-resolving capability, such as in silicon drift detectors. The TFY and PFY measurement should be delicately carried out to minimize effects of radiation

saturation effect, which is almost unavoidable in certain conditions. In contrast, IPFY avoids saturation, but it raises the complexity of the measurement. In general, fluorescence detection always raises the possibility of the distortion of measured intensities, which demands caution during data interpretation.¹⁷⁰

2.6.1.2 Experimental setups for X-ray absorption spectroscopy

Ex situ O K-edge X-ray absorption spectroscopy measurements were performed at 4-ID-C beamline at APS and at beamline 8 at the Advanced Light Source (ALS) at Lawrence Berkeley National Laboratory. Samples were attached to a copper sample holder using conductive carbon tape in an argon-filled glovebox and then transferred from the glovebox into a transport container and then into an X-ray absorption antechamber through an argon gas environment to minimize the potential exposure to air. Data were measured simultaneously in both TEY mode from the sample photocurrent at $\sim 10^{-9}$ Torr and TFY mode using a silicon drift diode detector. Data was obtained at a spectral resolution of ~ 0.2 eV, with a 2 s dwell time. During the measurement, three scans were performed at each absorption edge for each sample, and scans were then averaged to maximize the signal-to-noise ratio. The energy scale of the spectra was calibrated with an O reference measured simultaneously.

Ex situ Ru K-edge X-ray absorption near edge spectroscopy (XANES) data were collected under the transmission mode at 10-BM and 20-BM-B beamlines of the APS using an Oxford Si (111) double crystal monochromator with an energy resolution of 1.1 eV at 22 keV. Three consecutive ionization-chamber detectors were used to count the intensity of the monochromatic X-ray beam. Samples were placed between the first and second ionization chambers. Prior to the beam setup, the calibration for monochromatic energy was established by measuring the Ru K-edge of a standard foil of Ru metal located between the second and third ion-chamber. During the measurement, successive spectra were averaged out over periods of 5.5 min based on the scanning time of 0.3 second. The K-edge of the standard Ru foil was measured simultaneously with each sample for energy alignment. Pre-edge background subtraction and XANES normalization were carried out using the Demeter program pack with Athena.¹⁷¹

2.6.2 X-ray emission spectroscopy

2.6.2.1 Overview of X-ray emission spectroscopy

Complementary to XAS, X-ray emission spectroscopy (XES) is employed to probe the occupied electronic states below the Fermi level (valence band). In XES, the core hole created by the previous X-ray absorption process is filled by a valence electron in the form of a radiative decay. The decay releases energy through the emission of an X-ray photon which is subsequently measured by a high-resolution energy dispersive detector. The probability of an electron transition from the occupied state to fill the core hole also follows the Fermi's Golden Rule. Since we are less concerned with the efficiency of the excitation and more concerned with the relative distribution of emitted photons in XES, the electronic transition is limited to dipole transition. XES is divided into two subcategories: non-resonant, when the core electron is first promoted to the continuum well above the absorption threshold, and resonant, when promotion occurs close to the absorption threshold.¹⁶⁷ XES is generally bulk sensitive, and provides element-specific information. Furthermore, resonant XES can be used to probe the contribution of non-equivalent sites due to a large variation in the partial absorption cross-sections of these sites at certain excitation energy.¹⁷²

2.6.2.2 Experimental setups for X-ray emission spectroscopy

Ex situ O K-edge X-ray emission spectroscopy (XES) were performed at REIXS beamline (10ID-2) at the Canadian Light Source (CLS) in Saskatoon, Saskatchewan, Canada. The partial fluorescence yield (PFY) absorption spectra of O K-edge was also obtained by the integration of the corresponding emission. A Rowland circle type spectrometer with an effective resolving power, $E/\Delta E$, of approximately 1400 was employed for the measurement. The $E/\Delta E$ for the REIXS beamline is typically 5000. The samples to be measured were mounted on a carbon tape inside an argon filled glovebag before transferred into the endstation with a typical pressure of 3×10^{-9} Torr. The collected data were calibrated using a reference sample of amorphous silicon dioxide SiO_2 . The XAS data were calibrated with the first pre-peak of $\alpha\text{-SiO}_2$ located at 530.8 eV and then normalized for the incident X-ray beam intensity using the drain current from

the gold mesh upstream of the experimental chamber. In addition, the XES data were calibrated based on two peaks of α -SiO₂ located at 521.4 eV and 525.6 eV.

2.6.3 Resonant inelastic X-ray scattering

2.6.3.1 Overview of resonant inelastic X-ray scattering

Resonant inelastic X-ray scattering (RIXS) is an advanced X-ray technique, with a combination of coherent XAS and XES, in which the X-ray photons are inelastically scattered off matter. RIXS is a two-photon process (photon-in and photon-out) that starts with the promotion of a core electron into an unoccupied valence state, as in XAS, followed by the emission of a photon due to the decay of an electron from a different state filling the core hole, as in XES. The net result is a final state with an electron-hole excitation since a hole is created in the filled valence orbital and an electron in an empty valence orbital. Therefore, RIXS can probe the conduction and valence states directly. Due to a second-order optical process, in addition, RIXS could provide much greater information than that from the first-order optical process alone like XAS and XES. It provides a unique and direct way to measure the momentum resolved charge-charge correlation function of phenomena such as plasmons, charge-transfer excitations and crystal-field and orbital excitations. It also can utilize the polarization dependence of the incident and emitted photons to provide valuable information about the electronic structure. Moreover, RIXS is explicitly a bulk-sensitive probe. The RIXS data can be plotted as a two-dimensional (2D) map, with the incident energy on the y-axis and the emission energy on the x-axis, as shown by a representative spectrum of a cathode material LiNi_{1/3}Mn_{1/3}Co_{1/3}O₂ (Figure 2-6). Within the 2D map, RIXS can be used to generate an energy distribution curve by extracting a single data point from XAS, which provides a new dimension of information along emission energy that is missing in XAS. Furthermore, the emission energy resolved in RIXS offers a new approach to differentiate vital RIXS features within a particular emission energy range, allowing a more detailed investigation of particular chemical states that could be buried in XAS.¹⁷³⁻¹⁷⁷

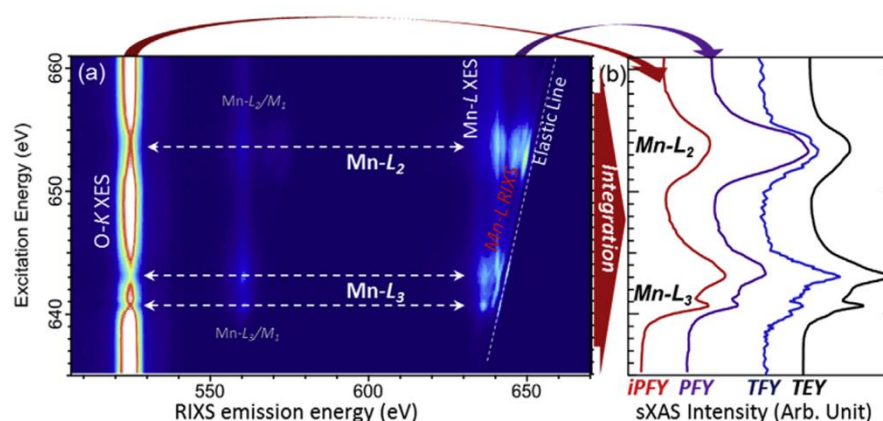


Figure 2-6. (a) Mn L-edge RIXS map of $\text{LiNi}_{1/3}\text{Mn}_{1/3}\text{Co}_{1/3}\text{O}_2$ with the excitation energy as the vertical axis and the emission energy as the horizontal axis. (b) Integration of RIXS intensity along the horizontal direction leads to different types of XAS spectra. Reprinted with permission from “Anionic and cationic redox and interfaces in batteries: Advances from soft X-ray absorption spectroscopy to resonant inelastic scattering”.¹⁷⁷ Copyright © 2018 Elsevier B.V.

2.6.3.1 Experimental setups for resonant inelastic X-ray scattering

Ex situ O K-edge resonant inelastic X-ray scattering (RIXS) was performed at REIXS beamline (10ID-2) at the Canadian Light Source (CLS) in Saskatoon, Saskatchewan, Canada, with the same experimental setups as XES measurement.

2.7 Differential electrochemical mass spectroscopy

2.7.1 Overview of differential electrochemical mass spectroscopy

Differential electrochemical mass spectroscopy (DEMS) is essentially an analytical technique that is a combination of an electrochemical experiment and mass spectrometry. This allows the *operando*, mass-resolved observation of gaseous, volatile electrochemical reactants, and reaction intermediates and/or products.¹⁷⁸ In Li-ion batteries, gas evolution can accompany (de)lithiation process due to various possibilities, including the electrolyte decomposition and lattice oxygen release, which are otherwise difficult to quantify. By correlating the mass spectroscopy and concurrent electrochemical measurements,

the evolved gas species could be identified and quantified, an ambiguously be ascribed to specific electrochemical processes.

2.7.2 Experimental setups for differential electrochemical mass spectroscopy

Quantitative outgassing measurements were performed by our collaborators at the University of California-Berkeley, in a hermetically-sealed cell fitted with gas capillaries connected to a custom-built DEMS system described in detail in previous publications.¹⁷⁹⁻¹⁸² The cell was assembled with the as-prepared electrode as the working electrode, Li foil (11 mm diameter) as the counter electrode, one Celgard® 2400 film and one QMA (WhaMan) glass fiber separators, each 12 mm in diameter. A 1 M solution of LiPF₆ (Sigma-Aldrich) in an ethylene carbonate (EC)–diethyl carbonate (DEC) solvent mixture (1:1, V/V, BASF) was employed as the electrolyte. Electrode preparation as well as cell fabrication were performed under air-free conditions in an argon-filled glovebox. The assembled cells were cycled with a Bio-Logic VSP series potentiostat at a rate of 0.1 Li⁺/hour. During battery cycling, the headspace of our custom cell was sampled with argon as the carrier gas. The CO₂ and O₂ evolved were quantified based on calibrations of the mass analyzer with known amounts of CO₂ and O₂ with argon as the carrier gas.

This technique was used here to study Li₃RuO₄. The total active cathode material used for the measurement was 5.9 mg disordered Li₃RuO₄ (32 μmol) and ordered Li₃RuO₄ 7.0 mg (38 μmol). Cells were cycled between 3.9 and 2.5 V for disordered Li₃RuO₄ and between 4.0 and 2.5 V for ordered Li₃RuO₄, under the current of 14 mA g⁻¹.

2.8 Density functional theory

Density functional theory (DFT) calculations were used to theoretically evaluate the evolution of the partial density of states of elements of interest and simulate the XAS spectra. By combining theoretical DFT calculations with experimental XAS data, the electronic structure variation of an electrode material with cycling can be elucidated, providing vital insights into the underlying redox chemistry. These calculations were carried out by our collaborators at the University of Montpellier (France).

2.8.1 Structural relaxation and electronic structures

Spin-polarized density functional theory (DFT) calculations as implemented in VASP (Vienna ab initio simulation package)^{183, 184} were performed, using the projected augmented wave method (PAW)¹⁸⁵. The generalized gradient approximation of Perdew–Burke–Ernzerhof (PBE)¹⁸⁶ in conjunction with the rotationally invariant Dudarev method (DFT + U)¹⁸⁷ were used to better describe strongly correlated d-electrons. Different U values were tested for Ir(d) metals (0, 2, 4 eV) with U = 2 and 4 eV leading to equivalent results. All input structures were relaxed until the forces on atoms are smaller than $5 \cdot 10^{-3}$ eV/Å. The cut-off value for energy was set to 600 eV and the k-point mesh for Brillouin zone integration was converged to a grid density of at least 1000/at. Electron localization function (ELF)¹⁸⁸ was computed for all structures in order to identify oxygen lone-pairs and to follow their participation in the redox process. ELF is a topological tool of the electron density that measures the Pauli repulsion through the probability of finding an electron of spin α in the vicinity of another electron with the same spin. According to its general formulation,¹⁸⁸ ELF goes to zero when electrons are delocalized over ionic-covalent bonds (bonding-pairs) and to 1 when electrons are localized and paired in a small volume (lone-pairs). According to the octet rule, four electron-pairs (8 electrons) per oxygen is required to stabilize its electronic structure. Such electron-pairs can be either bonding (covalent bonds) or non-bonding (lone-pairs), the ratio of which depends on how many transition metal(s) surround the oxygen atom. Therefore, an oxygen surrounded by n transition metal(s) has n bonding-pairs (not seen by ELF) and $4 - n$ lone-pairs (ELF lobes).

2.8.2 XAS simulation

The XAS spectra were computed for all structures using the OCEAN code^{189, 190}. OCEAN solves the Bethe-Salpeter equation (BSE)¹⁹¹ based on the ground-state charge density and wave function obtained from the DFT-based Quantum Espresso (QE) program package,¹⁹² using the local-density approximation (LDA or LDA+U)^{193, 194} in conjunction with norm-conserving pseudopotentials.¹⁹⁵ To solve the Kohn-Sham equation the cut-off value for the basis functions was set to 952 eV and the k-point grid for the electronic

density was converged with increasing k-point grids. As for VASP calculations, Hubbard correction was added to Ir d-electrons ($U = 2\text{eV}$).

The main advantage of the BSE approach is to explicitly account for the screened core-hole and photoelectron interaction and to include self-energy correction to the electronic states. In the present calculations, BSE was solved using 500 unoccupied bands and 800 bands were used to build the screened core-hole potential with the default k-point grid. Only dipole-allowed transitions were considered in the XAS calculations. The photon polarization vectors were set at [100], [010], and [001], and the final spectrum of each structure was obtained by averaging the spectra over all polarization vectors and individual oxygen atoms. The core level shifts (CLS) were included to account for the different local environments of the absorbing oxygen species. Absolute excitation energy is not available from the calculations and ad hoc shift was applied to the simulated spectra for a sake of comparison with experimental data.

Chapter 3 Elucidation of spectroscopic features of oxygen redox upon lithium intercalation in Li_2RuO_3

The content of this chapter is based on a manuscript in preparation “Elucidation of Spectroscopic Features of Oxygen redox upon Lithium Intercalation in Li_2RuO_3 ”.

3.1 Introduction

Although the class of Li-rich transition-metal oxides is a promising candidate for the next-generation battery cathode due to the exceptional capacity, the implicit charge compensation mechanism is still a barrier for the reality. Extensive research carried out via different transition-metal (i.e., $3d$, $4d$ and $5d$) oxides has demonstrated the cumulative presence of anionic redox and conventional TM redox.^{73, 117, 131, 142-144, 196-200} The involvement of different transition metals (TMs) makes the complex anionic redox even more elusive due to the different TM-O hybridization.

In this work, we aim to unravel the confusion hovering above the anionic redox in Li-rich layered oxides by probing the individual effect of TM-O hybridization and O $2p$ state on the oxygen redox. In order to diminish the effect from other transition metal ions, we choose Li_2RuO_3 as the model of Li-rich layered cathode material due to the presence of single transition metal element Ru, avoiding any interference during the cycling process. In addition, Ru^{4+} would encounter high energetic barriers in hopping to lithium layers, providing a stable structural environment for exploring anionic redox mechanism. Li_2RuO_3 exhibits an exceptional reversibility in terms of electrochemical performance, delivering outstanding capacities as high as 310 mAh/g due to the cumulative cationic and anionic redox. Herein, a combination of empirical X-ray spectroscopy techniques and computational density functional theory (DFT) simulation is performed to explore the redox reaction, especially the wherein oxygen activity.

3.2 Experimental methods

Li_2RuO_3 was prepared through a traditional solid-state reaction from oxide precursors, RuO_2 (Sigma-Aldrich, 99.9%) and with 10% excess of Li_2O (Sigma-Aldrich, 99.9%) weighted under the stoichiometric ratio. The reactants were ground by agate mortar and pestle and mixed homogeneously. After pelletizing

reactant mixtures, the pellets were transferred to an alumina crucible and sintered at 900°C for 24 hours and then at 1000°C for 48 hours in the air. After cooling to room temperature naturally, the as-obtained sample was ground into fine powders and stored in argon-filled glovebox for to-be measurements.

The method of electrode preparation can be found in Chapter 2. Here the as-prepared Li_2RuO_3 was used as the active materials.

Details about the characterization methods can be found in chapter 2. Galvanostatic cycling in Li cells was conducted at 25°C. Structural characterization was carried out using powder X-ray diffraction both at synchrotron and neutron facilities. Ru K-edge XANES and O K-edge XAS were characterized via the X-ray absorption spectroscopy.

3.3 Structural characterization of Li_2RuO_3

Although Li_2RuO_3 has been extensively explored by the physics community due to its profound properties in magnetism, heat capacity, and resistivity, and battery community as a model compound for Li-rich cathode material, the space group to describe its structure still remains debated between C2/c and $\text{P2}_1/\text{m}$.²⁰¹⁻²⁰⁵ In order to comprehensively understand the crystal structure, the free-standing pristine Li_2RuO_3 was evaluated via the high resolution SXRD and TOF-NPD at room temperature. The detailed structural information was studied by the routine Rietveld method. For comparison, both $\text{P2}_1/\text{m}$ and C2/c space groups were adopted for the analysis. It turns out that $\text{P2}_1/\text{m}$ displays a better fitting result, revealed by the presence of the peak at around 1.33 \AA^{-1} (Figures 3-1 and 3-2) which could be indexed, than the previous reported C2/c, in good agreement with the recent study via solid state NMR method.²⁰⁶ The joint Rietveld refinement under the space group of $\text{P2}_1/\text{m}$ was shown in Figure 3-2 and the corresponding structural parameters deduced from the Rietveld analysis were listed in Table 3-1. The occurrence of the superstructure peaks seen between 1.4 and 2.3 \AA^{-1} is attributed to the honeycomb-like ordering between Li and Ru in the transition metal layer, which well accords with the previous reports. The misfit of this range needs more advanced technique and is beyond the research of this paper. In addition, the refinement analysis also unraveled the cation mixing between Li and Ru within transition metal layers, while no migration of cations

between inter-layers was observed as confirmed by the high-magnification HAADF-STEM image and the diffraction pattern (Figure 3-3).

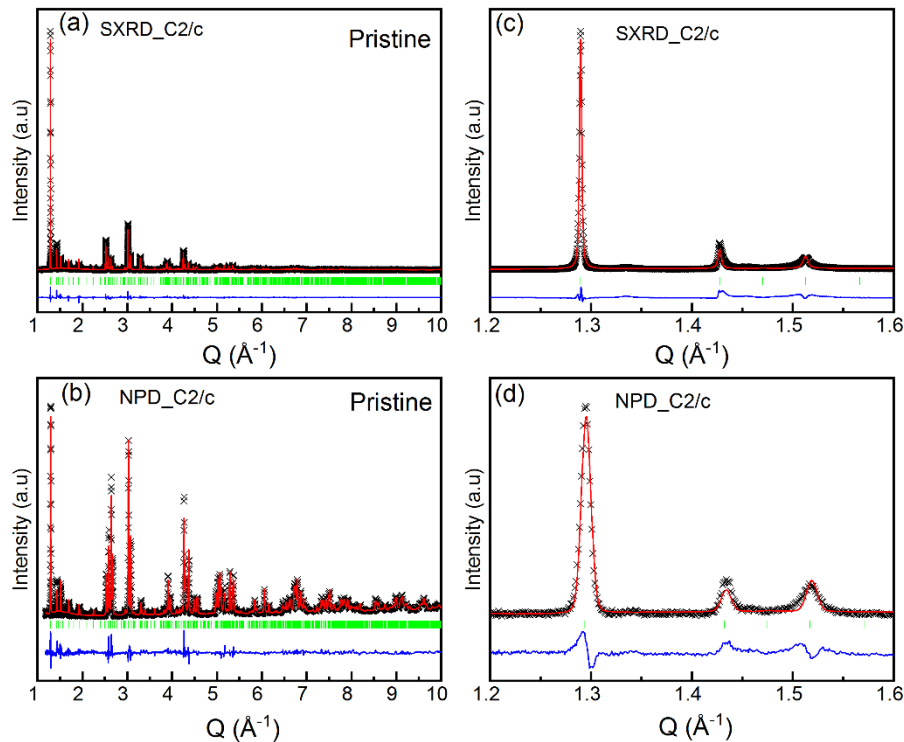


Figure 3-1. Rietveld refinement of SXRD (a) and NPD (b) patterns of pristine Li_2RuO_3 under space group of C2/c . Panels (b) and (d) show a zoom of a small angular region of (a) and (c), respectively. At around $Q = 1.33 \text{ \AA}^{-1}$, there is no corresponding Bragg reflection. Black crosses, red solid line and tick bars represent experimental data, calculated patterns, and Bragg reflects, respectively. Blue solid line stands for the difference between observed data and calculated one.

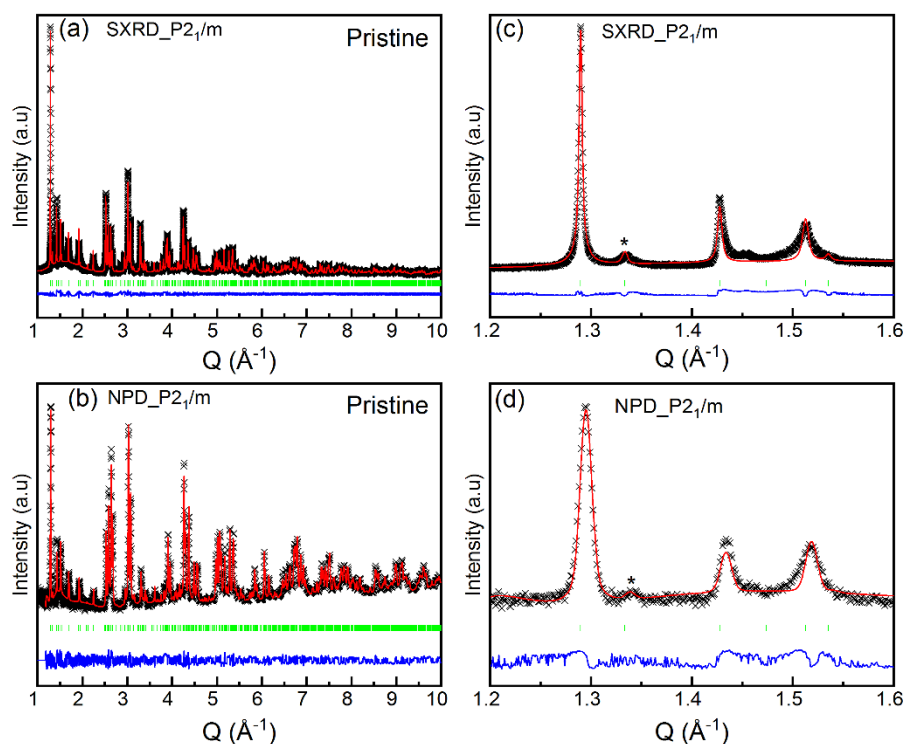


Figure 3-2. Rietveld refinement of SXRD (a) and NPD (b) patterns of pristine Li_2RuO_3 under space group of $\text{P2}_1/\text{m}$. (b) is the magnified part of (a) and (d) is the magnified part of (d). At $Q = 1.33 \text{ \AA}^{-1}$, there exists a corresponding Bragg reflection denoted by the asterisk symbol. Black crosses, red solid line and tick bars represent experimental data, calculated patterns, and Bragg reflects, respectively. Blue solid line stands for the difference between observed data and calculated one.

Table 3-1. Crystallographic parameters and reliability factors deduced from the joint Rietveld refinement of SXRD and NPD patterns for Li_2RuO_3 under the space group of $\text{P2}_1/\text{m}$.

Joint refinement of SXRD and NPD						
Space group: $\text{P2}_1/\text{m}$; $a = 4.96478(10) \text{ \AA}$; $b = 8.80236(11) \text{ \AA}$; $c = 5.91000(8) \text{ \AA}$; $\beta = 124.4782(11)$; $V = 212.909(6) \text{ \AA}^3$						
Atom	Site	x	y	z	Occupancy	Biso (\AA^2)
Li1	4f	0.2744(2)	0.07610(9)	-0.0021(2)	0.1191(8)	0.42(2)
Ru1	4f	0.2744(2)	0.07610(9)	-0.0021(2)	0.809(8)	0.190(9)
Li2	2e	0.743(2)	0.25	0.001(2)	0.7617(16)	0.42(2)
Ru2	2e	0.743(2)	0.25	0.001(2)	0.2383(16)	0.190(9)

Li3	2e	0.749(11)	0.25	0.476(9)	1	0.42(2)
Li4	4f	0.268(8)	0.051(2)	0.495(7)	1	0.42(2)
O1	4f	0.752(2)	0.0698(16)	0.250(2)	1	0.311(5)
O2	4f	0.772(2)	0.0827(15)	0.7676(19)	1	0.311(5)
O3	2e	0.272(3)	0.25	0.227(3)	1	0.311(5)
O4	2e	0.257(4)	0.25	0.766(3)	1	0.311(5)
$R_{WP} = 7.5\%$; $R_p = 10.1\%$; $\chi^2 = 5.0$						

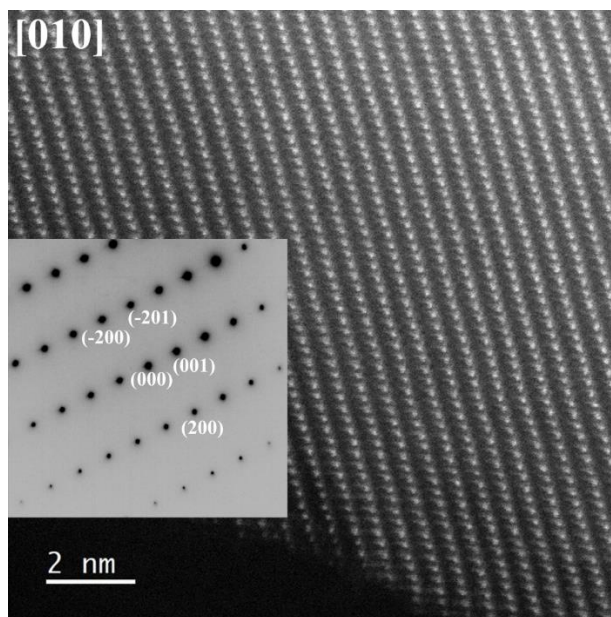


Figure 3-3. High-magnification HAADF-STEM image of pristine Li_2RuO_3 and the inset shows the diffraction pattern.

3.4 Electrochemical properties of Li_2RuO_3

The electrochemical profile of Li_2RuO_3 ($\text{Li}[\text{Li}_{1/3}\text{Ru}_{2/3}]\text{O}_2$) exhibited a staircase curve with two major distinct plateaus upon the first charge followed by a considerable change to a sloping, S-shaped behavior in the subsequent discharge (Figure 3-4a). Specifically, the charge profile displayed two distinctive plateaus located at 3.5 and 3.68 V, respectively, as well as a small one at 3.74 V. In addition, the presence of a small

process at ~ 3.92 V was revealed by plotting dQ/dV (Figure 3-4b). Further oxidation proceeded through a long plateau at around 4.25 V, associated with nearly 1 mol Li removed, assuming 100% faradaic efficiency. For the first discharge, dQ/dV analysis confirmed a single process spanning a large potential window, yet centered around 3.25 V (Figure 3-4b). Comparison of charge and discharge profile revealed a very obvious hysteresis, characteristic of systems with redox centered at O ligands.^{97, 151, 156, 200, 207} It is interesting to note that the process up to 3.9 V could be made to be highly reversible if the anodic cutoff was limited to this potential, bypassing the plateau at 4.25 V (Figure 3-5), with the profiles on charge and discharge becoming highly symmetric and showing much lower hysteresis. At the full potential window, Li_2RuO_3 delivered a charge capacity up to 310 mAh/g corresponding to 1.9 mol Li delithiation per mol compound, which increased slightly on discharge to 329 mAh/g corresponding to cycling 2 mol Li per mol compound. In contrast to the first charge, the second charge underwent a drastic evolution, with a sloping shape much closer to the first discharge. The profile remained sloping in the following cycles, with minor changes in fine structure (Figure 3-4c), suggesting a much more modest evolution compared to the first cycle. The compound still displayed a high discharge capacity, around 270 mAh/g, even after 50 cycles (Figure 3-4d), and very high coulombic efficiency (Figure 3-4d), indicating a good capacity retention.

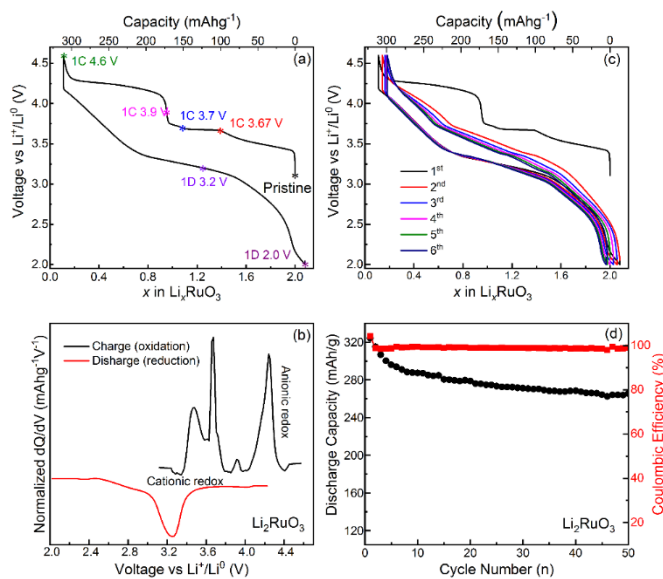


Figure 3-4. (a) Voltage-composition profiles of Li_2RuO_3 under the galvanostatic cycling, compared to the corresponding capacity in the first cycle (a) and upon extensive cycling (c). (b) Differential capacity (dQ/dV) analysis of Li_2RuO_3 in the first cycle. (d) Discharge capacity (black circles) and coulombic efficiency (red squares) as a function of cycle number.

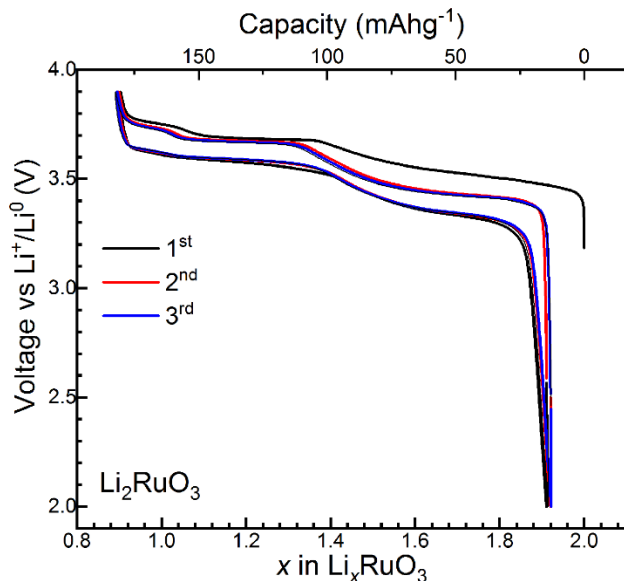


Figure 3-5. Voltage-composition profile of Li_2RuO_3 cycled galvanostatically between 2 and 3.9 V, compared to the corresponding capacity.

3.5 Structural evolution upon cycling

The voltage profile of Li_2RuO_3 reveals a rich compositional diagram to reach “ RuO_3 ”. Despite the interest in the electrochemical properties of this compound, a detailed structural description of this phase space is still missing. Structures favored by thermodynamics have been computed,²⁰⁸ but no experimental support is available upon a complete charge-discharge process. In order to build this picture, *operando* SXRD was collected concurrent with Li (de)intercalation during the first cycle at a constant current (Figure 3-6). The cycling curve (middle panel of Figure 3-6) recorded during the *operando* measurement was largely consistent with the data from the coin cell. Upon charge to 3.6 V, the Li removal was accompanied by a solid-solution reaction mechanism as indicated by a continuous peak shift without any new sets appearing. Upon oxidation beyond 3.6 V, a second phase emerged at the expense of the initial one, as

signaled by the emergence of a peak at $2\theta \sim 3^\circ$ with a gradual increase in intensity (Figure 3-6). The presence of the second phase explicitly accounted for the formation of the sharp peak at around 3.68 V in dQ/dV plot. Further oxidation to 3.9 V was accompanied by disappearance of old peaks and emergence of new peaks at $\sim 3.1^\circ$, indicating again a Li-driven formation of a new phase. Charging beyond this potential was only accompanied by a gradual broadening and shift of SXR peaks without observable generation of new reflections, indicating a solid-solution reaction mechanism with crystallinity decrease. This process induced structural disorder as demonstrated by superstructure peaks being barely existent at the end of charge. It should be noted that the rate of change was not constant at these potentials, with most obvious peak shift occurring beyond 4.2 V (Figure 3-6), which may indicate the existence of two distinct reaction steps in this long plateau, consistent with the asymmetry of the corresponding peak in dQ/dV.

Informed by the *operando* XRD results, a series of cells were charged to potentials corresponding to discrete phases, then the electrodes were harvested for *ex situ* analysis using a combination of high-resolution SXR and TOF-NPD. The selected potentials can be found in Figure 3-4a. The phase isolated at 3.6 V could be satisfactorily Rietveld refined with the same $P2_1/m$ space group of the pristine oxide, consistent with the observation of a solid-solution process (Figure 3-7 and Table 3-2). The peak shift manifested the anisotropic variation of the lattice parameters, with an increase in *a* and *c*, while a decrease in *b* and volume, extracted from the sequential fitting of *operando* diffraction. Whereas a distinct phase could be identified at 3.7 V based on the *operando* data, attempts to harvest a pure electrode for *ex situ* high-resolution diffraction failed, possibly due to its metastability; additional unexplained peaks were systematically obtained (Figure 3-8). The phase isolated at 3.9 V was fit with a $R\bar{3}$ space group (Figure 3-9 and Table 3-3). The change in space group suggested a structural rearrangement induced by Li deintercalation. The crystal structure at the end of charge, at 4.6 V, could be successfully fit on the basis of space group $R\bar{3}$, as well (Figure 3-10 and Table 3-4). To the best of our knowledge, it was the first time the crystal structure of this state has been experimentally evaluated. The results uncovered a significant shortening of the Ru-O bonding distance, reflecting an enhanced covalency. Unlike the previous report

about the possible formation of O-O dimers,⁷³ however, the information from the O-O distance of 2.59 Å herein did not highlight the existence of the dimers.

Upon reversing polarity to reduction back to ~3.2 V, the Li insertion was accompanied by a continuous shift of peak positions according to *operando* XRD. As a result, the obtained diffraction patterns could generally be indexed with the same space group $R\bar{3}$. However, the combined Rietveld refinement of *ex situ* high-resolution SXRD and TOF-NPD collected after discharge to 3.2 V revealed the existence of two phases with related atomic arrangements, which could not be distinguished in the *operando* measurement due to the large peak widths. The unit cells of the two phases matched well with the dimensions of the states isolated upon charge to 3.9 V and 4.6 V (Figure 3-11 and Table 3-5), indicating that a similar structural transition occurred upon charge and discharge at these potentials. Upon further reduction to 2.0 V, the diffraction peaks experienced a subtle increase in intensity variation and shift. The changes introduced asymmetric broadening, especially for the first Bragg reflection (Figure 3-12a). The final structure did not recover to the initial state, as indicated by the position of the first peak at lower angles, weaker superstructure peaks and pronounced peak broadening (Figure 3-12b).

In order to evaluate the reversibility after the first cycle, high resolution SXRD data of selected states during the second cycle was collected (Figure 3-13). The SXRD comparison at the same state between the first cycle and second cycle demonstrated almost identical diffraction patterns, unambiguously reflecting the structural reversibility associated with Li removal/uptake after the first oxidation, which is consistent with the preservation of the voltage-composition profile after the first cycle.

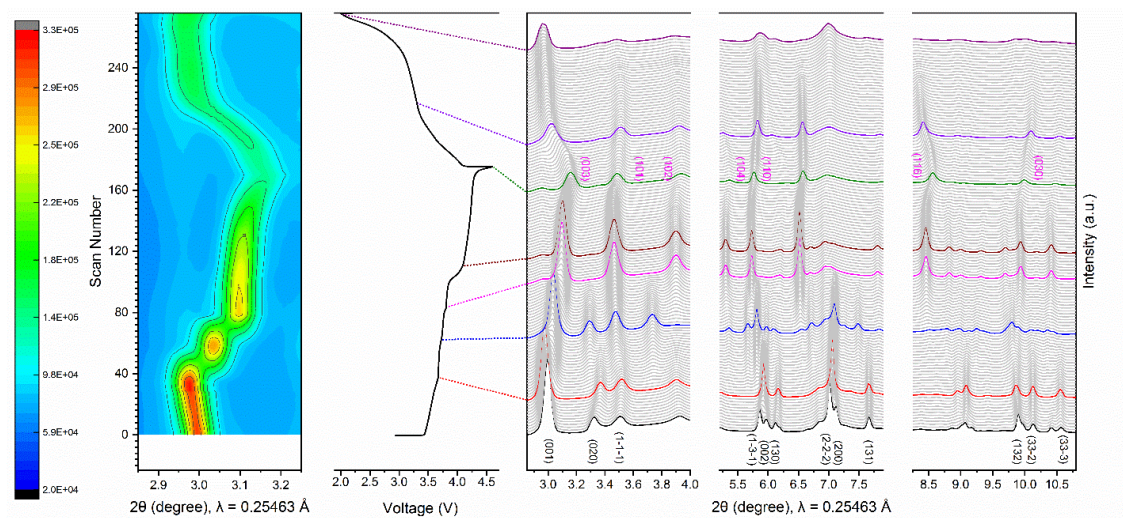


Figure 3-6. *Operando* synchrotron XRD of Li_2RuO_3 during the first charge-discharge process. The left panel displays the contour plot of synchrotron XRD patterns between 2.85° and 3.25° . The right panel demonstrates the representative diffraction patterns extracted from the *operando* data and the pure phase at certain state of charge are signified by different color line which is pertinent to the point in the corresponding electrochemical profile depicted in the middle part. Given the permitted experimental error, the profile is reasonable.

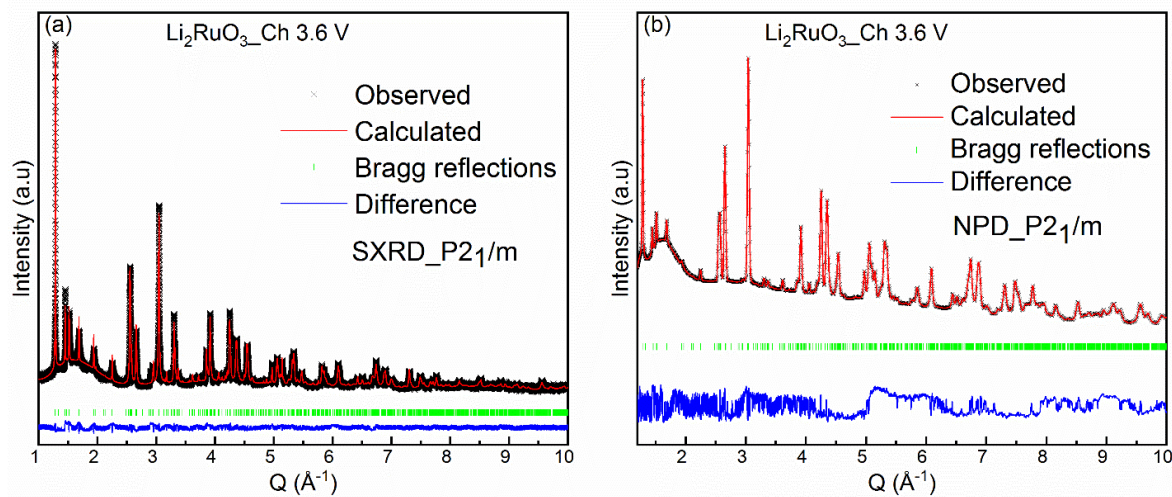


Figure 3-7. Rietveld refinement of SXRD (a) and NPD (b) patterns of Li_2RuO_3 charged to 3.6 V using space group $P2_1/m$.

Table 3-2. Crystallographic parameters and reliability factors deduced from the joint Rietveld refinement of SXRD and NPD patterns for Li_2RuO_3 charged to 3.6 V.

Joint refinement of SXRD and NPD						
Space group: $P2_1/m$; $a = 4.97715(10) \text{ \AA}$; $b = 8.65387(15) \text{ \AA}$; $c = 5.89982(8) \text{ \AA}$; $\beta = 124.0501(11)$; $V = 210.546(7) \text{ \AA}^3$						
Atom	Site	x	y	z	Occupancy	Biso (\AA^2)
Li1	4f	0.2505(7)	0.08136(11)	0.0006(6)	0.1442(8)	0.982(14)
Ru1	4f	0.2505(7)	0.8136(11)	0.0006(6)	0.8558(8)	0.982(14)
Li2	2e	0.7015(15)	0.25	0.0029(16)	0.7115(16)	0.982(14)
Ru2	2e	0.7015(15)	0.25	0.0029(16)	0.2885(16)	0.982(14)
Li3	2e	0.794(7)	0.25	0.612(4)	1.0	0.982(14)
Li4	4f	0.272(5)	0.0409(13)	0.468(4)	0.47(2)	0.982(14)
O1	4f	0.733(3)	0.0685(16)	0.241(3)	1.0	0.354(19)
O2	4f	0.768(3)	0.0754(18)	0.770(3)	1.0	0.354(19)
O3	2e	0.242(4)	0.25	0.218(3)	1.0	0.354(19)
O4	2e	0.231(3)	0.25	0.757(3)	1.0	0.354(19)
$R_{WP} = 6.4\%$; $R_p = 8.6\%$; $\chi^2 = 2.4$						

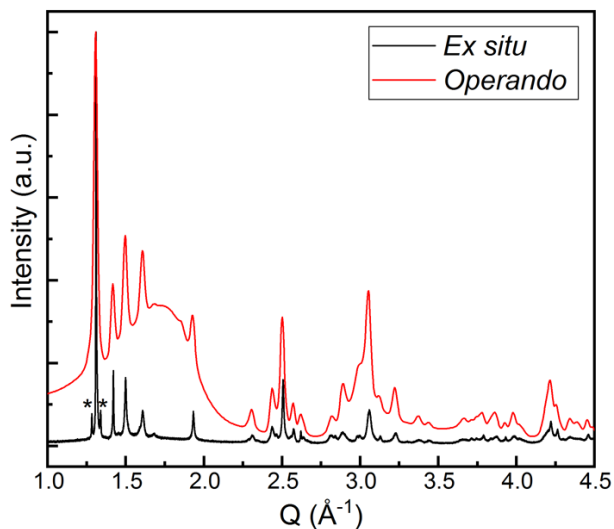


Figure 3-8. XRD patterns of Li_2RuO_3 during charged to 3.7 V collected under *ex situ* mode (black line) and *operando* mode (red line). The asterisk symbols represent the existence of peaks that could not be indexed and that were not observed under *operando* conditions.

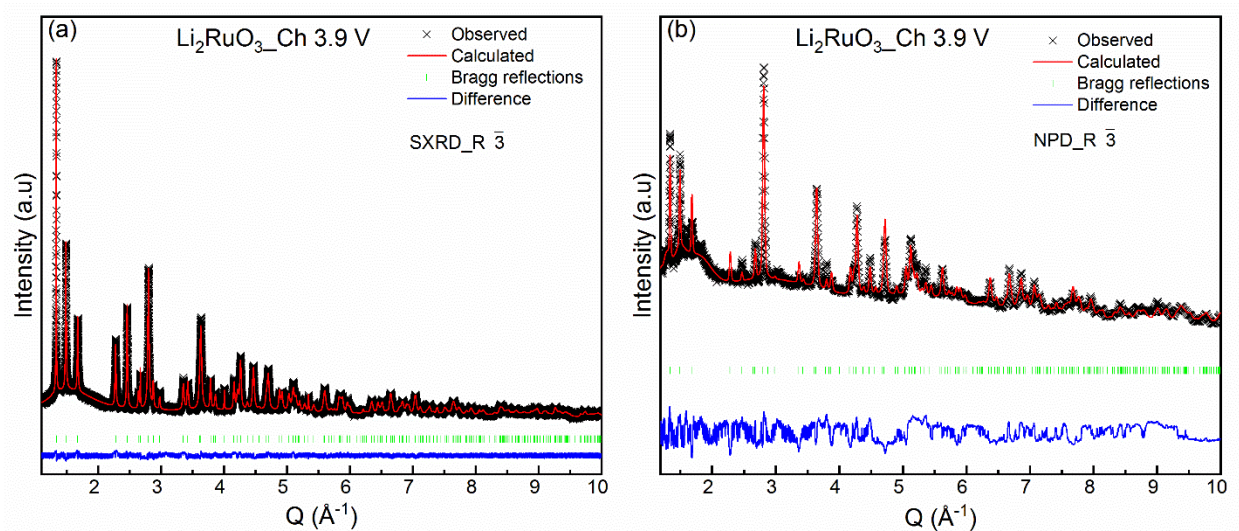


Figure 3-9. Rietveld refinement of SXRD (a) and NPD (b) patterns of Li_2RuO_3 charged to 3.9 V using space group $R\bar{3}$.

Table 3-3. Crystallographic parameters and reliability factors extracted from the joint Rietveld refinement of SXRD and NPD patterns for Li_2RuO_3 charged to 3.9 V.

Joint refinement of SXRD and NPD						
Space group: $R\bar{3}$; $a = b = 5.10404(3) \text{ \AA}$; $c = 14.11137(7) \text{ \AA}$; $\beta = 124.0501(11)$; $V = 210.546(7) \text{ \AA}^3$						
Atom	Site	x	y	z	Occupancy	Biso (\AA^2)
Ru1	6c	0	0	0.33943(3)	1.0	0.546(8)
Li1	3a	0	0	0	1.0	0.546(8)
Li2	3b	0	0	0.5	0.8	0.546(8)
O1	18f	0.2969(5)	-0.0273(4)	0.25883(12)	1.0	0.27(4)
$R_{\text{WP}} = 5.5\%$; $R_{\text{p}} = 6.5\%$; $\chi^2 = 1.8$						

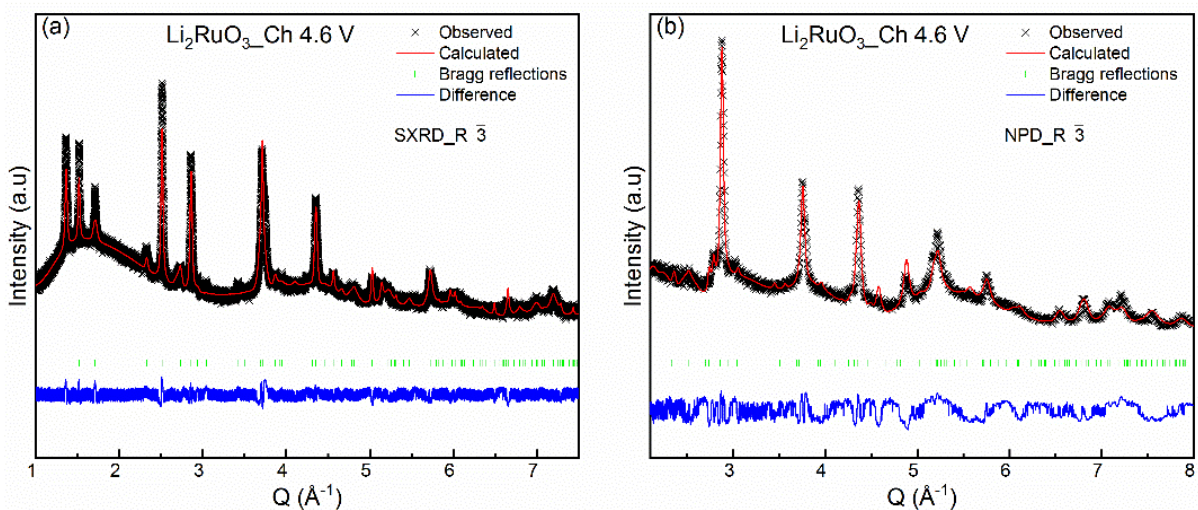


Figure 3-10. Rietveld refinement of SXRD (a) and NPD (b) patterns of Li_2RuO_3 charged to 4.6 V using space group $R\bar{3}$.

Table 3-4. Crystallographic parameters and reliability factors extracted from the joint Rietveld refinement of SXRD and NPD patterns for Li_2RuO_3 charged to 4.6 V.

Joint refinement of SXRD and NPD						
Space group: $R\bar{3}$; $a = b = 4.9971(2) \text{ \AA}$; $c = 13.7803(15) \text{ \AA}$; $\beta = 124.0$; $V = 298.00(4) \text{ \AA}^3$						
Atom	Site	x	y	z	Occupancy	Biso (\AA^2)
Ru1	6c	0	0	0.3109(14)	0.124(4)	0.5
Ru2		0	0	0.1770(5)	0.619(44)	0.5
Ru3		0	0	0	0.311(8)	0.5
Ru4	3b	0	0	0.5	0.297(9)	0.5
O1	18f	0.309(4)	0.021(4)	0.2481(7)	1.0	0.5
$R_{\text{WP}} = 3.3\%$; $R_p = 5.7\%$; $\chi^2 = 4.8$						

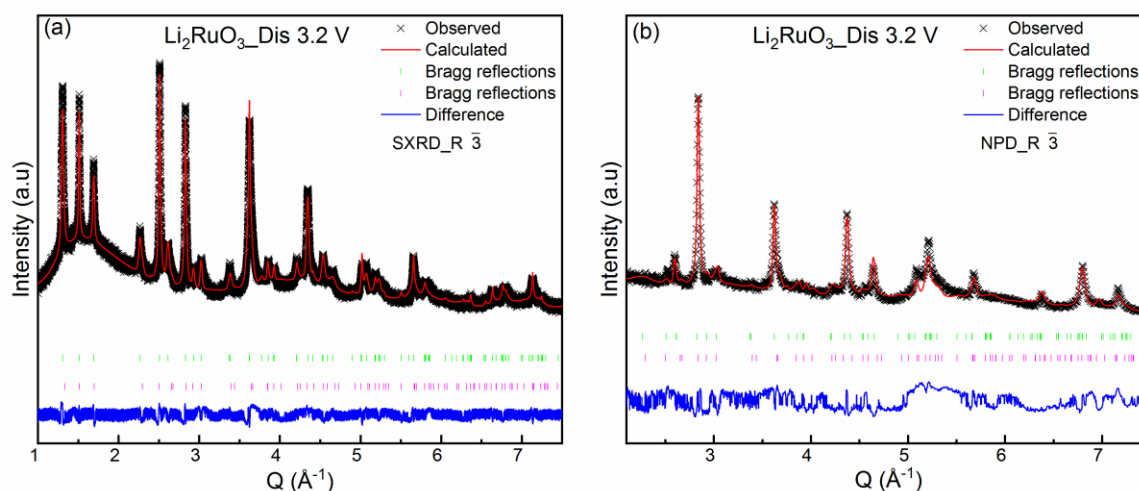


Figure 3-11. Rietveld refinement of SXRD (a) and NPD (b) patterns of Li_2RuO_3 discharged to 3.2 V using two phases with space group $\text{R}\bar{3}$.

Table 3-5. Crystallographic parameters and reliability factors extracted from the joint Rietveld refinement of SXRD and NPD patterns for Li_2RuO_3 discharged to 3.2 V.

Joint refinement of SXRD and NPD						
Component 1:						
Weight fraction: 60%; Space group: $\text{R}\bar{3}$; $a = b = 5.00677(7) \text{ \AA}$; $c = 14.42675(5) \text{ \AA}$; $\beta = 120.0$; $V = 313.195.00(4) \text{ \AA}^3$						
Atom	Site	x	y	z	Occupancy	Biso (\AA^2)
Ru1	6c	0	0	0.3158(9)	0.325(15)	1.56(2)
Ru2		0	0	0.3497(10)	0.301(15)	1.56(2)
Ru3		0	0	0	0.623(5)	1.56(2)
Ru4	3b	0	0	0.5	0.601(4)	1.56(2)
O1	18f	0.3288(15)	-0.0007(16)	0.2592(3)	1.0	1.56(2)
Component 2:						
Weight fraction: 40%; Space group: $\text{R}\bar{3}$; $a = b = 5.0214(3) \text{ \AA}$; $c = 14.094(7) \text{ \AA}$; $\beta = 120.0(0)$; $V = 307.77(15) \text{ \AA}^3$						
Atom	Site	x	y	z	Occupancy	Biso (\AA^2)

Ru1	6c	0	0	0.5	1.0	1.56(2)
Li1	3a	0	0	0	1.0	1.56(2)
Li2	3b	0	0	0.5	0.8	1.56(2)
O1	18f	0.273(5)	-0.063(6)	0.279(2)	1.0	1.56(2)
$R_{wp} = 6.2\%$; $R_p = 6.7\%$; $\chi^2 = 2.1$						

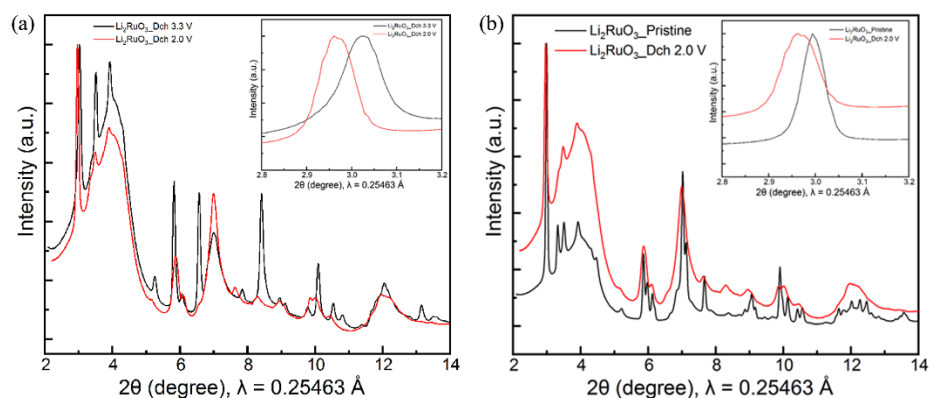


Figure 3-12. (a) SXRD of state discharged to 3.3 V (Dch 3.3 V) and state discharged to 2.0 V (Dch 2.0 V) extracted from *operando* data. The inset elucidates the asymmetric broadening of the first peak from Dch 3.3 V to Dch 2.0 V. (b) SXRD of the pristine state and state discharged to 2.0 V (Dch 2.0 V) extracted from *operando* data. The inset elucidates the lower position of the first peak after reduction to 2.0 V.

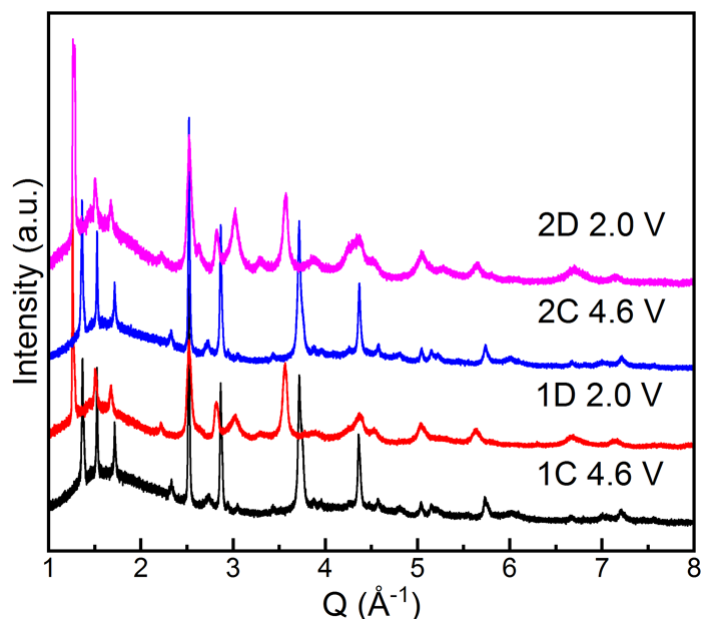


Figure 3-13. High resolution SXRD of Li_2RuO_3 of samples harvested after electrochemical cycling. 1C, 1D, 2C, and 2D represent the first charge and discharge, and the second charge and second discharge, respectively.

3.6 *Ex situ* Ru K-edge XAS

Ru K-edge X-ray absorption spectroscopy (XAS) of samples with various states of charge were recorded *ex situ* in transmission mode, at the same points as *ex situ* SXRD/NPD (Figure 3-14). The rising edge corresponds to the promotion of the core level electrons to the continuum state, which is accompanied by the change in the absorption coefficient and can be used to reflect the variation of the oxidation state. The rising edge is followed by two peaks, the first of which can be attributed to the dipole-allowed transition of $1s \rightarrow 5p$ levels, while the second one mainly originates from the single-scattering effects involving the absorber and its corresponding Ru neighbors.^{119, 209} The rising edge of the pristine Li_2RuO_3 neatly superimposed with that of the reference Ru^{4+}O_2 , thus confirming the oxidation state of (+4). Besides, the absence of the pre-edge feature for pristine Li_2RuO_3 indicates the centrosymmetric coordination environment of Ru. Upon oxidation to 3.67 V, the absorption edge experienced a pronounced shift toward higher energy by ~ 1.6 eV, demonstrating a clear oxidation of Ru. Further oxidation to 3.7 V continued to

shift the edge to higher energy by ~ 0.3 , followed by stabilization upon oxidation to 3.9 V (Figure 3-14). The comparison of the spectrum at 3.9 V with $\text{Li}_3\text{Ru}^{5+}\text{O}_4$ clearly illustrated that the oxidation of Ru at this stage was +5 (Figure 3-15a), indicating that the compensation of the Li deintercalation induced formal Ru oxidation. In contrast, further oxidation to 4.6 V by crossing the long plateau at ~ 4.2 V resulted in a noticeable lower energy shift by ~ 0.4 eV (Figure 3-14), suggesting an expected reduction of Ru with the oxidation state between (+4) to (+5) despite occurring during oxidation of the electrode. In addition, it should be noted that the pre-edge peak feature grew gradually after oxidation to 4.6 V (Figure 3-15b), reflecting a non-centrosymmetric distortion evolution of the RuO_6 coordination environment driven by a large amount of Li deintercalation. Upon the subsequent reduction, the rising edge shifted toward lower energy (Figure 3-14), implying a reduction of Ru. Compared with the initial state, the absorption edge at the end of discharge state was located at lower energy than the pristine state by ~ 0.4 eV indicative of a hysteresis in the chemical states involved in the first cycle that mirrored the electrochemical response. In addition, Li intercalation also promoted the recovery of the pre-edge state almost to the original state (Figure 3-15b).

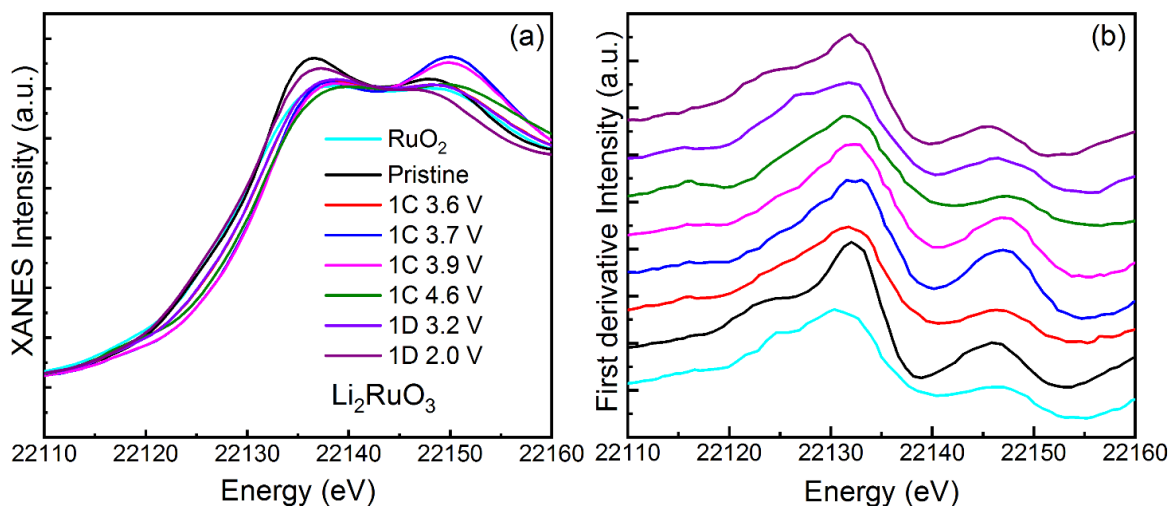


Figure 3-14. (a) *Ex situ* Ru K-edge XANES spectra of Li_2RuO_3 at different states of charge and (b) the corresponding first derivative plots for locating the position of the rising edge. RuO_2 was used as a standard reference for Ru^{4+} .

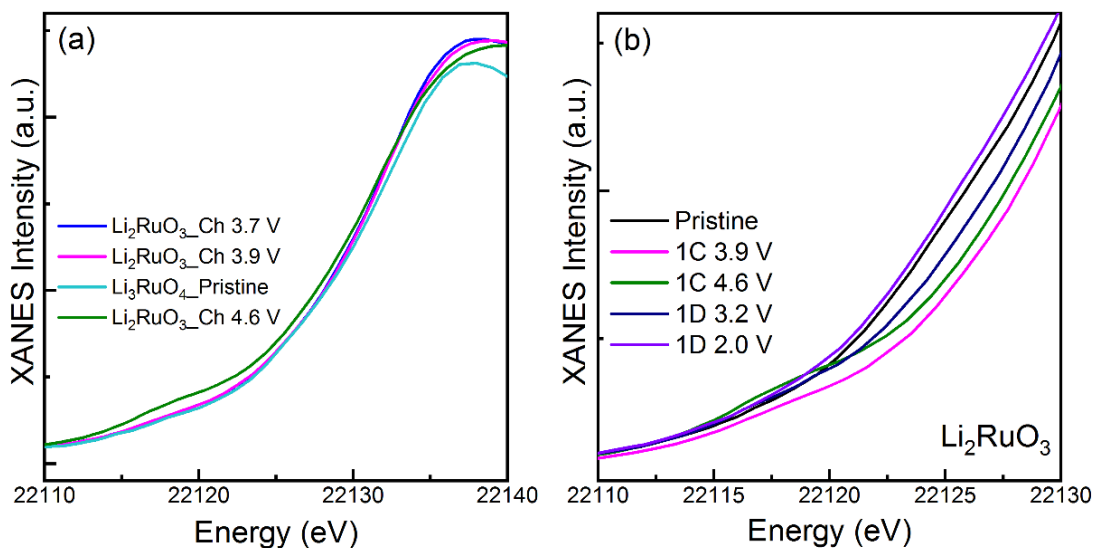


Figure 3-15. (a) *Ex situ* Ru K-edge XAS spectra of Li_2RuO_3 at different states of charge and pristine Li_3RuO_4 . (b) Zoom of the pre-edge region of Li_2RuO_3 at different states of charge.

In order to evaluate the variation of the oxidation state of Ru after the first cycle, Ru K-edge XANES spectra were collected at different states of charge after the second cycle and 25th cycle (Figure 3-16). The absorption edge of Ru K-edge XANES spectrum after the second oxidation to 4.6 V was shifted to higher energy compared with that of the pristine state, but was located at even lower energy in relative to the first oxidation to 4.6 V. Consistently, the subsequent reduction to 2.0 V induced a shift to lower energy than after the first reduction to 2.0 V. In contrast, the spectra of 2nd and 25th cycle were close at the same states of charge. This observation suggests that the evolution of the chemical pathway involving Ru persists beyond the first cycle, but stabilizes relatively quickly.

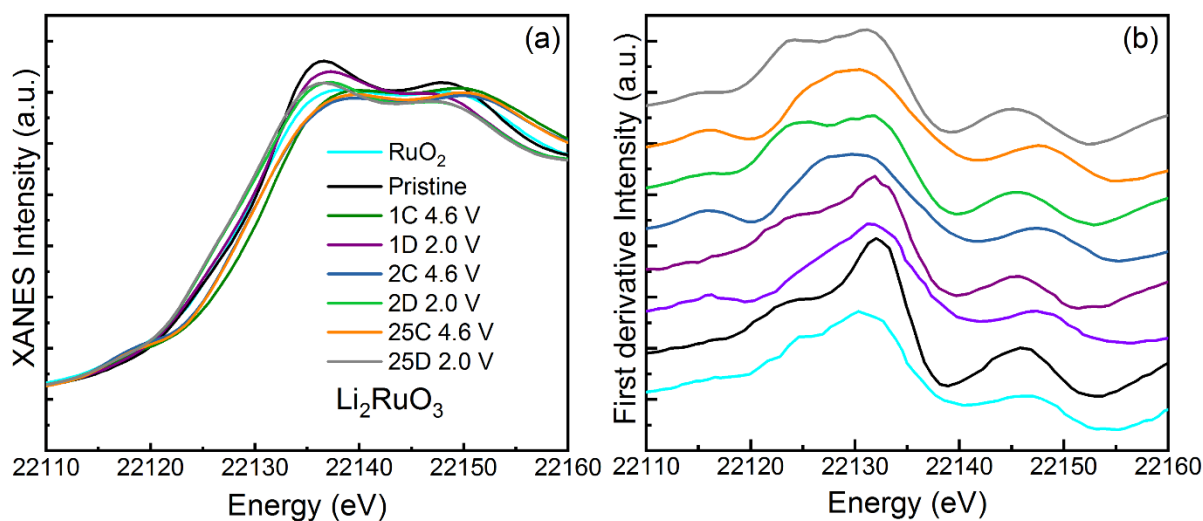


Figure 3-16. (a) *Ex situ* Ru K-edge XANES spectra of Li₂RuO₃ at different states of charge and (b) the corresponding first derivative plots.

3.7 *Ex situ* O K-edge XAS

O K-edge XAS was used to gather complementary information about the role of O in the charge compensation mechanism relative to Ru. The salient features of a generic O K-edge XAS spectrum have been described in Chapter 2. Note that the XAS spectra were measured simultaneously in both TEY and TFY modes, as well as PFY mode. TFY/PFY will be the focus of the discussion, given its greater penetration depth, ~100 nm into the electrode.

The spectrum of pristine Li₂RuO₃ exhibits two distinct features centered at 529.1 (peak α) and 531.1 eV (peak β) in the pre-edge region below 535 eV (Figure 3-17), corresponding to the transition to unoccupied t_{2g} and e_g states derived from O $2p$ -Ru $4d$ hybridization, respectively. It should be noted that there was a shoulder at around 532.0 eV (feature γ), which may indicate a subtle distortion of RuO₆ local structure. The broad features above 535 eV arise from O $2p$ -Ru $5s, p$ states. The rising edge inflection point was extracted to be about 536.4 eV by calculating the 1st derivative of O K-edge XAS spectrum (Figure 3-18). Comparison of the spectra collected under TEY and TFY/PFY modes revealed they were very similar, suggesting uniformity from surface to bulk, without any impurities, such as Li₂CO₃ (Figure 3-19a).

The Li removal upon oxidation to 3.6 V shifted the first pre-edge peak α to lower energy by 0.2 eV with a prominent increase in the peak intensity and instead brought about no variation in the second pre-edge feature β but rather led to a rise in the relative intensity of the shoulder γ , as clearly shown by the difference plot (Figure 3-17). There was no change in the rising edge inflection point relative to the previous state (Figure 3-18), reflecting the preservation of oxygen 1s core level and the invariance of the valence electrons. The lower energy move of peak α was ascribed to the decrease of the Ru 4d-manifold energy due to the oxidation concurrent with Li deintercalation based on Ru K-edge XANES. The rise in the intensity of peak α reflected the gain of the unoccupied states consistent with Ru oxidation. In addition, this increase was associated with the augment of the covalency due to the increased interaction between O 2p and Ru 4d driven by the Ru oxidation. This phenomenon that the feature γ evolved was attributed to the hybridization variation between O 2p and Ru 5d due to the electrochemically induced change in RuO₆ local structure.

The further oxidation to 3.7 V continued to shift peak α in the pre-edge part to lower energy by 0.2 eV, ended up being at 528.7, with a pronounced increased intensity with respect to the previous state, and caused little change for peak β , and invoked the addition increment of peak γ intensity (Figure 3-17). Similarly, the lower energy shift of peak α was induced by the Ru oxidation derived from Ru K-edge XANES spectra which also led to the appearance of more unoccupied states and more covalency of O 2p-Ru 4d interaction as evidenced by the large intensity augment. No change in the inflection point (Figure 3-18), again, reflected the remaining of the valence electrons of O, indicative of no involvement of O in compensating charge.

The continual oxidation to 3.9 V resulted in little change in the pre-edge peak positions and a small diminishment in the peak intensity relative to the previous state (Figure 3-17). Also, there was no change in the inflection point with respect to the former state (Figure 3-18), indicative of the constant of O valence electrons. The behavior of the remaining of the pre-edge peak positions accorded well with a tiny amount of Li deintercalated during this charging process, which was consolidated by the almost superimposition of Ru XANES spectra with the previous state. The small variation in the intensity reflected the subtle orbital interaction change, which is most likely due to the structural changes as demonstrated by XRD.

The Li removal upon oxidation to 4.6 V conserved peak positions but rather led to a large relative increase in intensity for peak α and β , which was largely unchanged and only experienced an increase in asymmetry toward energies associated with feature γ (Figure 3-17). The estimated inflection point of the rising edge experienced a significant blue-shift to 537.5 eV overall (Figure 3-18), which is typically associated with a notable increase in the Z_{eff} on O.

Upon reduction to 3.2 V, peak α shifted to higher energy by ~ 0.2 eV with a dramatically reduced intensity, while peak β and γ experienced a modest intensity decrease and rather constant peak positions (Figure 3-17). The inflection point of the edge experienced a red shift by ~ 0.7 eV (Figure 3-18), suggesting a reversal to lower values of Z_{eff} .

Further reduction to 2.0 V sustained the blue shift of peak α by a further ~ 0.3 eV, to 529.2 eV (Figure 3-17), with another significant drop in relative intensity. In comparison, the broad feature labelled by β again stayed rather constant (Figure 3-19b). At the end of the reduction, the position of the main absorption edge recovered to the pristine state. In contrast, the overall relative pre-edge intensity was significantly lower after 1 cycle than at the start, particularly for peak α .

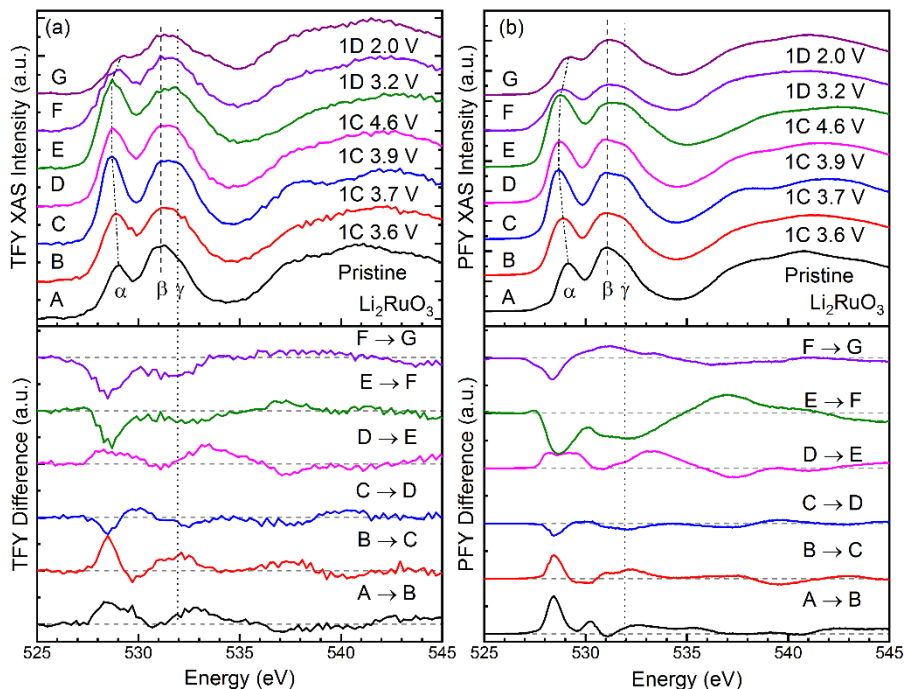


Figure 3-17. *Ex situ* O K edge XAS spectra of Li_2RuO_3 at different states of charge measured in TFY (a) and PFY modes (b), along with the difference spectra between the points indicated.

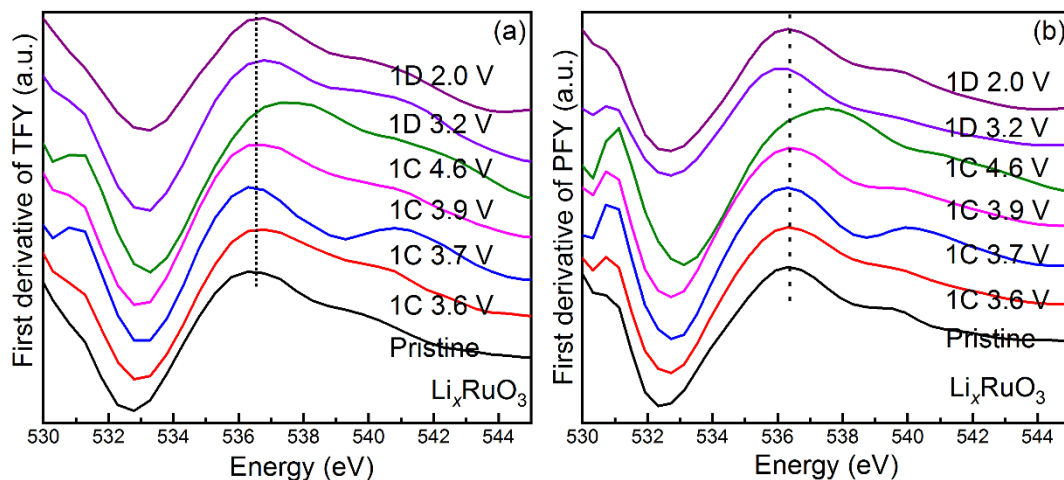


Figure 3-18. First derivative plots of the O K-edge XAS spectra measured in TFY and PFY modes.

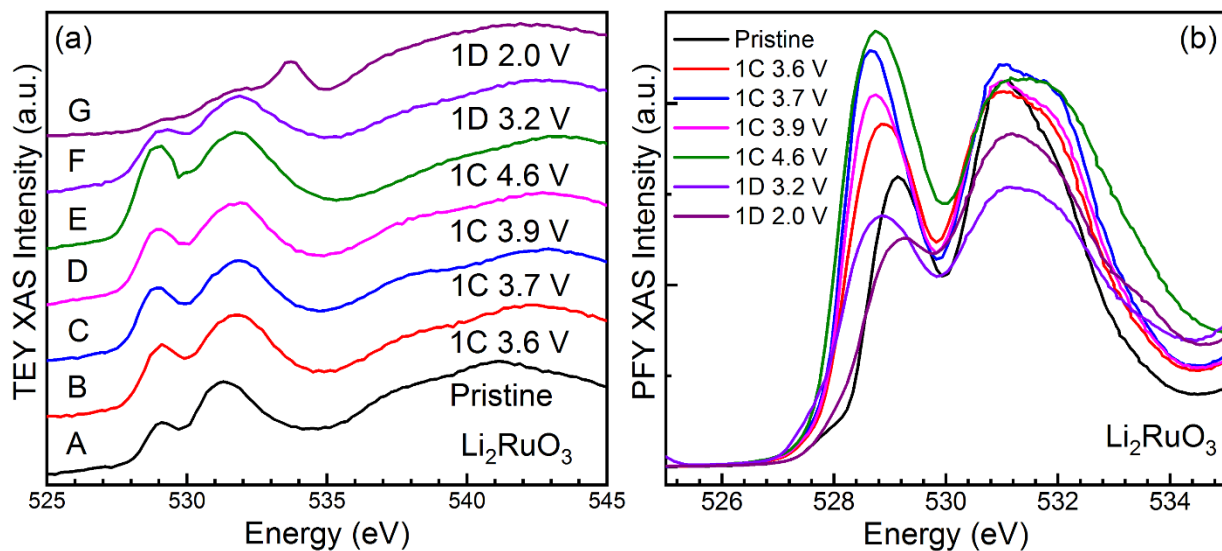


Figure 3-19. (a) *Ex situ* O K-edge XAS of Li_2RuO_3 at different states of charge measured in TEY mode. (b) O K-pre-edge part of Li_2RuO_3 at different states of charge measured in PFY mode.

The evolution of the O electronic structure upon cycling was also evaluated (Figure 3-20a). During the second cycle, oxidation to 3.5 V led to a slight red-shift and a small intensity rise for peak α , with a sharpening of the features between 530 and 533 eV (Figure 3-20a) and no visible shift of the absorption edge (Figure 3-20b). Further oxidation to 4.6 V reproduced largely the same spectrum as in the first cycle. Yet, overall, the trajectory of spectra in the second charge differed from the first. Subsequent reduction to 2.0 V reproduced the changes in the first cycle, but the pre-edge features were sharper. After 25 cycles, samples harvest at the end of charge and discharge presented spectra consistent with the 2nd cycle (Figure 3-20a). Altogether, the O K-edge spectra reflected different states in the first cycle, consistent with a high potential hysteresis, but the chemical pathway became reversible beyond cycle 2, and stayed constant at least up to 25 cycles, in congruence with the decreased hysteresis and stable electrochemical profiles.

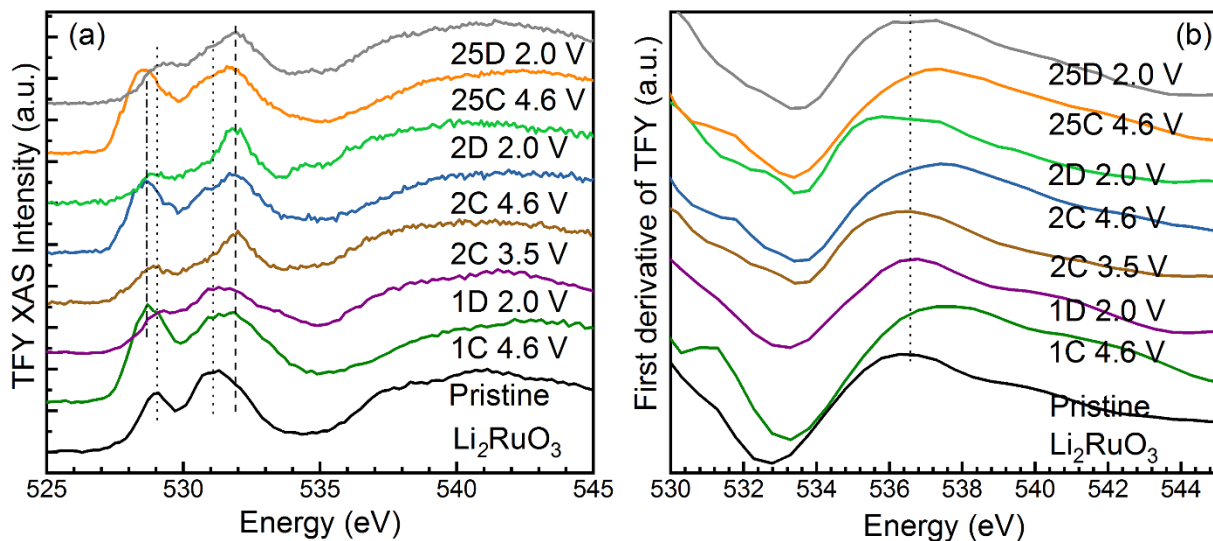


Figure 3-20. (a) *Ex situ* O K edge XAS spectra of Li_2RuO_3 at different states of charge under total fluorescence yield (TFY) mode and (b) the corresponding first derivative plots of O K-edge XAS spectra.

3.8 *Ex situ* O K α XES

Insight into the variation of the occupied states of O electronic structure induced by Li (de)intercalation was gained with *ex situ* O K α X-ray emission spectroscopy (XES, Figure 3-21). Certain O-O species that

could be associated to $(\text{O}_2)^{n-}$ ($n < 2$) exhibit narrow energy bands below the Fermi level, in contrast with the broad energy band associated with the O-TM hybridization. Non-resonant O $K\alpha$ XES spectra were collected at an excitation energy of 565 eV, well above the absorption edge, and thus the threshold of photoionization of O. Pristine Li_2RuO_3 displayed a broad emission peak centered at around 526.0 eV with shoulders at ~ 523.7 and ~ 528.3 eV, the latter being less intense (Figure 3-21). These features are attributed to a decay from the relatively broad (delocalized) oxygen valence states mixed with Ru to fill the excited O 1s core holes, as extensively reported in other transition metal oxides.¹⁷² Those three features were dominant throughout the whole reaction with just subtle variations in energy and intensity. Net shifts of the center of gravity to high energy were observed at 3.6 and 4.6 V (Figure 3-21b). The spectra also broadened at these steps, especially at high potential. Previous reports in the field of high- T_c superconductors have ascribed similar broadening of the O $K\alpha$ XES to increased covalency between O and transition metals.¹⁷² Reduction back to 3.2 V greatly reduced the spectral broadening and brought about a slight shift to a lower energy of the center of gravity (Figure 3-21b). Subsequent reduction to 2.0 V sustained these bands, particularly red-shift of the center of gravity (Figure 3-21b). The spectra at the end of discharge was shifted to high energy compared to the pristine state, and some broadening persisted.

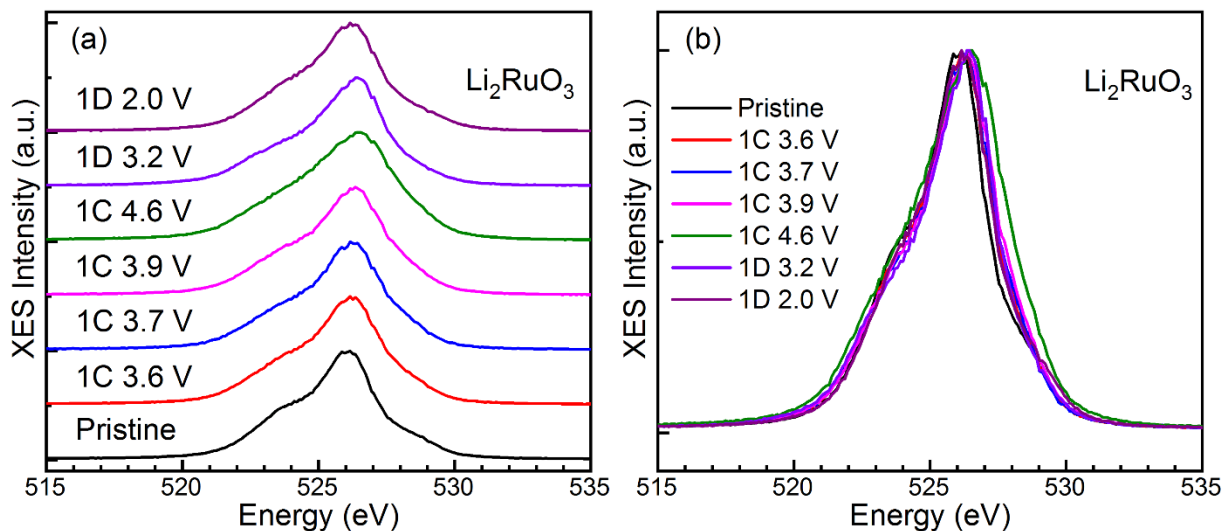


Figure 3-21. (a) Stacked and (b) overlaid *ex situ* non-resonant O K α XES spectra of Li₂RuO₃ at different states of charge.

3.9 *Ex situ* O K-edge RIXS

To further resolve occupied states due to O 2*p*-Ru 4*d* hybridization state upon Li removal, O K-edge resonant inelastic X-ray scattering (RIXS) was used (Figure 3-22). During the RIXS process, excitation of an O 1*s* electron into specific valence states, rather than to the continuum, is induced, followed by the repopulation of those core states by electrons transiting from occupied band with O 2*p* character. By carefully selecting excitation energies to specific XAS signals and, thus, unoccupied states, RIXS can resolve the states that are involved in these different excitations. The X-ray doses were controlled to avoid beam damage during the experiment.²¹⁰

RIXS is typically represented as a 2D map of the fluorescence intensity as a function of both photon-in energy (excitation energy in vertical axis) and photon-out energy (emission energy in horizontal axis). Figure 3-26 shows the RIXS maps of Li₂RuO₃ at different states of charge throughout the first cycle. In the RIXS map, features with excitation energy larger than 535 eV correspond to transitions from Ru 5*sp*-O 2*p* mixed states, whereas those below 535 eV are attributed to the involvement of Ru 4*d*-O 2*p* hybridization states (see red rectangle in Figure 3-22). Upon cycling, the changes in intensity in this region mirrored the trends from O K-edge XAS, as expected. No signals were observed at low emission energy, i.e., below 524 eV at any excitation energy. Such features result from excitation at 531 eV have been recently claimed as signatures of lattice O redox.¹⁷⁷ In contrast, there was an enhancement of the elastic peak (see white rectangle in Figure 3-22), corresponding to emission energies matching the excitation, upon oxidation to 4.6 V, as shown in a white rectangle. This signature has also been identified by others in the literature as originating from lattice O redox.¹¹¹

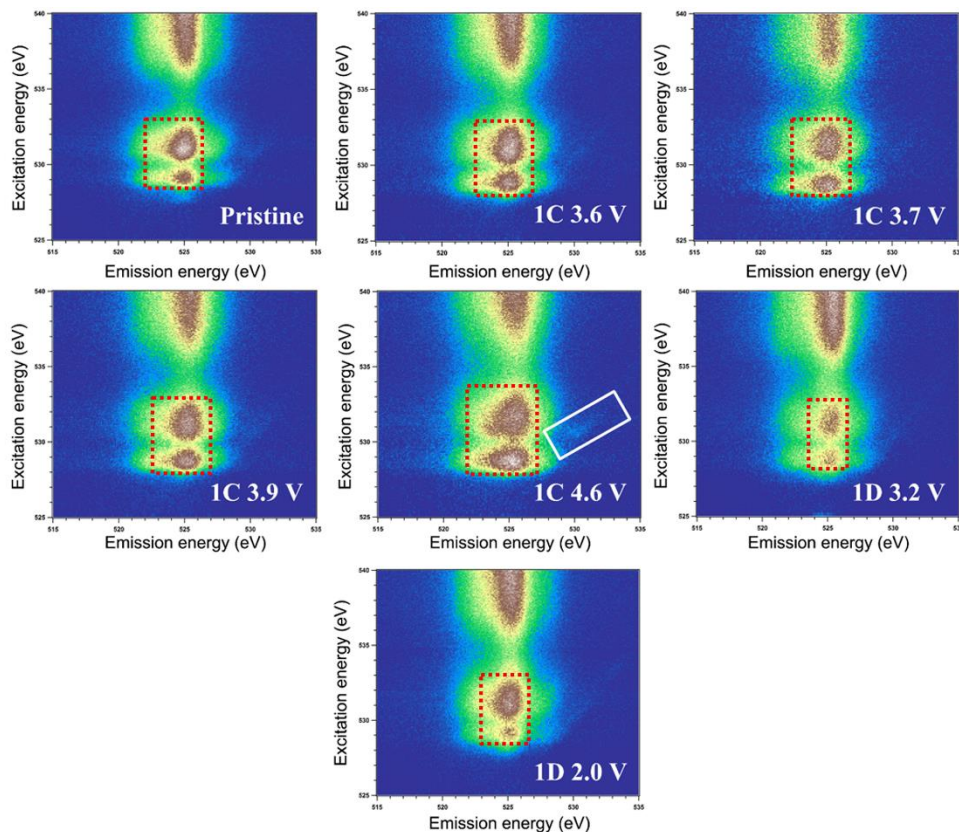


Figure 3-22. *Ex situ* RIXS map of Li_2RuO_3 at different states of charge through the first cycle. The red rectangles represent the pre-edge feature due to the transition of O 1s core electron to the Ru 4d-O 2p hybridization states. The white rectangle stands for the elastic peak enhancement.

3.10 Conclusion

The redox mechanism of Li_2RuO_3 , identified as a canonical model of Li-rich oxides displaying lattice O redox, was comprehensively evaluated from the perspective of both transition metal cations and oxide anions. Its electrochemical profile showed a drastic evolution in the first cycle, with large hysteresis between charge and discharge. The evolution was much less pronounced upon subsequent cycling, thus significantly lowering hysteresis. The electrochemical hysteresis was related to differing chemical pathways between oxidation and reduction in the first cycle, and upon subsequent cycling. *Operando* synchrotron X-ray diffraction demonstrated that the structure of Li_2RuO_3 evolved from monoclinic to trigonal arrangement upon the initial delithiation to 4.6 V and into a much more disordered structure than

the pristine state upon re-lithiation to 2.0 V. X-ray spectroscopy, both at Ru and O, was consistent with a conventional cationic redox reaction involving $\text{Ru}^{4+}/\text{Ru}^{5+}$ couple upon Li extraction to 3.9 V, but further oxidation was accompanied by a reduction of Z_{eff} of Ru while O states continued to shift to higher energy and increase in pre-edge intensity. This evolution could be viewed as a process of “reductive coupling”, whereby extraction of electrons from the compound is compensated primarily via O states, which then induces re-hybridization with Ru, increasing bond order and, thus, participation of O in the unoccupied d states. Interestingly, only an enhancement of the elastic peak was observed in RIXS, although an unconventional ligand-centered process occurred. Upon re-lithiation, a constant shift of Ru and O absorption edges and O $K\alpha$ XES to lower energy, together with a decrease in intensity in the pre-edge region of the O K-edge XAS are unequivocally associated with a mechanism where the formal oxidation state of Ru is reduced, even beyond the pristine state. Clearly, the changes in both crystal and electronic structure upon first oxidation were not mirrored upon reduction, providing an explanation to the electrochemical hysteresis. Study of samples upon extensive cycling showed that it was explained by changes at both Ru and O consistent with a conventional model of redox via changes in the formal Ru state. This work indicates that unconventional processes of lattice O redox are possible in Li_2RuO_3 , but that they lead to states that unlock an alternate pathway where the electrochemical response is suitably explained by a conventional model of transition metal redox.

Chapter 4 Definition of redox centers in reactions of lithium intercalation in Li_3RuO_4 polymorphs

The content of this chapter has been published as “Definition of Redox Centers in Reactions of Lithium Intercalation in Li_3RuO_4 Polymorphs”²⁰⁷, Haifeng Li, Srinivasan Ramakrishnan, John W. Freeland, Bryan D. McCloskey, Jordi Cabana. *J. Am. Chem. Soc.* **2020**, 142, 8160–8173. Reprinted with permission. Copyright © 2020 American Chemical Society. DEMS analysis was performed by Srinivasan Ramakrishnan and Bryan D. McCloskey.

4.1 Introduction

As described above, the number of pure lone O(2p) states relies on the O/TM ratio, which is proportional to the non-bonding O(2p) states at the Fermi level that could induce additional capacities in Li-rich cathode materials.⁹² These huge capacities were subsequently realized in layered Li_3IrO_4 .⁹⁸ Following the Li_3TMO_4 (or $\text{Li}[\text{Li}_{0.5}\text{TM}_{0.5}]\text{O}_2$) family, Yabuuchi *et al.* demonstrated that Li_3NbO_4 , with an ordered rock-salt structure, is electrochemically inactive due to the absence of electrons in the conduction band.²¹¹ Jacquet *et al.* reported ordered, layered structures showing a variety of interlayer arrangements can be generated by substituting Nb with Ru.⁹⁶ They revealed that it was possible to both remove Li to formally form $\text{Li}_3\text{Ru}_x\text{Nb}_{1-y}\text{O}_4$, with x largely correlating with y, and insert Li to form $\text{Li}_4\text{Ru}_y\text{Nb}_{1-y}\text{O}_4$. Subsequently, they explored the intercalation chemistry of $\text{Li}_3\text{Ru}_y\text{Ir}_{1-y}\text{O}_4$.⁹⁷ Focusing on Li_3RuO_4 , the two articles probed the extraction of the charge equivalent to full delithiation (“ RuO_4 ”), and reported a significant tendency toward dissolution of Ru in the form of oxo-complexes. However, the charge compensation mechanism was not completely elucidated, so it is unclear whether ligand-centered reactivity was realized. Furthermore, the role of structural ordering was not evaluated, yet both layered and disordered rock-salt forms of Li_3RuO_4 are known.^{212, 213}

In this study, the origin of the electrochemical properties of the two rock-salt polymorphs of Li_3RuO_4 , disordered and layered, was ascertained. The structures are composed of arrangements of LiO_6 and TMO_6 (TM = Ru) edge-sharing octahedra with different distributions. Both polymorphs show rich electrochemistry along a very broad compositional space, from Li_2RuO_4 to Li_4RuO_4 . To fully understand the Li intercalation chemistry, with the goal of defining the redox centers underpinning the reaction, the

different states were characterized with a combination of probes of crystal structure and the electronic structure at both Ru and O. The results revealed that both conventional metal-centered intercalation reactions and ligand-centered process are possible in this compound. Their reversibility and the broad implications for the design of materials with high capacity for charge storage are established.

4.2 Experimental methods

Two polymorphs of Li_3RuO_4 were prepared through a traditional solid-state reaction from mixtures of RuO_2 (Sigma-Aldrich, 99.9%) with a 10% stoichiometric excess of Li_2O (Sigma-Aldrich, 99.9%). The reactants were mixed in an agate mortar and pestle uniformly and then the homogeneous mixture was compacted into pellets. The pellets were reacted at either 650°C or 900°C for 24 hours in an alumina crucible under air, respectively. After cooling to room temperature naturally, the as-obtained polymorph samples were ground into fine powders. The particle size and morphology of pristine samples were analyzed by using scanning electron microscopy (SEM) technique at a Hitachi S-3000N microscope operated at 5 kV and 20 mA.

The method of electrode preparation can be found in Chapter 2. Here the as-prepared Li_3RuO_4 with two polymorphs were used as the active materials.

Details about the characterization methods can be found in chapter 2. Galvanostatic cycling in Li cells was conducted at 25°C. Structural characterization was carried out using powder X-ray diffraction both in the lab and at synchrotron and neutron facilities. The particle size and morphology were characterized by the scanning electron microscope. Ru K-edge XANES and O K-edge XAS were characterized via the X-ray absorption spectroscopy. The gas evolution was evaluated by using DEMS.

4.3 Structural Characterization of Li_3RuO_4

Li_3RuO_4 crystallizes in a rock-salt structure, but varies degree of Li/Ru ordering within the octahedral sites with increasing temperature.^{95, 212} Joint Rietveld refinement of SXRD and NPD confirmed the data in the literature and the success of the synthesis of materials at high purity. The material made at 650°C

crystallized in a simple rock-salt structure with a random arrangement of Li and Ru (D-Li₃RuO₄, Figures 4-1a and 4-2a, and Table 4-1a). A broad hump that could not be indexed by this disordered structure was found centered at $Q \sim 1.3 \text{ \AA}^{-1}$, which suggested short-range ordering of Li/Ru. The oxide made at 900°C shows Li/Ru ordering into alternating Li-only and Li/Ru layers within the rock-salt framework (O-Li₃RuO₄, Figures 4-1b and 4-2b, and Table 4-1b)^{94, 95} Li and Ru are also ordered within [Li_{1/2}Ru_{1/2}]O₂ layers forming zig-zag chains of [RuO₆] and [LiO₆] octahedral (Figure 4-2c). The refinements did not improve with introduction of Li vacancies or partial occupancy of Ru in Li sites as described previously.⁹⁶ The Ru adopts a slightly distorted environment with two short, two middle and two long Ru-O distances of 1.91, 1.98, and 2.05 Å, respectively (Figures 4-2e and 4-2f, and Table 4-2), with Ru displaced from the octahedron center.²¹³ The Ru coordination environment cannot be evaluated for D-Li₃RuO₄ because of the Li and Ru disorder (Figure 4-2a).

The particles of both polymorphs were around 1 μm and displayed irregular morphologies (Figure 4-3), consistent with the expectation of samples made at such high temperature from micrometric precursors.

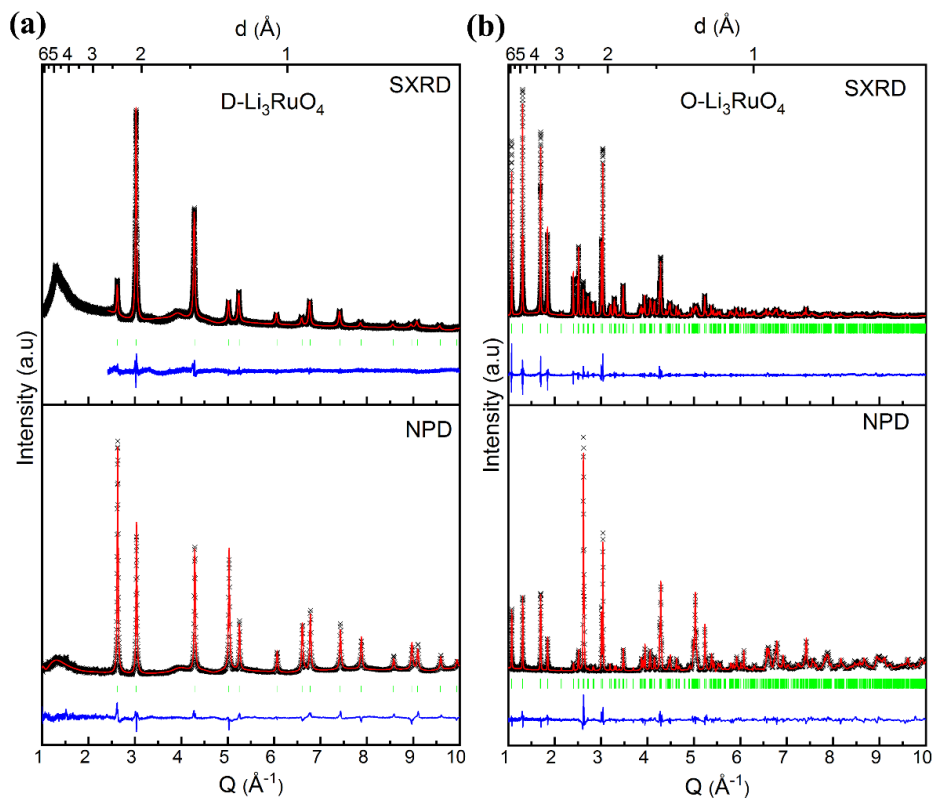


Figure 4-1. Structural characterization of disordered and ordered Li_3RuO_4 . Combined Rietveld refinement of SXR and NPD patterns of (a) $\text{D-Li}_3\text{RuO}_4$ and (b) $\text{O-Li}_3\text{RuO}_4$. Black crosses: experimental patterns, red solid line: calculated patterns, blue solid line: difference and green bars: Bragg reflections.

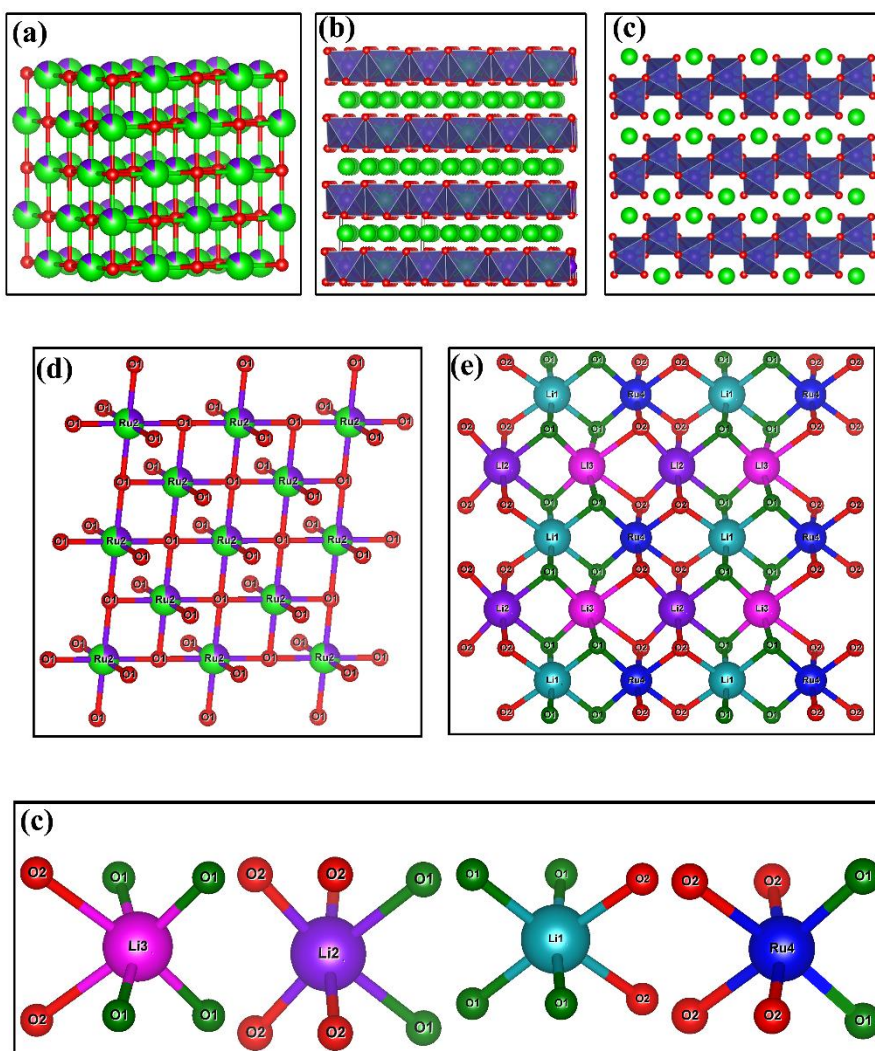


Figure 4-2. Structure of (a) D- and (b) O-Li₃RuO₄. Oxide ions (red) stack in a cubic close-packed arrangement while both Li (green) and Ru (purple) occupy octahedral sites for both polymorphs. D-Li₃RuO₄ has mixed Li and Ru arrangement in the metallic layers. O-Li₃RuO₄ has a long-range distribution of zig-zag chains (c). Schematic arrangement of various bonds in (d) D- and (e) O-Li₃RuO₄. (f) Individual coordination environment for each cation in O-Li₃RuO₄.

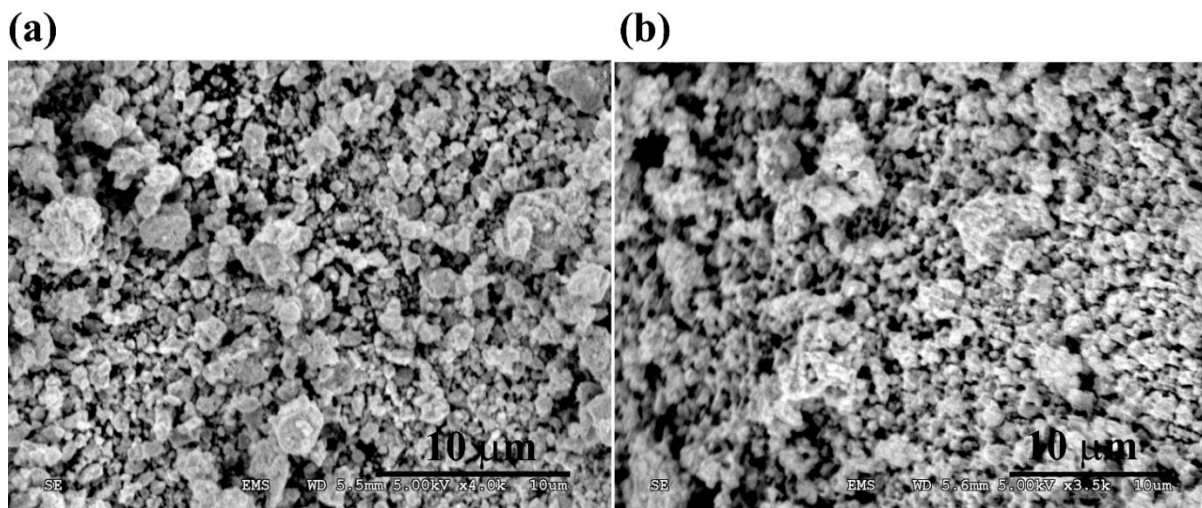


Figure 4-3. SEM images of (a) D- and (b) O-Li₃RuO₄.

Table 4-1. Crystallographic parameters and reliability factors extracted from the joint Rietveld refinement of SXRD and NPD for (a) D- and (b) O-Li₃RuO₄.

(a) D-Li ₃ RuO ₄						
Space group: Fm $\bar{3}$ m; a = b = c = 4.14570(8) Å; $\alpha = \beta = \gamma = 90^\circ$; V = 71.252(4) Å ³						
Atom	Wyckoff position	x	y	z	U _{iso} (Å ²)	Occupancy
O	4b	0.5	0.5	0.5	0.013	1
Li	4a	0.0	0.0	0.0	0.00966	0.75
Ru	4a	0.0	0.0	0.0	0.00966	0.25
R _{WP} = 8.283%; χ^2 = 1.808						
(b) O-Li ₃ RuO ₄						
Space group: P2/a; a = 5.08609(30) Å; b = 5.86578(5) Å; c = 5.12048(30) Å; $\beta = 110.1506(8)^\circ$; V = 143.4134(25) Å ³						
Atom	Wyckoff position	x	y	z	U _{iso} (Å ²)	Occupancy
O1	4g	0.01853(11)	0.63695(12)	0.75681(10)	0.01058(7)	1
O2	4g	0.50395(12)	0.11326(11)	0.222587(9)	0.01058	1

Li1	2e	0.7500	0.6195(6)	0.0000	0.0251(3)	1
Li2	2f	0.7500	0.9064(6)	0.5000	0.0251	1
Li3	2f	0.7500	0.4209(5)	0.5000	0.0251	1
Ru4	2e	0.2500	0.85995(12)	0.0000	0.06578(22)	1
R _{WP} = 12.316%; χ^2 = 2.869						

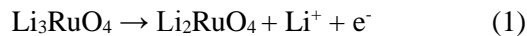
Table 4-2. Selected bond lengths (Å) O-Li₃RuO₄ at 298 K

Bonds	Distance (Å)
Li1-O1	2.1443(6)
Li1-O1	2.1443(6)
Li1-O1	2.0469(25)
Li1-O1	2.0469(25)
Li1-O2	2.1056(26)
Li1-O2	2.1056(26)
Li2-O1	2.2034(24)
Li2-O1	2.2034(24)
Li2-O2	1.9490(20)
Li2-O2	1.9490(20)
Li2-O2	2.2138(6)
Li2-O2	2.2138(6)
Li3-O1	1.9906(19)
Li3-O1	1.9906(19)
Li3-O1	2.0729(7)
Li3-O1	2.0729(7)
Li3-O2	2.3629(23)
Li3-O2	2.3629(23)
Ru4-O1	1.9072(7)
Ru4-O1	1.9072(7)
Ru4-O2	2.0456(8)
Ru4-O2	2.0456(8)
Ru4-O2	1.9813(6)
Ru4-O2	1.9813(6)

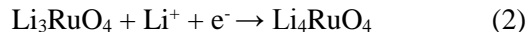
4.4 Voltage cutoff window of 2.5-3.9 V

Potential-composition profiles were measured galvanostatically under two windows: 2.5-3.9 V and 1.5-

2.5 V vs Li^+/Li^0 , respectively. In the first window, the experiment was initially started upon oxidation of Li_3RuO_4 , to explore the hypothetical reaction



while minimizing effects from amorphization and transition metal dissolution at higher potential,²⁸ whereas reduction was the first step in the latter window, for the hypothetical reaction:



4.4.1 Electrochemical properties of Li_3RuO_4

Electrochemical activity of D- Li_3RuO_4 : Starting from oxidation, the electrochemical cell with D- Li_3RuO_4 displayed a plateau with an average voltage of 3.8-3.85 V vs Li^+/Li^0 (Figure 4-4a), accumulating a capacity equivalent to the removal of just under 2 mol Li per mol compound. The corresponding derivative curve (Figure 4-4b) showed a sharp process centered at 3.8 and a small one at 3.84 V. Upon reduction, the slope of the potential-composition profile notably increased, leading to the absence of plateaus and broad features in the derivative profile, with a peak at 3.6 V displaying a shoulder at 3.4 V, for a smaller associated charge, equivalent to 1.1 mol Li per mol compound. Upon subsequent cycling, the electrochemical profiles continued to wash out, with most activity occurring below 3.8 V, and the total capacity declined (Figures 4-4c and 4-4d).

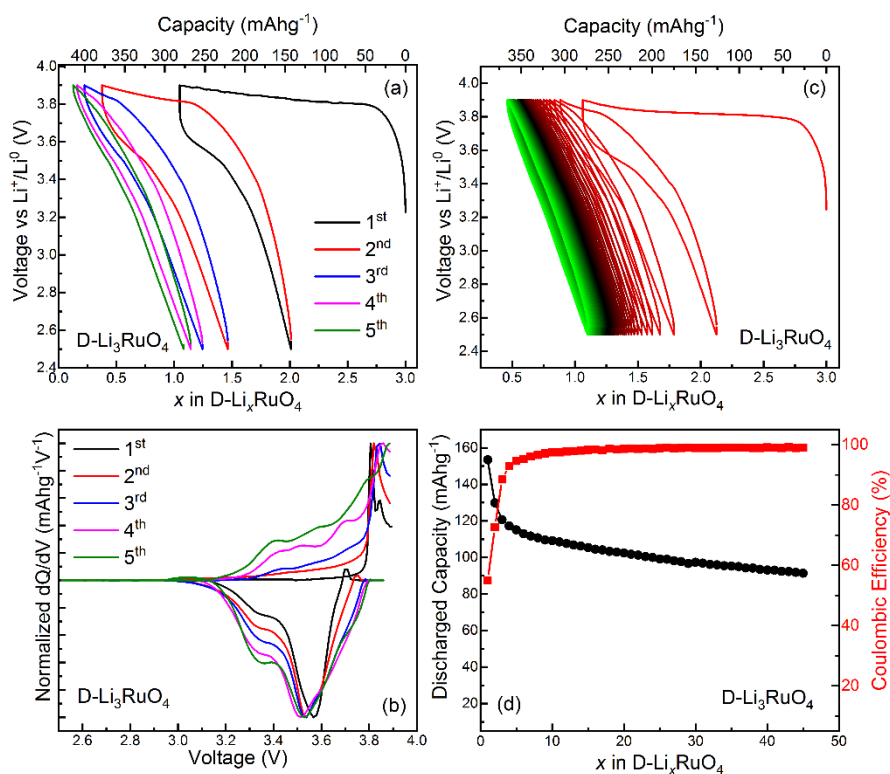


Figure 4-4. Voltage-composition profiles of D-Li₃RuO₄ between 2.5-3.9 V upon (a) the first five cycling and (c) extensive cycling. (b) Differential capacity analysis (dQ/dV) of D-Li₃RuO₄. (d) Discharge capacity and coulombic efficiency as a function of the cycle number.

Electrochemical activity of O-Li₃RuO₄: Turning to O-Li₃RuO₄, beginning with oxidation, according to the hypothetical reaction (1), the profile shows a flat plateau at around 3.87 V vs Li⁺/Li⁰, corresponding to the removal of 0.5 mol Li per mol compound at 3.9 V (Figure 4-5a), less than D-Li₃RuO₄. On the subsequent reduction, the plateau in the voltage-composition was centered at 3.67 V, followed by a sharp decrease in the voltage, denoting again a significant hysteresis. The coulombic efficiency in this first cycle was also low, only ~0.3 mol Li being recovered. The profiles significantly evolved with cycling. First, the anodic step above 3.85 V gave way to a new process at 3.75 V, which was accompanied by a cathodic process at 3.7 V, resulting in a notable reduction in hysteresis of potential. Upon further cycling, the anodic profile evolved to consist of a long sloping feature up to 3.75 V, followed by a rather flat plateau at 3.8 V. This profile was highly reversible upon reduction, with the plateau centered at 3.7 V, followed by a sloping

feature. This evolution was complete around cycle 20, and it was accompanied by a dramatic increase in the amount of charge equivalent of 1 mol Li per mol O-Li₃RuO₄. The capacity was almost 100% reversible upon cycling, and it remained stable for several subsequent cycles (Figure 4-5d). Overall, the evolution in the electrochemical profiles suggests that the compound is activated by cycling, with a notable complexity in the associated redox reaction.

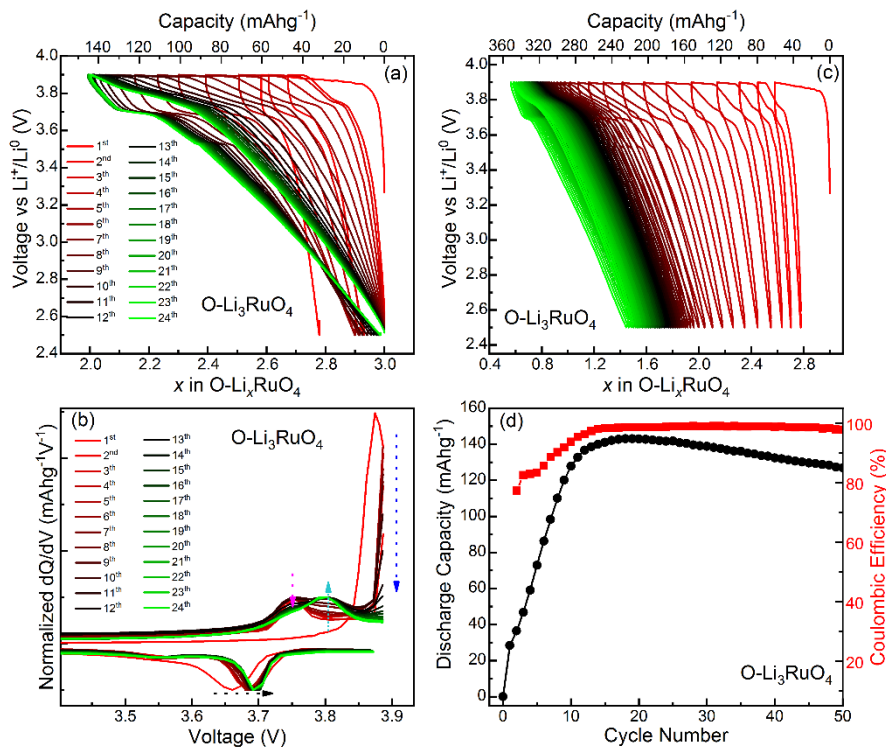


Figure 4-5. Voltage-composition profiles of O-Li₃RuO₄ between 2.5-3.9 V upon (a) the first 24th cycling and (c) extensive cycling. The profiles in (a) were re-scaled back to x=3 (0 mAhg⁻¹) for clarity. (b) Differential capacity analysis (dQ/dV) of O-Li₃RuO₄. (d) Discharge capacity and coulombic efficiency as a function of the cycle number.

4.4.2 Structural evolution of Li₃RuO₄

D-Li₃RuO₄ between 2.5 and 3.9 V: Figure 4-6 presents the variation of SXRD patterns of D-Li₃RuO₄ at the end points in the first cycle collected *operando* (Figure 4-7). There was a general decrease in the peak intensity and increase in the peak width, indicating a significant loss of crystallinity. It was accompanied

by a shift to lower angle in their position, indicating an increase in unit cell volume, which was unexpected from a conventional reaction of deintercalation of Li^+ . In addition, the delithiation led to the appearance of three new peaks located at Q (2θ angle) of 2.5 \AA^{-1} (5.9°), 2.5 \AA^{-1} (8.3°) and 2.5 \AA^{-1} (10.2°) as denoted by stars (Figure 4-6), accompanied by a tail at low angles in the intense reflection at 3.3 \AA^{-1} , possibly indicating growth of either a newly formed phase or a lowering of the symmetry of the disordered rock-salt framework. Upon subsequent reduction to 2.5 V, the broad low-angle peak experienced no obvious changes while the other peaks returned to the position of the pristine state with a partial recovery of intensity, and the new peaks induced by oxidation almost vanished. Due to the limited number of Bragg reflections and the broadening of the patterns, it was not possible to assign the newly formed peaks to a specific phase or distortion. Therefore, the cell parameters were obtained by the Pawley refinement based on disordered rock-salt with a cubic space group $\text{Fm}\bar{3}\text{m}$ without including the low- Q broad peak, as shown in Figure 4-8 and Table 4-3. The underlying lattice volume of the fully delithiated state increased by 1.6% compared with that of the pristine state and, while it diminished after the following reduction, it remained larger than the pristine state by 0.5%.

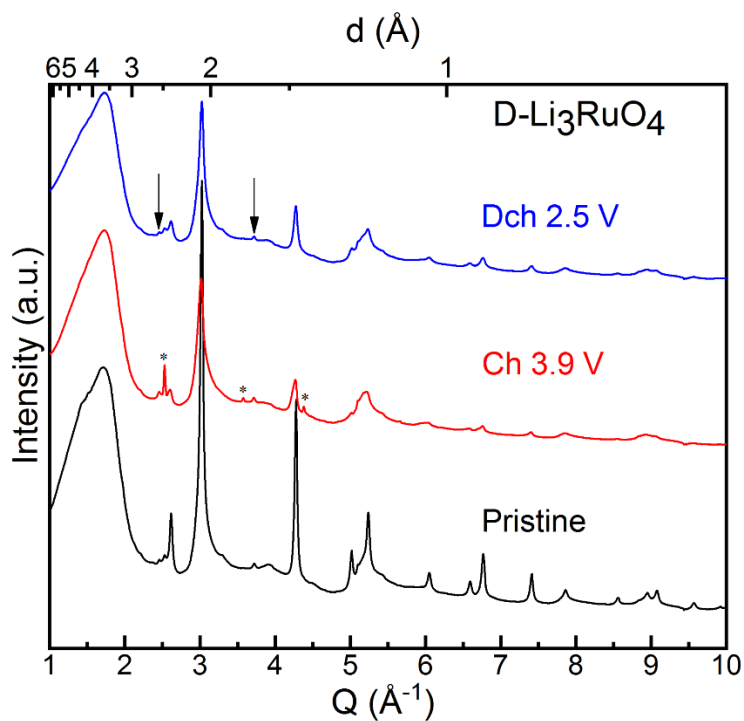


Figure 4-6. SXR D patterns of D-Li₃RuO₄ at selected points during the first cycle within a potential range of 2.5-3.9 V, collected *operando*. The complete evolution of the data is found in Figure S7. The black arrows denote Bragg reflections that could not be indexed by the parent rock-salt lattice, which also did not change with cycling. The stars represent the newly formed peaks concurrent with Li (de)intercalation.

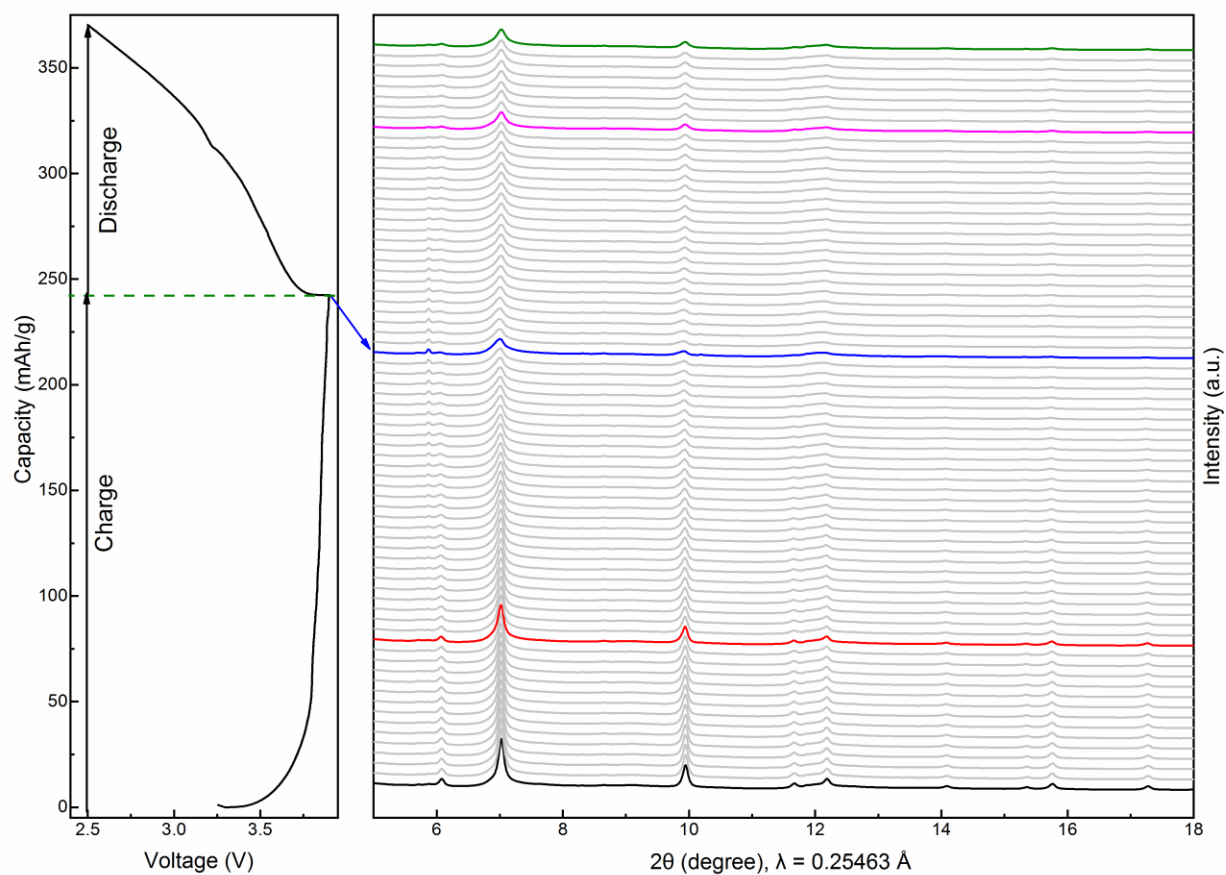


Figure 4-7. *Operando* SXR D patterns in the first cycle of a D-Li₃RuO₄/Li half-cell at a rate of C/20. The left panel shows the corresponding galvanostatic curve between 2.5 and 3.9 V. Colored lines indicate key points in the experiment, discussed in the text.

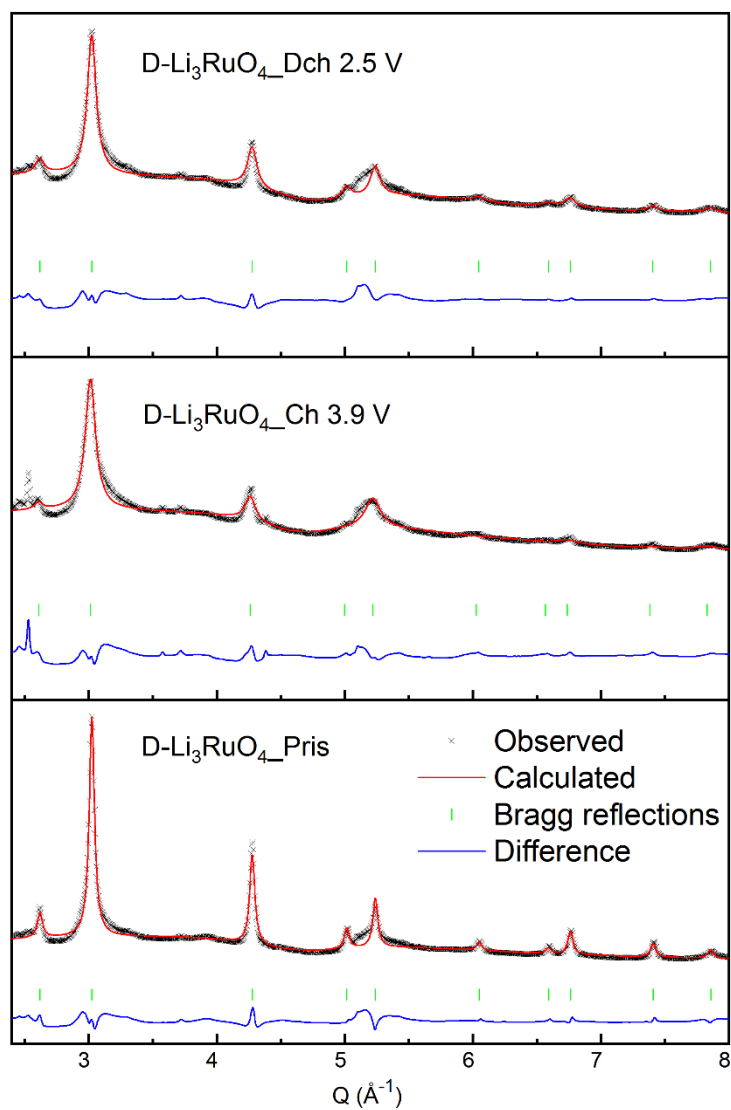


Figure 4-8. Pawley refinements of SXRD patterns of D-Li₃RuO₄ at different electrochemical states between 2.5 V and 3.9 V.

Table 4-3. Calculated Unit Cell Parameters via Pawley refinement of the data in Figure 4-6.

D-Li ₃ RuO ₄		
State	a = b = c (Å)	Volume (Å ³)
Pristine	4.14929	71.436
Ch 3.9 V	4.17061	72.543

O-Li₃RuO₄ between 2.5 and 3.9 V: The *ex situ* XRD patterns of O-Li₃RuO₄ after the 1st oxidation-reduction cycle showed little change in the position and width of Bragg reflections, with, at most, minor changes in intensity (Figures 4-9a, 4-9c, 4-9d, and 4-10a, and Table 4-4). The marginal variations are consistent with the small number electrode capacity. Samples were also harvested at cycles where the highest capacity was observed (Figure 4-9b). The XRD pattern upon oxidation at the maximum charge capacity was significantly different from both pristine and the first charge, with the peak positions changing and observable broadening. Subsequent reduction then brought about a narrowing and shift of the peaks to the original positions. According to Pawley fits of the data (Figure 4-10b and Table 4-4) using a P2/a space group, the unit cell volume expanded by 5.1% relative to the pristine state upon charging, whereas it shrunk back upon discharge, being 0.2% smaller than the pristine state. It must be noted that the fit of the pattern of the charged state failed to completely account for some of the complex peak shapes at low Q. This effect suggests a subtle distortion of the structure.

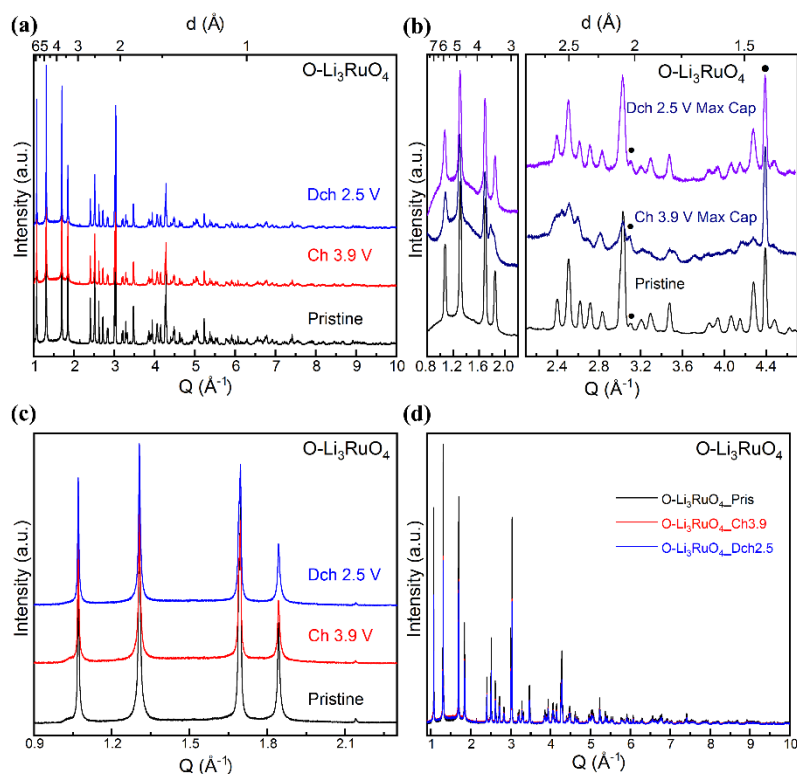


Figure 4-9. (a) *Ex situ* SXR patterns of ordered Li_3RuO_4 after the first cycling; (b) *Ex situ* Laboratory XRD patterns when the capacity reached maximum. The black dots represent the Bragg reflections from Al foil. “Max Cap” in (b) is the abbreviation of “Maximum Capacity”. (c) Enlarged and (d) overlaid SXR patterns of $\text{O-Li}_3\text{RuO}_4$ during the first cycle. There was no obvious peak shift upon cycling. The intensity experienced substantial decrease after oxidation to 3.9 V, while the subsequent reduction did not bring about remarkable change in the intensity in relative to that of the previous oxidation.

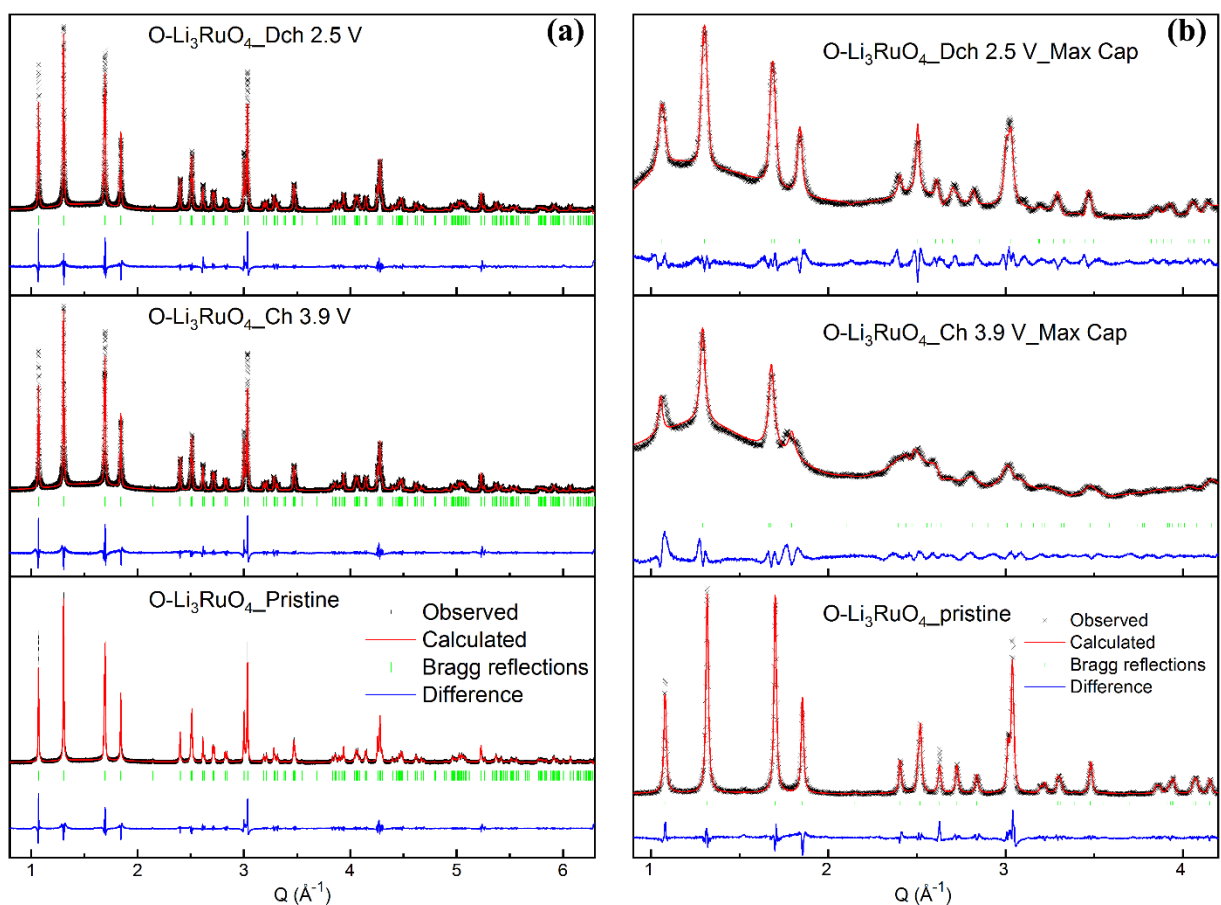


Figure 4-10. Pawley refinements of XRD patterns of O-Li₃RuO₄ at different electrochemical states. Panel a shows the SXR patterns. Panel b portraits the XRD results collected by the Cu K α irradiation.

Table 4-4. Calculated Unit Cell Parameters via Pawley refinement of the data in Figure 10.

O-Li ₃ RuO ₄					
State	a (Å)	b (Å)	c (Å)	β (°)	Volume (Å ³)
Pristine	5.08809	5.86792	5.12213	110.154	143.566
Ch 3.9 V	5.08869	5.86786	5.12070	110.128	143.565
Dch 2.5 V	5.08832	5.86845	5.11979	110.123	143.548
Ch 3.9 V Max Cap	5.19202	5.96737	5.25034	111.963	150.863

Dch 2.5 V Max Cap	5.05296	5.89378	5.12716	110.264	143.241
----------------------	---------	---------	---------	---------	---------

4.4.3 *Ex situ* Ru K-edge XAS of Li₃RuO₄

Ex situ Ru K-edge X-ray absorption near edge structure (XANES) spectra were collected of D- and O-Li₃RuO₄ (Figures 4-12 and 4-13). The first derivative of the spectra was used to establish the position of the absorption edge, using the first inflection point above 22120 eV. The main absorption edge arises from the electric dipole-allowed transition from the *1s* to *5p* level, whilst the pre-edge arises from two primary transitions.²¹⁴ One is the electric quadrupole-allowed and dipole-forbidden *1s*→*4d* transition. The probability of the electric quadrupole-allowed transitions is much lower compared with the dipole, leading to a much lower intensity in the pre-edge peak. However, an enhancement of its intensity can be induced by certain symmetry-breaking distortions of an octahedron that can remove its inversion center, thus promoting the mixing between *4d* and *5p* orbitals. The pre-edge peak has very low intensity in all the spectra collected, indicating that the distortion induced by a displacement of Ru off the center of the RuO₆ octahedra did not appear to be enough to induce visible pre-edge peaks. The spectrum of pristine D-Li₃RuO₄ was very similar to O-Li₃RuO₄ (Figure 4-11), suggesting similar local coordination environment of Ru. The oxidation state of Ru⁵⁺ in both polymorphs was confirmed by comparing the rising edge and the first derivative curve of the Ru K-edge XANES spectra with Ru⁴⁺O₂ (Figures 4-11, 4-12a, and 4-13a).

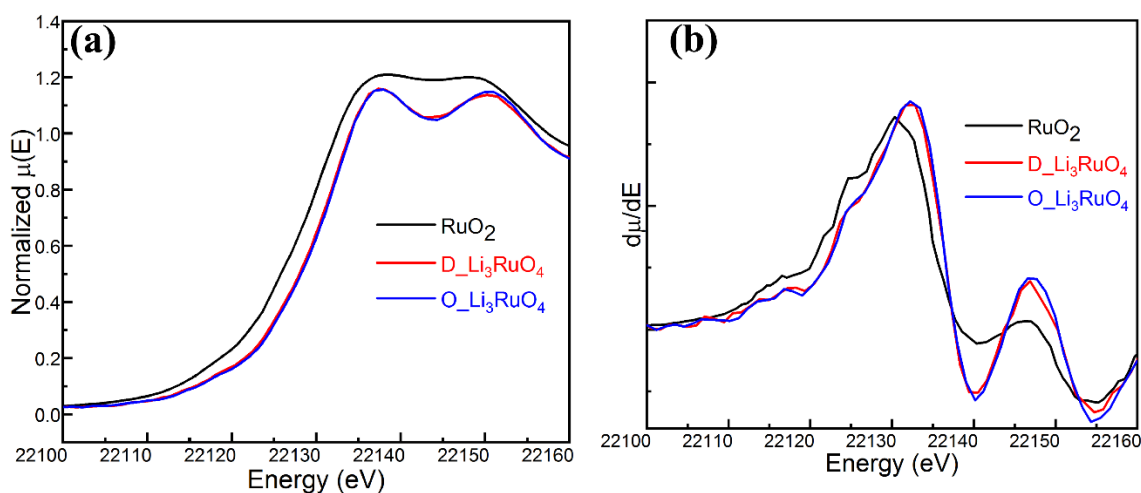


Figure 4-11. (a) *Ex situ* Ru K-edge XANES spectra and (b) the corresponding derivative curves of RuO₂, disordered Li₃RuO₄ and ordered Li₃RuO₄.

D-Li₃RuO₄ between 3.9 and 2.5 V: Upon oxidation of D-Li₃RuO₄ to 3.9 V, there was almost no energy shift of the rising edge compared with the pristine state (Figure 4-12a). However, there was an apparent growth of the pre-edge peak after oxidation (Figure 4-12b), denoted by the growth of a small derivative peak at 22117 eV, and a decrease in the ratio between the whiteline peaks at 22138 and 22150 eV. This observation could be attributed to the distortion of the coordination environment of Ru through enhanced hybridization between Ru 5*p* and 4*d* orbitals. Overall, the changes are consistent with the onset of a new Ru species reported by Jacquet et al. at similar potentials, on the way to complete nominal delithiation.⁹⁷ In contrast, there was a notable shift of ~1.9 eV of the absorption edge towards lower energy after the subsequent reduction process to 2.5 V. Indeed, the resulting spectrum largely overlapped with Ru⁴⁺O₂, hence unambiguously demonstrating the reduction of Ru and the existence of different chemical pathways upon oxidation and reduction in this first cycle. A pre-edge peak was no longer resolved, implying the recovery of a largely centrosymmetric coordination environment of Ru.

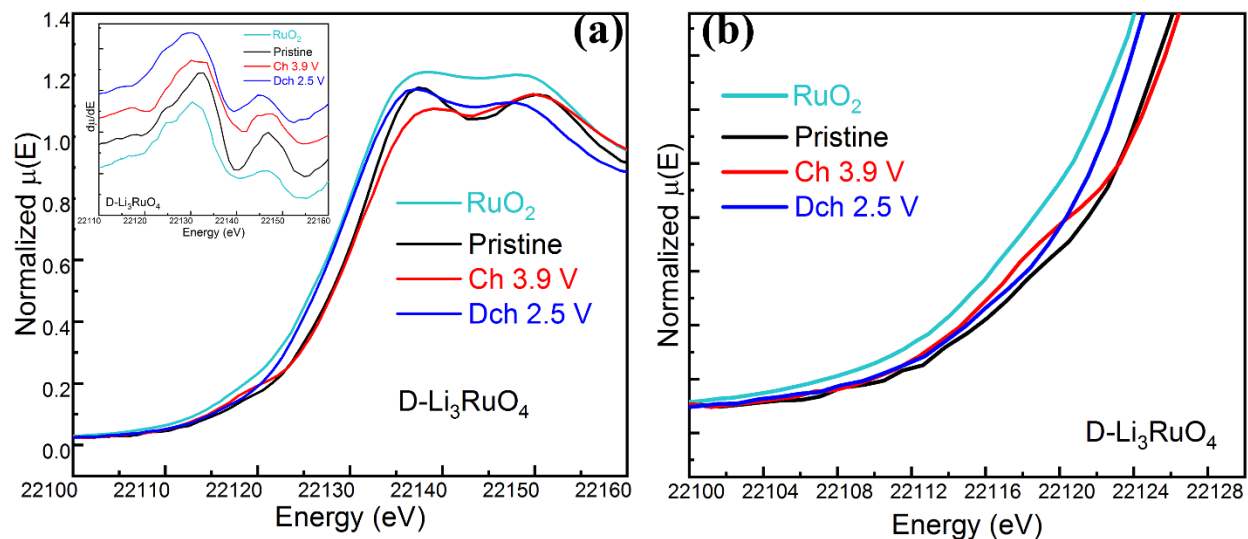


Figure 4-12. (a) *Ex situ* Ru K-edge XANES spectra of D-Li₃RuO₄ at different electrochemical states and (b) zoom of the pre-edge region. The inset in (a) presents the corresponding derivative curves, used to define the position of the absorption edge. RuO₂ was used as reference for Ru⁴⁺.

O-Li₃RuO₄ between 3.9 and 2.5 V: The Ru K-edge XANES spectrum of O-Li₃RuO₄ after initial oxidization to 3.9 V (Figure 4-13a) overlapped with the pristine state, with only a slight increase in the pre-edge intensity. The following reduction process to 2.5 V caused the rising edge to shift toward lower energy by ~1.1 eV relative to the pristine state, close to the RuO₂ standard, with loss of any pre-edge features. When the electrochemical reactivity reached its maximum after multiple cycles (Figure 4-13a), the position of the absorption edge of the charged electrode still overlapped with the pristine state, revealing the existence of Ru⁵⁺ (derivative peak in the inset of Figure 4-13a), but there was an increase in the intensity of the pre-edge peak (Figure 4-13b). This phenomenon is likely due to the redox-driven distortion in the symmetry of RuO₆. The subsequent reduction shifted the edge to lower energy by ~1.5 eV relative to the pristine state, close again to the Ru⁴⁺ state of RuO₂, with low pre-edge intensity, again suggesting RuO₆ centrosymmetry.

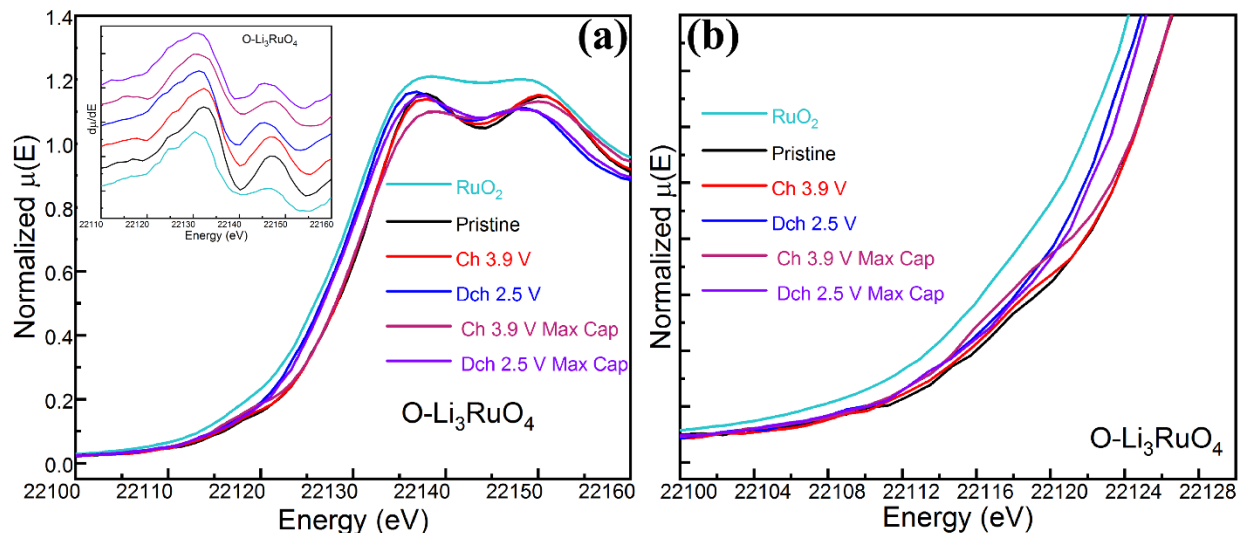


Figure 4-13. (a) *Ex situ* Ru K-edge XANES spectra of O-Li₃RuO₄ at different electrochemical states and (b) zoom of the pre-edge region. The inset in (a) presents the corresponding derivative curves, used to define the position of the absorption edge. RuO₂ was used as reference for Ru⁴⁺. “Max Cap” here denotes data at cycles with maximum capacity (see text).

4.4.4 *Ex situ* O K-edge XAS of Li₃RuO₄

General features of the pristine states. The O K-edge XAS probes dipole-allowed transition from core O 1s to empty O 2p states.¹⁶⁷ In general, the spectra of these transition metal compounds can be divided into two regions. The pre-edge, at ≤ 535 eV, represents the unoccupied states resulting from O 2p orbitals hybridized with Ru 4d orbitals, and the broad band above 535 eV corresponds to the excitation from O 1s orbital to empty states of O 2p orbitals mixed with the Ru 5s and 5p orbitals, followed by higher states and multiple scattering events of the ejected electrons. The position of the pre-edge peak is affected by the change in the net electron density of the ligand via donating charge to the surrounding metal ion, which affects the attraction of electrons by the effective nuclear charge Z_{eff} , the degree of d orbital splitting induced by the crystal field effect, and the overall d-manifold energy determined by the strength of the covalent Ru-O bonds.²¹⁵ The intensity of these peaks reflects both the number of unoccupied hybridized states and the contribution of O to their wavefunction.²¹⁶ Therefore, the measurements offer insight into the role of O states and any changes in covalency. Note that the XAS spectra were measured simultaneously under both

TEY and TFY modes. The TEY mode with a probing depth around 10 nm provides the surface information, whereas TFY mode probes 100-nm into the electrode, offering insight into the interior of the material. It is worthy of notice that spectral intensities in this mode are distorted by the self-absorption of fluorescent photons by the material, so only qualitative trends between samples will be established.

The O K-edge XAS spectra of pristine D- and O-Li₃RuO₄ exhibits distinct pre-edge features centered at 528.4, 529.2, and 531.5 eV (Figure 4-14). There was also a prominent peak at 533.8 eV in both TEY and TFY spectra of D-Li₃RuO₄ (Figure 15a), but it was only clearly visible in the TEY of O-Li₃RuO₄ (Figure 15b). Since the O K-edge spectrum of Li₂CO₃ has a strong feature at similar energy,²¹⁷ the higher intensity in the surface-sensitive spectra suggests that it contributed as an impurity in the sample, which could not be detected by XRD (Figure 4-1). Electrochemical decomposition of Li₂CO₃ usually occurs above 4.3 V.²¹⁸ Since a cutoff voltage of 3.9 V was used here, the peak arising from Li₂CO₃ largely remained after charging (Figure 4-15), confirming that it was not significantly electroactive in these conditions. Due to the dominant role of Li₂CO₃ in the TEY spectra, analysis mainly focused on the TFY mode.

In accordance with crystal field theory, the envelope below 530 eV is assigned to the unoccupied states with contribution from Ru $4d_{xz}$, $4d_{yz}$, and $4d_{xy}$, whereas the broad signal centered at 531.5 eV is assigned to states hybridized with $4d_z^2$ and $4d_{x^2-y^2}^2$. The fine structure observed in the peaks, especially below 530 eV strongly suggests a lifting of the t_{2g}/e_g degeneracy in an ideal octahedral field, consistent with the distortion of the RuO₆ octahedra in the rock-salt framework, triggered by the off-center positioning of Ru. The high similarity in the pre-edge signals between D- and O-Li₃RuO₄ strongly suggests that the local distortion is similar in both structures. The qualitatively lower intensity in the $4d_{xz}/d_{yz}/d_{xy}$ compared to $d_z^2/d_{x^2-y^2}^2$ signals reflects the d³ configuration of Ru(V).

D-Li₃RuO₄ between 3.9 and 2.5 V: On oxidation of D-Li₃RuO₄ to 3.9 V, the main absorption threshold moved to higher energy by ~0.5 eV relative to the pristine state (Figures 4-14a), denoting variations in the O 1s energy level relative to the continuum due to an increase in Z_{eff} . The two peaks below 530 eV were reduced to one located at 529.9 eV with a diminished absorption intensity, while the broad peak centered

at 531.5 eV in the pristine state moved to higher energy, around 532.3 eV, along with an increased intensity. The changes in the peak position and intensity of pre-edge part reflected the notable changes taking place in the hybridization of the O 2*p*-Ru 4*d* orbitals. Given that Ru states remained largely unchanged, according to Ru K-edge XANES, those changes should originate from a localized variation in the oxygen electronic changes concurrent with oxidation.

Upon subsequent reduction to 2.5 V, the onset position of the absorption edge experienced a lower-energy shift of ~0.6 eV in comparison with the oxidized state, but was slightly lower, by ~0.1 eV, relative to the pristine state (Figures 4-14a). Both pre-edge peaks slightly shifted to lower energy, appearing at 529.4 and 532.2 eV, with a concurrent decrease in intensity by 25.0% and 14%, respectively, when compared with the oxidized state. The decrease in the intensity would be consistent with the reduction leading to electrons into previously unoccupied orbitals, in conjunction with the observed Ru⁵⁺/Ru⁴⁺ reduction in the Ru K-edge XANES.

O-Li₃RuO₄ between 3.9 and 2.5 V: The oxidation of O-Li₃RuO₄ crossing 3.9 V shifted the threshold of the absorption edge to higher energy relative to the pristine state (Figure 4-14b). There was an apparent increase in the intensity of the pre-edge region in comparison with the pristine state, with very minor changes in shape and peak distribution. The subsequent reduction led to a low-energy shift of the absorption threshold, to a position lower than the pristine state. There was a loss of intensity of the pre-edge peaks below 530 eV, especially at the lowest energies, leaving a dominant peak at around 529.4 eV, with a small shoulder to the left. Above 530 eV, the position and shape of the broad pre-edge peak remained almost invariable, yet with an observable decrease in the intensity.

Analogous with Ru K-edge XANES, the O K-edge XAS spectra were also recorded after multiple cycles when the electrochemical capacity reached its maximum. The trends observed in the first cycle were mirrored at this point, suggesting a reversible cycling between the same states after cycle 2, as the electrochemical curve evolved into a multi-step process.

Overall, the observed qualitative trends in the O K-edge spectra were the same in both polymorphs.

The most salient observation is that reduced states upon cycling were systematically different from the initial spectrum for O- Li_3RuO_4 , emphasizing the different pathways during the first charge and subsequent redox cycling observed by Ru K-edge XANES.

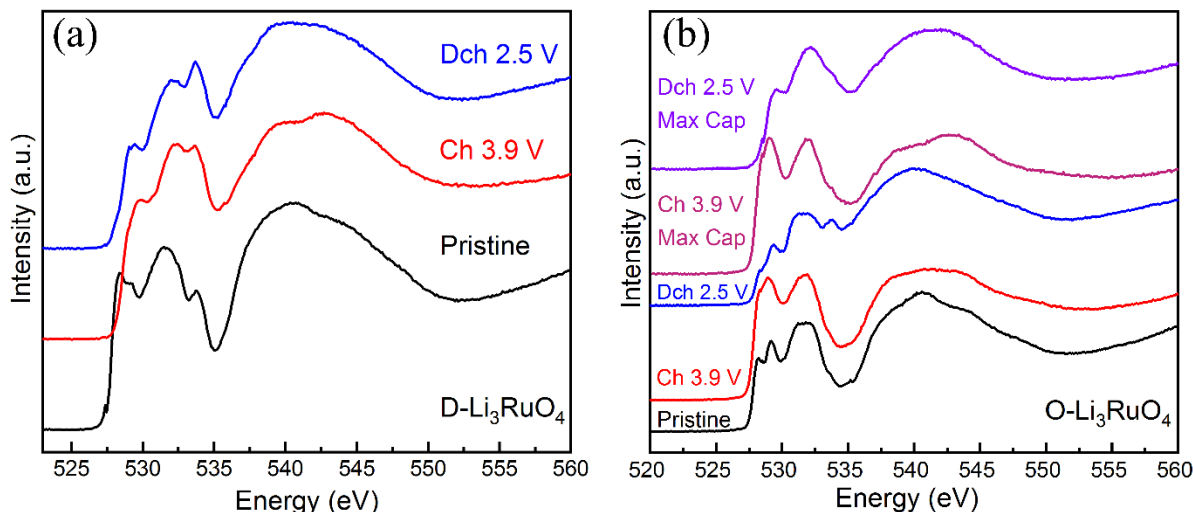


Figure 4-14. *Ex situ* O K-edge XAS spectra of (a) D- and (b) O- Li_3RuO_4 measured at different electrochemical states between 2.5-3.9 V. “Max Cap” in (b) is the abbreviation of “Maximum Capacity”. The peak at ~533.8 eV is ascribed to the existence of Li_2CO_3 in both (a) and (b).

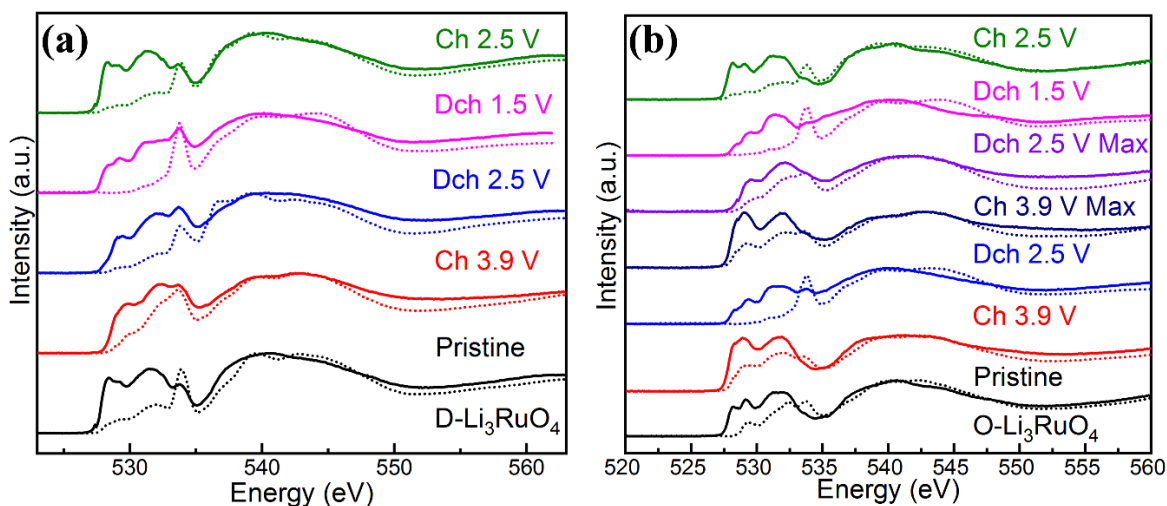


Figure 4-15. *Ex situ* O K-edge XAS spectra of (a) disordered Li_3RuO_4 and (b) ordered Li_3RuO_4 at different states collected under TEY (dot line) and TFY (solid line) detection modes.

4.4.5 *Operando* analysis of gas evolution

A charge and discharge capacity of 205 mAh/g and 131 mAh/g, respectively were obtained for D-Li₃RuO₄ during *operando* gas analysis using differential electrochemical mass spectrometry (DEMS, Figure 4-16), only slightly lower than the analogous values from coin cell testing. O₂ evolution, likely originating from the active cathode material, had an onset near the beginning of the long plateau region in the charge profile with a cumulative 0.42 μ mol, whereas CO₂ evolution was slightly delayed, with an overall 1.9 μ mol much larger than O₂ (Table 4-5). Since residual surface Li₂CO₃ decomposes to produce CO₂ above 4.3 V,^{181, 219} and based on the analysis of O K-edge XAS in TEY mode discussed above, we assign the CO₂ in Figure 7 to electrolyte decomposition. The amount of O₂ evolved from the cathode (0.42 μ mol) corresponds to 0.64% of the lattice oxygen (5.9 mg has an equivalent of 64 μ mol O). Considering the electron stoichiometry of 4 e⁻/O₂, the total irreversible capacity brought about by the oxygen loss was ~8 mAh/g.

O-Li₃RuO₄ exhibited a voltage profile similar to the results in coin cells, with higher capacity during both charge (200.3 mAh/g) as well as discharge (69.1 mAh/g) in the first cycle, mainly derived from the high cutoff voltage of 4.0 V. Both O₂ and CO₂ started to appear simultaneously as the delithiation occurred, with a cumulative amount of 0.3 and 2.2 μ mol, respectively, after the first cycle (Table 4-5). The total O₂ evolved corresponds to 0.40% of the lattice oxygen (7.0 mg has an equivalent of 76 μ mol O), which corresponds to an irreversible capacity of ~5 mAh/g, lower than in D-Li₃RuO₄.

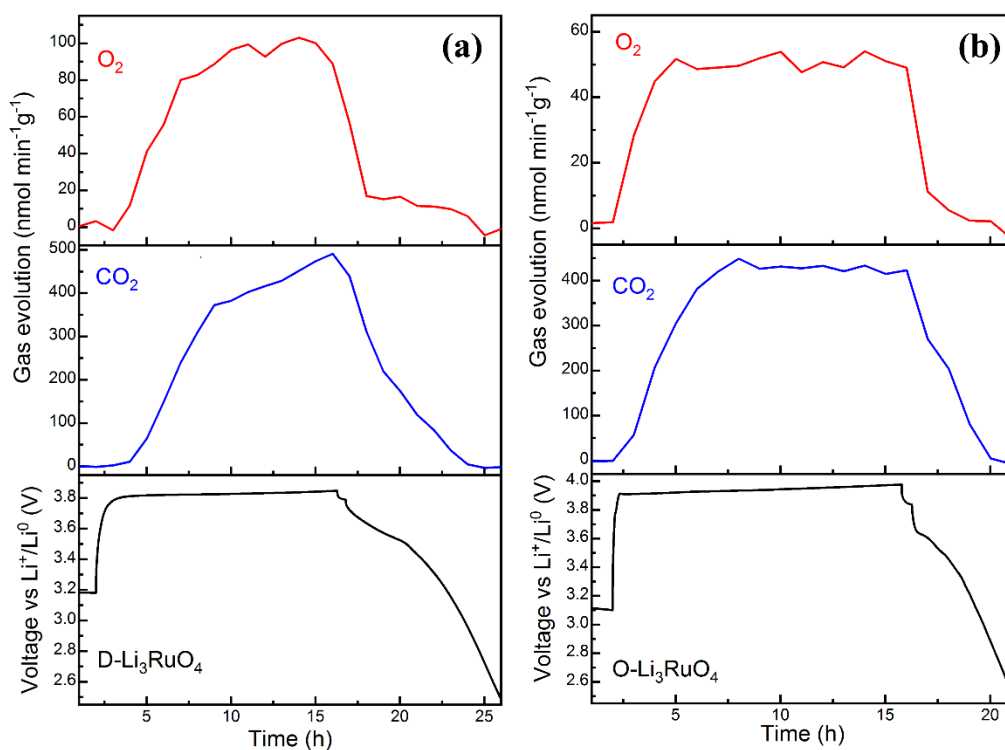


Figure 4-16. *Operando* gas evolution of D- (a) and O- (b) Li_3RuO_4 , as measured by DEMS for the first cycle.

Table 4-5. Delivered capacities and the corresponding O_2 and CO_2 evolution during the *operando* DEMS measurement.

First cycle				
	D- Li_3RuO_4		O- Li_3RuO_4	
	Charge	Discharge	Charge	Discharge
Capacity (mAhg^{-1})	205.4	131.1	200.3	69.1
Evolved O_2 (μmol)	0.42		0.30	
Evolved CO_2 (μmol)	1.98		2.43	

4.5 Voltage cutoff window of 1.5-2.5 V

4.5.1 Electrochemical properties of Li_3RuO_4

D-Li₃RuO₄ between 1.5 and 2.5 V: When a cathodic current is applied onto pristine $\text{D-Li}_3\text{RuO}_4$, reduction was centered at 1.68 V vs Li^+/Li^0 (Figure 4-17a), accumulating charge equivalent to the intercalation of 0.8 mol Li per mol compound, consistent with the hypothetical reaction (2). A small step was further observed at 1.53 V. The profile of the following oxidation process showed a pseudo-plateau at 1.71 V, denoting a very small hysteresis, especially compared with the anodic process at high potential (Figures 4-4a and 4-4b). Approximately 0.7 mol Li was reversibly cycled at 2.5 V. The profiles remained almost the same upon subsequent redox cycles, with the exception of a subtle increase in the slope of the main pseudo-plateau (Figure 4-17a), manifested in an increased broadening of the associated peak in dQ/dV (Figure 4-17b), and the disappearance of any resolved signals below 1.55 V upon reduction. The amount of charge passed decreased only slightly with cycling (Figures 4-17c and 4-17d), demonstrating a high reversibility of the redox process associated Li^+ insertion/removal.

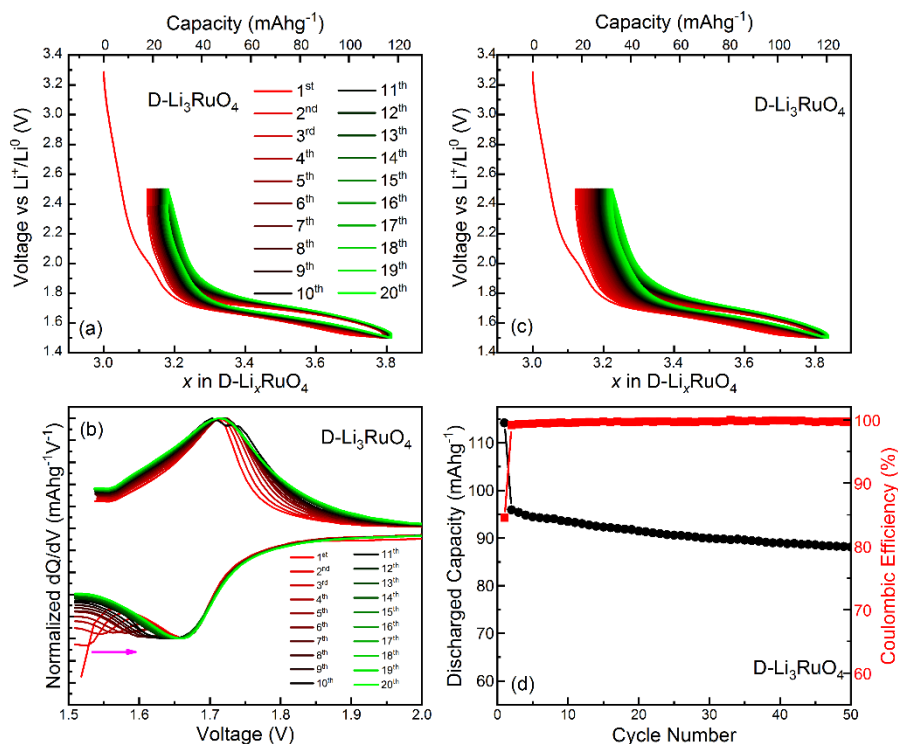


Figure 4-17. Voltage-composition profiles of D-Li₃RuO₄ between 1.5 and 2.5 V upon (a) the first 20th cycling and (c) extensive cycling. (b) Differential capacity analysis (dQ/dV) of D-Li₃RuO₄. (d) Discharge capacity and coulombic efficiency as a function of the cycle number.

O-Li₃RuO₄ between 1.5 and 2.5 V: When the initial reduction was attempted on pristine O-Li₃RuO₄ (reaction (2)), a cathodic process proceeded via a long plateau around 1.72 V (Figure 4-18a), with the corresponding charge equivalent to the insertion of more than 1.6 mol Li per mol compound. The subsequent Li⁺ removal proceeded through two processes located at 1.8 and 1.89 V (Figure 4-18b), accounting for more than 1.3 mol Li. The electrochemical profile subtly evolved with cycling. In the second cycle, the cathodic profile shows two processes, at 1.74 and 1.7 V (Figure 4-18b), reversed at 1.8 and 1.9 V upon oxidation, denoting a greater hysteresis compared to the disordered polymorph. With cycling, the two cathodic steps merged into a single pseudo-plateau centered at 1.68 V (black arrow in Figure 4-18b). In contrast, two processes remained, with an increase in slope (and width of the associated dQ/dV feature) and a slight shift toward lower potentials. The washing out of the profiles could be ascribed to an increased kinetic impediment to the reaction. The coulombic efficiency of each cycle was high (around 99.5%), but there was a progressive loss of capacity with cycling (Figures 4-18c and 4-18d). The electrochemical signals in this low potential window were typical of conventional intercalation reactions in both polymorphs.

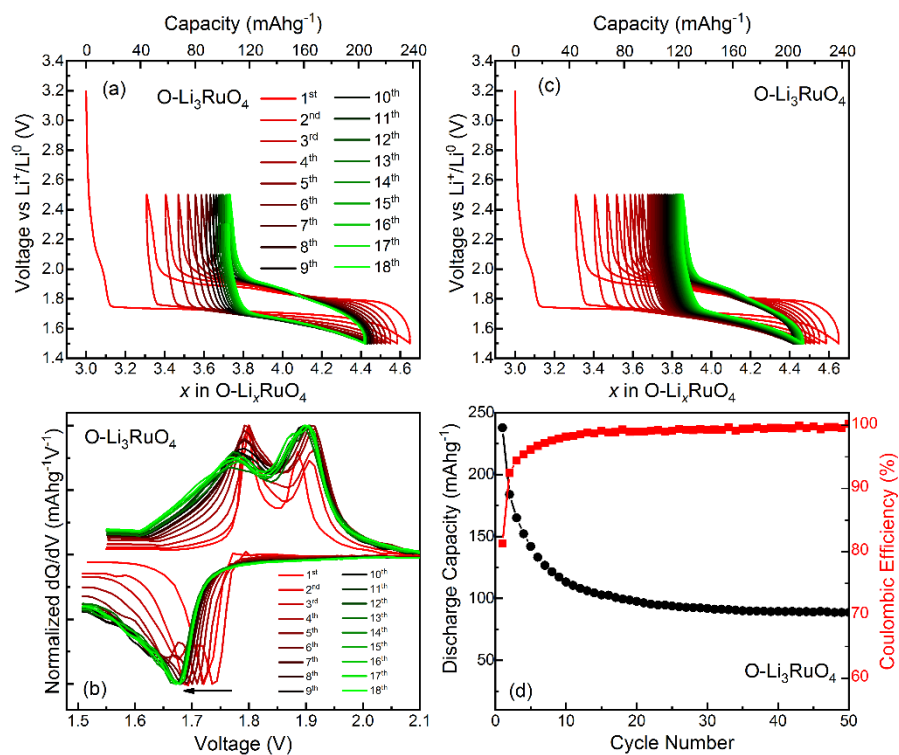


Figure 4-18. Voltage-composition profiles of O-Li₃RuO₄ between 1.5 and 2.5 V upon (a) the first 20th cycling and (c) extensive cycling. (b) Differential capacity analysis (dQ/dV) of O-Li₃RuO₄. (d) Discharge capacity and coulombic efficiency as a function of the cycle number.

4.5.2 Structural variation of Li₃RuO₄

D-Li₃RuO₄ between 1.5 and 2.5 V: The reduction of pristine D-Li₃RuO₄ to 1.5 V (reaction 2) gave rise to a pronounced shift of SXRD peak positions to lower angles, consistent with the insertion of Li⁺ into D-Li₃RuO₄, with no new reflections appearing, with the exception of a high angle tail in the most intense peak at $Q = 3.3 \text{ \AA}^{-1}$ (Figure 4-19). It also brought about peak broadening and intensity reduction in the *operando* SXRD patterns (Figure 4-20). The peak positions and intensity largely recovered via the following delithiation, indicating a reversible discharge and charge process. Pawley refinements were used to extract the corresponding cell parameters (Figure 4-21 and Table 4-6). In comparison with the lattice size of the pristine state, the reduction expanded the unit cell by 5.2% compared with the pristine state, while the following oxidation shrank the unit cell with a slightly larger volume, by 0.32%, relative to the pristine

state, indicating a small loss. Patterns collected at intermediate states during the *operando* measurement demonstrated a reversible solid solution process (Figure 4-21).

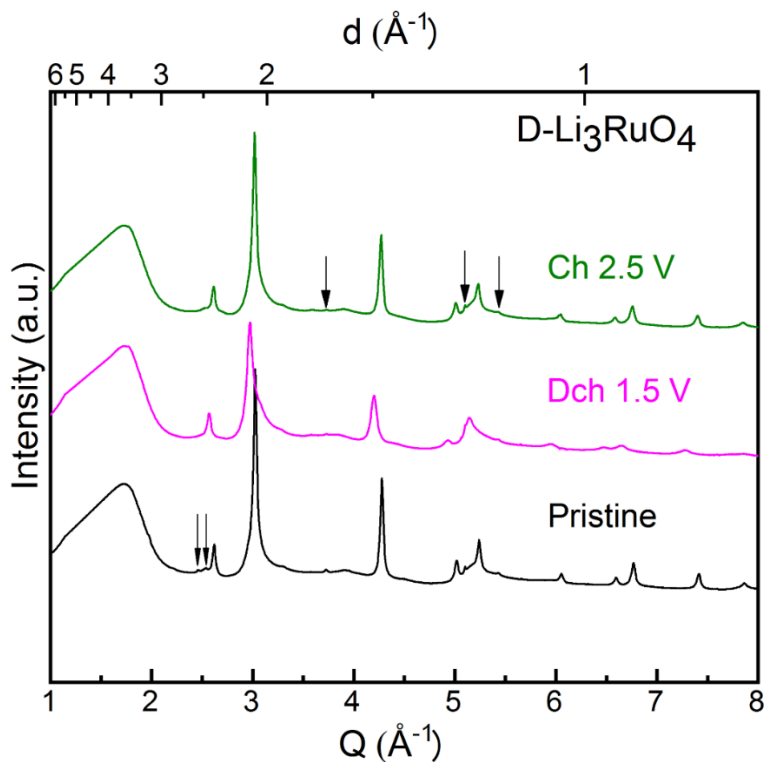


Figure 4-19. SXRD patterns of D-Li₃RuO₄ at selected points during the first cycle within a potential range of 1.5-2.5 V, collected *operando*. The complete evolution of the data is found in Figure 4-22. The black arrows denote the invariant Bragg reflections from the background only.

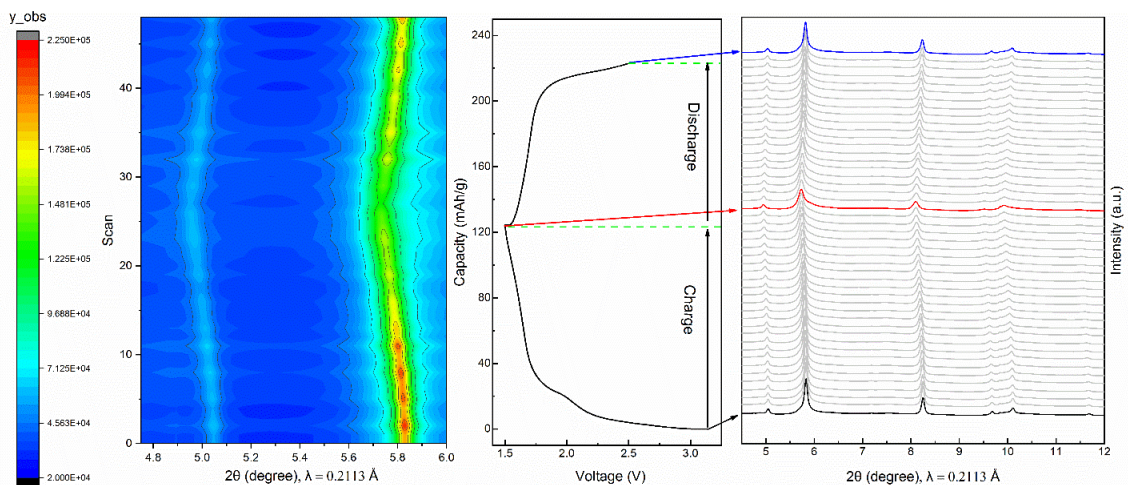


Figure 4-20. *Operando* SXRD patterns in the first cycle of a D-Li₃RuO₄/Li half-cell at a rate of C/20. The left and middle panels show the contour plot and the corresponding galvanostatic curve between 1.5 V and 2.5 V. Black, red and blue patterns represent the pristine, the fully discharged and the fully charged state, respectively.

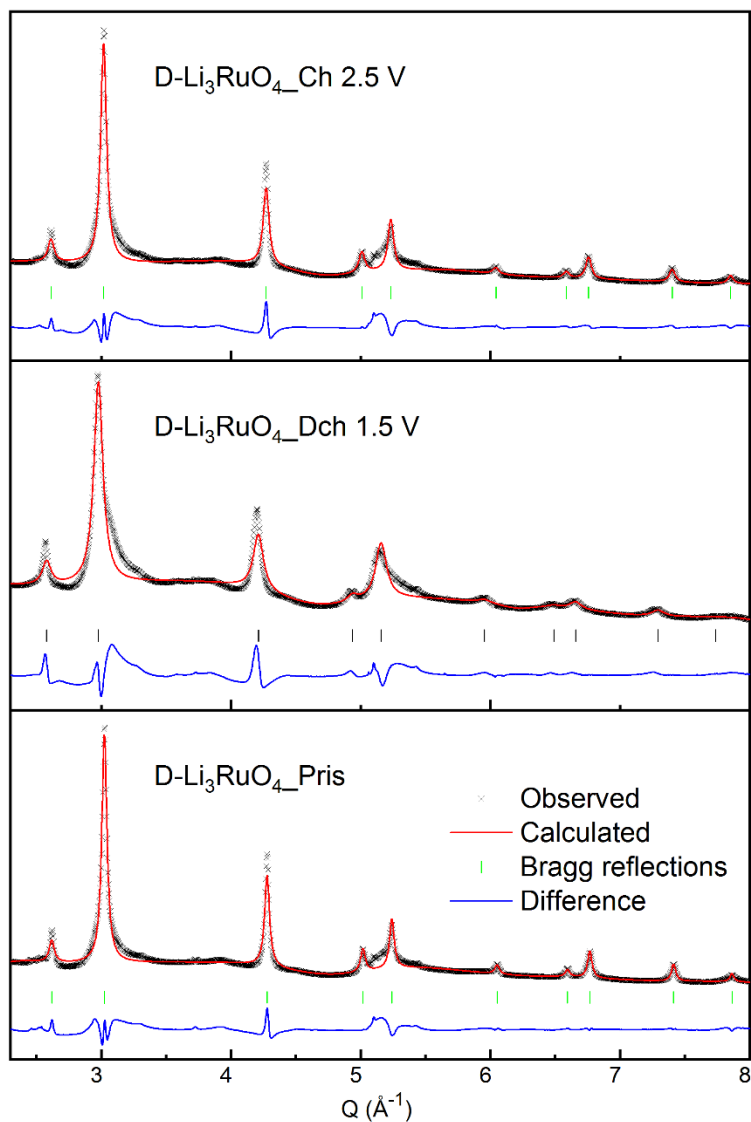


Figure 4-21. Pawley refinements of SXRD patterns of D-Li₃RuO₄ at different electrochemical states within 1.5 and 2.5 V.

Table 4-6. Calculated Unit Cell Parameters from SXRD patterns through Pawley refinement

D-Li ₃ RuO ₄		
State	a = b = c (Å)	Volume (Å ³)
Pristine	4.14927	71.436
Dch 1.5 V	4.22021	75.163
Ch 2.5 V	4.15366	71.663

O-Li₃RuO₄ between 1.5 and 2.5 V: Reduction of pristine O-Li₃RuO₄ to 1.5 V (reaction 2) resulted in a shift of the diffraction peaks towards lower angles, concomitant to a decrease in their intensities (Figure 4-22a). The final phase (Li_{4.6}RuO₄) was refined by the Rietveld refinement with a space group of P2/a, as in the pristine phase (Figure 4-22b and Table 4-7).⁹⁶ The unit cell size expanded by 18.0% in comparison with the pristine state after the reduction to 1.5 V (Figure 4-23 and Table 4-8), in good agreement with Jacquet *et al.*⁹⁶ The refinement was most satisfactory when electrochemically inserted Li⁺ ions were located in the tetrahedral sites of Li_{4.6}RuO₄, preserving ordering of Ru and Li in the metallic layer. In addition, there was a transition of the oxygen stacking from O3 type (ABCABC) to T1 type (ABAB) denoted by the large decrease in β angle with respect to the pristine state.⁹⁶ After the following oxidation process, the structure recovered to the pristine state, except for an irreversible increase in peak widths, which is most likely ascribed to cycling-induced strain and the generation of stacking faults associated with the gliding of the transition-metal layers during the otherwise reversible transformation. The process was accompanied by a smaller volume change with respect to the pristine state by 6.9% (Figure 4-23 and Table 4-8), consistent with the observation that not all capacity corresponding to intercalated Li was recovered on oxidation (Figure 4-18). According to Jacquet *et al.*,⁹⁶ the peak splitting in dQ/dV plot upon oxidation, indicated by the discontinuity in the corresponding voltage-composition profile in the vicinity of $x = 1.0$, reflected a two-phase transition.²²⁰

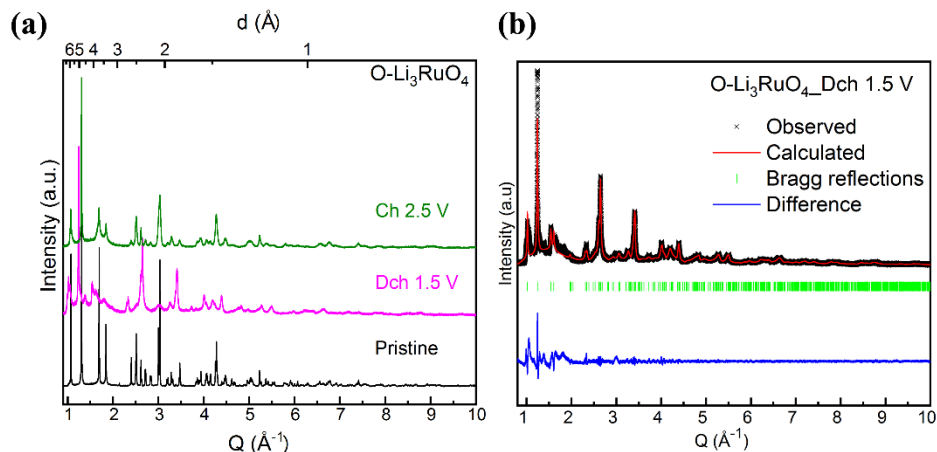


Figure 4-22. (a) *Ex situ* SXR D patterns of O-Li₃RuO₄ at different electrochemical state within the range of 1.5-2.5 V. (b) Rietveld refinement of SXR D pattern of Li_{4.6}RuO₄. The black crosses and red solid line represent the observed and calculated patterns. The green vertical tick bars denote the Bragg reflections. The blue continuous line is the difference between calculation and observation.

Table 4-7. Crystallographic parameters and reliability factors extracted from Rietveld refinement of SXR D of Li_{4.6}RuO₄.

Li _{4.6} RuO ₄						
Space group: P 2/a; a = 5.4354(4) Å; b = 6.1659(4) Å; c = 5.05606(23) Å; β = 90.650(6)°; V = 169.438(15) Å ³						
Atom	Wyckoff position	x	y	z	Uiso (Å ²)	Occupancy
O1	4g	-0.60433	0.14054	-0.74482	0.0080(8)	1
O2	4g	-0.59751	0.63175	0.75443	0.0080	1
Li3	2e	0.25000	0.898645	0.00000	0.0159	0.292
Ru4	2e	0.25000	0.898645	0.00000	0.0159(5)	0.708
Li5	2f	0.7500	0.63450	0.00000	0.0168	0.292
Ru6	2f	0.7500	0.63450	0.00000	0.0168(4)	0.708
Li7	4g	0.44111	0.09520	-0.32889	0.001	1
Li8	4g	0.47553	0.62858	-0.33087	0.001	1
R _{WP} = 10.817%; χ ² = 2.11						

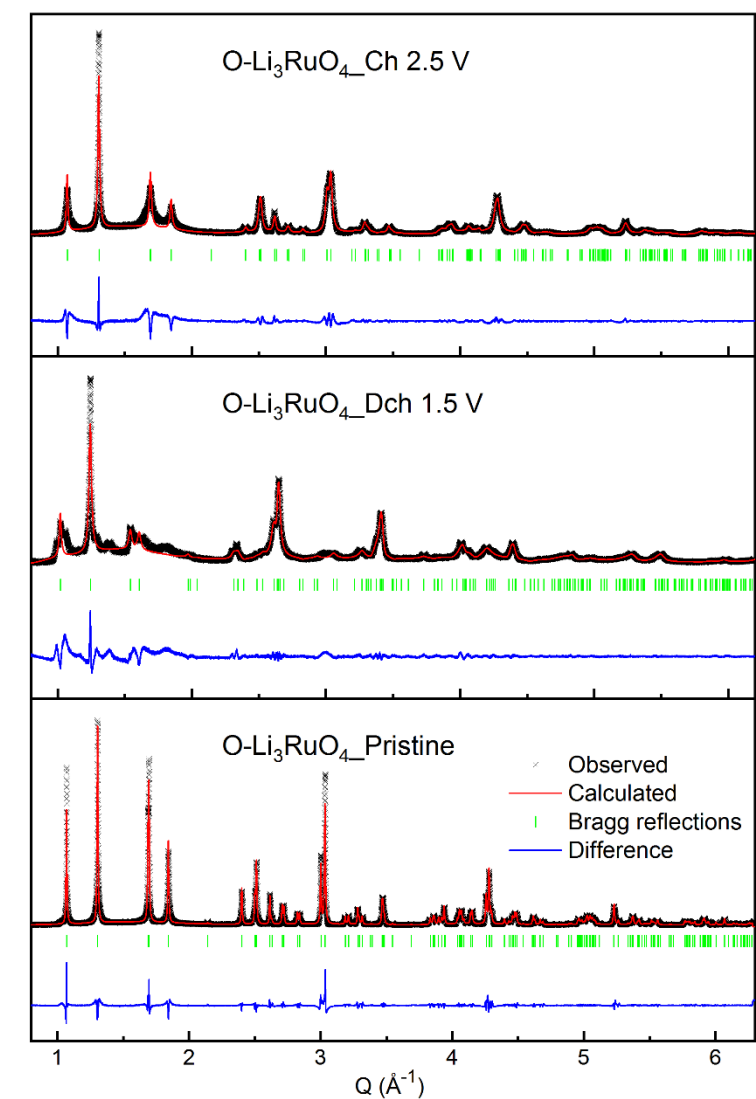


Figure 4-23. Pawley refinements of SXRD patterns of O-Li₃RuO₄ at different electrochemical states between 1.5 and 2.5 V.

Table 4-8. Calculated Unit Cell Parameters from SXRD patterns through Pawley refinement

O-Li ₃ RuO ₄					
State	a (Å)	b (Å)	c (Å)	β (°)	Volume (Å ³)
Pristine	5.08809	5.86792	5.12213	110.154	143.566

Dch 1.5 V	5.43544	6.16594	5.05606	90.6506	169.438
Ch 2.5 V	5.07882	5.85193	5.10592	110.0275	142.574

4.5.3 *Ex situ* Ru K-edge XAS of Li₃RuO₄

Reduction of D-Li₃RuO₄ to 1.5 V induced a pronounced shift of the absorption edge to lower energy by ~1.2 eV with respect to the pristine state, placing it close to RuO₂ (Figure 4-24a). The subsequent oxidation induced ~0.9 eV shift back toward higher energy, corresponding to an almost completely reversible recovery of the absorption edge (Figure 4-24a). The shift of the absorption edge to lower energy upon reduction was larger for O-Li₃RuO₄ (~2.6 eV relative to the pristine state, Figure 4-24c). The final position was even lower than RuO₂ by around 0.6 eV, suggesting the final oxidation state of Ru was less than 4+, as could be expected from a capacity corresponding to 1.6 mol of inserted Li per formula unit. Upon oxidation to 2.5 V, the spectrum shifted back to higher energy, and almost superimposed with the pristine state (Figure 4-24c), clearly demonstrating the reversibility in electronic structure of Ru, in agreement with the observed electrochemical and structural changes.

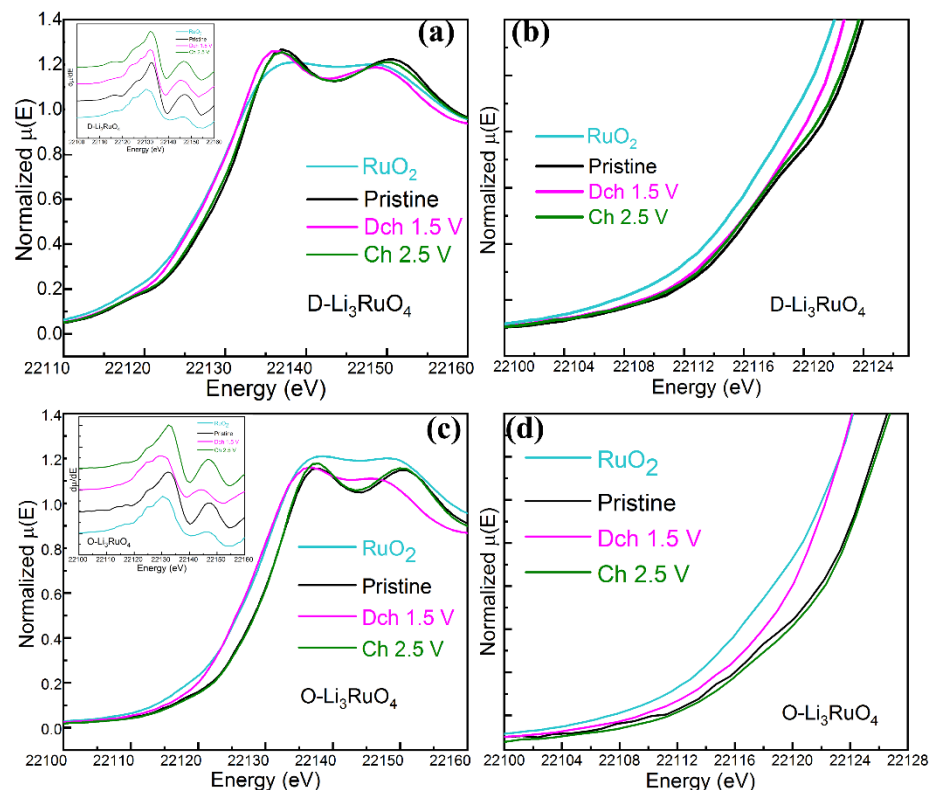


Figure 4-24. *Ex situ* Ru K-edge XANES spectra of (a) D-Li₃RuO₄ and (b) O-Li₃RuO₄ at different electrochemical states in the 1.5-2.5 V window, and (b) zoom of the pre-edge region. The insets in (a) and (c) present the corresponding derivative curves, used to define the position of the absorption edge. RuO₂ was used as reference for Ru⁴⁺.

4.5.4 *Ex situ* O K-edge XAS of Li₃RuO₄

Li⁺ intercalation induced a shift of the O K-edge absorption threshold (jump above 535 eV) in both D- and O-Li₃RuO₄ to lower energy (Figures 4-25). The reduction led to a decrease in absorption intensity below 530 eV relative to the pristine state, especially at the lowest energies, leading to a broad feature dominated by a peak centered at 529.2 eV. The loss of intensity was more pronounced with the ordered polymorph, consistent with the higher measured capacity and degree of Ru reduction. The changes reflected the reversible occupation of state above the Fermi level during lithiation without severe reorganization of the O 2p-Ru 4d hybridization orbitals. The population of bands with a notable O character would reduce

Z_{eff} , lowering the ionization threshold. The process was largely reversed upon oxidation in both compounds, indicating a high reversibility of the intercalation reaction.

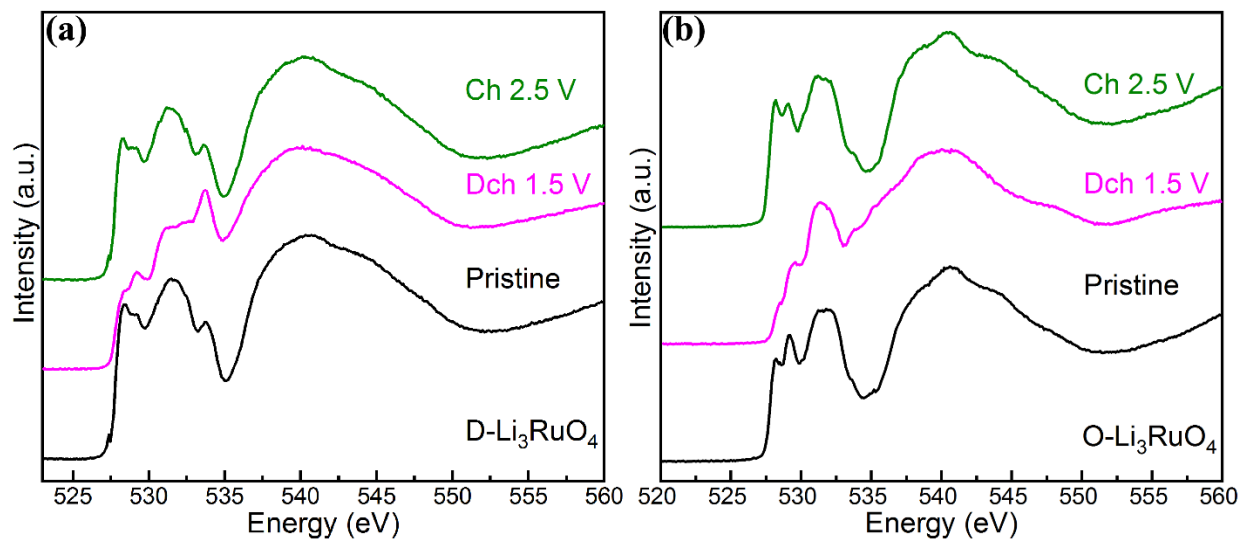


Figure 4-25. *Ex situ* O K-edge XAS spectra of (a) D- and (b) O-Li₃RuO₄ measured at different electrochemical states between 1.5 and 2.5 V.

4.6 Discussion

In this report, we comprehensively studied the intercalation chemistry of two Li₃RuO₄ polymorphs with a rock-salt framework to define charge compensation mechanisms at both metal and ligands. While some knowledge was available from O-Li₃RuO₄,^{96,97} the comparison with D-Li₃RuO₄ enriches our understanding of the effect of crystallographic order, which is a design knob explored in recent research.⁸² Both compounds are capable of undergoing oxidation reactions above 3 V or reduction to 1.5 V from their pristine state, revealing a rich redox chemistry and varying degrees of reversibility. A visual summary is presented in Figure 4-26.

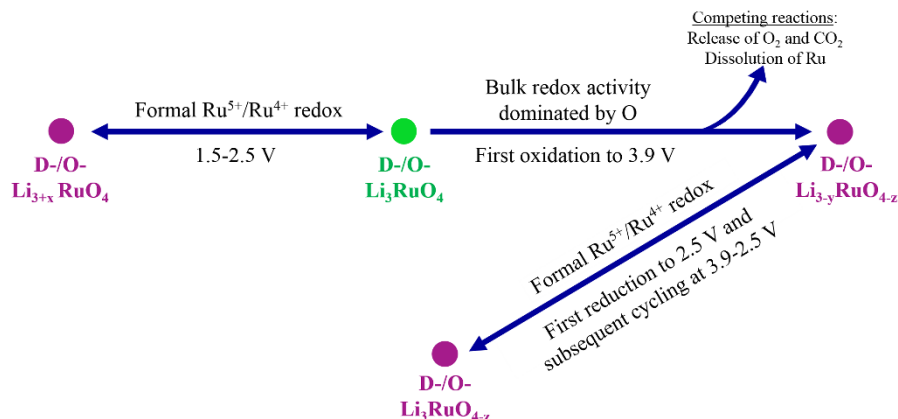


Figure 4-26. Schematic summary of the electrochemical reactions of Li_3RuO_4 systems observed in this study.

Reactions within the 1.5-2.5 V window. We start discussing the electrochemical reaction observed when Li_3RuO_4 was cycled in the voltage window of 1.5-2.5 V because of its simplicity. XAS results reveal in the electrochemical cell the induced reduction of Ru from an initial +5 to a final +4 formal state in the disordered polymorph, and even lower states for the ordered phase, as was also observed by Jacquet *et al.*⁹⁶
⁹⁷ This behavior is accompanied by a commensurate decrease in the density of unoccupied states just above the Fermi level with an O 2p-Ru 4d contribution. Therefore, both Ru and O contribute to the states that accommodate the injected electrons. The fact that no new states were observed in the O 2p-Ru 4d states indicates similar Ru-O interactions, with perhaps the exception of a slight decrease in covalency of the bond. This observation is supported by the topotactic change in crystal structure and the absence of obvious deviations from an octahedral coordination of Ru by O ligands.⁹⁷ The reaction was chemically reversible, with the compound returning close to the pristine state upon re-oxidation, and energy efficient, measured by a combined high coulombic efficiency and low hysteresis in potential. All these characteristics correspond to a conventional mechanism of interaction of lithium:¹⁵



Where charge compensation is assigned based on the changes in the formal oxidation state of the metal as

proxy for states with participation of both metal and O due to the high covalency of these compounds. There were only slight differences in the reversibility of the two polymorphs, with the disordered polymorph showing lower losses in capacity upon many cycles. This disparate behavior likely stems from the different reaction mechanisms: solid solution for D-Li₃RuO₄, and as reported by Jacquet *et al.* multiphasic for O-Li₃RuO₄.⁹⁶ These different mechanisms will also lead to differences in kinetic barriers to the transformation, providing an explanation to the different degrees of hysteresis in potential, likely due to polarization.

Reactions during the first oxidation to 3.9 V. During this first oxidation, the reactions were not conventional, yet fundamentally the same in both polymorphs. The measured capacities were large, especially in D-Li₃RuO₄, in a faradaic process that changed the bulk structure of the oxide in a seemingly topotactic manner, consistent with Li deintercalation, according to XRD (Figures 4-6 and 4-9a). The increase in the unit cell volume may be due to the increased electrostatic repulsion between transition metal clusters that are less screened because of the Li⁺ removal. Yet only small apparent changes were observed by XAS in the electronic state of Ru in the oxidized phase (Figure 4-11 and 4-12), especially in comparison with the notable reorganization of the O 2*p*-Ru 4*d* states probed by the pre-edge features in the O K-edge spectra (Figure 4-14). Furthermore, the onset position of the absorption edge of O shifted to higher energies, indicative of a greater Z_{eff} , which decreases the O 1*s* orbital binding energy so as to increase the transition energy to O 2*p* and ionization.^{215, 221} Therefore, Li deintercalation was accompanied by changes in electronic structure of the solid oxide that heavily involved changes at the O ligands, including depletion of their charge.

The overall oxidation process also involved the evolution of O₂ and CO₂ at the onset of the oxidation in our experiments (Figure 4-16), possibly indicating the robust surface activity. The fact that spectral signals associated with Li₂CO₃ persisted throughout oxidation (Figure 4-15) suggests that CO₂ does not primarily arise from decomposition of these solid impurities, consistent with observations of its redox potential in the literature.²¹⁸ Recently, an interfacial mechanism was proposed by Jacquet *et al.* whereby Ru ions could be oxidized and then partially dissolved, after removing Li from O-Li₃RuO₄, in the form of

soluble RuO_4 and RuO_4^- species, leading to black coloring, which could react with the electrolyte and release CO_2 .⁹⁷ This mechanism could also explain the observation of the black color on the surface of the separator after disassembling the coin cell after charging $\text{O-Li}_3\text{RuO}_4$ to 3.9 V (Figure 4-27), despite the relatively small capacity compared to the disordered polymorph. However, soluble RuO_4 and RuO_4^- species should not be detectable in our XAS experiments, which were collected on washed solid electrodes, especially considering the detection modes used in all cases.

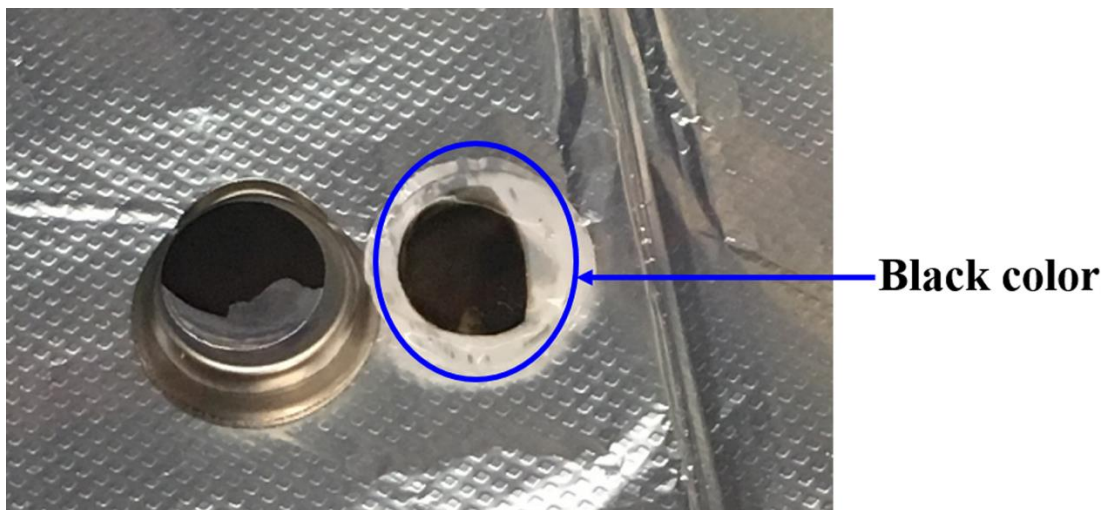
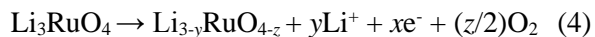


Figure 4-27. Image of a coin cell after the removal of 0.5 mol Li from per mol $\text{O-Li}_3\text{RuO}_4$. Clear black color can be observed on the otherwise white separator.

Taking all these facts together, the following reaction could be postulated



Where $y = x + 2z$, reflecting both the loss of O from the lattice ($z \sim 0.05\text{-}0.1$ based solely on the evolution of O_2) and the charge compensation at lattice O. Formal charges are challenging to ascribe, since both Ru and O underwent spectroscopic changes, albeit much more pronounced in the latter case. Indeed, XAS clearly points at a strong increase in the contribution of O to states above the Fermi level from Li_3RuO_4 to $\text{Li}_{3-y}\text{RuO}_{4-z}$. While the RuO_6 octahedron is reported to distort during the first oxidation, no structural evidence is available of the existence of O-O interactions,⁹⁷ which is primarily a structural feature that

cannot be probed by XAS unless other information is available.²²²

This reaction competes with deleterious Ru dissolution and electrolyte decomposition. Dissolution is not constant during charging, depending on the actual amount of electrons extracted from the material. Using data provided by Jacquet *et al.*,⁹⁷ we estimate that the oxidation of O-Li₃RuO₄ in our conditions (Figure 4-5) led to less than 5% loss of mass because the capacity never exceeded the equivalent of 1 mol Li per mol oxide. In contrast, the capacity D-Li₃RuO₄ was equivalent to 1.9 mol Li per mol oxide. No data on dissolution is available for this polymorph, but it is reasonable to assume that the trends for O-Li₃RuO₄ reported by Jacquet *et al.* are a good approximation. At this level of oxidation their data would predict a ~15-20% loss of mass of the active material, which would account for 0.375-0.5 mol electrons out of a total of ~1.9 mol electrons extracted. All in all, the data from Jacquet *et al.* support that the bulk process is dominant in our experiments.

Reactions during the first reduction from 3.9 V to 2.5 V, and subsequent cycling. The existence of irreversible interfacial reactions contributed to the coulombic inefficiency observed in the first oxidation-reduction cycle of both polymorphs. Nonetheless, there was significant electrochemical and structural activity above 2.5 V upon subsequent reduction. Since pristine Li₃RuO₄ would not intercalate Li at these potentials (*vide supra*), this behavior further confirms the deintercalation of Li upon oxidation. Consistent with an intercalation reaction, the rock-salt structure was found to shrink back toward the initial volume. However, this reaction did not restore either the Ru K-edge or O K-edge XAS spectrum for the pristine state. Indeed, clear reduction of formal Ru⁵⁺ to Ru⁴⁺ occurred, as indicated by the shift of the Ru K-edge. If the electrode was discharged all the way to 1.5 V, the Ru K-edge appeared at even lower energies than Li_{3+x}RuO₄ formed directly via reaction 3 (Figures 4-28 and 4-29).

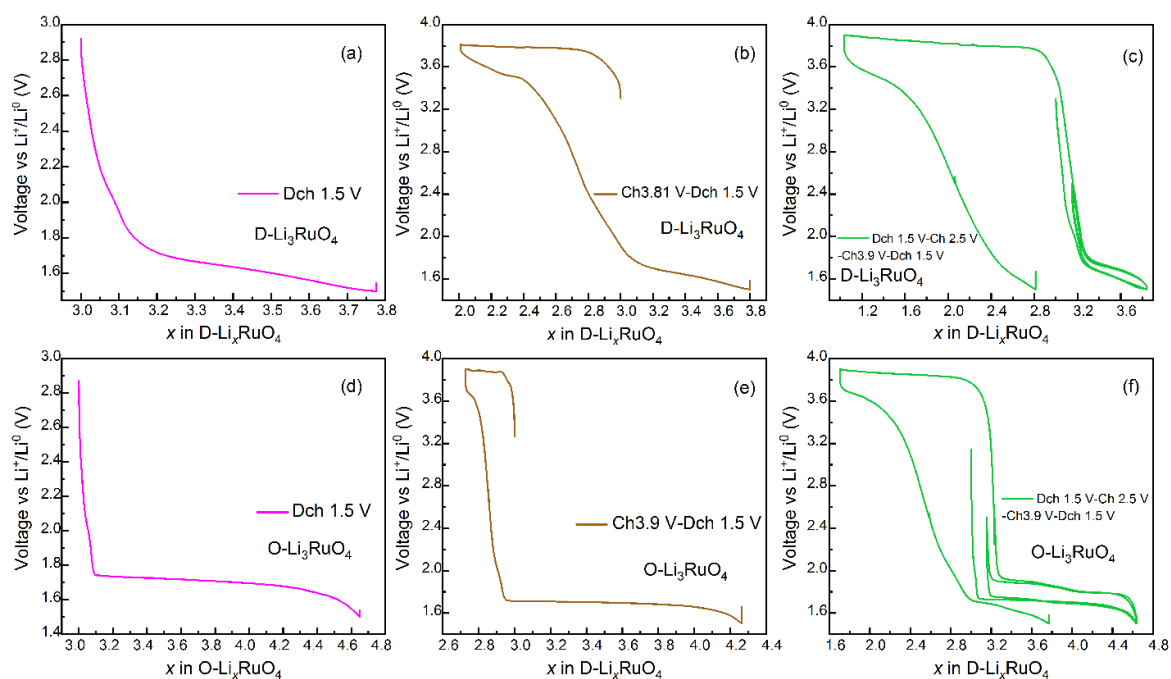


Figure 4-28. Voltage-composition profiles of (a-c) D-Li₃RuO₄ and (d-f) O-Li₃RuO₄ at different states of charge. (a) and (d) directly discharged to 1.5 V, (b) charged to 3.81 V and discharged to 1.5 V, (e) charged to 3.9 V and discharged to 1.5 V, (c) and (f) cycled between 1.5-2.5 V and then charged to 3.9 V and discharged to 1.5.

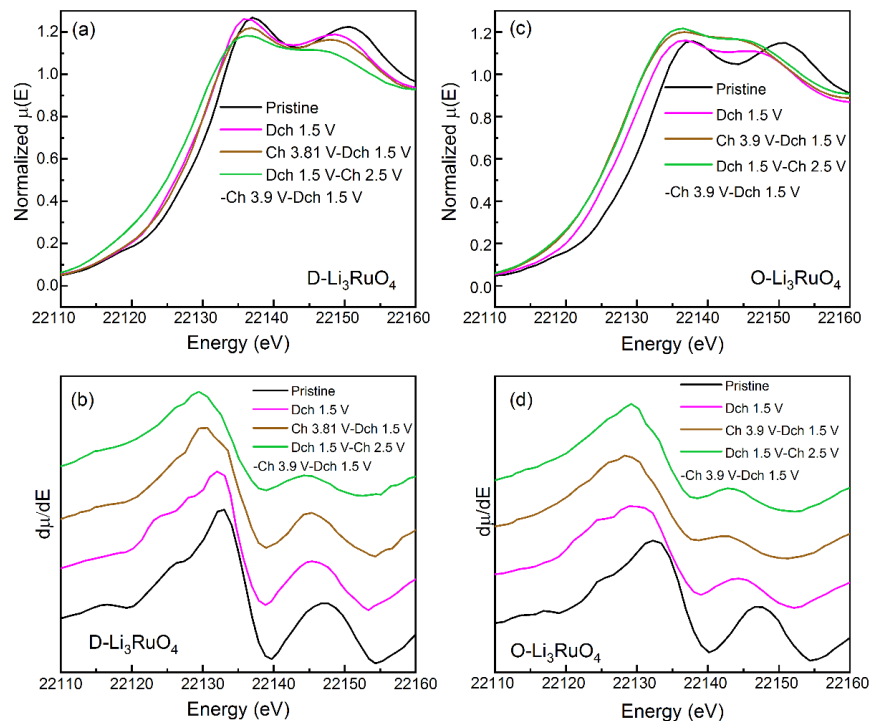


Figure 4-29. *Ex situ* Ru K-edge XANES spectra of (a) D-Li₃RuO₄ and (c) O-Li₃RuO₄ electrodes in Figure 4-27, compared to the pristine state, with the corresponding 1st derivative curves in (b) and (d).

The different pathway of changes in electronic state during oxidation-reduction are consistent with the large hysteresis in the electrochemical profile of the first cycle. Although no specific analysis was made, we observed that measurements of Ru by Jacquet *et al.* also revealed different pathways during the first cycle,⁹⁷ where equal electrode capacities led to notably greater Ru participation during reduction than oxidation. The prominent decrease in the population of unoccupied O 2*p*-Ru 4*d* states in O K-edge XAS, especially at the lowest energies, would also be in good agreement with the Ru⁵⁺/Ru⁴⁺ formal redox couple. This conclusion is reinforced by the comparison of both the Ru K-edge and the pre-edge part in the O K-edge TFY spectrum between the first reduction from 3.9 to 2.5 V and the initial reduction from pristine to 1.5 V, which revealed a strong similarity in the spectra (Figures 4-30, 4-31 and 4-32), suggesting similar electronic changes in both cases. However, it is important to emphasize that the crystal structure of these two reduced state is different, as can be most clearly seen for the ordered polymorph by comparing “Dch

2.5 V Max Cap” in Figure 4-9b with “Dch 1.5 V” in Figure 4-23. Therefore, overall, the reactions happening are different in both potential ranges.

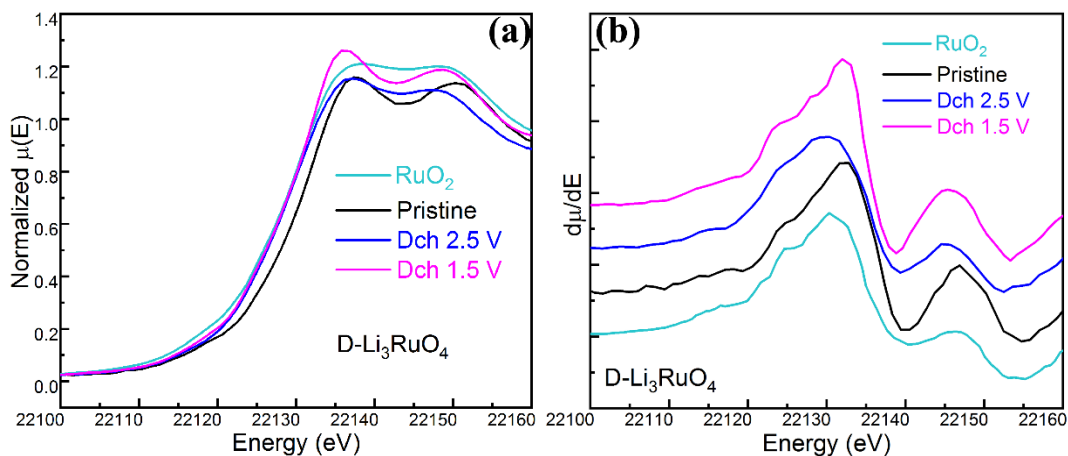


Figure 4-30. Comparison of *ex situ* Ru K-edge XANES spectra of D-Li₃RuO₄ in different electrochemical state and (b) corresponding derivative curves.

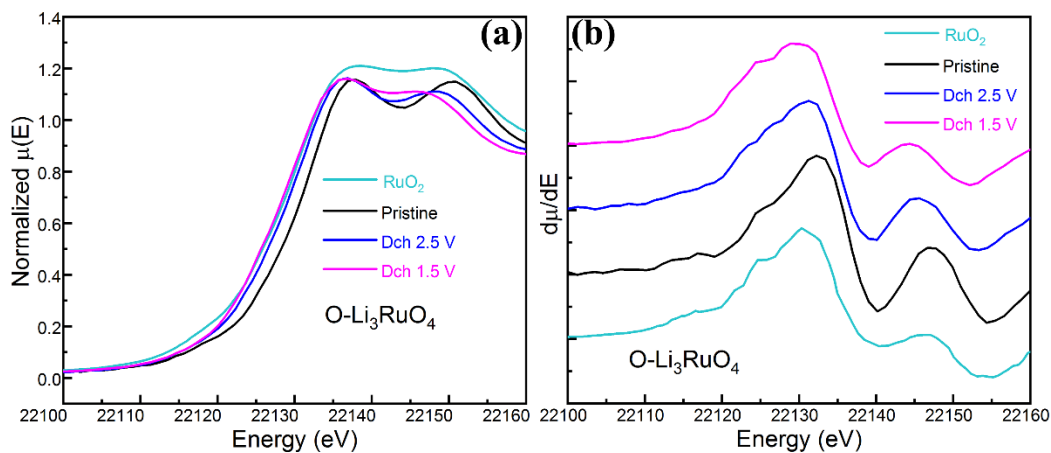


Figure 4-31. Comparison of *ex situ* Ru K-edge XANES spectra of O-Li₃RuO₄ in different electrochemical states and (b) corresponding derivative curves.

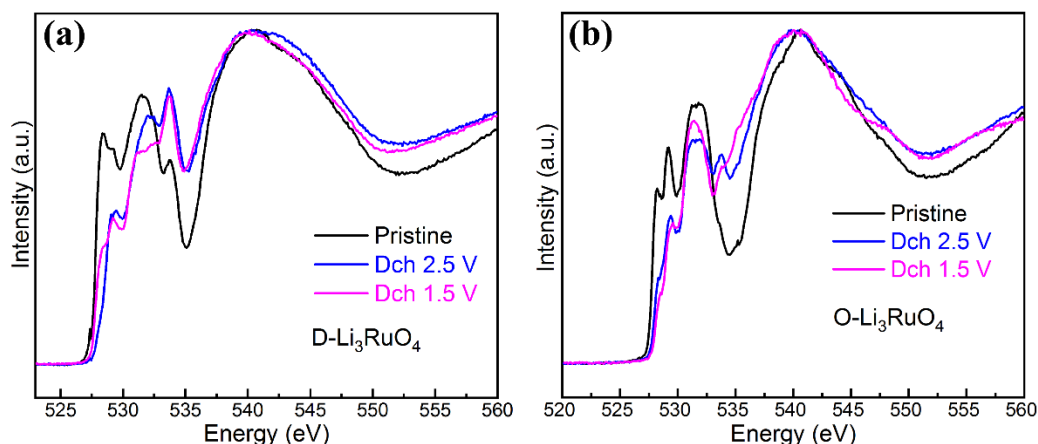
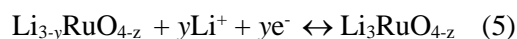


Figure 4-32. Overlaid *ex situ* O K-edge XAS spectra of (a) D- and (b) O-Li₃RuO₄ measured at different electrochemical states. See text for discussion.

The changes at both O and Ru in O-Li₃RuO₄ during the first cycle were very similar with the cycle at which the highest electrochemical activity was achieved. In other words, while the first oxidation was chemically irreversible, subsequent cycling proceeded through the same Ru-O couples. Therefore, the following mechanism is postulated to operate upon the first reduction to 2.5 V:



This mechanism corresponds to a conventional intercalation reaction centered on the formal state of the transition metal, which again, in reality, reflects the covalence of the Ru-O bond. It is important to note that this change in mechanism was accompanied by a significant decrease in hysteresis of the voltage profile, to a degree reminiscent of conventional intercalation reactions. Indeed, the changes in the XRD patterns of O-Li₃RuO₄ were more pronounced upon activation than in the first cycle, but they appeared topotactic in nature. This behavior is ascribed to a progressive activation of a larger portion of the electrode as cycling proceeded, indicating that the first oxidation was limited by sluggish kinetics. The much smaller O₂ release in the second cycle, compared with the first is in agreement with both the proposed mechanism and the progressive activation of pristine domains upon cycling (Figure 4-33 and Table 4-9).

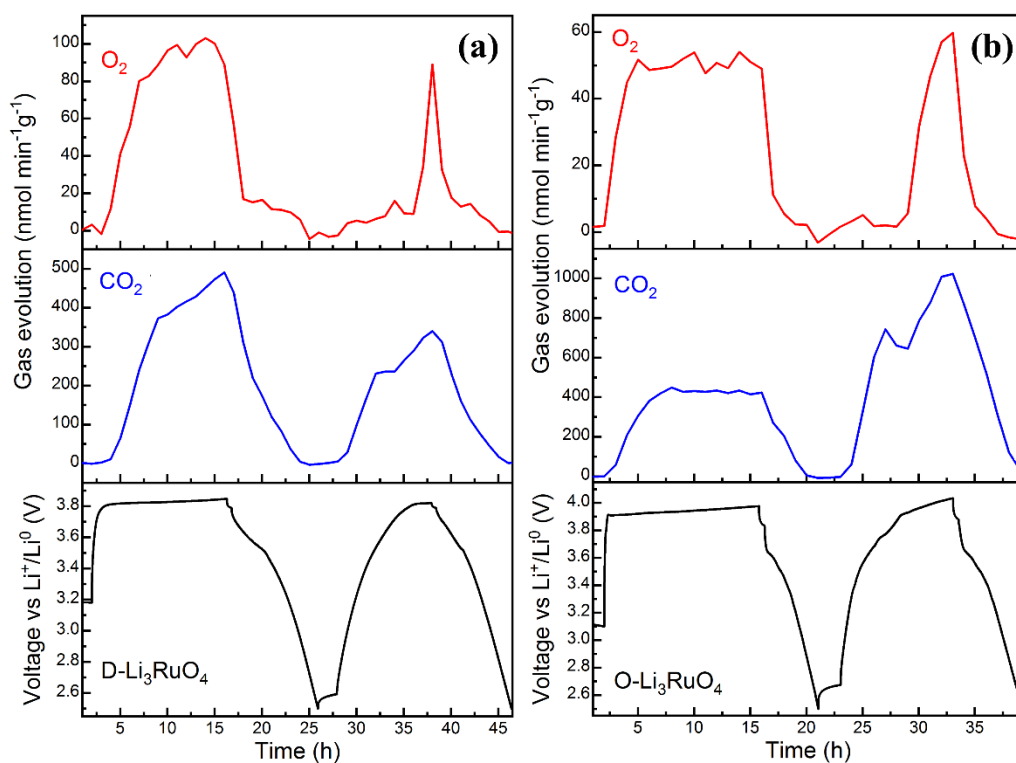


Figure 4-33. Gas evolution during the first two cycles of D- (black line) and O- (red line) Li_3RuO_4 measured by *operando* DEMS. The voltage profiles are shown in the bottom panels.

Table 4-9. Delivered capacities and the corresponding O_2 and CO_2 evolution during the *operando* DEMS measurement.

Second cycle				
	D- Li_3RuO_4		O- Li_3RuO_4	
	Charge	Discharge	Charge	Discharge
Capacity (mAhg^{-1})	143.7	114.3	145.3	81.9
Evolved O_2 (μmol)	0.09		0.10	

Evolved CO ₂ (μmol)	1.13	3.94
--------------------------------	------	------

Upon extensive cycling, both polymorphs displayed a quite different trend in performance, with a continuous decay from a very high to a low capacity for D-Li₃RuO₄ (Figure 4-4), compared to a sustained electrochemical activation for O-Li₃RuO₄ until its highest electrochemical reactivity was equivalent to the cycling of 1 mol Li per mol Li₃RuO₄ (Figure 4-5). The faradaic yields are expected to be high at this point in the reaction, since XAS reveals cycling between Ru⁵⁺ and Ru⁴⁺, a 1 e⁻ process. In comparison with the report by Jacquet *et al.* that oxidation of O-Li₃RuO₄ to 4.2 V could remove around 3 mol Li, but led to an irreversible change in the lattice,⁹⁶ the solution was to limit the voltage (decrease the capacity) to stay in a range of structural stability. The large removal of Li from D-Li₃RuO₄ upon the first oxidation to the same potential as O-Li₃RuO₄ could be an indication of better kinetics due to the enhanced diffusion due to improved percolation of active Li diffusion channels in a disordered rock-salt.⁸² Indeed, it is possible that the very high capacity reached for D-Li₃RuO₄ in the first cycle was detrimental to its cycling stability because more dissolution of Ru would be expected at these capacities. Indeed, experiments where the first charge capacity was further limited yielded a similar evolution in voltage profile as O-Li₃RuO₄, with an increase in cycling stability (Figure 4-34).

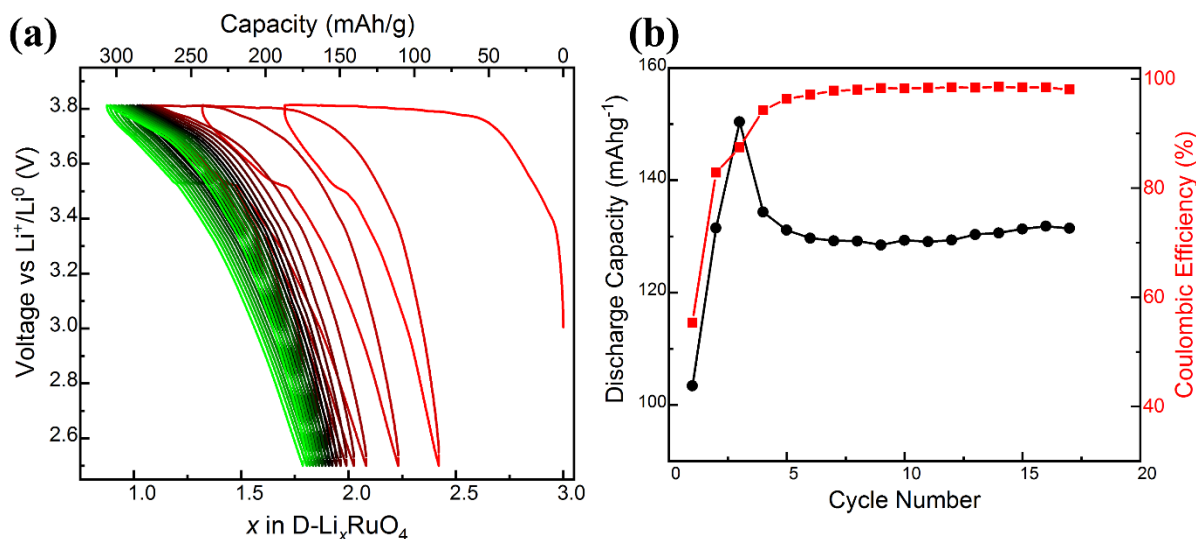


Figure 4-34. (a) Evolution of the voltage-composition profile upon cycling of a D-Li₃RuO₄ electrode, when the first charge capacity was limited to 1.25 mol Li extracted; (b) Discharge capacity and coulombic efficiency as a function of the cycle number.

It is striking that the same formal redox couple (Ru⁵⁺/Ru⁴⁺) could be accessed at two very different potentials, 3.7-3.8 V vs. ~1.8 V. The difference appears to be rooted in the role of crystal structure in defining the chemical potential of Li in each structure, Li₃RuO_{4-z} vs. Li_{3+x}Ru^{(5-x)+}O²⁻⁴, respectively. Whereas Li would be expected to (de)intercalate (from) into octahedral sites in the former, the excess of Li (*x*) in the latter stuffs the rock-salt framework, leading to the introduction of Li in tetrahedral sites. The different relative location of cations in the structure in both cases is hypothesized to be a stronger driver than the formal redox couple in this system. This behavior is reminiscent of LiMn₂O₄, a classical battery material with a spinel structure. It undergoes removal of Li from tetrahedral sites at ~4 V to form Mn₂O₄, whereas insertion of Li at 2.9 V displaces all alkali metal cations to octahedral sites to form Li₂Mn₂O₄.²²³ The formal Mn³⁺/Mn⁴⁺ couple is involved in both cases, but it is worth noting the smaller difference in potential (1.1 V) compared to Li₃RuO₄ here (~2 V), and the fact that different metal centers are involved in each process, as the initial material contains both Mn³⁺ and Mn⁴⁺.

4.7 Conclusion

Two rock-salt polymorphs of Li₃RuO₄ were successfully synthesized with disordered and ordered Li/Ru arrangements. Synchrotron diffraction and X-ray absorption spectroscopy were employed to define the changes in crystal and electronic structure when Li was cycled from the structure. Between 1.5 and 2.5 V, both polymorphs undergo a conventional, reversible reaction of Li intercalation compensated by the formal Ru⁵⁺-Ru⁴⁺ couple via O 2*p*-Ru 4*d* hybridization. Greater reversibility and stability was observed for the disordered compound due to its solid-solution mechanism. When Li₃RuO₄ is oxidized to 3.9 V instead, charge compensation follows an unconventional mechanism with much more noticeable changes in the O than Ru states, accompanied by competing irreversible, yet minor O₂ loss and Ru dissolution. When this oxidized state is reduced to 2.5 V and subsequently cycled, a reversible topotactic intercalation takes place,

with the charge compensation following a conventional redox process through the formal $\text{Ru}^{5+}\text{-Ru}^{4+}$ couple. This process reduces irreversibility compared to the first charge, leading to stable cycling, especially in the ordered polymorph. Overall, the combined study comprehensively demonstrates the complex intercalation chemistry of Li_3RuO_4 and the significance of the Ru-O covalency in compensating the associated electrochemical changes. This compound can access the formal $\text{Ru}^{5+}\text{-Ru}^{4+}$ couple at two very different potentials, an unusual occurrence in solid state chemistry. In turn, the chemical irreversibility of the reaction of Li deintercalation to 3.9 V, to directly access O states, highlights the challenge of efficiently using this reactivity in an electrochemical device without capacity loss or hysteresis. This fundamental study offers new light into our ability to tap the chemical bond in solids to conduct electrochemical reactions that have significance to energy storage with high energy density.

Chapter 5 Resolving oxygen contribution to charge Compensation in lithiation reactions of Li_3IrO_4

The content of this chapter is based on a submitted manuscript “Elucidation of active oxygen sites upon delithiation of Li_3IrO_4 ”.

5.1 Introduction

In a bid to disrupt the constraints of the formal TM redox, researchers have sought to tap into the redox activity of the oxide anions with layered oxides showing an over-stoichiometry of Li, $\text{Li}[\text{Li}_x\text{TM}_{1-x}]\text{O}_2$, which display capacities approach 300 mAhg^{-1} while undergoing topotactic transformations.^{57, 70, 224-226} This vertical step in performance is proposed to stem from a combination of formal redox activity of the transition metals (“cationic redox”, CR, through *TM* nd-O 2p mixed states) and participation of non-bonding states of O (commonly termed as “lattice O redox”, LOR, to imply “O-only”).^{131, 227} The most reversible cases of LOR involve heavy metals, such as Ir,^{74, 78, 98} which are not viable for use in a battery cathode. However, they could be valuable model systems to understand the triggers and mechanisms of LOR to design materials containing base metals which can achieve high capacity for charge storage in a highly efficient and reversible manner.

The most striking LOR activity has been achieved with Li_3IrO_4 (equivalently, $\text{Li}[\text{Li}_{1/2}\text{Ir}_{1/2}]\text{O}_2$), which exhibits reversible cycling of 2 mol Li at high potential, in a reaction that produces a high-valent redox compound, but cannot be explained by conventional CR, according to spectroscopic measurements.⁹⁸ As a result, Li_3IrO_4 shows the highest extent of LOR per mol *TM* of any known compound. However, the key reasons that make Li_3TMO_4 in general, and Ir in particular, so special remain to be fully elucidated. Prior evidence indicates that no out-of-plane migration of Ir occurs in Li_3IrO_4 ,⁹⁸ in accordance with its low driving force in a layered structure.¹²² The TM layer in Li_3TMO_4 tends toward zig-zag ordering of LiO_6 and TMO_6 chains of octahedra, an anisotropy that generates different O sites. The number of holes per O site is a critical parameter that defines this reactivity and its reversibility.²²⁸ Therefore, it is important to experimentally ascertain whether key states can explain the ability to undergo LOR.

Here, we follow the changes and reversibility of O in the high-valent states reached via deintercalation of Li_3IrO_4 using a combination of experiments and computations already described in Chapter 2. In particular, we focus on O K-edge X-ray absorption and O K α X-ray emission spectroscopy (XAS and XES), including resonant inelastic X-ray scattering (RIXS), with bulk penetration,^{86, 117, 131, 142, 146, 177, 211, 229, 230} complemented with magnetic measurements. The findings solidify our understanding of the triggers of unconventional, yet chemically reversible ligand reactivity transcending the classical paths involving covalent *TM*-O, which should be applied to the design of a broad class of oxides that cross the frontier of current Li-ion battery cathodes.

5.2 Experimental methods

Li_3IrO_4 was prepared by our collaborators at the Collège de France via a same procedure already reported in the literature.⁹⁸ The methods of sample preparation can be found in Chapter 2.

Details about the characterization methods can also be found in chapter 2. Magnetism was measured through a SQUID magnetometer by our collaborators at the Collège de France. Spin-polarized density functional theory (DFT) calculations for structural relaxation and electronic structures were performed in VASP by our collaborators at the University of Montpellier (France). The XAS spectra were computed for all structures using the OCEAN code.^{189, 190}

5.3 Results

5.3.1 Electronic structure and electrochemistry of Li_3IrO_4

This article combines data from XAS/XES (Figure 5-1) and magnetic measurements (Figure 5-2), all of which probe the electronic structure centered at O 2p and Ir 5d states. Computational analysis probed the changes in electronic structure and quantitatively related them to the XAS. The O K-edge XAS of pristine Li_3IrO_4 (Figures 5-1c) exhibits three distinct features centered at 527.9, 529.1, and 531.7 eV below 535 eV, corresponding to transitions to unoccupied O 2p-Ir 5d hybridized states, and the broad features above 535 eV arising from O 2p-Ir 6s, p states and the multiple scattering events upon photoionization. The spectrum

was measured in partial fluorescence yield (PFY) to maximize signals from the interior of the electrode because the surface signals (total electron yield, TEY) were dominated by a peak at ~533.7 eV (Figure 5-3) ascribed to Li_2CO_3 impurities due to the transition to π^* ($\text{C}=\text{O}$) orbitals.²¹⁷ These samples showed a notable sensitivity to air, with batches where contamination was enough to produce these signals, albeit at much lower relative intensity, even in fluorescence yield measurements (total fluorescence yield, TFY, Figure 5-3).

The O pre-edge (<535 eV) signals reflect a splitting of the O 2*p*-Ir 5*d* states in a distorted octahedral ligand field, with π and σ interactions appearing below and above 530 eV, respectively. These interactions would give rise to t_{2g} and e_g states, respectively, in an undistorted octahedral field, so they will be labelled as such for brevity hereafter. The qualitatively lower pre-edge intensity below than above 530 eV reflects the ratio of unoccupied states in the low-spin d^4 configuration of Ir(V) and, possibly, differences in the extent of overlap between Ir 5*d* and O 2*p* states. Indeed, measurements of zero-field cooled magnetization between 25 and 300 K showed a weak paramagnetic behavior with $\mu_{\text{eff}} = 0.84 \mu_B/\text{Ir}$ (Figure 5-2), similar to other Ir(V) phases in the literature^{231, 232} and consistent with previous EPR measurements.⁹⁸

The additional splitting observed in the O pre-edge regions, around 1.2 eV, appeared to be beyond the range expected from spin-orbit coupling, which has been reported as frustrated in other Ir(V) oxides.²³² Its origin was probed by X-ray emission spectroscopy (XES) through selective excitations at 527.85 and 529.05 eV (Figure 5-1b). XES generally probes transitions from occupied O 2*p* states to fill the 1*s* core-hole. Excitation at 529.05 eV induced a blueshift of 0.6 eV on the main emission peak compared to 527.85 eV, accompanied by a broadening of the shoulder at higher energy (Figures 5-1b and 5-4). This behavior was consistent with the existence of two different non-equivalent sites for O in the crystal structure, connected to two and one distorted IrO_6 octahedra.⁹⁸ The blueshift was much smaller than the splitting of the two corresponding pre-edge peaks, reflecting a different core-hole screening for the two non-equivalent O sites. Excitations at higher energy did not substantially change the emission features, except for subtle shifts reflecting the balance between exciting two O sites with different binding energy.

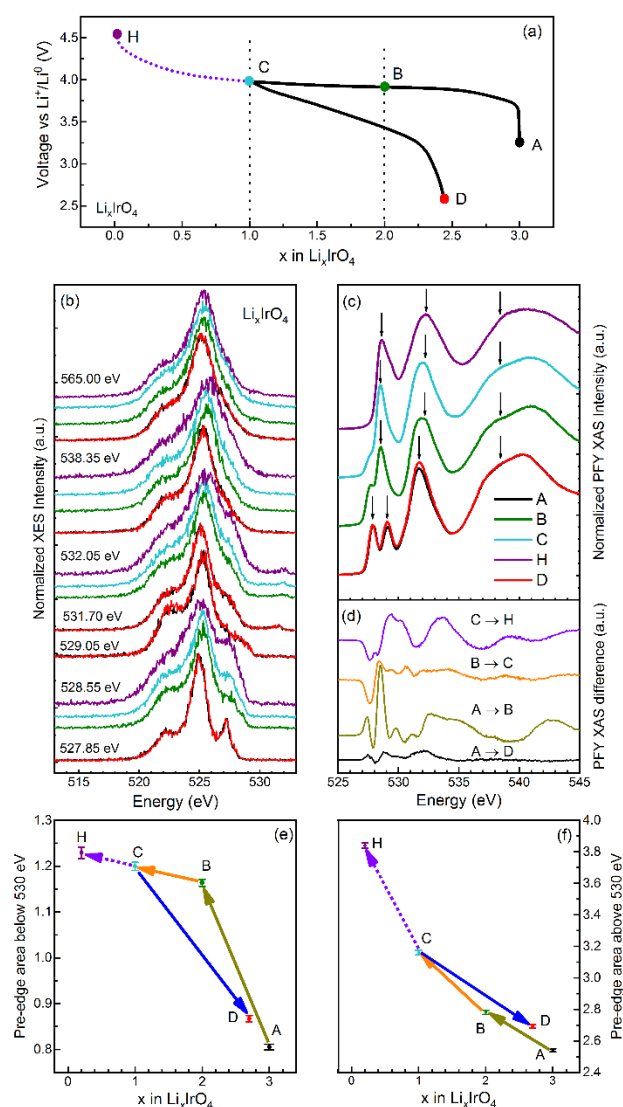


Figure 5-1. (a) Voltage-composition profile of Li_3IrO_4 collected electrochemically. The states of interest for *ex situ* analysis are marked. (b) *Ex situ* O $K\alpha$ XES spectra of Li_3IrO_4 with the specific excitation energy set to the respective arrows on the right. The excitation energy is displayed to the left of the O $K\alpha$ emission spectra. (c) *Ex situ* O K-edge XAS spectra of Li_3IrO_4 at difference electrochemical states of charge measured under PFY mode. (d) Differential XAS spectra between states of charge indicated. Integrated intensity under the pre-edge region between 525 and 530 eV (t_{2g} region in an undistorted ligand field) (e) and between 530 and 535 eV (e_g) (f) for PFY O K-edge XAS at states indicated.

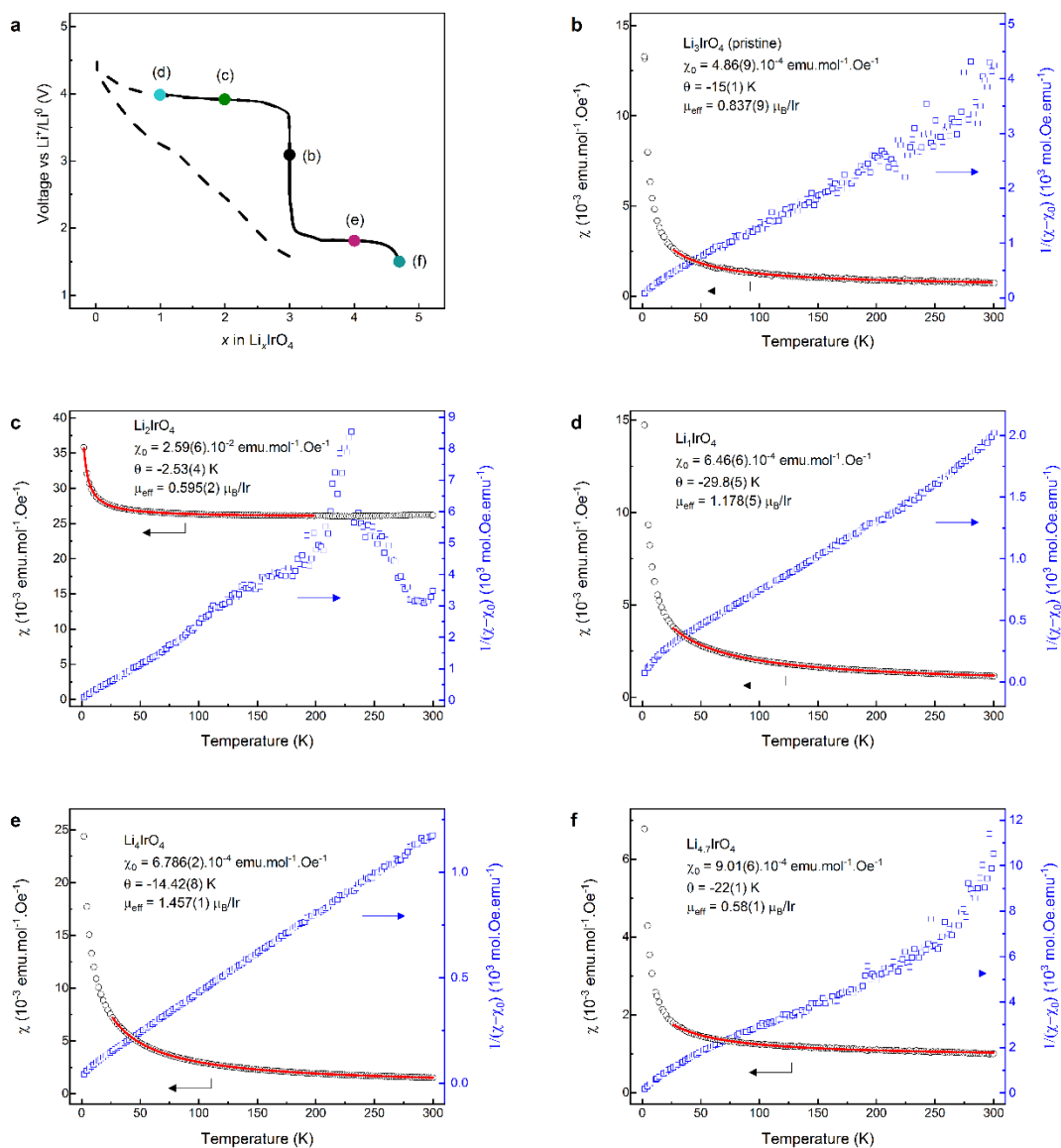


Figure 5-2. (a) Voltage-composition profile of Li_3IrO_4 collected electrochemically. The states of interest for *ex situ* analysis are marked. Magnetization measurement of Li_xIrO_4 with different Li contents at $x = 3$ (b), $x = 2$ (c), $x = 1$ (d), $x = 4$ (e) and $x = 4.7$ (f). The black circles are zero-field cooled magnetic susceptibility measurements, the red line is obtained from fitting the data with a modified Curie-Weiss law, with the fitting parameters indicated, and the blue circles are the inverse magnetic susceptibility after removing the temperature independent contribution χ_0 .

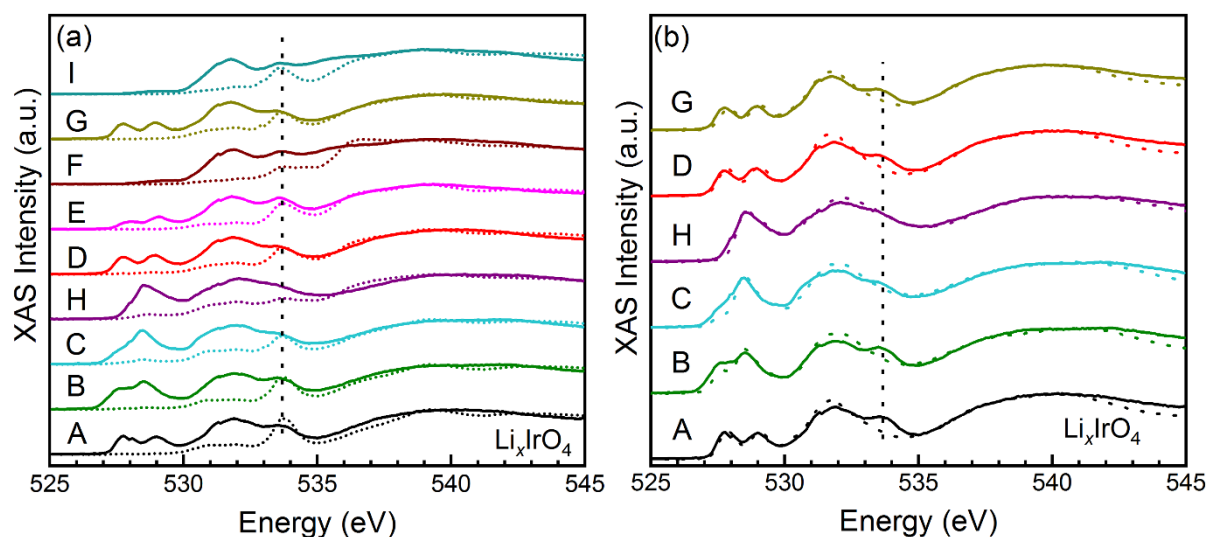


Figure 5-3. O K-edge XAS spectra of Li_3IrO_4 at different electrochemical states measured under (a) TFY (solid) and TEY (short dot) and (b) TFY (solid) and PFY (dot) modes. The intense peak at approximate 533.7 eV dictated by the vertical dot line in TEY implied a predominant presence of Li_2CO_3 in the surface. The corresponding small peak in TFY showed Li_2CO_3 was present at thickness significant enough to be visible in a measurement probing ~ 100 nm into the material. PFY spectra of samples handled in Ar-filled glovebox immediately after the synthesis showed the absence of this peak from Li_2CO_3 .

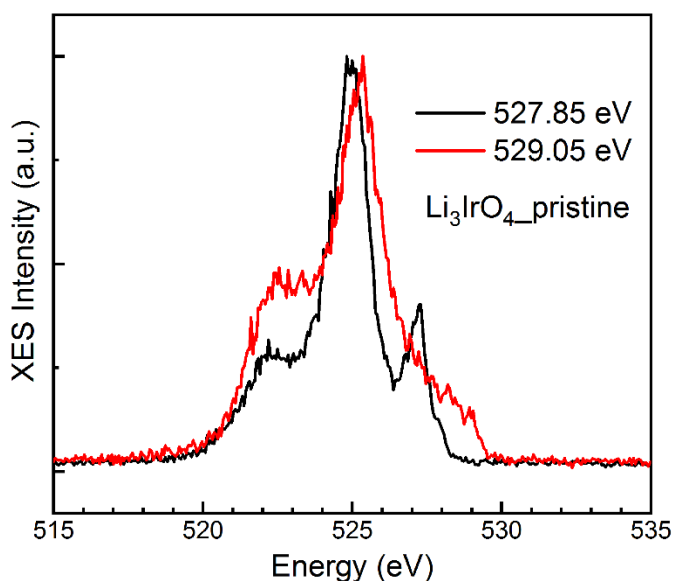


Figure 5-4. *Ex situ* O $K\alpha$ X-ray emission spectra of pristine Li_3IrO_4 at an excitation energy of 527.85 and 529.05 eV.

The electronic and spectroscopic features of Li_3IrO_4 were reproduced computationally (Figure 5-5). Two and three localized electron lone pairs, respectively, were revealed by the computed Electron Localization Functions (ELF) of the two O sites ($\text{O}_{2\text{LP}}$ and $\text{O}_{3\text{LP}}$, hereafter, where LP = electron lone pairs, Figures 5-5a and 5-6), in line with the octet rule.²²⁸ The lone pairs of $\text{O}_{3\text{LP}}$ lie higher than $\text{O}_{2\text{LP}}$ in the density of states of Li_3IrO_4 (Figure 2b), in agreement with their weaker electrostatic stabilization energy expressed by the computed Madelung potential (\mathcal{M}_O). The simulated XAS spectrum assuming a structure with Li/Ir ordering in the layers qualitatively reproduced the three main regions observed experimentally (Figure 5-5c). The significant splitting of the hybridized t_{2g} states could only be obtained when the core-level shift (CLS) of the absorbing species was introduced into the calculations, which became even more pronounced when Li/Ir disorder was introduced, according to the observed structure. Such disorder affects the distribution of $\text{O}_{2\text{LP}}$ and $\text{O}_{3\text{LP}}$ in each IrO_6 octahedron (Table 5-1), which splits the bands and shrinks the band gap computed for the ordered phase (Figure 5-5b). All in all, the XAS spectrum can be viewed as the sum of the individual spectra of $\text{O}_{3\text{LP}}$ and $\text{O}_{2\text{LP}}$, with the former being responsible for the features at lower energy, in perfect agreement with its higher electronic charge (i.e. less covalent bonds to Ir) and subsequently lower 1s binding energy of the 1s electrons.

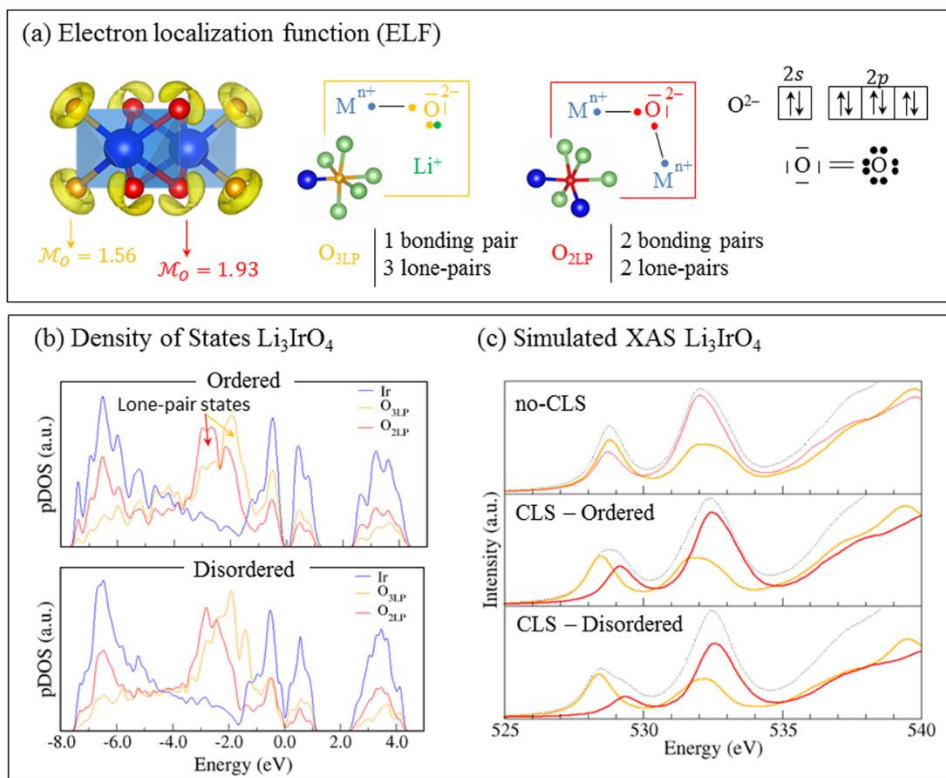


Figure 5-5. (a) Electron localization Function (ELF), as computed within the DFT framework for the pristine Li_3IrO_4 phase showing 2 and 3 lone-pairs around $\text{O}_{2\text{LP}}$ (red) and $\text{O}_{3\text{LP}}$ (orange), respectively, in agreement with their different local environments. The Lewis structures of the two different oxygen sites obey the octet rule stating that O^{2-} is stable with four electron-pairs distributed into n bonding-pairs (involved in Ir-O) and $4 - n$ lone-pairs (un-hybridized to Ir). (b) Atom-projected density of states (pDOS) showing a shift in energy of $\text{O}_{3\text{LP}}$ lone-pair states with respect to $\text{O}_{2\text{LP}}$ due to a lower Madelung potential (\mathcal{M}_O). A Mott insulator electronic ground-state is obtained for Li_3IrO_4 , with a small energy gap for the Li/Ir ordered structure that cancels out when disorder is introduced in the model. (c) Simulated XAS spectra of the ordered and disordered Li_3IrO_4 structures (see Supplementary Information for details) with or without including core-level shift (CLS) in the calculations. The XAS projected on the $\text{O}_{3\text{LP}}$ and $\text{O}_{2\text{LP}}$ absorbing species showing that the splitting of the first excitation peak arises from the different oxygen electronic structures, the $\text{O}_{3\text{LP}}$ 1s core-level having a lower binding energy than $\text{O}_{2\text{LP}}$ 1s.

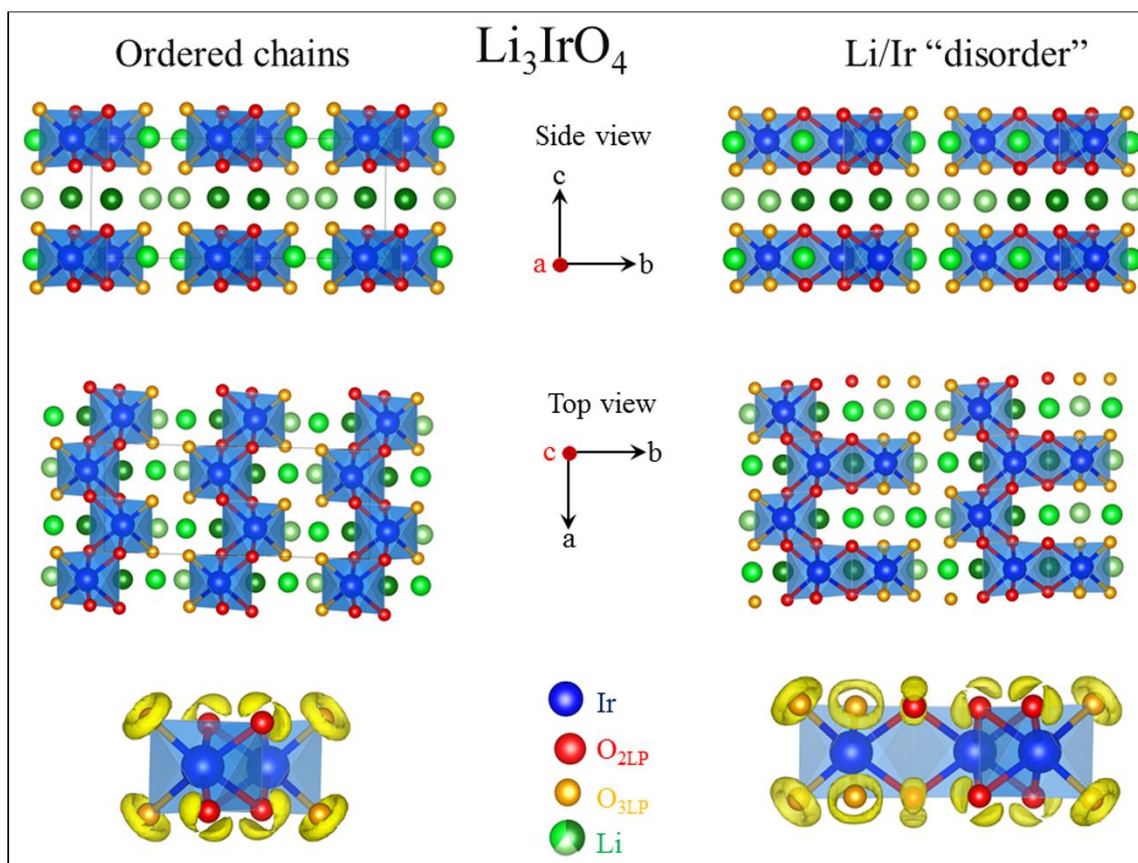


Figure 5-6. Crystal structure of the Li_3IrO_4 pristine phase and its associated Electron Localization Function (ELF), as considered in DFT calculations with (right) and without (left) Li/Ir disorder. The ordered structure displays regular zig-zag chains of edge-shared octahedra with red oxygens connected to 2 Ir atoms and orange oxygens connected to only 1 Ir atom. The disordered structures are obtained by exchanging one Li and one Ir atoms, leading in the present case to three different IrO_6 octahedra occurring in the unit cell (instead of one only in the ordered structure) with different number of red and orange oxygens (see Table S1). Electron Localization Functions (ELF) invariably show that all oxygens connected to 1 and 2 Ir atoms display 3 and 2 lone pairs (yellow volumes), respectively, in perfect accord with the octet rule and with the Li^+ , O^{2-} and Ir^{5+} formal oxidation states.

Table 5-1. Number of $\text{O}_{3\text{LP}}$ and $\text{O}_{2\text{LP}}$ in the non-equivalent IrO_6 octahedra occurring in the Li/Ir ordered and disordered phases considered in the calculations.

	Ir(Oh)	$\text{O}_{2\text{LP}}$	$\text{O}_{3\text{LP}}$
Li/Ir order	Ir	4	2
Li/Ir disorder in the layer	Ir1	2	4
	Ir2	6	0
	Ir3	4	2

Li/Ir disorder between the layer	Ir1	4	2
	Ir2	0	6
	Ir3	0	6
	Ir4	4	2

The electrochemical properties of Li_3IrO_4 were reported by Perez et al. (Figures 5-1a and 5-7).⁹⁸ It can be oxidized to extract Li through a long plateau at 3.9-4.0 V vs Li^+/Li^0 , with a capacity equivalent to the removal of 2 mol of Li, to LiIrO_4 . Further oxidation to 4.5 V is accompanied with a sloping profile, and amorphization to a phase formulated as “a- IrO_3 ”. The latter step is irreversible, leading to notable voltage hysteresis and capacity loss upon subsequent reduction to 2.0 V (Gray lines in Figure 5-7a). These losses are alleviated if the oxidation is limited to LiIrO_4 . Perez et al. also reported a minor shift of the Ir L_{III} -edge XANES to high energy in the initial stages of deintercalation, with the position staying largely constant thereafter.⁹⁸ Given the large change in the charge compared to the small change at the Ir centers, a process centered at the O ligands was formulated. This unusual process motivates this study.

It is worth noting that Li can also be intercalated into Li_3IrO_4 at low potential (black lines in Figure 5-7a). Intercalation proceeds via a long plateau at ~1.7 V, corresponding to a capacity equivalent to the insertion of 1.7 mol of Li per mol of compound at 1.3 V. The subsequent oxidation to 2.5 V proceeds through two processes located at 1.8 and 1.9 V, respectively, leading to almost reversible re-extraction of 1.5 mol of Li. Ir L_{III} -edge XANES reveals significant, yet fully reversible changes in absorption energy associated with a conventional redox mechanism based on formal cationic centers, which reflect population of Ir $5d$ -O $2p$ covalent states. If oxidation to LiIrO_4 is followed by reduction to 1.3V, an extraordinarily high capacity equivalent to 3.5 mol of Li can be accumulated. In order to study how and in what form O was involved in the electrochemical reactions, electrodes were harvested at representative state points of these electrochemical reactions, as indicated in Figure 5-7.

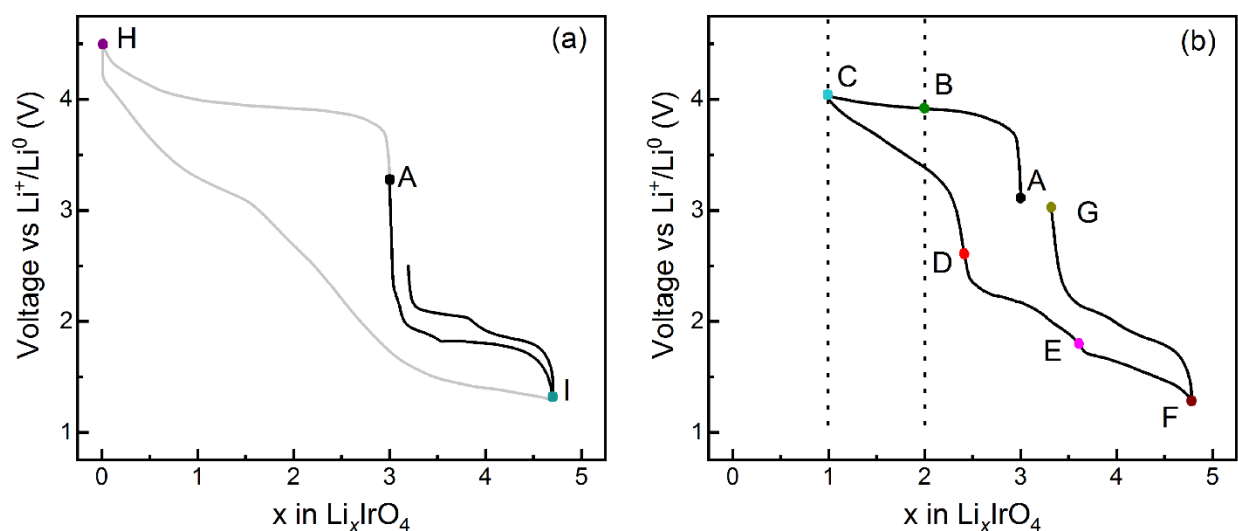


Figure 5-7. Voltage-composition profiles of Li_3IrO_4 at different cutoff voltage window. The electrochemical states of interest are represented with labels of different colors. Samples were harvested from the representative states.

5.3.2 Changes at O states upon delithiation

We start with the deintercalation of the first 2 mol of Li from Li_3IrO_4 because it induces a topotactic change of the layered structure with high electrochemical reversibility.⁹⁸ Deintercalation of the first 2 mol of Li from Li_3IrO_4 induced minor changes in μ_{eff} , to 0.595 and 1.178 μ_{B}/Ir at $x = 2$ and 1 (in Li_xIrO_4 , Figures 5-2b and 5-2c), in all cases reflecting a relatively weak paramagnetism that does not quite reach values expected even for $S = 1/2$. Upon delithiation, the fine structure of the O K-edge XAS above 535 eV was modified, with the centroid shifting toward high energy (Figure 5-1c). Derivatives of the data revealed a subtle blueshift of its onset for $x = 1$ (Figure 5-8). The centroid of the XES of the two delithiated states also shifted to higher energy with respect to the pristine state, at all excitations except 528.55 eV. The changes were most pronounced with the first Li removed. All these changes could be viewed as resulting from the lowering of the energy of the O 1s states due to an increase in average Z_{eff} (effective nuclear charge) resulting from depletion of electron density of the O anions to compensate deintercalation.

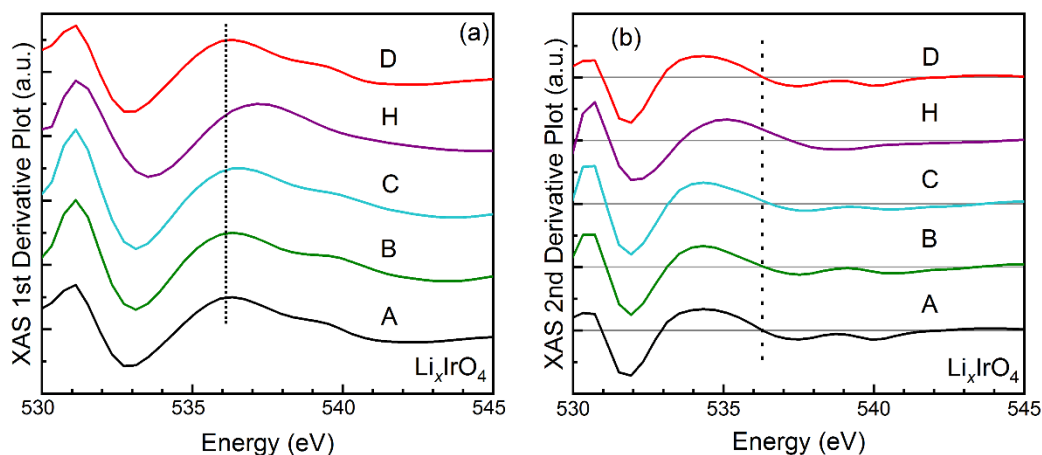


Figure 5-8. First (a) and second derivative (b) plots of O K-edge XAS spectra of Li_xIrO_4 at different states of charge indicated in the electrochemical profiles (Figures 5-1a).

The most drastic changes in the O K-edge XAS took place below 530 eV, with a dominant peak at 528.5 eV showing a shoulder at 527.7 eV in both $x = 2$ and $x = 1$ (Figure 5-1c). These changes signify a change in both position and, especially, relative intensity of the maxima in this region compared to the pristine state. Their increased overlap prevented selective excitation of $\text{O}_{2\text{LP}}$ and $\text{O}_{3\text{LP}}$ in the resonant XES (Figure 5-1b). Overall, the integrated intensity under the pre-edge XAS signals below 530 eV significantly increased from pristine to $x = 2$ (Figure 5-1e), but remained comparatively unchanged between $x = 2$ and $x = 1$ (Figure 5-1e). Above 530 eV, the onset of the third pre-edge peak was static (Figures 5-1c, and 5-1d), but its area progressively increased through a significant broadening toward higher energy (Figure 5-1c). The net result was a rather proportional increase in its integrated intensity with delithiation (Figure 5-1f). These observations indicate an increase in unoccupied states with O character upon oxidation.

The origin of the changes O K-edge XAS was revealed by computational analysis (Figure 5-9). Upon oxidation from pristine to $x = 2$, the existence of Li/Ir disorder shifts the charge compensation from only depleting O $2p$ -Ir $5d$ states (i.e., classical formal oxidation of cations) in the ideal lattice to inducing significant involvement of one of the three lone pairs of $\text{O}_{3\text{LP}}$ (Figure 5-10), as can be visualized in the ELFs

computed for one of the possible disordered structures of Li_2IrO_4 (Figure 5-9). Similar results are obtained for other patterns of Li/Ir disorder, with $\text{O}_{2\text{LP}}$ systematically participating to a much lesser extent than $\text{O}_{3\text{LP}}$ (Figure 5-10), consistent with the relative positioning of their lone-pair states in the pDOS (Figure 5-5). This change in electronic structure perfectly reproduces the change in the ratio of intensity below 530 eV in the XAS spectrum of Li_2IrO_4 (Figure 5-9), as the newly depleted $\text{O}_{3\text{LP} \rightarrow 2\text{LP}}$ states (orange O connected to 1 Ir) showed similar energy to $\text{O}_{2\text{LP}}$ (red O connected to 2 Ir). Further oxidation to $x = 1$ was compensated exclusively via O lone pairs. The initial $\text{O}_{2\text{LP}}$ states in Li_3IrO_4 became involved at this stage, yet still to a lower extent than $\text{O}_{3\text{LP}}$. The computations revealed that the oxidation of the two $\text{O}_{2\text{LP}}$ between two IrO_6 octahedra (red oxygens in Figures 5-5 and 5-9) decreased their bond length toward 2.4 Å. In contrast, $\text{O}_{3\text{LP}}$ located on corners of each given octahedra tended to shorten their Ir-O length upon lone-pair depletion, to below 1.9 Å,⁹⁸ most likely leading to a higher bond order with Ir, as previously proposed for $\text{Li}_{2-x}\text{Ir}_{1-y}\text{Sn}_y\text{O}_3$.¹²² The collapse of the two signals below 530 eV is ascribed to all O ions becoming electronically equivalent (Figure 5-9). The remaining shoulder at low energy in the experiment spectra could arise from incomplete oxidation of the electrode to $x = 1$, since the experimental cut-off was set assuming a faradaic efficiency of 100%.

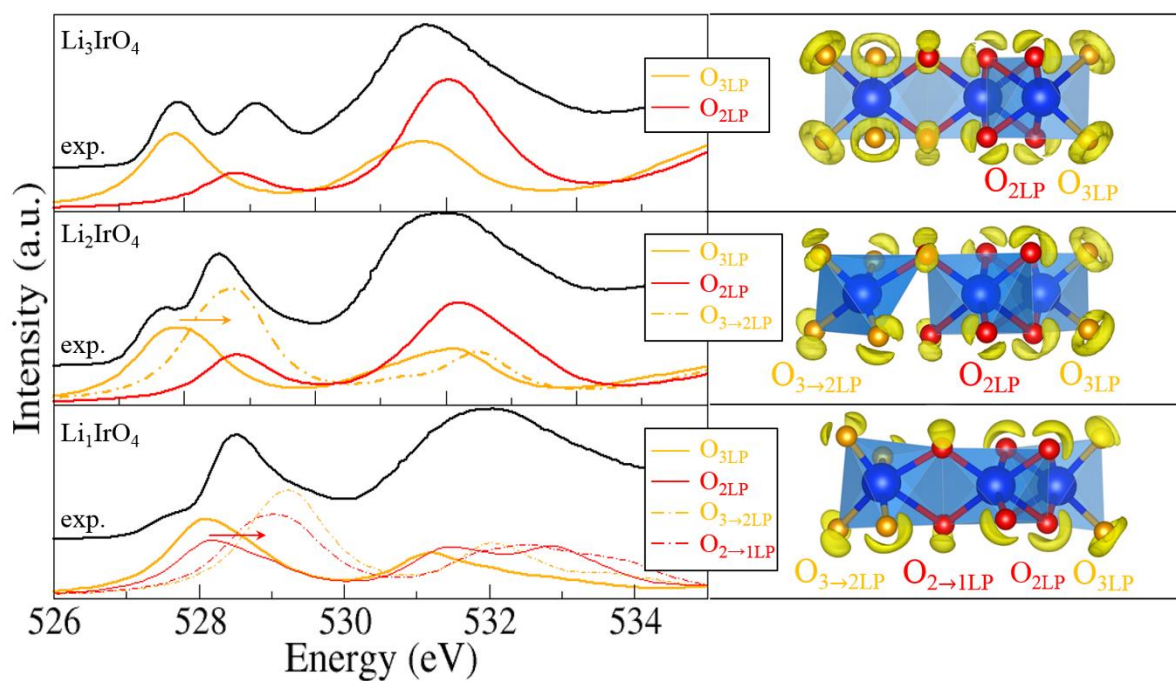


Figure 5-9. (left) Simulated vs. experimental XAS spectra for Li_3IrO_4 , Li_2IrO_4 and LiIrO_4 showing that the evolution of the excitation peaks are due to the progressive participation of the two oxygen sites in the oxidation process of the pristine material. (right) Electron localization functions (right) computed for each structure and confirming the main oxidation of $\text{O}_{3\text{LP}}$ (orange) from $x=3$ to $x=2$ and a mixed oxidation of $\text{O}_{2\text{LP}}$ (orange) and $\text{O}_{2\text{LP}}$ (red) from $x=2$ to $x=1$. Other results with different Li/Ir disorder are shown in Figure 5-9.

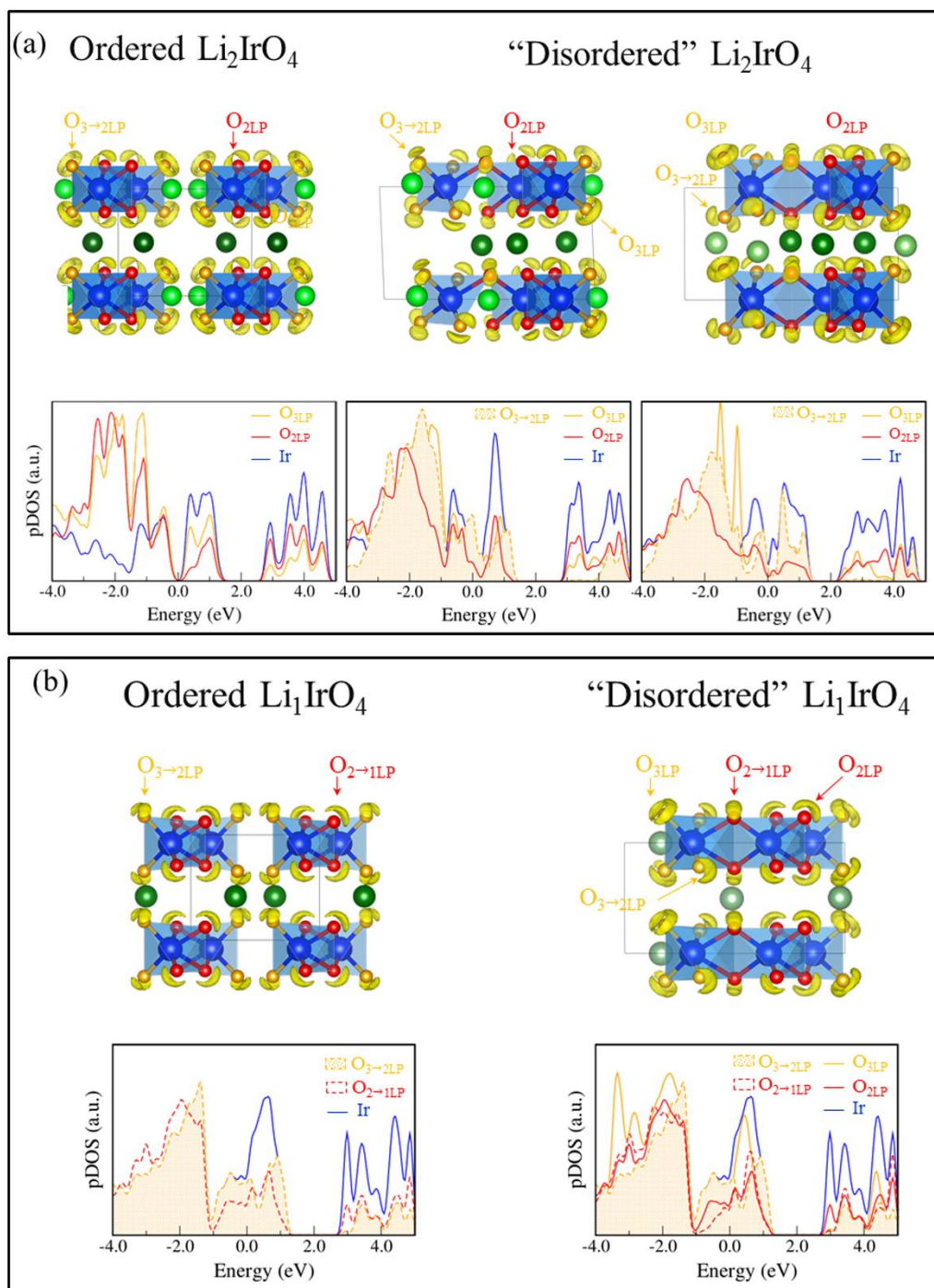


Figure 5-10. (a) ELF and atom-projected Density of States (pDOS) for the partially delithiated Li_2IrO_4 phase showing that $\text{O}_{3\text{LP}}$ becomes redox-active when Li/Ir disorder is introduced in the calculation. It is labelled $\text{O}_{3\rightarrow 2\text{LP}}$ (orange), the color and the subscript referring to the connection to 1 Ir atom and the involvement of one lone pairs in the electrochemical process, respectively. (b) ELF and pDOS for the

ordered and disordered Li_xIrO_4 phases showing now the involvement of both orange ($\text{O}_3 \rightarrow 2\text{LP}$) and red ($\text{O}_2 \rightarrow 1\text{LP}$) oxygens in the process, with a relative participation depending on the Li/Ir distribution.

The O K-edge XAS spectrum of the electrode oxidized to 4.5 V (close to theoretical capacity $x = 0$), associated with the irreversible transition to amorphous $\alpha\text{-IrO}_3$,⁹⁸ possessed a single peak at 528.6 eV, with no shoulders at lower energy and a significant asymmetry spanning toward 530 eV (Figures 5-1c). The integrated (relative) area under this single signal was slightly greater than $x = 1$ (~2.4%, Figure 5-1e). Similarly, the centroid of the feature between 530 and 535 eV blue shifted by 0.3 eV with an increase in the integrated area that qualitatively followed the trend starting from $x = 3$ (Figure 5-1f). Blueshifts with respect to $x = 1$ were also observed with both the inflection point in the main absorption edge (see C \rightarrow E in Figures 5-1d and 5-8) and all O K α emission spectra (Figure 5-1b). These changes indicate a shift of the O 1s core level to lower energy, signifying an increased Z_{eff} ,^{215, 233} consistent with the strong participation of the anions in the compensation of the process of oxidation. Overall, both XAS and XES spectra became broader at this high state of charge, which is ascribed to the increased structural disorder induced by the amorphization of the material.⁹⁸

5.3.3 Chemical reversibility of the process of LOR

While other oxides have conclusively been shown to display unconventional redox activity of ligands upon delithiation, many display chemical hysteresis, whereby subsequent reduction does not return the compound to its original pristine crystal and/or electronic structure via a different pathway involving conventional transitions of formal state of the transition metal, such as Mn in $\text{Li}_{1.3}\text{Nb}_{0.3}\text{Mn}_{0.4}\text{O}_2$,²¹¹ $\text{Li}_{1.3}\text{Mn}_{0.4}\text{Ta}_{0.2}\text{O}_2$,²⁰⁰ $\text{Li}_{1.16}\text{Ni}_{0.15}\text{Co}_{0.19}\text{Mn}_{0.50}\text{O}_2$,¹⁴⁶ $\text{Li}_{1.2}[\text{Ni}_{0.13}\text{Co}_{0.13}\text{Mn}_{0.54}]\text{O}_2$,^{151, 234} and Ni in $\text{Li}_{1.3}\text{Ni}_{0.27}\text{Ta}_{0.43}\text{O}_2$ ²⁰⁰ and Ru in Li_3RuO_4 .^{97, 207} Therefore, the ensuing discussion will evaluate the existence of such chemical hysteresis in Li_xIrO_4 . Since Perez et al. already reported that the final step of O_2 loss is irreversible,⁹⁸ we will only elaborate on the reduction of an electrode charged to $x = 1$, or LiIrO_4 . Its reduction to 2.6 V produced a capacity equivalent to 1.5 mol of Li, and almost completely restored the O

K-edge XAS and O K α XES to the pristine state (Figure 5-1). In addition to the central feature in all XES spectra discussed above, a shoulder feature at high energy, which vanished gradually upon delithiation, became prominent again after discharge to 2.6 V, suggesting that it is correlated to the (de)intercalation process. All in all, the O state before and after a full cycle were almost identical.

Further reduction was also possible, accumulating Li beyond the initial state (Figures 5-11 and 5-7).⁹⁸ This process induced an increase in μ_{eff} at 1.8 V, to 1.46 μ_{B}/Ir (Figure 5-2e), which is close to value reported for Ir⁴⁺ (1.7-2.0). In the O K-edge XAS, there was a shift of the first two pre-edge peaks to higher energy, at 528.1 and 529.1 eV, concurrent with a large decrease of their intensity (Figures 5-11c), particularly at the lowest energy. These features are confirmed by DFT calculations for which a cationic reduction is predicted, consistent with a sharp decrease in intensity of the two peaks corresponding to the t_{2g}- and e_g-like peaks (Figure 5-12). Above 530 eV, the main feature also shifted to higher energy, with an obvious, yet comparably smaller, reduction in intensity. Lastly, the rising absorption edge shifted to lower energy by ~0.2 eV compared to 2.6 V (Figure 5-13), indicating a relative decrease in the Z_{eff} of O and shallower binding energy shift. These trends exacerbated upon further reduction to 1.3 V, corresponding to a swing of almost 4 mol of Li, and a nominal composition Li_{4.7}IrO₄.⁹⁸ There was an almost complete disappearance of pre-edge signals below 530 eV (Figures 5-11c), with the exception of a small, broad peak centered at 529.3 eV with little change above 530 eV. The spectrum significantly broadened at higher energy, around the absorption edge, with a redshift of the inflection point by ~0.6 eV in comparison with the previous state (Figure 5-13). At this point, μ_{eff} was 0.58 μ_{B}/Ir at 1.3 V (Figure 5-2f), suggesting a large proportion of Ir³⁺ with filled t_{2g} orbitals. It is worth noting that the samples used for these measurements seemingly contained greater levels of Li₂CO₃ impurity than in Figure 5-1c, which did not affect the spectral evolution (Figure 5-3).

Li intercalation led to the injection of electrons into unoccupied O 2*p*-Ir 5*d* states, particularly, resulting in the decrease in the normalized intensity, and consistent with magnetic measurements. The large decrease below 530 eV indicates that electron mainly populated states arising from π interactions (t_{2g} in an ideal O_h

field). It is possible that the smaller reduction of the pre-edge above 530 eV reflected a change in the contribution of O to the σ (e_g) states due to a decreased covalence of the Ir-O bond. This distinct variation in the intensity reflects a greater role of unoccupied states at the lowest energy, in a behavior reminiscent of a rigid band. The redshift of the main absorption threshold indicates a decrease in the binding energy of the O 1s core level, consistent with re-population with electrons, and decrease in the Z_{eff} of O. These changes are accompanied by a steady shift of the Ir L_{III}-edge XANES to lower energy reported by Perez et al.⁹⁸ All in all, the data support the occupation of O 2p-Ir 5d states following a conventional redox mechanism that can be explained by changes in the formal oxidation state of Ir as a proxy for the Ir-O covalent bond.

The O K-edge XAS of the electrode harvested at 1.3 V after being charged to $x = 1$ was almost perfectly equal to the spectrum of an electrode obtained by direct reduction of pristine Li_3IrO_4 to 1.3 V (Figure 5-11c), further reinforcing the notion that the initial oxidation to Li_1IrO_4 is extremely reversible both from the electrochemical capacity and chemical perspectives. This reversibility is further demonstrated by the highly similar spectra of pristine Li_3IrO_4 and the sample re-charged to 3 V after a full cycle of oxidation to $x = 1$ and reduction to 1.3 V. These observations emphasize the extremely high reversibility of the redox reaction between Li_1IrO_4 and $\text{Li}_{4.7}\text{IrO}_4$.

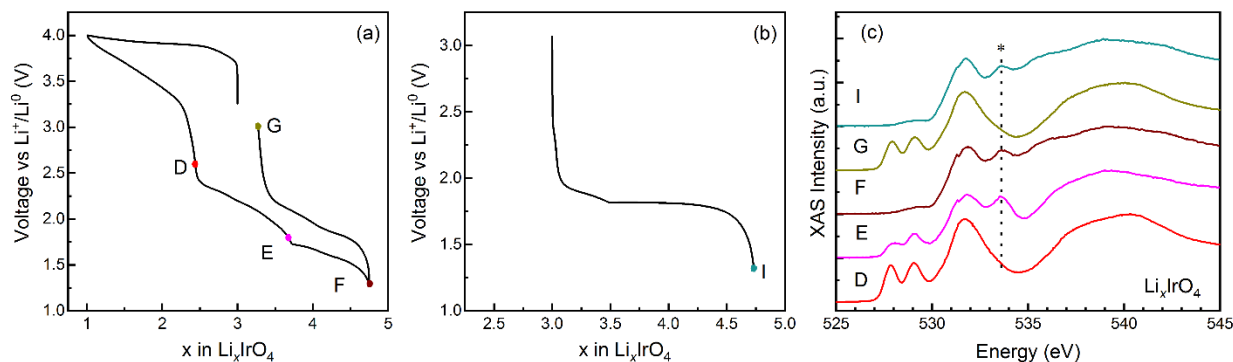


Figure 5-11. (a) and (b) Voltage-composition profiles of Li_3IrO_4 collected under the galvanostatic mode. The electrochemical states of interest are marked. D is the state after the sample was reduced to 2.6 V followed by 1 mol Li removal. E is the state after the sample was reduced to 1.8 V followed by 1 mol Li removal. F is the state after the sample was reduced to 1.3 V followed by 1 mol Li removal. G is the state after the sample was re-oxidized to 3.0 V followed by 1 mol Li removal. I is the state after the sample was initially reduced to 1.3 V. (c) *Ex situ* O 1s XAS spectra of Li_xIrO_4 at difference electrochemical states of

charge measured under PFY mode (D, and G) and TFY mode (E, F and I). The peak at around 533.7 eV (denoted by the asterisk symbol) for samples E, F and I is related to carbonate-related peak due to the transitions to π^* (C=O) orbitals, which has little influence on the spectral interpretation.

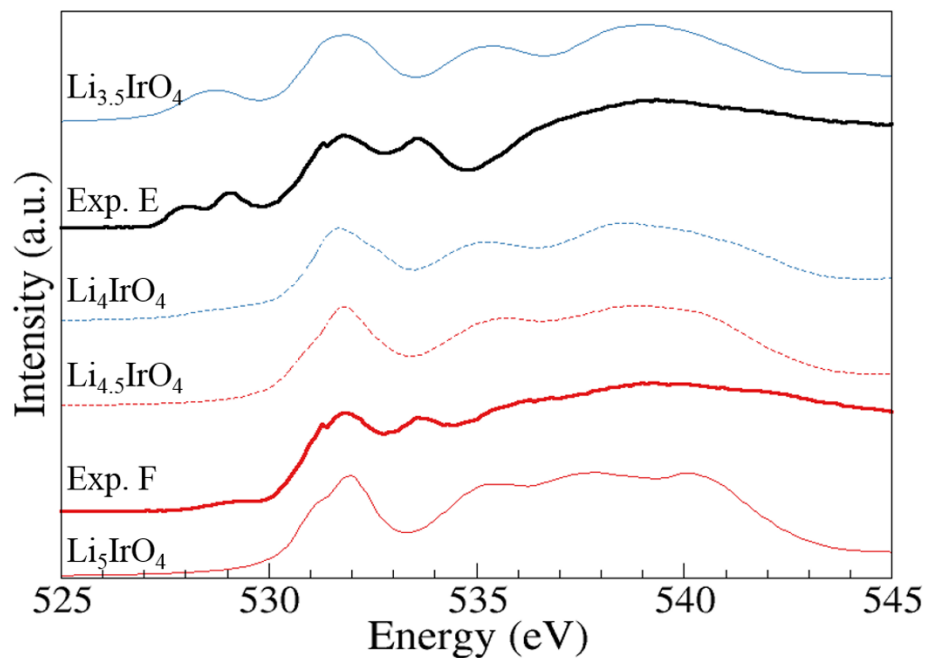


Figure 5-12. Simulated XAS spectra of different electrochemical states and the corresponding experimental ones.

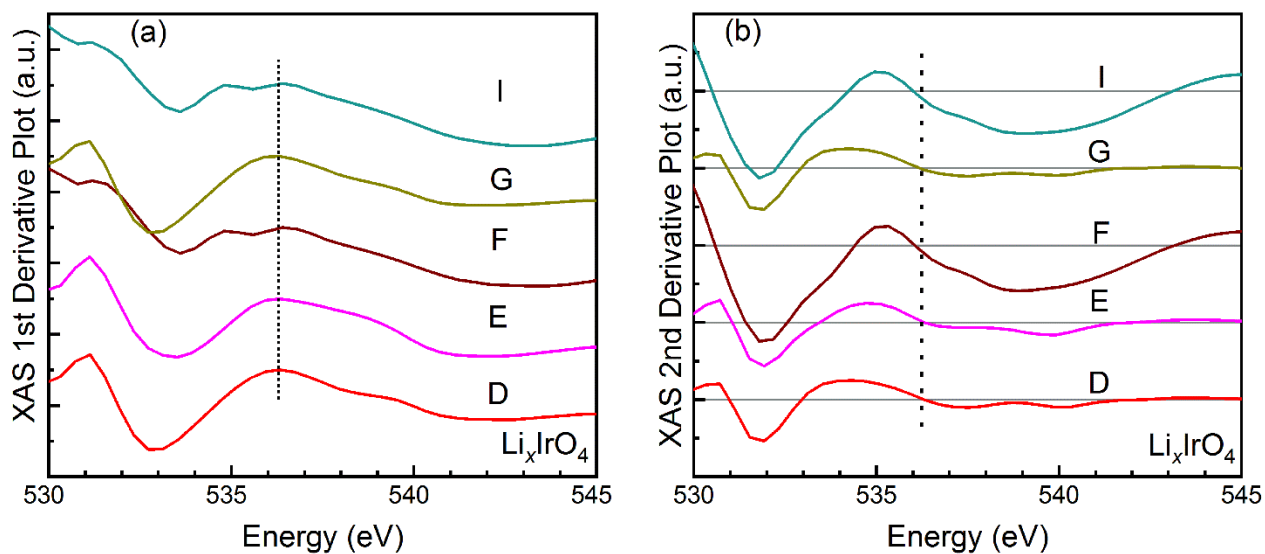


Figure 5-13. The first (a) and second derivative (b) plots of O K-edge XAS spectra of Li_3IrO_4 at different states of charge indicated in the electrochemical profile.

5.3.4 Implications for the existence and mechanism of LOR

Taking all these results together, the evolution of the O spectra clearly demonstrates the participation of ligand states in the charge compensation of the high capacity of delithiation shown by Li_3IrO_4 . In particular, the results reveal the shifting contribution from $\text{O}_{3\text{LP}}$, which are at higher energy in the pristine state, to $\text{O}_{2\text{LP}}$ as the delithiation progressed, with the transition happening after around 1 mol of Li was removed. Yet, although the last 1/3 of Li removed induces loss of O_2 accompanied by amorphization, the resulting compound, amorphous $\alpha\text{-IrO}_3$, has a similar distribution of O electronic states to LiIrO_4 , but with an increase in the 1s binding energy. These features indicate that the loss of O from the lattice was not sufficient to relax the compound to a state where O ligands were restored to a reduced state.

In the preceding study by Perez et al., Ir L_{III} -edge XANES of the same states revealed only a minor change at the transition metal in the early stages of the reaction, which was essentially arrested after about 0.5 mol of Li were removed from Li_3IrO_4 .⁹⁸ Our DFT calculations show that this effect is related to the statistical Li/Ir disorder in the pristine material. Since O_2 loss does not occur when the oxidation is limited to $x = 1$,⁹⁸ we can indisputably ascribe the behavior of $\text{Li}_3\text{IrO}_4\text{-LiIrO}_4$ to what has loosely been classified in the literature as LOR, to differentiate from conventional redox activity through formal activity of the transition metal observable via the corresponding X-ray spectroscopy.²⁰⁷ Interestingly, although evolution of O_2 accompanied by amorphization is induced when the last 1/3 of Li are removed, the O spectra indicate that ligands in $\alpha\text{-IrO}_3$ remained highly oxidized despite the loss of O from the lattice.

This unconventional LOR activity is most often probed by RIXS maps in other Li-rich transition metal oxides. In particular, it is associated with the onset of a sharp feature, located at ~ 523 eV emission when the excitation was at ~ 531 eV.^{122, 141, 149, 177} Such RIXS maps were also measured for Li_xIrO_4 (Figure 4), with an estimated flux ($5 \times 10^{10} - 1 \times 10^{11}$ photons/s), below the reported threshold to induce sample damage that could lead to the disappearance of the energy loss feature.²¹⁰ There was an increase in the dispersion of

emitted state (along the x axis in Figure 5-14), as well as the intensity of the elastic peak for all oxidized phases. But delithiation from Li_3IrO_4 did not produce any features at ~ 523 eV emission for a ~ 531 eV excitation. This feature was concurrent with the existence of out-of-plane Sn migration in layered $\text{Li}_{2-x}\text{Ir}_{1-y}\text{Sn}_y\text{O}_3$, which only displays LOR at $y > 0$.^{122, 235} This effect has recently been specifically ascribed to the formation of short O-O bridges between Ir atoms when these defects are introduced.²³⁶ Most importantly, it is also observed in conventional layered oxides like $\text{LiNi}_{0.8}\text{Co}_{0.15}\text{Al}_{0.05}\text{O}_2$,¹¹¹ where the charge compensation could formally be accounted by conventional CR. In that case, the appearance of the loss feature at 523 eV correlates with the collapse of the interlayer distance in the oxide, concurrent with a deformation of the octahedral coordination of the transition metals. No evidence of Ir migration exists for Li_xIrO_4 before amorphization, consistent with a predicted low driving force.¹²² Furthermore, the change in the interlayer distance is very small up to $x = 1$.⁹⁸ Therefore, our work indicates that: i) LOR is not uniquely associated with specific loss features in the RIXS maps, ii) careful evaluation of both XAS and XES of metals and ligands is required to determine its existence, and iii) different processes may fall under the umbrella of LOR with subtle differences in structural and electronic features.

The DFT calculations presented here indicate that delithiation is compensated by O 2p states that are initially non-bonding. The IrO_6 octahedra are predicted to distort to form short Ir-O bonds, and introduce O-O distances at ~ 2.4 Å, characteristic of the so-called reductive coupling mechanism.^{73, 92} The principle by which LOR occurs in Li_3IrO_4 is consistent with $\text{Li}_{2-x}\text{Ir}_{1-y}\text{Sn}_y\text{O}_3$.¹²² It involves a high density of uncoordinated O 2p states, or lone pairs. However, unlike $\text{Li}_{2-x}\text{Ir}_{1-y}\text{Sn}_y\text{O}_3$, the high Li/Ir ratio of Li_3IrO_4 generates sufficient states in its pristine state, as originally predicted by Xie et al.⁹² Therefore, it does not require out-of-plane migration of heavy cations like Sn(IV),¹²² a prominent driver of voltage hysteresis and losses in reversibility.^{154, 236} Formation of peroxo (O-O) bridges between Ir, with a bond distance of 1.5 Å¹²² is also not predicted by our models, possibly explaining the RIXS observations. The redox transitions of the ligands are extremely reversible if delithiation is stopped at LiIrO_4 , with the material returning to its initial state. The absence of chemical hysteresis distinguished Li_3IrO_4 from other oxides where LOR

unlocks a different pathway involving conventional transitions of formal state of the transition metal, such as Mn in layered and disordered rock-salt oxides^{146, 151, 211, 234} and Ru in Li_3RuO_4 ^{97, 207}.

Through a combination of experiments and theory, this report clearly pinpoints the O states that enable the shift of the redox centers to the ligands. While $\alpha\text{-Li}_2\text{IrO}_3$ also possesses two non-equivalent O sites, similar measurements did not find any significant difference in their contribution to the charge compensation.²³⁵ This fact convincingly reinforces that measurable levels of LOR require O sites like $\text{O}_{3\text{LP}}$, namely with connectivity to only one transition metal, to avoid cation migration, which is not favorable for Ir. These sites are present in Li_3IrO_4 , but not $\alpha\text{-Li}_2\text{IrO}_3$,²³⁷ or similar honeycomb oxides. At the same time, comparison with Li_3TMO_4 like Ru, Nb or V emphasizes that connectivity to a d^n ($n > 0$) transition metals is crucial in the process of LOR, as it allows rehybridization that stabilizes the structure and renders it reversible. In previous work,^{92, 120, 228} we have proposed that transition metal oxides having no empty d-orbitals to enable such rehybridization should undergo irreversible reactions with O_2 release. Further disentangling the role of Ir, in contrast to other d^n metals such as Ru,²⁰⁷ as enabling effective rehybridization²²⁸ and/or preventing the formation of defects²³⁶ will be indispensable moving forward if this reversible reactivity is to be mimicked with base metals, an crucial step for this concept to have technological impact.

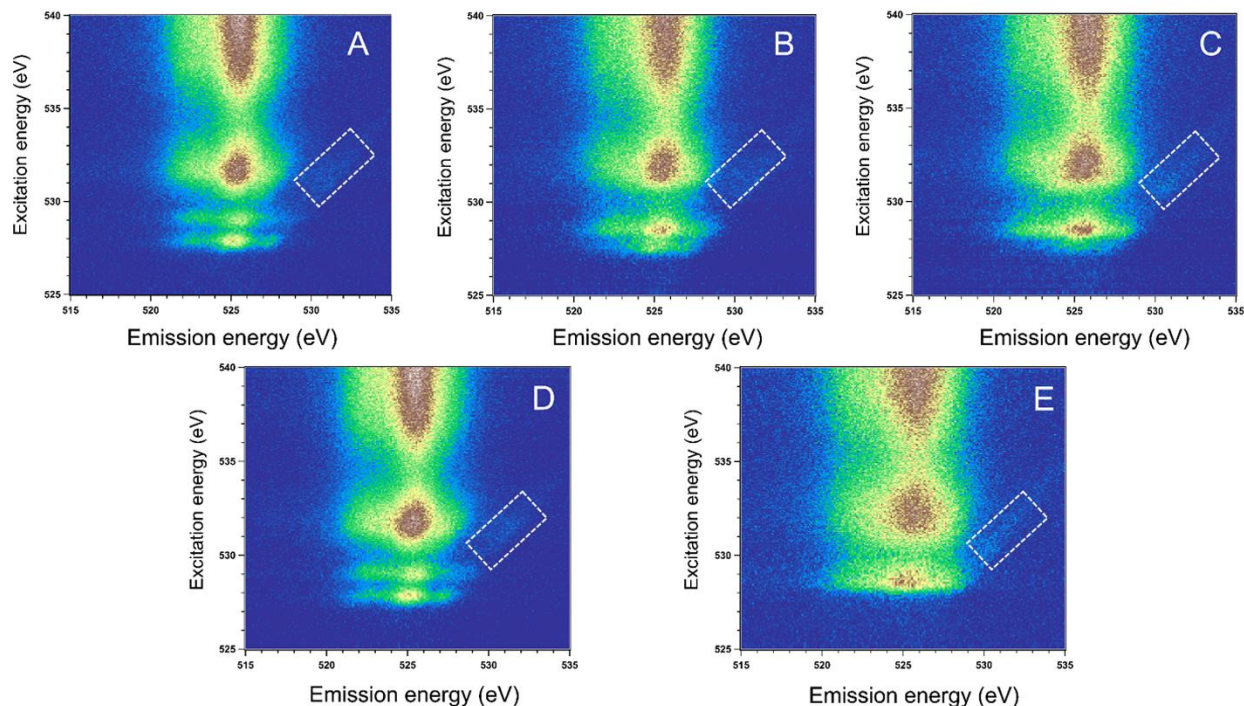


Figure 5-14. *Ex situ* O K-edge RIXS maps of Li_3IrO_4 at the different electrochemical states indicated. The white rectangular regions represent the elastic peak.

5.4 Conclusion

Although Li_3IrO_4 exhibits reversible cycling of 2 mol Li per mol TM upon cycling, the minor changes in Ir oxidation state reported cannot account for associated charges, which enables it an ideal compound to investigate the oxygen redox. Via a combination of experiments and computations, the existence of non-equivalent O sites with different number of non-bonding O 2p states in the pristine state was confirmed to exist due to the disordered Li/Ir arrangement. Upon oxidation of Li removal, the O site with 3 electron lone pairs was mainly involved in the oxygen redox for the charge compensation, a process that was fully reversible for the subsequent reduction of Li re-intercalation process. In spite of the pronounced oxygen redox, the commonly reported RIXS signatures were absent, indicating multiple possible pathways of the oxygen redox may exist, with different electronic and structural implications. In addition, lithiation to

$\text{Li}_{4.7}\text{IrO}_4$ is highly reversible both electrochemically (capacity) and chemistry (redox transitions), following a conventional intercalation process accompanied by changes in the formal oxidation state of Ir.

Chapter 6 Definition of redox centers in reactions of lithium intercalation in Li_7RuO_6

The content of this chapter is based on a submitted manuscript “Definition of Redox Centers in Reactions of Lithium Intercalation in Li_7RuO_6 ”.

6.1 Introduction

Research published in recent years has demonstrated that the number of pure lone O($2p$) states in a transition metal oxide is key to enabling lattice oxygen redox (LOR) that imparts high capacity for energy storage. Xie *et al.* showed that this figure of merit relies on the O/ TM ratio, which is proportional to the non-bonding O($2p$) states at the Fermi level that could induce additional capacities in Li-rich cathode electrode materials.⁹² This predication, so far, has been validated by Li_3TMO_4 system with a O/ TM ratio of 4, which exhibits that a huge capacity upon the first charge is attributed to the ligand O-centered contribution.^{96-98, 207} As far as we know, so far, there is no experimental report of Li-rich compounds with higher O/ TM ratio exhibiting clear evidence of lattice oxygen redox activity, which requires insight by X-ray absorption spectroscopy.

The search for Li-rich structures with higher O/ TM ratio guided us toward Li_7RuO_6 . Li_7RuO_6 is a layered compound with an unusual defective character of the lithium partial occupation.^{238, 239} In addition, Li_7RuO_6 with the highest O/ TM ratio ever reported renders the highest possibility in favoring the ligand oxygen-only redox reaction upon Li deintercalation. In this report, we studied the electrochemical properties of Li_7RuO_6 under the galvanostatic cycling and mainly emphasized on the mechanism exploration of electrochemical reactions accounting for the Li extraction/removal.

6.2 Experimental methods

Li_7RuO_6 was synthesized via a traditional solid-state reaction from oxide precursors, RuO_2 (Sigma-Aldrich, 99.9%) and with 10% excess of Li_2O (Sigma-Aldrich, 99.9%) weighted under the stoichiometric ratio. The reactants were homogeneously ground by agate mortar and pestle. After appropriate amount of uniform reactant mixtures were pelletized, the pellets were transferred to an alumina crucible and sintered at 950°C for 20 hours in the oxygen atmosphere. After cooling to room temperature naturally, the as-

obtained sample was ground into fine powders and stored in the argon-filled glovebox for to-be measurements.

The method of electrode preparation can be found in Chapter 2. Here the as-prepared Li_7RuO_6 was used as the active material.

Details about the characterization methods can be found in chapter 2. Galvanostatic cycling in Li cells was conducted at 25°C. Characterization was carried out using powder X-ray diffraction and X-ray absorption spectroscopy in synchrotron and neutron facilities are detailed in Chapter 2.

6.3 Structural Characterization of Li_7RuO_6

The pristine Li_7RuO_6 belongs to an extended family of lithium hexaoxometalates and crystals into a triclinic metric with a space group $P\bar{1}$.^{238, 239} In order to understand the phase purity and structural details of the pristine Li_7RuO_6 , the high resolution SXRD and TOF-NPD were collected. A joint Rietveld refinement was performed for the detailed structural information (Figure 6-1). In spite of small diffraction peaks which are attributed to impurities like minor Li_3RuO_4 , unknown phase and some Li_2O (Figure 6-2), consistent with previous reports, most of the diffraction peaks can be indexed with the previously reported lattice of Li_7RuO_6 , reflecting the predominance of Li_7RuO_6 phase in the sample. Within the structure, oxygen atoms constitute into a slightly distorted hexagonal closed packing (hcp). Ru occupies the octahedral sites and RuO_6 octahedra are connected to each other via strong distorted octahedral of $\text{Li}(4)\text{O}_6$. Half of the tetrahedral interstices between the resulting slabs $[\text{Li}(4)_{1/3}\text{Ru}_{1/3}\square_{1/3}\text{O}_2]$ (\square represents the cationic vacancies) are filled with Li(1)-Li(3) atoms, building a double layer of edge-shared $(\text{Li}(1-3)\text{O}_4)$ tetrahedra. The Ru adopts a slightly distorted environment with two short, two middle and two long Ru-O distances of 1.978, 1.987, and 1.994 Å, respectively, with Ru displaced from the octahedron center. The detailed information derived from the Rietveld refinement is listed in Table 6-1 and the structure is shown in Figure 6-3.

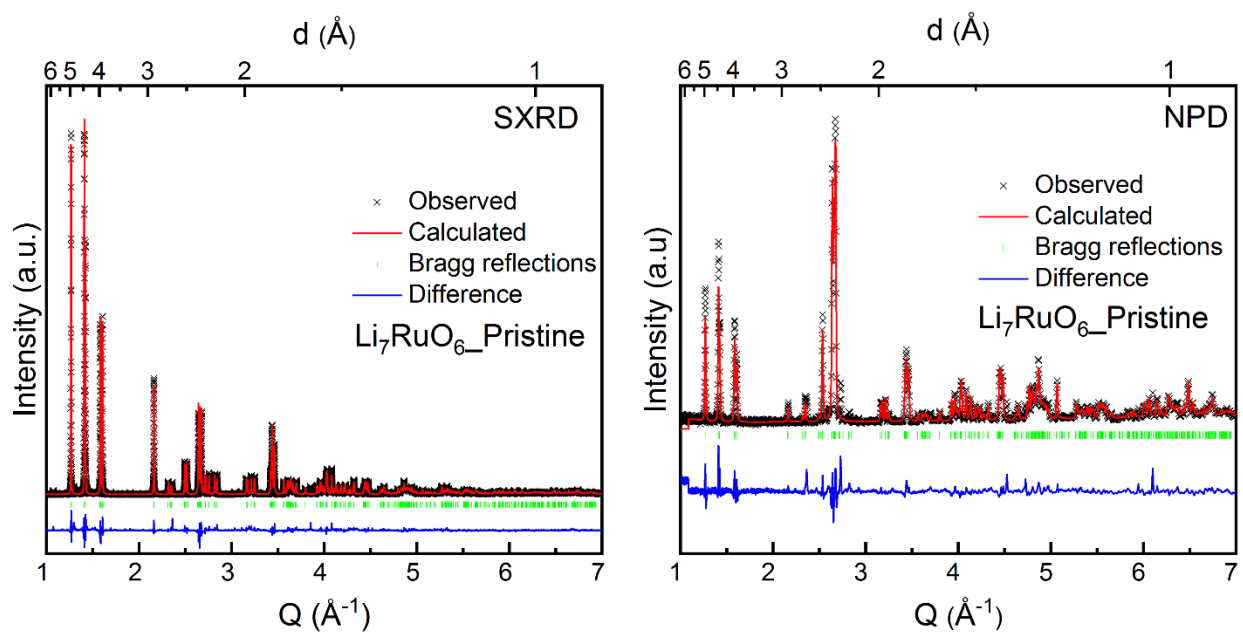


Figure 6-1. Joint Rietveld refinement of SXR and NPD patterns of Li_7RuO_6 pristine. Black crosses: experimental patterns, red solid line: calculated patterns, blue solid line: difference and green bars: Bragg reflections.

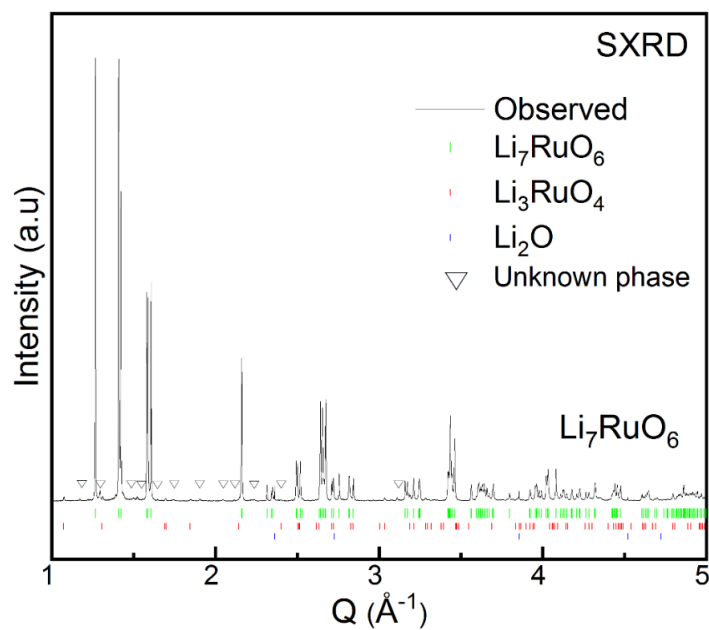


Figure 6-2. SXR patterns of Li_7RuO_6 pristine sample and the Bragg diffractions of references. The down triangles signify the unknown phase.

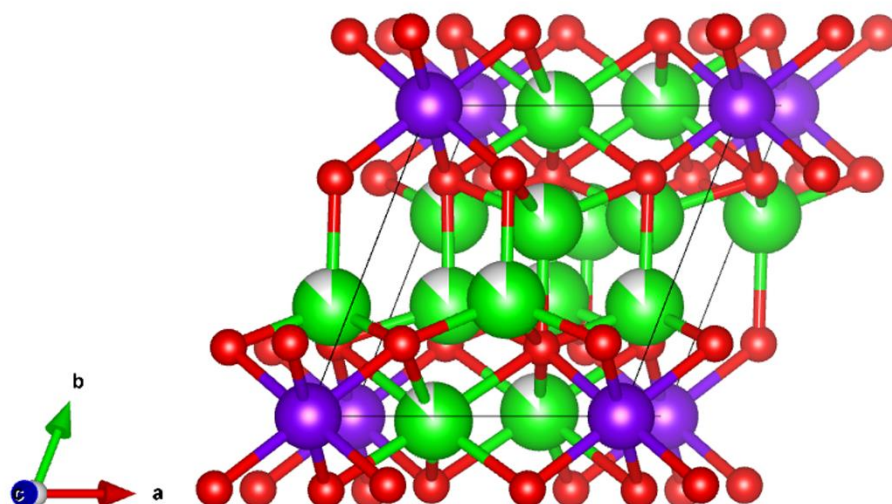


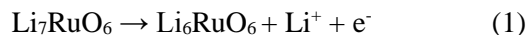
Figure 6-3. Crystal structure of pristine Li_7RuO_6 . Red sphere represents oxygen atom, and green sphere represent lithium atom, and purple sphere represents ruthenium atom.

Table 6-1. Crystallographic parameters and reliability factors extracted from the combined Rietveld refinement of SXRD and NPD for Li_7RuO_6 .

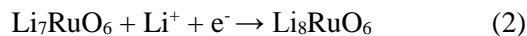
Li_7RuO_6						
Space group: $\text{P}\bar{1}$; $a = 5.36567 \text{ \AA}$; $b = 5.86049 \text{ \AA}$; $c = 5.35015 \text{ \AA}$; $\alpha = 117.1729^\circ$; $\beta = 119.1174^\circ$; $\gamma = 62.6432^\circ$; $V = 124.511 \text{ \AA}^3$						
Atom	Wyckoff position	x	y	z	Uiso (\AA^2)	Occupancy
Ru1	1a	0.000000	0.000000	0.000000	0.01112(14)	1.000
O1	2i	0.9030(4)	0.2367(4)	0.3716(4)	0.01582(25)	1.000
O2	2i	0.2203(5)	0.2334(4)	0.0797(4)	0.01582(25)	1.000
O3	2i	0.3728(4)	0.7782(4)	0.2371(4)	0.01582(25)	1.000
Li1	2i	0.5025(19)	0.3755(19)	0.1056(19)	0.0343(8)	0.8750
Li2	2i	0.0948(18)	0.6477(18)	0.2413(18)	0.0343(8)	0.8750
Li3	2i	0.7565(18)	0.6438(18)	0.4940(18)	0.0343(8)	0.8750
Li4	2i	0.6375(20)	0.0147(14)	0.3144(20)	0.0343(8)	0.8750
$R_{\text{WP}} = 14.220\%$; $\chi^2 = 2.98$						

6.3 Voltage cutoff window of 2.6-3.68 V

Similar to our previous report,²⁰⁷ the electrochemical properties in terms of potential-composition profiles were evaluated in galvanostatical conditions under two separate windows: 2.6-3.68 V and 1.5-2.6 V vs Li⁺/Li⁰. In the first window, the initial oxidation of Li₇RuO₆ was carried out, to explore the following hypothetical reaction:



Meanwhile, the reduction of Li₇RuO₆ was the incipient step in the latter voltage window, corresponding to the following hypothetical reaction:



Starting with a step of oxidation, the electrochemical cell displayed a long plateau at around 3.1 V, corresponding to a capacity equivalent to 0.7 mol Li per mol compound (Figure 6-4a). The differential capacity curve showed a sharp process centered at 3.1 V and a small shoulder at higher potential (Figure 6-4b), consistent with the charge profile. Further oxidation to 3.68 V proceeded via a plateau ~3.67 V with an accumulation of the capacity equivalent to 0.6 mol Li per mol Ru (Figure 6-4a). The reverse reduction consisted of a steep voltage drop and a small 2.9-V plateau (Figure 6-4a) with a sharp peak in the differential capacity plot (Figure 6-4b). During the reduction, an overall 0.5 mol Li per mol compound was reinserted into the delithiated Li₇RuO₆. In addition, the disappearance of the 3.68 V plateau demonstrates an electrochemical irreversibility at high voltage. Indeed, if charging was allowed to proceed beyond 3.68 V, the chemical profile presented a very long plateau with an unreasonably high capacity, followed by a sharp voltage fall with a substantial capacity loss during reduction (Figure 6-5a). This observation confirms excessive charging leads to an irreversible process that destroys the function of the oxide. In contrast, the presence of the 2.9 V plateau reflects a reasonable reversibility at relative low voltage with a small voltage hysteresis (Figure 6-4b). Upon subsequent cycling, the electrochemical profile underwent a gradual

disappearance of the 3.1 V plateau followed by a sloping shape upon charge and a gradual shortening of the plateau upon discharge and the total capacity diminished (Figures 6-4c and 6-4d). The voltage profiles demonstrated a similar evolution with cycling even for an electrochemical experiment with a constrained cutoff voltage of 3.5 V (Figure 6-5b), indicating that the reversible process also suffered from long-term loss.

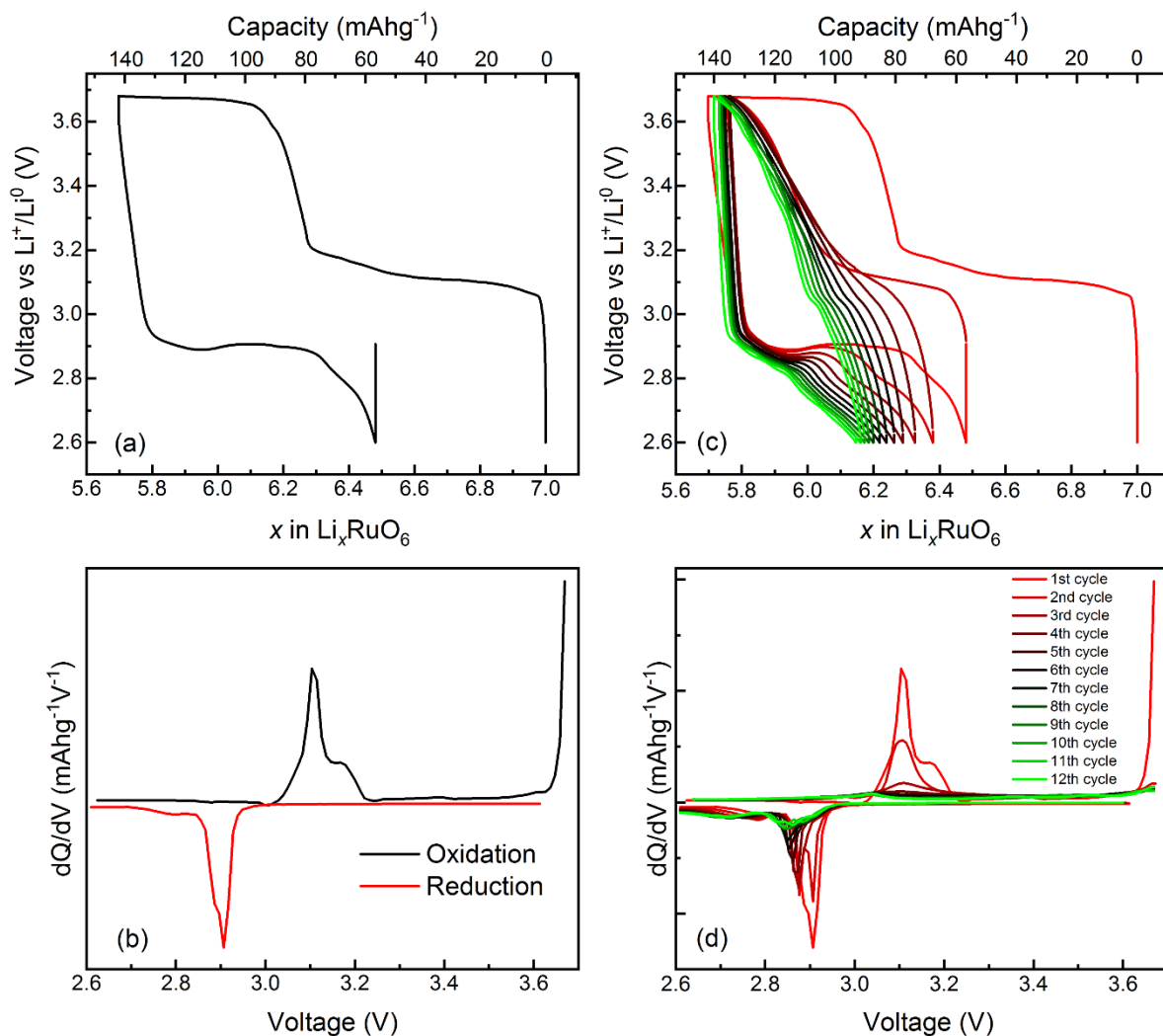


Figure 6-4. Voltage-composition profile of Li_7RuO_6 in the voltage window of 2.6-3.68 V upon the first cycling (a) and (c) upon extensive cycling. The dQ-dV plots of the first charge-discharge process (b) and the extensive cycling processes (d).

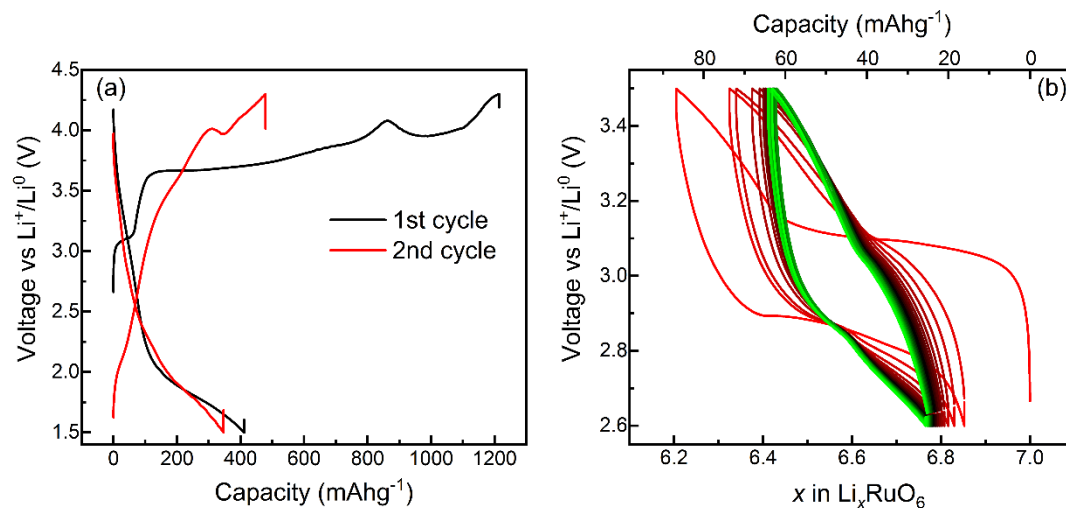


Figure 6-5. (a) Voltage-capacity profiles of Li_7RuO_6 between 1.5 and 4.3 V. (b) Voltage-composition profiles of Li_7RuO_6 under a constrained voltage window between 2.6 V and 3.5 V upon extensive cycling.

In order to assess the structural variation coupled with the delithiation, *ex situ* SXRD data were collected at different states of charge (Figure 6-6). The oxidation to 3.4 V brought about new Bragg peaks, suggesting a variation in the crystal symmetry and likely a change in volume of the unit cell. The peak broadening and loss of intensity associated with the extraction of Li reflected a decrease in crystallinity. This pattern could not be matched to any known phases. As a result, the structure of the charged state could not be solved and remains under study. The final structure harvested at the full oxidation resembled the previous state without a shift of peak positions, except a little broadening in peak width and a small reduction in peak intensity, implying a minimal loss in the crystallinity related to the further oxidation. The subsequent reduction with Li reinsertion largely recovered the peak positions to the pristine state, indicating a reversible process, but with a minor reduction in the peak intensity and a small peak broadening, suggesting a permanent decrease in crystallinity from the electrochemical reactions. The SXRD data collected after the 2nd cycle demonstrated the same pattern evolution as the first cycle (Figure 6-6b), further supporting the reversible (de)intercalation process.

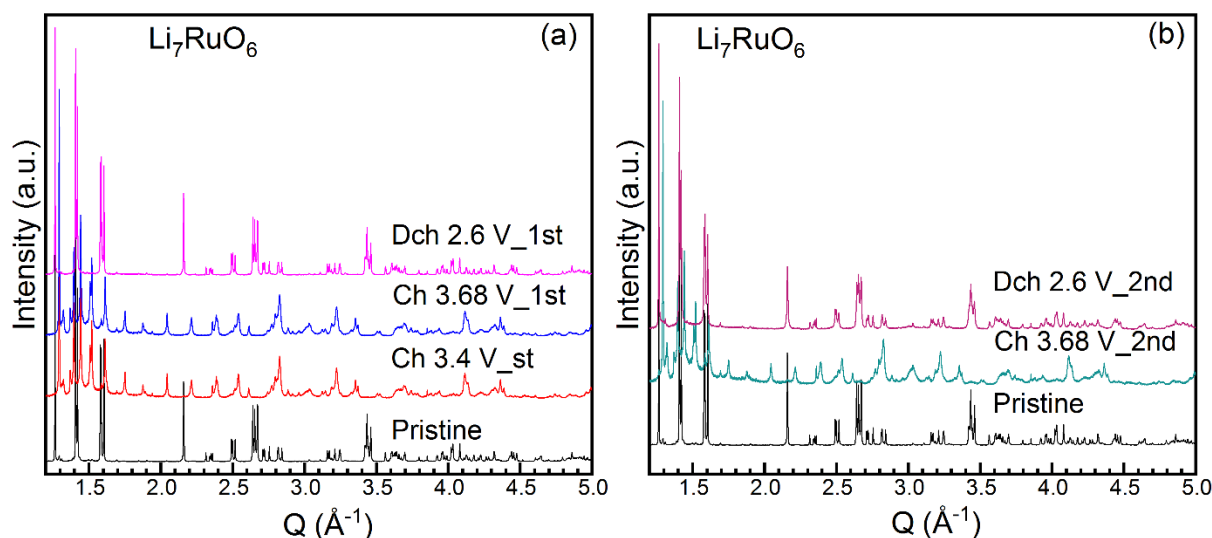


Figure 6-6. *Ex situ* SXRD patterns of Li_7RuO_6 upon (a) the first and (b) the second charge and discharge in the voltage window of 2.6-3.68 V.

In order to understand the charge compensation mechanism associated with Li removal/insertion, *ex situ* Ru K-edge X-ray absorption near edge structure (XANES) spectroscopy was performed for Li_7RuO_6 samples at different states of charge. The first derivative of the spectrum was used to establish the position of the absorption edge, using the first inflection point above 22120 eV. The typical XANES spectrum is composed of two parts. The main absorption edge arises from the electric dipole-allowed transition from the $1s$ to $5p$ level, which could probe the variation of the oxidation state via monitoring the energy shift of the edge, whilst the pre-edge feature originates from two primary transitions. One is the electric quadrupole-allowed and dipole-forbidden $1s \rightarrow 4d$ transition. The probability of the electric quadrupole-allowed transition is much lower compared with the dipole, leading to a much weaker intensity in the pre-edge peak. However, certain symmetry-breaking-induced distortions of an octahedron can eliminate its inversion center, thus promoting the mixing between $4d$ and $5p$ orbitals, leading to an enhancement in the intensity of the pre-edge feature. The pre-edge peak of pristine Li_7RuO_6 has very low intensity, indicating that the distortion induced by a displacement of Ru off the center of the RuO_6 octahedra did not appear to be enough

to induce visible pre-edge peaks. The oxidation state of Ru^{5+} in pristine Li_7RuO_6 was verified by comparing the absorption rising edge and the first derivative curve of the Ru K-edge XANES spectra with Ru^{4+}O_2 and $\text{Li}_3\text{Ru}^{5+}\text{O}_4$ (Figure 6-7).

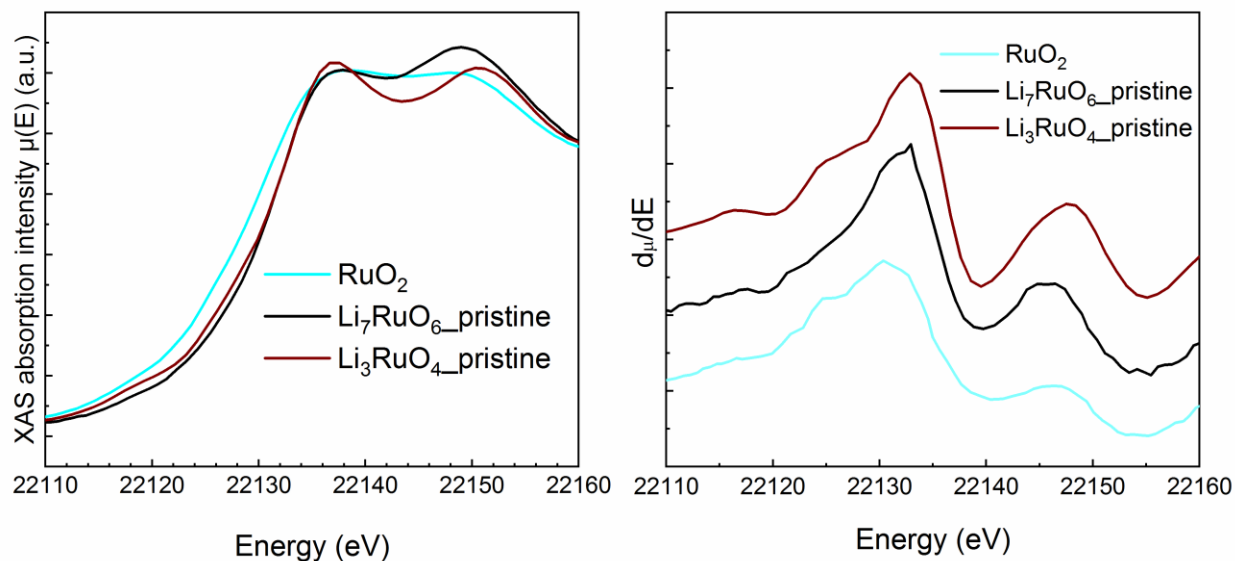


Figure 6-7. (a) *Ex situ* Ru K-edge XANES spectra of RuO_2 reference, Li_7RuO_6 pristine, and Li_3RuO_4 pristine and (b) the corresponding first derivative.

Upon the initial oxidation of Li_7RuO_6 to 3.4 V, the absorption rising edge underwent a shift by (+0.8 eV) relative to the pristine state (Figure 6-8), clearly reflecting the oxidation of Ru with a final oxidation state less than (6+) based on the already reported energy position of K_2RuO_4 ⁹⁷. This observation is consistent with the fact that less than 1 mol electron was removed per mol compound. Further oxidation to 3.68 V did not affect either the position of the absorption edge or the pre-edge intensity in comparison with the previous state, confirming that depleted electrons should originate from other reactions in the cell, such as catalytic decomposition of the electrolyte. As a result, it was not studied further. The reverse reduction shifted the rising edge to lower energy to closely approach the pristine state (Figure 6-8), implying the reduction of Ru upon discharge with very high efficiency.

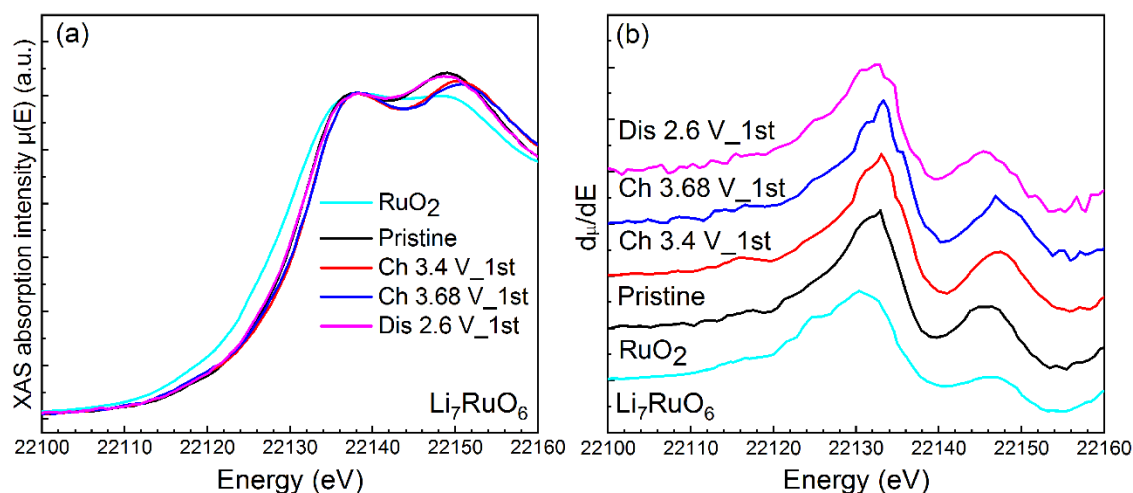


Figure 6-8. (a) *Ex situ* Ru K-edge XANES spectra of Li_7RuO_6 at different states of charge in the voltage window of 2.6-3.68 V as well as RuO_2 reference, and (b) the corresponding first derivative.

To explore the variation of the electronic structure of O during the same redox reactions, *ex situ* O K-edge XAS measurements were carried out. Note that the XAS spectra were measured simultaneously under both TEY and TFY modes. The TEY mode with a probing depth around 10 nm could provide the surface information, while the TFY mode probes 100-nm into the electrode, offering insight into the interior of the material. It is worthy of notice that spectral intensities in this mode are distorted by the self-absorption of fluorescent photons by the material, which is not present in TEY, so only qualitative trends between samples will be established.

The TFY O K-edge XAS spectrum of Li_7RuO_6 pristine displayed distinct pre-edge features centered at 528.4, 530.5, and 532 eV, respectively (Figure 6-9a). In terms of the TEY spectrum, the feature at ~ 528.4 eV was much lower (Figure 6-10a). In contrast, there was a very prominent peak at 533.8 eV (Figure 6-10), which has been attributed to the transition to π^* (C=O) orbitals in carbonated-related species (like Li_2CO_3) present on the sample surface (Figure 6-10b). Due to the presence of Li_2CO_3 and the potential side reactions on the surface, the analysis mainly focused on the TFY mode to probe volumes where the bulk dominates the signal (Figure 6-9).

In accordance with ligand field theory, the sharp peak at 528.4 eV is assigned to unoccupied orbitals of O 2p-Ru 4d states with an σ interaction, whereas the intensive signal at 532 eV and a shoulder at around 530.5 eV is assigned to unoccupied orbitals of O 2p-Ru 4d states with a π interaction. The complex lineshape in the pre-edge region strongly suggests a lifting of the t_{2g}/e_g degeneracy in an ideal octahedral field, consistent with the distortion of the RuO₆ octahedra in the rock-salt framework. The qualitatively lower intensity in the σ interaction-related peak compared to π interaction-related signals reflects the d^3 configuration of Ru(V). In terms of the small shoulder peak at 534.8 eV, it is tentatively assigned to the transition to the unoccupied states of O 2p hybridized with Ru 5s based on its high energy.²¹⁵

Upon the initial oxidation to 3.4 V, the peak at lowest energy redshifted by 0.3 eV concurrent with a noticeable intensity reduction relative to the pristine state (Figures 6-9a, 6-9b, and 6-9c). The intensive peak at 532 eV underwent a remarkable intensity rise, although the peak position was stable (Figures 6-9a, 6-9b, and 6-9d). The corresponding shoulder initially located at 530.5 eV moved to 531.1 eV with increased intensity. Compared to the pristine state, the oxidation gave rise to formation of a new shoulder feature at around 527.2 eV, indicating a formation of new unoccupied states. The O 1s core level strongly affected by the effective charge (Z_{eff}) on O can be reflected by the absorption edge inflection point obtained by the first derivative calculation of XAS spectrum. The Li removal led to little shift of the rising edge inflection point derived from the first derivative plot of the corresponding XAS spectra (Figure 6-11), suggesting the preservation of the Z_{eff} of O. The changes in the peak position and intensity of pre-edge part reflected the notable changes taking place in the hybridization of the O 2p-Ru 4d orbitals. Given the conservation of the Z_{eff} of O, those changes should originate from the Ru oxidation according to Ru K-edge XANES spectrum.

Further oxidation to 3.68 V remained the position of lower energy peak at around 528.1 eV but greatly raised its intensity in comparison with the previous state (Figures 6-9a, 6-9b, and 6-9c). This process brought about a minor increase in the intensity of the peak at 532 eV without modifying the position and slightly shifted the shoulder feature to lower energy with little variation in the intensity (Figures 6-9a, 6-9b, and 6-9d). In contrast, this oxidation largely increased the intensity of the shoulder at 527.2 eV generated

in the previous process (Figures 6-9a, 6-9b, and 6-9c), suggesting the augment of the unoccupied states. The inflection point in the absorption edge experienced little energy shift relative to the previous state as indicated by the arrow (Figure 6-11), indicating the remaining of the Z_{eff} of O. Considering that Ru states remained largely unchanged, based on the Ru K-edge XANES spectrum, those changes in the intensity should derive from oxygen electronic changes concurrent with the oxidation. The reverse reduction process restored the spectrum to the pristine state, implying a near reversible process consistent with the structural evolution according to XRD.

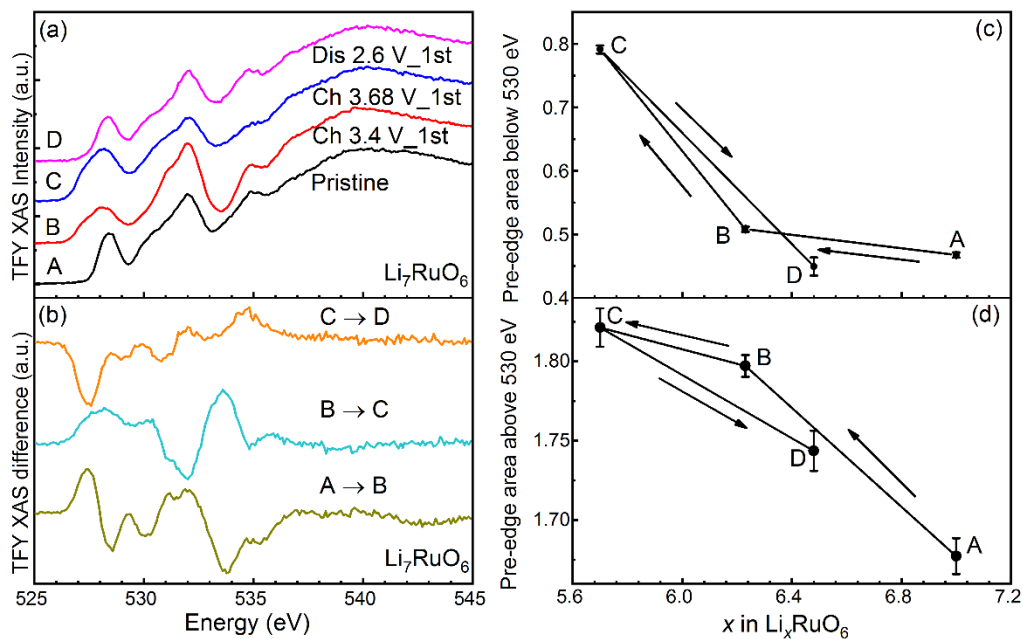


Figure 6-9. (a) *Ex situ* O K-edge XAS spectra of Li_7RuO_6 at different states of charge in the voltage window of 2.6-3.68 V measured under TFY mode. (b) Differential XAS spectra between states of charge indicated. (c) The integrated pre-edge area below 530 eV as a function of x in Li_xRuO_6 . (d) The dependence of the integrated pre-edge above 530 eV on x in Li_xRuO_6 .

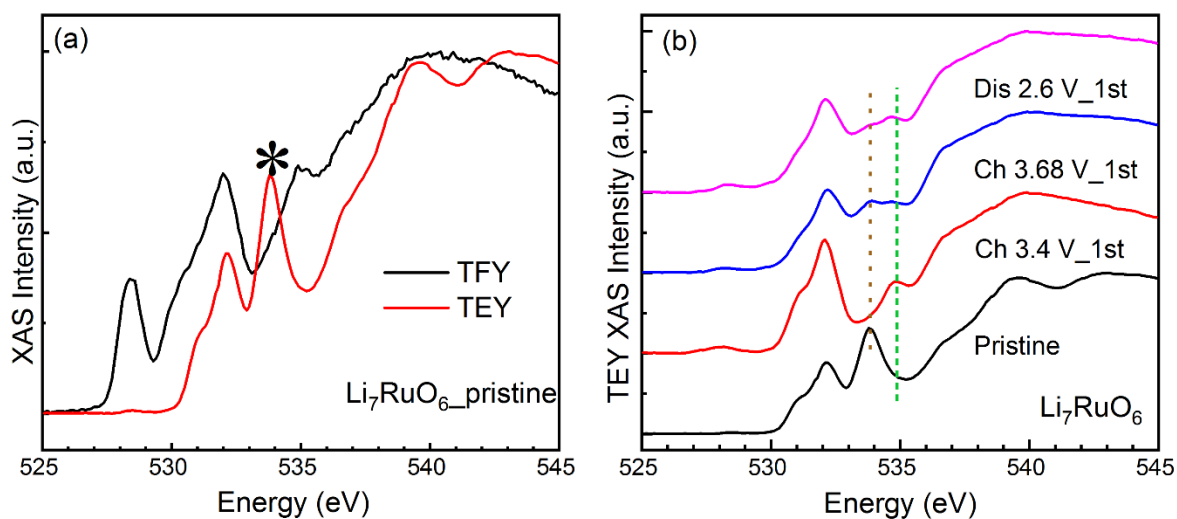


Figure 6-10. (a) *Ex situ* O K-edge XAS spectra of Li_7RuO_6 pristine state measured the total electron yield (TEY) mode and the total fluorescence yield (TFY) mode. The asterisk denotes a peak associated with the presence of Li_2CO_3 on the surface of the material. (b) *Ex situ* O K-edge XAS spectra of Li_7RuO_6 at different states of charge, measured in TEY mode. The green dot line denotes the preservation of the 535-eV feature in both modes. The purple short-dash line represents the feature associated with the carbonate-related species.

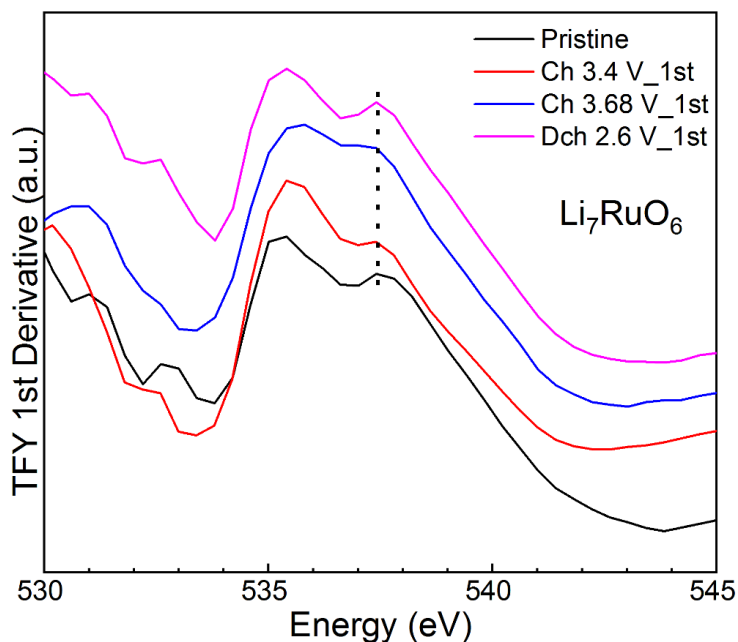


Figure 6-11. First derivative of the TFY O K-edge XAS spectra of Li_7RuO_6 at different states of charge in the voltage window of 2.6-3.68 V. The black dot line represents the reservation of the position of the inflection point.

6.4 Voltage cutoff window of 1.5-2.6 V

The galvanostatic testing was carried out to study the electrochemical performance of Li_7RuO_6 between 1.5 and 2.6 V. Upon the initial reduction to 1.5 V with the applied cationic current, the Li insertion proceeded via a long plateau at around 2.2 eV versus Li^+/Li (Figures 6-12a and 6-12b), accumulating a capacity equivalent to approximate 1 mol Li per mol compound. The reverse oxidation occurred at ~ 2.23 eV, concomitant with the extraction of 1 mol Li, reflecting minor voltage hysteresis. The profiles of subsequent cycling remained with a slight loss in the capacity (Figures 6-12c and 6-12d), indicating a high reversibility of the redox process associated Li^+ insertion/removal.

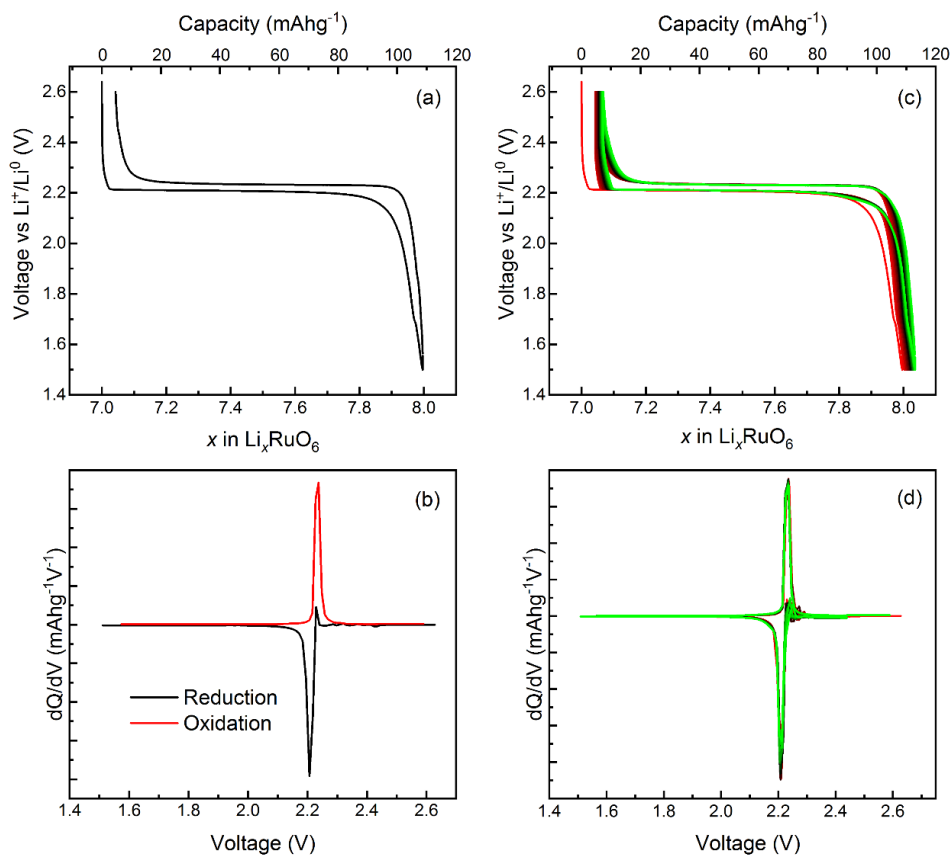


Figure 6-12. Voltage-composition profiles of Li_7RuO_6 in the voltage window between 1.5 and 2.6 V upon the first cycle (a) and upon extensive cycling processes (b). The dQ-dV plots of the first charge-discharge process (b) and the extensive cycling processes (d).

Ex situ SXRD was performed to explore the structural variation of Li_7RuO_6 with electrochemical reactions (Figure 6-13). The pattern after reduction to 1.5 V could be indexed to $R\bar{3}$ space group with a trigonal structure (Figure 6-14). Rietveld refinement was carried out to extract detailed structural information (Figure 6-14 and Table 6-2) and the resulting structure was shown in Figure 6-15. The results demonstrated that vacant sites in pristine Li_7RuO_6 were filled by the intercalated Li, leading to the formation of two kinds of Li with one occupying the tetrahedral sites in Li layers and the other in the octahedral sites in metal layers. The peak positions and intensity returned to the pristine state after the subsequent oxidation (Figure 6-13a), reflecting a highly reversible cycling process. Again, similar to the 2.5-3.68 V cycling voltage window, *ex situ* SXRD data collected after the 2nd discharge-charge cycle (Figure 6-13b) further substantiated the high chemical reversibility associated with Li insertion and removal.

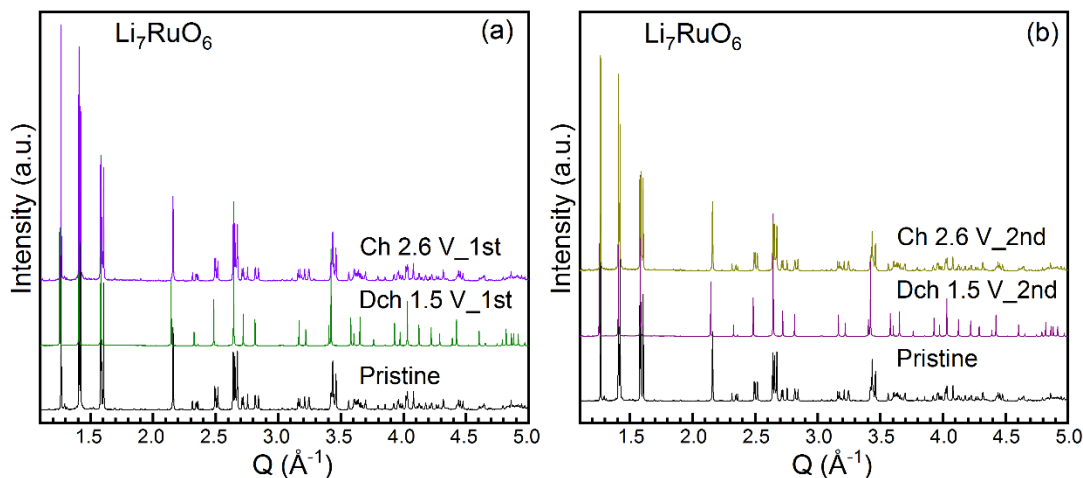


Figure 6-13. *Ex situ* SXRD patterns of Li_7RuO_6 upon (a) the first and (b) the second cycling between 1.5 V and 2.6 V.

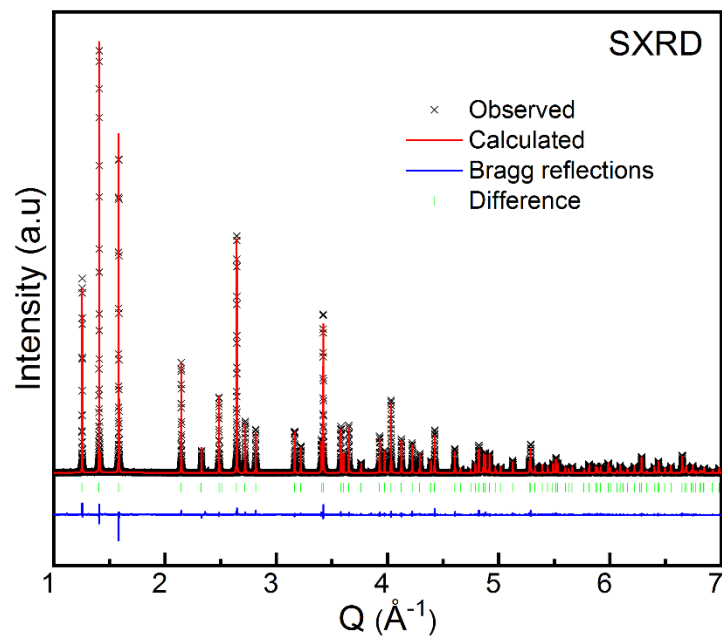


Figure 6-14. Rietveld refinement of SXRD patterns of Li_7RuO_6 after reduction to 1.5 V. Black crosses: experimental patterns, red solid line: calculated patterns, blue solid line: difference and green bars: Bragg reflections.

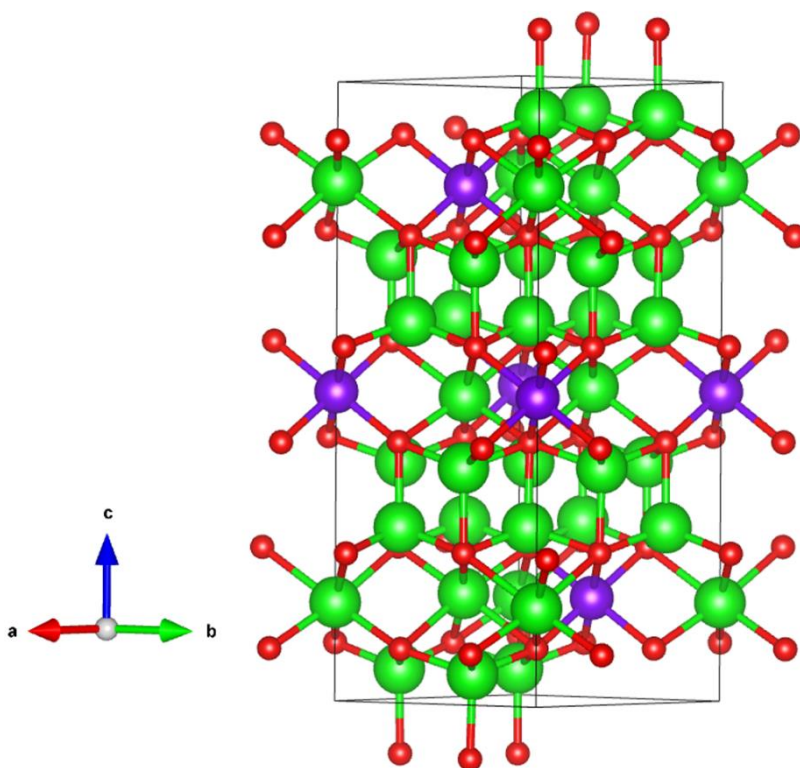


Figure 6-15. Crystal structure of pristine Li_8RuO_6 . Red sphere represents oxygen atom, and green sphere represent lithium atom, and purple sphere represents ruthenium atom.

Table 6-2. Crystallographic parameters and reliability factors extracted from the combined Rietveld refinement of SXRD for Li_7RuO_6 after reduction to 1.5 V.

Li_7RuO_6						
Space group: $R\bar{3}$; $a = 5.399156 \text{ \AA}$; $b = 5.399156 \text{ \AA}$; $c = 10.031876 \text{ \AA}$; $\alpha = 90^\circ$; $\beta = 90^\circ$; $\gamma = 120^\circ$; $V = 379.486 \text{ \AA}^3$						
Atom	Wyckoff position	x	y	z	Uiso (\AA^2)	Occupancy
Ru1	3a	0.33333	0.66667	0.16667	0.001	1.000
O1	18f	0.02331	0.65405	0.24524	0.004	1.000
Li3	18f	0.31870	1.02000	0.28389	0.008	1.000
Li4	6c	0.66667	1.33333	0.17400	0.014	1.000
$R_{\text{WP}} = 10.245\%$; $\chi^2 = 2.01$						

Similarly, *ex situ* Ru K-edge XANES spectra were collected to evaluate the change of the Ru oxidation state. The initial Li intercalation brought about a large low-energy shift of the absorption edge by 2.2 eV (Figure 6-16) closely vicinity to the position of RuO_2 , indicating the $\text{Ru}^{5+}/\text{Ru}^{4+}$ reduction. The subsequent oxidation reaction led to the recovery of the absorption edge position (Figure 6-16), clearly illustrating a reversible evolution of Ru electronic structure coupled with the interaction-deintercalation process.

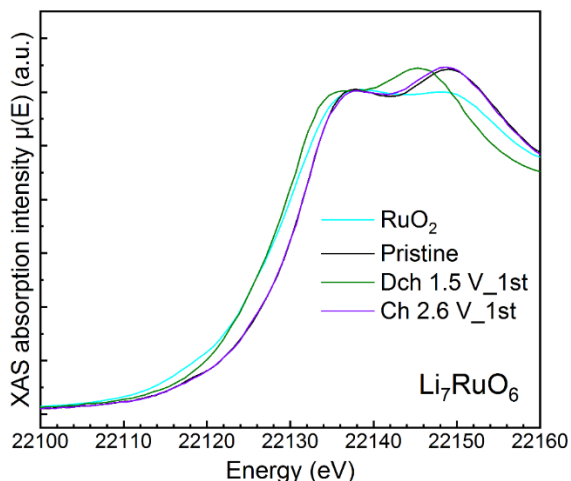


Figure 6-16. *Ex situ* Ru K-edge XANES spectra of Li_7RuO_6 at different states of charge in the 1.5-2.6 voltage window as well as the reference RuO_2 .

To explore the variation of the electronic structure of O during the same redox reactions, *ex situ* O K-edge XAS measurements were carried out (Figures 6-17a and 6-18a). Similar to the voltage window of 2.6-3.68, the focus was placed on the TFY spectra. The most visible change upon Li intercalation was the shift of the peak at lowest energy peak from 528.4 eV to 528.7 eV, concurrent to a noticeable decrease in its intensity associated with the occupation of the states at lowest energy in Li_7RuO_6 (Figures 6-17a, 6-17b, and 6-17c). The other spectral features underwent little variation in the position and a small reduction in the normalized integrated intensity (Figures 6-17a, 6-17b, and 6-17d). The absorption edge inflection point remained the same as the pristine state (Figure 6-18b), suggesting a constant effective charge on O atoms across the process.

The subsequent oxidation to 2.6 V restored the spectrum to the pristine state (Figures 6-17a, 6-17b, and 6-17d). The inflection point was preserved throughout the process, indicating little change in the charge of O (Figure 6-18b). The variations in the peak position and the intensity were consistent with the $\text{Ru}^{4+}/\text{Ru}^{5+}$ oxidation. Overall, the variation in the XAS spectra reflects a highly reversible intercalation reaction in the voltage window of 1.5-2.6 V.

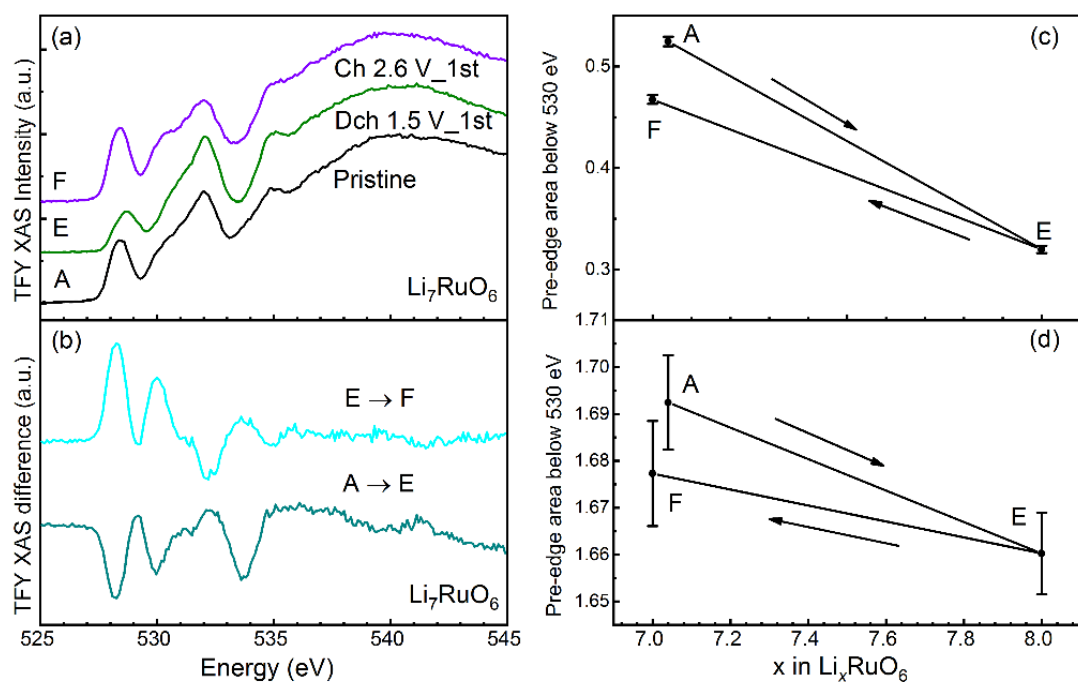


Figure 6-17. (a) *Ex situ* O K-edge XAS spectra of Li_7RuO_6 at different states of charge in the voltage window of 1.5–2.6 V V measured under TFY mode. (b) Differential XAS spectra between states of charge indicated. (c) The integrated pre-edge area below 530 eV as a function of x in Li_xRuO_6 . (d) The dependence of the integrated pre-edge above 530 eV on x in Li_xRuO_6 .

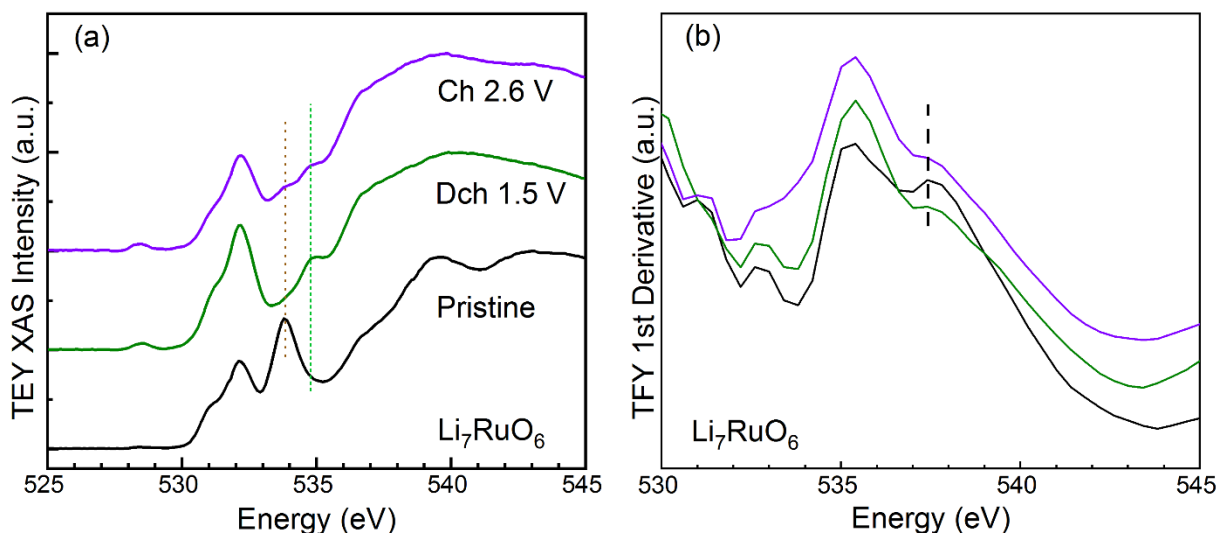


Figure 6-18. (a) *Ex situ* O K-edge XAS spectra of Li_7RuO_6 at different states of charge under the total electron yield (TEY) mode. The green dot line betokens the preservation of the 535-eV feature under both

modes. The purple dot line represents the feature associated with the carbonate-related species. (b) The first derivative plots of the TFY O K-edge XAS spectra of Li_7RuO_6 at different states of charge in the voltage window of 1.5-2.6 V. The black dash line represents the remaining of the position of the inflection point.

6.5. Conclusion

Li_7RuO_6 displays perfect reversibility between 1.5 and 2.6 V not only in the chemical point but in the electrochemical aspect. The electronic structure characterization in both Ru and O unambiguously demonstrate a classical Li (de)intercalation process with the charge compensation mechanism manifested as the changes in the formal oxidation state of Ru as a proxy for states with the Ru and O covalent hybridization. The behavior of Li_7RuO_6 in this voltage window can be used as a benchmark to better understand the electrochemical and chemical performance of Li_7RuO_6 at high voltage.

Li_7RuO_6 can undergo reversible Li deintercalation in the window 2.6-3.5 V, but it was comparably less efficient than at low potential. It is important to emphasize that reversible capacity was accompanied by a complete return to the initial chemical state, without any hysteresis. This observation places $\text{Li}_{7-x}\text{RuO}_6$ in staggering contrast with what we observed in $\text{Li}_{3-x}\text{RuO}_4$. It appears that this difference is underpinned by the significantly different charge compensation, with Ru having a strong participation in $\text{Li}_{7-x}\text{RuO}_6$, and not in $\text{Li}_{3-x}\text{RuO}_4$. The O participation is through this covalent interaction and does not involve tapping any existing lone pairs. In contrast, further oxidation to 3.68 V led to a distinct electrochemical behavior. The resulting additional capacity was associated with the lattice oxygen redox and little involvement of Ru redox. The reverse reduction was irreversible and resulted in a noticeable hysteresis, reflecting a different pathway from the oxidation, with a dominant contribution from Ru.

Chapter 7 Summary and future work

Lattice oxygen redox in Li-rich transition metal oxides has gained considerable attention since it can surpass the current barriers of performance by increasing the capacity of the cathode. However, several drawbacks impede large-scale practical application, which will remain unsolvable until unknowns in the underlying mechanisms of lattice oxygen redox are resolved. The focus of this thesis is to study the underpinnings of the mechanisms of lattice oxygen redox in a series of Li-rich 4d/5d transition metal oxides via various spectroscopic probes to establish a comprehensive picture of lattice oxygen redox.

For this purpose, Li_2RuO_3 , Li_3RuO_4 , Li_3IrO_4 and Li_7RuO_6 were studied. Li_2RuO_3 , one of the classical oxides proposed for lattice oxygen redox, displayed a dramatic evolution of its crystal and electronic structure during the first cycle with a large hysteresis, which notably decreased in subsequent cycles. X-ray spectroscopy revealed a different extent of involvement of Ru and O upon various (de)lithiation stages, indicating different pathways upon charge and discharge and possibly providing an explanation to the electrochemical hysteresis. Li_3RuO_4 exhibited unambiguous lattice oxygen redox upon first oxidation to 3.9 V, which unlocked a conventional cationic redox with the formal $\text{Ru}^{5+}/\text{Ru}^{4+}$ couple in the following re-intercalation to 2.5 V. This compound was also capable of reversible (de)lithiation accompanied by a conventional cationic redox with $\text{Ru}^{5+}/\text{Ru}^{4+}$ couple between 1.5 and 2.5 V. In spite of having the same O/M ratio as Li_3RuO_4 , Li_3IrO_4 displayed reversible activity of non-equivalent O sites with different number of non-bonding O 2p states in the pristine state. In contrast, this compound also presented a typical conventional interaction to $\text{Li}_{4.7}\text{IrO}_4$ accompanied by the formal oxidation of Ir in the reversible manner. Li_7RuO_6 , with the highest O/M ratio of all oxides evaluated, showed highly reversible lithiation to Li_8RuO_6 between 1.5 and 2.6 V, obeying a conventional cationic redox via the formal $\text{Ru}^{5+}/\text{Ru}^{4+}$ couple. In contrast to all other Ru oxides evaluated, Li_7RuO_6 underwent reversible delithiation to 3.5 V, but it was accompanied by a formal $\text{Ru}^{5+}/\text{Ru}^{6+}$ redox reaction.

The investigation in the charge compensation mechanism of electrochemical reactions of 4d/5d Li-rich transition metal oxides revealed that the covalent interaction between transition metal and oxygen plays a significant role in the charge compensation mechanism of Li (de)intercalation. Lattice oxygen redox triggers highly active oxygen species, which can be released in the form of molecule O_2 , leading to a different reduction from the oxidation, unless they are stabilized via the high covalent interaction. Our work revealed that the O/M ratio important to activate lattice oxygen redox, but it may be promoted through a disordered local structural arrangement between Li and M.

In spite of intensive studies in lattice oxygen redox, its mechanism is still not fully understood. Recent spectroscopic features uniquely associated as the fingerprint of lattice oxygen redox were not observed in our study even though lattice oxygen redox was clearly present. This indicates that “lattice oxygen redox” could actually encompass multiple different pathways, rather than a unique mechanism. The origins of these spectroscopic signals need to be further studied in the future by combining experimental observations and advanced computational techniques so as to fully understand lattice oxygen redox.

Even though Li-rich 4d/5d transition metal oxides display relatively reversible lattice oxygen redox, base metal oxides are required for practical application. We found that the highly covalent interaction between 4d/5d M and O could stabilize oxidized oxygen species generated during cycling. In contrast, the comparably lower covalence in base metal oxides cannot protect oxidized oxygen species from being evolved. Therefore, designing Li-rich base metal oxides with reversible lattice oxygen redox is still a challenge. Although the base metal oxides with specific structural arrangement exhibit relative reversible lattice oxygen redox, their cyclability is still unsatisfactory. The combination of covalence and structural order to design Li-rich base metal oxides with high reversible lattice oxygen redox should be a topic of future exploration.

Bibliography

1. Nagaura, T.; Tozawa, K., Lithium ion rechargeable battery. *Prog. Batteries Solar Cells* **1990**, 9, 209.
2. Whittingham, M. S., Lithium Batteries and Cathode Materials. *Chem. Rev.* **2004**, 104, (10), 4271-4302.
3. Tarascon, J. M.; Armand, M., Issues and challenges facing rechargeable lithium batteries. *Nature* **2001**, 414, (6861), 359-367.
4. Whittingham, M. S., Electrical Energy Storage and Intercalation Chemistry. *Science* **1976**, 192, (4244), 1126-1127.
5. Whittingham, M. S. Chalcogenide battery. U.S. 4,009,052 (Cl. 429-191), Appl. 673,696, 5 Apr 1976; 22 Feb 1977.
6. Armand, M. B., in *Materials for Advanced Batteries* Plenum, New York, 1980.
7. Murphy, D. W.; Di Salvo, F. J.; Carides, J. N.; Waszczak, J. V., Topochemical reactions of rutile related structures with lithium. *Mater. Res. Bull.* **1978**, 13, (12), 1395-1402.
8. Lazzari, M., A Cyclable Lithium Organic Electrolyte Cell Based on Two Intercalation Electrodes. *J. Electrochem. Soc.* **1980**, 127, (3), 773.
9. Goodenough, J. B.; Park, K.-S., The Li-Ion Rechargeable Battery: A Perspective. *J. Am. Chem. Soc.* **2013**, 135, (4), 1167-1176.
10. Christine, L.; Pierre, F.; Jean-Claude, P., *Electrochemistry*. Springer, 2009.
11. Ceder, G., Opportunities and challenges for first-principles materials design and applications to Li battery materials. *MRS Bull.* **2011**, 35, (9), 693-701.
12. Kang, K.; Meng, Y. S.; Bréger, J.; Grey, C. P.; Ceder, G., Electrodes with High Power and High Capacity for Rechargeable Lithium Batteries. *Science* **2006**, 311, (5763), 977-980.
13. Kang, B.; Ceder, G., Battery materials for ultrafast charging and discharging. *Nature* **2009**, 458, (7235), 190-193.
14. Etacheri, V.; Marom, R.; Elazari, R.; Salitra, G.; Aurbach, D., Challenges in the development of advanced Li-ion batteries: a review. *Energy Environ. Sci.* **2011**, 4, (9), 3243-3262.
15. Whittingham, M. S., Ultimate Limits to Intercalation Reactions for Lithium Batteries. *Chem. Rev.* **2014**, 114, (23), 11414-11443.
16. Xu, J.; Dou, S.; Liu, H.; Dai, L., Cathode materials for next generation lithium ion batteries. *Nano Energy* **2013**, 2, (4), 439-442.
17. Julien, C. M.; Mauger, A.; Zaghib, K.; Groult, H., Comparative Issues of Cathode Materials for Li-Ion Batteries. *Inorganics* **2014**, 2, (1), 132-154.
18. Shin, Y.; Manthiram, A., Factors Influencing the Capacity Fade of Spinel Lithium Manganese Oxides. *J. Electrochem. Soc.* **2004**, 151, (2), A204.

19. Aurbach, D.; Levi, M. D.; Gamulski, K.; Markovsky, B.; Salitra, G.; Levi, E.; Heider, U.; Heider, L.; Oesten, R., Capacity fading of $\text{Li}_x\text{Mn}_2\text{O}_4$ spinel electrodes studied by XRD and electroanalytical techniques. *J. Power Sources* **1999**, 81-82, 472-479.
20. Jang, D. H., Electrolyte Effects on Spinel Dissolution and Cathodic Capacity Losses in 4 V $\text{LiLi}_x\text{Mn}_2\text{O}_4$ Rechargeable Cells. *J. Electrochem. Soc.* **1997**, 144, (10), 3342.
21. Thackeray, M. M.; David, W. I. F.; Bruce, P. G.; Goodenough, J. B., Lithium insertion into manganese spinels. *Mater. Res. Bull.* **1983**, 18, (4), 461-472.
22. Thackeray, M. M.; Johnson, P. J.; de Picciotto, L. A.; Bruce, P. G.; Goodenough, J. B., Electrochemical extraction of lithium from LiMn_2O_4 . *Mater. Res. Bull.* **1984**, 19, (2), 179-187.
23. Xia, Y., Capacity Fading on Cycling of 4 V $\text{LiLiMn}_2\text{O}_4$ Cells. *J. Electrochem. Soc.* **1997**, 144, (8), 2593.
24. Dai, Y.; Cai, L.; White, R. E., Capacity Fade Model for Spinel LiMn_2O_4 Electrode. *J. Electrochem. Soc.* **2012**, 160, (1), A182-A190.
25. Wang, J.; Sun, X., Understanding and recent development of carbon coating on LiFePO_4 cathode materials for lithium-ion batteries. *Energy Environ. Sci.* **2012**, 5, (1), 5163-5185.
26. Wang, J.; Yang, J.; Tang, Y.; Li, R.; Liang, G.; Sham, T.-K.; Sun, X., Surface aging at olivine LiFePO_4 : a direct visual observation of iron dissolution and the protection role of nano-carbon coating. *J. Mater. Chem. A* **2013**, 1, (5), 1579-1586.
27. Wang, J.; Yang, J.; Zhang, Y.; Li, Y.; Tang, Y.; Banis, M. N.; Li, X.; Liang, G.; Li, R.; Sun, X., Interaction of Carbon Coating on LiFePO_4 : A Local Visualization Study of the Influence of Impurity Phases. *Adv. Funct. Mater.* **2013**, 23, (7), 806-814.
28. Padhi, A. K., Phospho-olivines as Positive-Electrode Materials for Rechargeable Lithium Batteries. *J. Electrochem. Soc.* **1997**, 144, (4), 1188.
29. Geller, S.; Durand, J. L., Refinement of the structure of LiMnPO_4 . *Acta Crystallogr.* **1960**, 13, (4), 325-331.
30. Santoro, R. P.; Newnham, R. E., Antiferromagnetism in LiFePO_4 . *Acta Crystallogr.* **1967**, 22, (3), 344-347.
31. Moring, J.; Kostiner, E., The crystal structure of NaMnPO_4 . *J. Solid State Chem.* **1986**, 61, (3), 379-383.
32. Prosini, P. P.; Lisi, M.; Zane, D.; Pasquali, M., Determination of the chemical diffusion coefficient of lithium in LiFePO_4 . *Solid State Ion.* **2002**, 148, (1), 45-51.
33. Prosini, P. P.; Zane, D.; Pasquali, M., Improved electrochemical performance of a LiFePO_4 -based composite cathode. *Electrochim. Acta* **2001**, 46, (23), 3517-3523.
34. Amin, R.; Balaya, P.; Maier, J., Anisotropy of Electronic and Ionic Transport in LiFePO_4 Single Crystals. *Electrochem. Solid-State Lett.* **2007**, 10, (1), A13.
35. Mizushima, K.; Jones, P. C.; Wiseman, P. J.; Goodenough, J. B., Li_xCoO_2 ($0 < x < -1$): A new cathode material for batteries of high energy density. *Mater. Res. Bull.* **1980**, 15, (6), 783-789.

36. Cho, J.; Kim, Y. J.; Park, B., Novel LiCoO₂ Cathode Material with Al₂O₃ Coating for a Li Ion Cell. *Chem. Mater.* **2000**, 12, (12), 3788-3791.
37. Dahn, J. R., Rechargeable LiNiO₂/Carbon Cells. *J. Electrochem. Soc.* **1991**, 138, (8), 2207.
38. Dahn, J. R.; von Sacken, U.; Michal, C. A., Structure and electrochemistry of Li_{1±y}NiO₂ and a new Li₂NiO₂ phase with the Ni(OH)₂ structure. *Solid State Ion.* **1990**, 44, (1), 87-97.
39. Ohzuku, T., Electrochemistry and Structural Chemistry of LiNiO₂ (R3m) for 4 Volt Secondary Lithium Cells. *J. Electrochem. Soc.* **1993**, 140, (7), 1862.
40. Li, W.; Reimers, J. N.; Dahn, J. R., In situ x-ray diffraction and electrochemical studies of Li_{1-x}NiO₂. *Solid State Ion.* **1993**, 67, (1), 123-130.
41. Delmas, C.; Pérès, J. P.; Rougier, A.; Demourgues, A.; Weill, F.; Chadwick, A.; Broussely, M.; Pertion, F.; Biensan, P.; Willmann, P., On the behavior of the Li_xNiO₂ system: an electrochemical and structural overview. *J. Power Sources* **1997**, 68, (1), 120-125.
42. Dahn, J. R.; Fuller, E. W.; Obrovac, M.; von Sacken, U., Thermal stability of Li_xCoO₂, Li_xNiO₂ and λ-MnO₂ and consequences for the safety of Li-ion cells. *Solid State Ion.* **1994**, 69, (3), 265-270.
43. Mishra, S. K.; Ceder, G., Structural stability of lithium manganese oxides. *Phys. Rev. B* **1999**, 59, (9), 6120-6130.
44. Thackeray, M. M., Manganese oxides for lithium batteries. *Prog. Solid State Chem.* **1997**, 25, (1), 1-71.
45. Reed, J.; Ceder, G.; Van Der Ven, A., Layered-to-Spinel Phase Transition in Li_xMnO₂. *Electrochem. Solid-State Lett.* **2001**, 4, (6), A78.
46. Delmas, C.; Saadoune, I., Electrochemical and physical properties of the Li_xNi_{1-y}Co_yO₂ phases. *Solid State Ion.* **1992**, 53-56, 370-375.
47. Armstrong, A. R.; Robertson, A. D.; Gitzendanner, R.; Bruce, P. G., The Layered Intercalation Compounds Li(Mn_{1-y}Co_y)O₂: Positive Electrode Materials for Lithium-Ion Batteries. *J. Solid State Chem.* **1999**, 145, (2), 549-556.
48. Armstrong, A. R.; Robertson, A. D.; Bruce, P. G., Structural transformation on cycling layered Li(Mn_{1-y}Co_y)O₂ cathode materials. *Electrochim. Acta* **1999**, 45, (1), 285-294.
49. Rossen, E.; Jones, C. D. W.; Dahn, J. R., Structure and electrochemistry of Li_xMn_yNi_{1-y}O₂. *Solid State Ion.* **1992**, 57, (3), 311-318.
50. Weaving, J. S.; Coowar, F.; Teagle, D. A.; Cullen, J.; Dass, V.; Bindin, P.; Green, R.; Macklin, W. J., Development of high energy density Li-ion batteries based on LiNi_{1-x-y}Co_xAl_yO₂. *J. Power Sources* **2001**, 97-98, 733-735.
51. Jo, M.; Noh, M.; Oh, P.; Kim, Y.; Cho, J., A New High Power LiNi_{0.81}Co_{0.1}Al_{0.09}O₂ Cathode Material for Lithium-Ion Batteries. *Adv. Energy Mater.* **2014**, 4, (13), 1301583.
52. Liu, Z.; Yu, A.; Lee, J. Y., Synthesis and characterization of LiNi_{1-x-y}Co_xMn_yO₂ as the cathode materials of secondary lithium batteries. *J. Power Sources* **1999**, 81-82, 416-419.

53. Yoshio, M.; Noguchi, H.; Itoh, J.-i.; Okada, M.; Mouri, T., Preparation and properties of $\text{LiCo}_y\text{Mn}_x\text{Ni}_{1-x-y}\text{O}_2$ as a cathode for lithium ion batteries. *J. Power Sources* **2000**, 90, (2), 176-181.
54. Robert, R.; Villevieille, C.; Novák, P., Enhancement of the high potential specific charge in layered electrode materials for lithium-ion batteries. *J. Mater. Chem. A* **2014**, 2, (23), 8589-8598.
55. Cho, Y.; Cho, J., Significant Improvement of $\text{LiNi}_{0.8}\text{Co}_{0.15}\text{Al}_{0.05}\text{O}_2$ Cathodes at 60°C by SiO_2 Dry Coating for Li-Ion Batteries. *J. Electrochem. Soc.* **2010**, 157, (6), A625.
56. Tsutomu, O.; Yoshinari, M., Layered Lithium Insertion Material of $\text{LiCo}_{1/3}\text{Ni}_{1/3}\text{Mn}_{1/3}\text{O}_2$ for Lithium-Ion Batteries. *Chem. Lett.* **2001**, 30, (7), 642-643.
57. Lu, Z.; MacNeil, D. D.; Dahn, J. R., Layered Cathode Materials $\text{Li}[\text{Ni}_x\text{Li}_{1/3-2x/3}]\text{Mn}_{2/3-x/3}\text{O}_2$ for Lithium-Ion Batteries. *Electrochem. Solid-State Lett.* **2001**, 4, (11), A191.
58. Kim, J. S.; Johnson, C. S.; Thackeray, M. M., Layered $x\text{LiMO}_2 \cdot (1-x)\text{Li}_2\text{M}'\text{O}_3$ electrodes for lithium batteries: a study of $0.95\text{LiMn}_{0.5}\text{Ni}_{0.5}\text{O}_2 \cdot 0.05\text{Li}_2\text{TiO}_3$. *Electrochem. Commun.* **2002**, 4, (3), 205-209.
59. Kim, J.-S.; Johnson, C. S.; Vaughey, J. T.; Thackeray, M. M.; Hackney, S. A.; Yoon, W.; Grey, C. P., Electrochemical and Structural Properties of $x\text{Li}_2\text{M}'\text{O}_3 \cdot (1-x)\text{LiMn}_{0.5}\text{Ni}_{0.5}\text{O}_2$ Electrodes for Lithium Batteries ($\text{M}' = \text{Ti, Mn, Zr}$; $0 \leq x \leq 0.3$). *Chem. Mater.* **2004**, 16, (10), 1996-2006.
60. Jansen, M.; Hoppe, R., Zur Kenntnis der NaCl -Strukturfamilie: Neue Untersuchungen an Li_2MnO_3 . *Z. Anorg. Allg. Chem.* **1973**, 397, (3), 279-289.
61. Strobel, P.; Lambert-Andron, B., Crystallographic and magnetic structure of Li_2MnO_3 . *J. Solid State Chem.* **1988**, 75, (1), 90-98.
62. Kalyani, P.; Chitra, S.; Mohan, T.; Gopukumar, S., Lithium metal rechargeable cells using Li_2MnO_3 as the positive electrode. *J. Power Sources* **1999**, 80, (1), 103-106.
63. Robertson, A. D.; Bruce, P. G., The origin of electrochemical activity in Li_2MnO_3 . *Chem. Commun.* **2002**, (23), 2790-2791.
64. Robertson, A. D.; Bruce, P. G., Mechanism of Electrochemical Activity in Li_2MnO_3 . *Chem. Mater.* **2003**, 15, (10), 1984-1992.
65. Koichi, N.; Chie, S.; Shoji, Y., Synthesis of Solid Solutions in a System of LiCoO_2 - Li_2MnO_3 for Cathode Materials of Secondary Lithium Batteries. *Chem. Lett.* **1997**, 26, (8), 725-726.
66. Numata, K.; Sakaki, C.; Yamanaka, S., Synthesis and characterization of layer structured solid solutions in the system of LiCoO_2 - Li_2MnO_3 . *Solid State Ion.* **1999**, 117, (3), 257-263.
67. Lu, Z.; Beaulieu, L. Y.; Donabarger, R. A.; Thomas, C. L.; Dahn, J. R., Synthesis, Structure, and Electrochemical Behavior of $\text{Li}[\text{Ni}_x\text{Li}_{1/3-2x/3}]\text{Mn}_{2/3-x/3}\text{O}_2$. *J. Electrochem. Soc.* **2002**, 149, (6), A778.
68. Lu, Z.; Dahn, J. R., Understanding the Anomalous Capacity of $\text{Li}/\text{Li}[\text{Ni}_x\text{Li}_{1/3-2x/3}]\text{Mn}_{2/3-x/3}\text{O}_2$ Cells Using In Situ X-Ray Diffraction and Electrochemical Studies. *J. Electrochem. Soc.* **2002**, 149, (7), A815.
69. Ammundsen, B.; Paulsen, J.; Davidson, I.; Liu, R.-S.; Shen, C.-H.; Chen, J.-M.; Jang, L.-Y.; Lee, J.-F., Local Structure and First Cycle Redox Mechanism of Layered $\text{Li}_{1.2}\text{Cr}_{0.4}\text{Mn}_{0.4}\text{O}_2$ Cathode Material. *J. Electrochem. Soc.* **2002**, 149, (4), A431.

70. Thackeray, M. M.; Kang, S.-H.; Johnson, C. S.; Vaughey, J. T.; Benedek, R.; Hackney, S. A., Li_2MnO_3 -stabilized LiMO_2 (M = Mn, Ni, Co) electrodes for lithium-ion batteries. *J. Mater. Chem.* **2007**, 17, (30), 3112.
71. Koga, H.; Croguennec, L.; Mannessiez, P.; Ménétrier, M.; Weill, F.; Bourgeois, L.; Duttine, M.; Suard, E.; Delmas, C., $\text{Li}_{1.20}\text{Mn}_{0.54}\text{Co}_{0.13}\text{Ni}_{0.13}\text{O}_2$ with Different Particle Sizes as Attractive Positive Electrode Materials for Lithium-Ion Batteries: Insights into Their Structure. *J. Phys. Chem. C* **2012**, 116, (25), 13497-13506.
72. Okubo, M.; Yamada, A., Molecular Orbital Principles of Oxygen-Redox Battery Electrodes. *ACS Appl. Mater. interfaces* **2017**, 9, (42), 36463-36472.
73. Sathiya, M.; Rousse, G.; Ramesha, K.; Laisa, C. P.; Vezin, H.; Sougrati, M. T.; Doublet, M. L.; Foix, D.; Gonbeau, D.; Walker, W.; Prakash, A. S.; Ben Hassine, M.; Dupont, L.; Tarascon, J. M., Reversible anionic redox chemistry in high-capacity layered-oxide electrodes. *Nat. Mater.* **2013**, 12, (9), 827-35.
74. McCalla, E.; Abakumov, A. M.; Saubanère, M.; Foix, D.; Berg, E. J.; Rousse, G.; Doublet, M.-L.; Gonbeau, D.; Novák, P.; Van Tendeloo, G.; Dominko, R.; Tarascon, J.-M., Visualization of O-O peroxo-like dimers in high-capacity layered oxides for Li-ion batteries. *Science* **2015**, 350, (6267), 1516-1521.
75. Sathiya, M.; Ramesha, K.; Rousse, G.; Foix, D.; Gonbeau, D.; Prakash, A. S.; Doublet, M. L.; Hemalatha, K.; Tarascon, J. M., High Performance $\text{Li}_2\text{Ru}_{1-y}\text{Mn}_y\text{O}_3$ ($0.2 \leq y \leq 0.8$) Cathode Materials for Rechargeable Lithium-Ion Batteries: Their Understanding. *Chem. Mater.* **2013**, 25, (7), 1121-1131.
76. Biffin, A.; Johnson, R. D.; Choi, S.; Freund, F.; Manni, S.; Bombardi, A.; Manuel, P.; Gegenwart, P.; Coldea, R., Unconventional magnetic order on the hyperhoneycomb Kitaev lattice in $\beta\text{-Li}_2\text{IrO}_3$: Full solution via magnetic resonant x-ray diffraction. *Phys. Rev. B* **2014**, 90, (20), 205116.
77. Takayama, T.; Kato, A.; Dinnebier, R.; Nuss, J.; Kono, H.; Veiga, L. S. I.; Fabbris, G.; Haskell, D.; Takagi, H., Hyperhoneycomb Iridate $\beta\text{-Li}_2\text{IrO}_3$ as a Platform for Kitaev Magnetism. *Phys. Rev. Lett.* **2015**, 114, (7), 077202.
78. Pearce, P. E.; Perez, A. J.; Rousse, G.; Saubanère, M.; Batuk, D.; Foix, D.; McCalla, E.; Abakumov, A. M.; Van Tendeloo, G.; Doublet, M.-L.; Tarascon, J.-M., Evidence for anionic redox activity in a tridimensional-ordered Li-rich positive electrode $\beta\text{-Li}_2\text{IrO}_3$. *Nat. Mater.* **2017**, 16, (5), 580-586.
79. Barpanda, P.; Ati, M.; Melot, B. C.; Rousse, G.; Chotard, J. N.; Doublet, M. L.; Sougrati, M. T.; Corr, S. A.; Jumas, J. C.; Tarascon, J. M., A 3.90 V iron-based fluorosulphate material for lithium-ion batteries crystallizing in the triplite structure. *Nat. Mater.* **2011**, 10, (10), 772-779.
80. Van der Ven, A.; Bhattacharya, J.; Belak, A. A., Understanding Li Diffusion in Li-Intercalation Compounds. *Acc. Chem. Res.* **2013**, 46, (5), 1216-1225.
81. Urban, A.; Lee, J.; Ceder, G., The Configurational Space of Rocksalt-Type Oxides for High-Capacity Lithium Battery Electrodes. *Adv. Energy Mater.* **2014**, 4, (13), 1400478.
82. Lee, J.; Urban, A.; Li, X.; Su, D.; Hautier, G.; Ceder, G., Unlocking the Potential of Cation-Disordered Oxides for Rechargeable Lithium Batteries. *Science* **2014**, 343, (6170), 519-522.

83. Kang, K.; Ceder, G., Factors that affect Li mobility in layered lithium transition metal oxides. *Phys. Rev. B* **2006**, 74, (9), 094105.
84. Seo, D. H.; Lee, J.; Urban, A.; Malik, R.; Kang, S.; Ceder, G., The structural and chemical origin of the oxygen redox activity in layered and cation-disordered Li-excess cathode materials. *Nat. Chem.* **2016**, 8, (7), 692-7.
85. Koyama, Y.; Tanaka, I.; Nagao, M.; Kanno, R., First-principles study on lithium removal from Li_2MnO_3 . *J. Power Sources* **2009**, 189, (1), 798-801.
86. Yabuuchi, N.; Nakayama, M.; Takeuchi, M.; Komaba, S.; Hashimoto, Y.; Mukai, T.; Shiiba, H.; Sato, K.; Kobayashi, Y.; Nakao, A.; Yonemura, M.; Yamanaka, K.; Mitsuhashi, K.; Ohta, T., Origin of stabilization and destabilization in solid-state redox reaction of oxide ions for lithium-ion batteries. *Nat. Commun.* **2016**, 7, (1), 13814.
87. Lee, J.; Seo, D.-H.; Balasubramanian, M.; Twu, N.; Li, X.; Ceder, G., A new class of high capacity cation-disordered oxides for rechargeable lithium batteries: Li–Ni–Ti–Mo oxides. *Energy Environ. Sci.* **2015**, 8, (11), 3255-3265.
88. Wang, R.; Li, X.; Liu, L.; Lee, J.; Seo, D.-H.; Bo, S.-H.; Urban, A.; Ceder, G., A disordered rock-salt Li-excess cathode material with high capacity and substantial oxygen redox activity: $\text{Li}_{1.25}\text{Nb}_{0.25}\text{Mn}_{0.5}\text{O}_2$. *Electrochem. Commun.* **2015**, 60, 70-73.
89. Chen, R.; Ren, S.; Yavuz, M.; Guda, A. A.; Shapovalov, V.; Witter, R.; Fichtner, M.; Hahn, H., Li^+ intercalation in isostructural Li_2VO_3 and $\text{Li}_2\text{VO}_2\text{F}$ with O^{2-} and mixed O^{2-}/F^- anions. *Phys. Chem. Chem. Phys.* **2015**, 17, (26), 17288-17295.
90. Freire, M.; Kosova, N. V.; Jordy, C.; Chateigner, D.; Lebedev, O. I.; Maignan, A.; Pralong, V., A new active Li-Mn-O compound for high energy density Li-ion batteries. *Nat. Mater.* **2016**, 15, (2), 173-7.
91. Yabuuchi, N.; Takeuchi, M.; Komaba, S.; Ichikawa, S.; Ozaki, T.; Inamasu, T., Synthesis and electrochemical properties of $\text{Li}_{1.3}\text{Nb}_{0.3}\text{V}_{0.4}\text{O}_2$ as a positive electrode material for rechargeable lithium batteries. *Chem. Commun.* **2016**, 52, (10), 2051-2054.
92. Xie, Y.; Saubanère, M.; Doublet, M. L., Requirements for reversible extra-capacity in Li-rich layered oxides for Li-ion batteries. *Energy Environ. Science* **2017**, 10, (1), 266-274.
93. Ukei, K.; Suzuki, H.; Shishido, T.; Fukuda, T., Li_3NbO_4 . *Acta Crystallogr. Sect. C* **1994**, 50, (5), 655-656.
94. Bush, T. S.; Catlow, C. R. A.; Battle, P. D., Evolutionary programming techniques for predicting inorganic crystal structures. *J. Mater. Chem.* **1995**, 5, (8), 1269-1272.
95. Alexander, A.; Battle, P. D.; Burley, J. C.; Gallon, D. J.; Grey, C. P.; Kim, S. H., Structural and magnetic properties of Li_3RuO_4 . *J. Mater. Chem.* **2003**, 13, (10), 2612.
96. Jacquet, Q.; Perez, A.; Batuk, D.; Van Tendeloo, G.; Rousse, G.; Tarascon, J.-M., The $\text{Li}_3\text{Ru}_y\text{Nb}_{1-y}\text{O}_4$ ($0 \leq y \leq 1$) System: Structural Diversity and Li Insertion and Extraction Capabilities. *Chem. Mater.* **2017**, 29, (12), 5331-5343.
97. Jacquet, Q.; Iadecola, A.; Saubanère, M.; Lemarquis, L.; Berg, E. J.; Alves Dalla Corte, D.; Rousse, G.; Doublet, M.-L.; Tarascon, J.-M., Competition between Metal Dissolution and Gas Release in

- Li-Rich $\text{Li}_3\text{Ru}_y\text{Ir}_{1-y}\text{O}_4$ Model Compounds Showing Anionic Redox. *Chem. Mater.* **2018**, 30, (21), 7682-7690.
98. Perez, A. J.; Jacquet, Q.; Batuk, D.; Iadecola, A.; Saubanère, M.; Rousse, G.; Larcher, D.; Vezin, H.; Doublet, M.-L.; Tarascon, J.-M., Approaching the limits of cationic and anionic electrochemical activity with the Li-rich layered rocksalt Li_3IrO_4 . *Nat. Energy* **2017**, 2, (12), 954-962.
 99. Goodenough, J. B.; Kim, Y., Challenges for Rechargeable Li Batteries. *Chem. Mater.* **2010**, 22, (3), 587-603.
 100. Ceder, G.; Chiang, Y. M.; Sadoway, D. R.; Aydinol, M. K.; Jang, Y. I.; Huang, B., Identification of cathode materials for lithium batteries guided by first-principles calculations. *Nature* **1998**, 392, (6677), 694-696.
 101. Li, B.; Xia, D., Anionic Redox in Rechargeable Lithium Batteries. *Adv. Mater.* **2017**, 29, (48), 1701054.
 102. Rouxel, J., Anion–Cation Redox Competition and the Formation of New Compounds in Highly Covalent Systems. *Chem. Eur. J.* **1996**, 2, (9), 1053-1059.
 103. Rouxel, J., Some solid state chemistry with holes: Anion–cation redox competition in solids. *Curr. Sci.* **1997**, 73, (1), 31-39.
 104. Amatucci, G. G.; Tarascon, J. M.; Klein, L. C., CoO_2 , The End Member of the Li_xCoO_2 Solid Solution. *J. Electrochem. Soc.* **1996**, 143, (3), 1114.
 105. G. G., A. Investigations of the Structure, Electrochemistry, and Processing of the Layered Lithium Cobalt Dioxide Lithium Intercalation Host Material. Rutgers University, New Jersey, 1995.
 106. Aydinol, M. K.; Kohan, A. F.; Ceder, G.; Cho, K.; Joannopoulos, J., Ab initio study of lithium intercalation in metal oxides and metal dichalcogenides. *Phys. Rev. B* **1997**, 56, (3), 1354-1365.
 107. Yoon, W.-S.; Balasubramanian, M.; Chung, K. Y.; Yang, X.-Q.; McBreen, J.; Grey, C. P.; Fischer, D. A., Investigation of the Charge Compensation Mechanism on the Electrochemically Li-Ion Deintercalated $\text{Li}_{1-x}\text{Co}_{1/3}\text{Ni}_{1/3}\text{Mn}_{1/3}\text{O}_2$ Electrode System by Combination of Soft and Hard X-ray Absorption Spectroscopy. *J. Am. Chem. Soc.* **2005**, 127, (49), 17479-17487.
 108. Petersburg, C. F.; Li, Z.; Chernova, N. A.; Whittingham, M. S.; Alamgir, F. M., Oxygen and transition metal involvement in the charge compensation mechanism of $\text{LiNi}_{1/3}\text{Mn}_{1/3}\text{Co}_{1/3}\text{O}_2$ cathodes. *J. Mater. Chem.* **2012**, 22, (37), 19993-20000.
 109. Yoon, W.-S.; Kim, K.-B.; Kim, M.-G.; Lee, M.-K.; Shin, H.-J.; Lee, J.-M.; Lee, J.-S.; Yo, C.-H., Oxygen Contribution on Li-Ion Intercalation–Deintercalation in LiCoO_2 Investigated by O K-Edge and Co L-Edge X-ray Absorption Spectroscopy. *J. Phys. Chem. B* **2002**, 106, (10), 2526-2532.
 110. Dahéron, L.; Dedryvère, R.; Martinez, H.; Ménétrier, M.; Denage, C.; Delmas, C.; Gonbeau, D., Electron Transfer Mechanisms upon Lithium Deintercalation from LiCoO_2 to CoO_2 Investigated by XPS. *Chem. Mater.* **2008**, 20, (2), 583-590.
 111. Lebens-Higgins, Z. W.; Faenza, N. V.; Radin, M. D.; Liu, H.; Sallis, S.; Rana, J.; Vinckeviciute, J.; Reeves, P. J.; Zuba, M. J.; Badway, F.; Pereira, N.; Chapman, K. W.; Lee, T.-L.; Wu, T.; Grey, C. P.; Melot, B. C.; Van Der Ven, A.; Amatucci, G. G.; Yang, W.; Piper, L. F. J., Revisiting the charge compensation mechanisms in $\text{LiNi}_{0.8}\text{Co}_{0.2-y}\text{Al}_y\text{O}_2$ systems. *Mater. Horiz.* **2019**, 6, (10), 2112

-2123.

112. Tarascon, J. M.; Vaughan, G.; Chabre, Y.; Seguin, L.; Anne, M.; Strobel, P.; Amatucci, G., In Situ Structural and Electrochemical Study of $\text{Ni}_{1-x}\text{Co}_x\text{O}_2$ Metastable Oxides Prepared by Soft Chemistry. *J. Solid State Chem.* **1999**, 147, (1), 410-420.
113. Zaanen, J.; Sawatzky, G. A.; Allen, J. W., Band gaps and electronic structure of transition-metal compounds. *Phys. Rev. Lett.* **1985**, 55, (4), 418-421.
114. Assat, G.; Tarascon, J.-M., Fundamental understanding and practical challenges of anionic redox activity in Li-ion batteries. *Nat. Energy* **2018**, 3, (5), 373-386.
115. Yu, D. Y. W.; Yanagida, K.; Kato, Y.; Nakamura, H., Electrochemical Activities in Li_2MnO_3 . *J. Electrochem. Soc.* **2009**, 156, (6), A417.
116. Armstrong, A. R.; Holzapfel, M.; Novák, P.; Johnson, C. S.; Kang, S.-H.; Thackeray, M. M.; Bruce, P. G., Demonstrating Oxygen Loss and Associated Structural Reorganization in the Lithium Battery Cathode $\text{Li}[\text{Ni}_{0.2}\text{Li}_{0.2}\text{Mn}_{0.6}]\text{O}_2$. *J. Am. Chem. Soc.* **2006**, 128, (26), 8694-8698.
117. Luo, K.; Roberts, M. R.; Hao, R.; Guerrini, N.; Pickup, D. M.; Liu, Y. S.; Edstrom, K.; Guo, J.; Chadwick, A. V.; Duda, L. C.; Bruce, P. G., Charge-compensation in 3d-transition-metal-oxide intercalation cathodes through the generation of localized electron holes on oxygen. *Nat. Chem.* **2016**, 8, (7), 684-91.
118. Strehle, B.; Kleiner, K.; Jung, R.; Chesneau, F.; Mendez, M.; Gasteiger, H. A.; Piana, M., The Role of Oxygen Release from Li- and Mn-Rich Layered Oxides during the First Cycles Investigated by On-Line Electrochemical Mass Spectrometry. *J. Electrochem. Soc.* **2017**, 164, (2), A400-A406.
119. Assat, G.; Iadecola, A.; Delacourt, C.; Dedryvère, R.; Tarascon, J.-M., Decoupling Cationic–Anionic Redox Processes in a Model Li-Rich Cathode via Operando X-ray Absorption Spectroscopy. *Chem. Mater.* **2017**, 29, (22), 9714-9724.
120. Saubanière, M.; McCalla, E.; Tarascon, J. M.; Doublet, M. L., The intriguing question of anionic redox in high-energy density cathodes for Li-ion batteries. *Energy Environ. Sci.* **2016**, 9, (3), 984-991.
121. Li, B.; Shao, R.; Yan, H.; An, L.; Zhang, B.; Wei, H.; Ma, J.; Xia, D.; Han, X., Understanding the Stability for Li-Rich Layered Oxide Li_2RuO_3 Cathode. *Adv. Funct. Mater.* **2016**, 26, (9), 1330-1337.
122. Hong, J.; Gent, W. E.; Xiao, P.; Lim, K.; Seo, D. H.; Wu, J.; Csernica, P. M.; Takacs, C. J.; Nordlund, D.; Sun, C. J.; Stone, K. H.; Passarello, D.; Yang, W.; Prendergast, D.; Ceder, G.; Toney, M. F.; Chueh, W. C., Metal-oxygen decoordination stabilizes anion redox in Li-rich oxides. *Nat. Mater.* **2019**, 18, (3), 256-265.
123. Lubin, F.; Lecerf, A.; Broussely, M.; Labat, J., Chemical lithium extraction from manganese oxides for lithium rechargeable batteries. *J. Power Sources* **1991**, 34, (2), 161-173.
124. Rossouw, M. H.; Thackeray, M. M., Lithium manganese oxides from Li_2MnO_3 for rechargeable lithium battery applications. *Mater. Res. Bull.* **1991**, 26, (6), 463-473.
125. Paik, Y.; Grey, C. P.; Johnson, C. S.; Kim, J.-S.; Thackeray, M. M., Lithium and Deuterium NMR Studies of Acid-Leached Layered Lithium Manganese Oxides. *Chem. Mater.* **2002**, 14, (12), 5109-5115.

126. Dogan, F.; Croy, J. R.; Balasubramanian, M.; Slater, M. D.; Iddir, H.; Johnson, C. S.; Vaughey, J. T.; Key, B., Solid State NMR Studies of Li_2MnO_3 and Li-Rich Cathode Materials: Proton Insertion, Local Structure, and Voltage Fade. *J. Electrochem. Soc.* **2014**, 162, (1), A235-A243.
127. Armstrong, A. R.; Bruce, P. G., Electrochemistry Beyond Mn^{4+} in $\text{Li}_x\text{Mn}_{1-y}\text{Li}_y\text{O}_2$. *Electrochem. Solid-State Lett.* **2004**, 7, (1), A1-A4.
128. Armstrong, A. R.; Bruce, P. G., Layered $\text{Li}_x\text{Mn}_{1-y}\text{Li}_y\text{O}_2$ intercalation electrodes: synthesis, structure and electrochemistry. *J. Mater. Chem.* **2005**, 15, (1), 218-224.
129. Francis Amalraj, S.; Markovsky, B.; Sharon, D.; Talianker, M.; Zinigrad, E.; Persky, R.; Haik, O.; Grinblat, J.; Lampert, J.; Schulz-Dobrick, M.; Garsuch, A.; Burlaka, L.; Aurbach, D., Study of the electrochemical behavior of the “inactive” Li_2MnO_3 . *Electrochim. Acta* **2012**, 78, 32-39.
130. Lee, E.; Persson, K. A., Structural and Chemical Evolution of the Layered Li-Excess Li_xMnO_3 as a Function of Li Content from First-Principles Calculations. *Adv. Energy Mater.* **2014**, 4, (15), 1400498.
131. Oishi, M.; Yamanaka, K.; Watanabe, I.; Shimoda, K.; Matsunaga, T.; Arai, H.; Ukyo, Y.; Uchimoto, Y.; Ogumi, Z.; Ohta, T., Direct observation of reversible oxygen anion redox reaction in Li-rich manganese oxide, Li_2MnO_3 , studied by soft X-ray absorption spectroscopy. *J. Mater. Chem. A* **2016**, 4, (23), 9293-9302.
132. Rana, J.; Papp, J. K.; Lebens-Higgins, Z.; Zuba, M.; Kaufman, L. A.; Goel, A.; Schmuck, R.; Winter, M.; Whittingham, M. S.; Yang, W.; McCloskey, B. D.; Piper, L. F. J., Quantifying the Capacity Contributions during Activation of Li_2MnO_3 . *ACS Energy Lett.* **2020**, 5, (2), 634-641.
133. Radin, M. D.; Vinckeviciute, J.; Seshadri, R.; Van der Ven, A., Manganese oxidation as the origin of the anomalous capacity of Mn-containing Li-excess cathode materials. *Nat. Energy* **2019**, 4, (8), 639-646.
134. Robertson, A. D.; Bruce, P. G., Overcapacity of $\text{Li}[\text{Ni}_x\text{Li}_{1/3-2x/3}\text{Mn}_{2/3-x/3}\text{O}_2]$ Electrodes. *Electrochem. Solid-State Lett.* **2004**, 7, (9), A294.
135. Armstrong, A. R.; Robertson, A. D.; Bruce, P. G., Overcharging manganese oxides: Extracting lithium beyond Mn^{4+} . *J. Power Sources* **2005**, 146, (1), 275-280.
136. Boulineau, A.; Simonin, L.; Colin, J.-F.; Bourbon, C.; Patoux, S., First Evidence of Manganese–Nickel Segregation and Densification upon Cycling in Li-Rich Layered Oxides for Lithium Batteries. *Nano Lett.* **2013**, 13, (8), 3857-3863.
137. Tran, N.; Croguennec, L.; Ménétrier, M.; Weill, F.; Biensan, P.; Jordy, C.; Delmas, C., Mechanisms Associated with the “Plateau” Observed at High Voltage for the Overlithiated $\text{Li}_{1.12}(\text{Ni}_{0.425}\text{Mn}_{0.425}\text{Co}_{0.15})_{0.88}\text{O}_2$ System. *Chem. Mater.* **2008**, 20, (15), 4815-4825.
138. Hy, S.; Felix, F.; Rick, J.; Su, W.-N.; Hwang, B. J., Direct In situ Observation of Li_2O Evolution on Li-Rich High-Capacity Cathode Material, $\text{Li}[\text{Ni}_x\text{Li}_{(1-2x)/3}\text{Mn}_{(2-x)/3}\text{O}_2]$ ($0 \leq x \leq 0.5$). *J. Am. Chem. Soc.* **2014**, 136, (3), 999-1007.
139. Muhammad, S.; Kim, H.; Kim, Y.; Kim, D.; Song, J. H.; Yoon, J.; Park, J.-H.; Ahn, S.-J.; Kang, S.-H.; Thackeray, M. M.; Yoon, W.-S., Evidence of reversible oxygen participation in anomalously high capacity Li- and Mn-rich cathodes for Li-ion batteries. *Nano Energy* **2016**, 21, 172-184.

140. Yabuuchi, N.; Yoshii, K.; Myung, S.-T.; Nakai, I.; Komaba, S., Detailed Studies of a High-Capacity Electrode Material for Rechargeable Batteries, $\text{Li}_2\text{MnO}_3\text{--LiCo}_{1/3}\text{Ni}_{1/3}\text{Mn}_{1/3}\text{O}_2$. *J. Am. Chem. Soc.* **2011**, 133, (12), 4404-4419.
141. Xu, J.; Sun, M.; Qiao, R.; Renfrew, S. E.; Ma, L.; Wu, T.; Hwang, S.; Nordlund, D.; Su, D.; Amine, K.; Lu, J.; McCloskey, B. D.; Yang, W.; Tong, W., Elucidating anionic oxygen activity in lithium-rich layered oxides. *Nat. Commun.* **2018**, 9, (1), 947.
142. Luo, K.; Roberts, M. R.; Guerrini, N.; Tapia-Ruiz, N.; Hao, R.; Massel, F.; Pickup, D. M.; Ramos, S.; Liu, Y.-S.; Guo, J.; Chadwick, A. V.; Duda, L. C.; Bruce, P. G., Anion Redox Chemistry in the Cobalt Free 3d Transition Metal Oxide Intercalation Electrode $\text{Li}[\text{Li}_{0.2}\text{Ni}_{0.2}\text{Mn}_{0.6}]\text{O}_2$. *J. Am. Chem. Soc.* **2016**, 138, (35), 11211-11218.
143. Oishi, M.; Yogi, C.; Watanabe, I.; Ohta, T.; Orikasa, Y.; Uchimoto, Y.; Ogumi, Z., Direct observation of reversible charge compensation by oxygen ion in Li-rich manganese layered oxide positive electrode material, $\text{Li}_{1.16}\text{Ni}_{0.15}\text{Co}_{0.19}\text{Mn}_{0.50}\text{O}_2$. *J. Power Sources* **2015**, 276, 89-94.
144. Koga, H.; Croguennec, L.; Ménétrier, M.; Douhil, K.; Belin, S.; Bourgeois, L.; Suard, E.; Weill, F.; Delmas, C., Reversible Oxygen Participation to the Redox Processes Revealed for $\text{Li}_{1.20}\text{Mn}_{0.54}\text{Co}_{0.13}\text{Ni}_{0.13}\text{O}_2$. *J. Electrochem. Soc.* **2013**, 160, (6), A786-A792.
145. Koga, H.; Croguennec, L.; Ménétrier, M.; Mannessiez, P.; Weill, F.; Delmas, C., Different oxygen redox participation for bulk and surface: A possible global explanation for the cycling mechanism of $\text{Li}_{1.20}\text{Mn}_{0.54}\text{Co}_{0.13}\text{Ni}_{0.13}\text{O}_2$. *J. Power Sources* **2013**, 236, 250-258.
146. Oishi, M.; Fujimoto, T.; Takanashi, Y.; Orikasa, Y.; Kawamura, A.; Ina, T.; Yamashige, H.; Takamatsu, D.; Sato, K.; Murayama, H.; Tanida, H.; Arai, H.; Ishii, H.; Yogi, C.; Watanabe, I.; Ohta, T.; Mineshige, A.; Uchimoto, Y.; Ogumi, Z., Charge compensation mechanisms in $\text{Li}_{1.16}\text{Ni}_{0.15}\text{Co}_{0.19}\text{Mn}_{0.50}\text{O}_2$ positive electrode material for Li-ion batteries analyzed by a combination of hard and soft X-ray absorption near edge structure. *J. Power Sources* **2013**, 222, 45-51.
147. Koga, H.; Croguennec, L.; Ménétrier, M.; Mannessiez, P.; Weill, F.; Delmas, C.; Belin, S., Operando X-ray Absorption Study of the Redox Processes Involved upon Cycling of the Li-Rich Layered Oxide $\text{Li}_{1.20}\text{Mn}_{0.54}\text{Co}_{0.13}\text{Ni}_{0.13}\text{O}_2$ in Li Ion Batteries. *J. Phys. Chem. C* **2014**, 118, (11), 5700-5709.
148. Han, S.; Xia, Y.; Wei, Z.; Qiu, B.; Pan, L.; Gu, Q.; Liu, Z.; Guo, Z., A comparative study on the oxidation state of lattice oxygen among $\text{Li}_{1.14}\text{Ni}_{0.136}\text{Co}_{0.136}\text{Mn}_{0.544}\text{O}_2$, Li_2MnO_3 , $\text{LiNi}_{0.5}\text{Co}_{0.2}\text{Mn}_{0.3}\text{O}_2$ and LiCoO_2 for the initial charge-discharge. *J. Mater. Chem. A* **2015**, 3, (22), 11930-11939.
149. Gent, W. E.; Lim, K.; Liang, Y.; Li, Q.; Barnes, T.; Ahn, S. J.; Stone, K. H.; McIntire, M.; Hong, J.; Song, J. H.; Li, Y.; Mehta, A.; Ermon, S.; Tylliszczak, T.; Kilcoyne, D.; Vine, D.; Park, J. H.; Doo, S. K.; Toney, M. F.; Yang, W.; Prendergast, D.; Chueh, W. C., Coupling between oxygen redox and cation migration explains unusual electrochemistry in lithium-rich layered oxides. *Nat. Commun.* **2017**, 8, (1), 2091.
150. Hong, J.; Lim, H.-D.; Lee, M.; Kim, S.-W.; Kim, H.; Oh, S.-T.; Chung, G.-C.; Kang, K., Critical Role of Oxygen Evolved from Layered Li-Excess Metal Oxides in Lithium Rechargeable Batteries. *Chem. Mater.* **2012**, 24, (14), 2692-2697.
151. Assat, G.; Foix, D.; Delacourt, C.; Iadecola, A.; Dedryvère, R.; Tarascon, J.-M., Fundamental interplay between anionic/cationic redox governing the kinetics and thermodynamics of lithium-rich cathodes. *Nat. Commun.* **2017**, 8, (1), 2219.

152. Sathiya, M.; Leriche, J. B.; Salager, E.; Gourier, D.; Tarascon, J. M.; Vezin, H., Electron paramagnetic resonance imaging for real-time monitoring of Li-ion batteries. *Nat. Commun.* **2015**, 6, (1), 6276.
153. Foix, D.; Sathiya, M.; McCalla, E.; Tarascon, J.-M.; Gonbeau, D., X-ray Photoemission Spectroscopy Study of Cationic and Anionic Redox Processes in High-Capacity Li-Ion Battery Layered-Oxide Electrodes. *J. Phys. Chem. C* **2016**, 120, (2), 862-874.
154. Sathiya, M.; Abakumov, A. M.; Foix, D.; Rousse, G.; Ramesha, K.; Saubanere, M.; Doublet, M. L.; Vezin, H.; Laisa, C. P.; Prakash, A. S.; Gonbeau, D.; VanTendeloo, G.; Tarascon, J. M., Origin of voltage decay in high-capacity layered oxide electrodes. *Nat. Mater.* **2015**, 14, (2), 230-8.
155. Eum, D.; Kim, B.; Kim, S. J.; Park, H.; Wu, J.; Cho, S.-P.; Yoon, G.; Lee, M. H.; Jung, S.-K.; Yang, W.; Seong, W. M.; Ku, K.; Tamwattana, O.; Park, S. K.; Hwang, I.; Kang, K., Voltage decay and redox asymmetry mitigation by reversible cation migration in lithium-rich layered oxide electrodes. *Nat. Mater.* **2020**, 19, 419-427.
156. House, R. A.; Maitra, U.; Pérez-Osorio, M. A.; Lozano, J. G.; Jin, L.; Somerville, J. W.; Duda, L. C.; Nag, A.; Walters, A.; Zhou, K.-J.; Roberts, M. R.; Bruce, P. G., Superstructure control of first-cycle voltage hysteresis in oxygen-redox cathodes. *Nature* **2020**, 577, (7791), 502-508.
157. Bard, A. J.; Faulkner, L. R., *Electrochemical Methods: Fundamentals and Applications*. John Wiley & Sons, Inc., 2008.
158. Xiao, J.; Li, Q.; Bi, Y.; Cai, M.; Dunn, B.; Glossmann, T.; Liu, J.; Osaka, T.; Sugiura, R.; Wu, B.; Yang, J.; Zhang, J.-G.; Whittingham, M. S., Understanding and applying coulombic efficiency in lithium metal batteries. *Nat. Energy* **2020**, 5, (8), 561-568.
159. Ovejas, V. J.; Cuadras, A., Effects of cycling on lithium-ion battery hysteresis and overvoltage. *Sci. Rep.* **2019**, 9, (1), 14875.
160. Als-Nielsen, J.; McMorrow, D., *Elements of Modern X-ray Physics, 2nd Edition*. Chichester, West Sussex: John Wiley, 2011.
161. Bacon, G. E., *X-ray and Neutron Diffraction*. Pergamon Press, 1966.
162. Tilley, R., *Crystals and Crystal Structures*. John Wiley & Sons, Ltd., 2006.
163. Kisi, E. H.; Howard, C. J., *Applications of Neutron Powder Diffraction*. Oxford Science Publications, 2008.
164. Toby, B. H.; Von Dreele, R. B., GSAS-II: the genesis of a modern open-source all purpose crystallography software package. *J. Appl. Crystallogr.* **2013**, 46, (2), 544-549.
165. Giridhar, P.; Weidenfeller, B.; El Abedin, S. Z.; Endres, F., Electrodeposition of iron and iron–aluminium alloys in an ionic liquid and their magnetic properties. *Phys. Chem. Chem. Phys.* **2014**, 16, (20), 9317-9326.
166. Borkiewicz, O. J.; Shyam, B.; Wiaderek, K. M.; Kurtz, C.; Chupas, P. J.; Chapman, K. W., The AMPIX electrochemical cell: a versatile apparatus for in situ X-ray scattering and spectroscopic measurements. *J. Appl. Crystallogr.* **2012**, 45, (6), 1261-1269.
167. Groot, F. d.; Kotani, A., *Core Level Spectroscopy of Solids*. CRC Press, 2008.

168. Bokhoven, J. A. V.; Lamberti, C., *X-Ray Absorption and X-Ray Emission Spectroscopy: Theory and Applications*. John Wiley & Sons, Ltd., 2016.
169. Groot, F. d., Multiplet effects in X-ray spectroscopy. *Coord. Chem. Rev.* **2005**, 249, (1), 31-63.
170. Stöhr, J., *NEXAFS Spectroscopy*. Springer, 1992.
171. Ravel, B.; Newville, M., ATHENA, ARTEMIS, HEPHAESTUS: data analysis for X-ray absorption spectroscopy using IFEFFIT. *J. Synchrotron Radiat.* **2005**, 12, (4), 537-541.
172. Butorin, S. M.; Guo, J.; Wassdahl, N.; Nordgren, E. J., Tunable-excitation soft X-ray fluorescence spectroscopy of high-Tc superconductors: an inequivalent-site seeing story. *J. Electron Spectros. Relat. Phenomena* **2000**, 110-111, 235-273.
173. Kotani, A.; Shin, S., Resonant inelastic x-ray scattering spectra for electrons in solids. *Rev. Mod. Phys.* **2001**, 73, (1), 203-246.
174. Ament, L. J. P.; van Veenendaal, M.; Devereaux, T. P.; Hill, J. P.; van den Brink, J., Resonant inelastic x-ray scattering studies of elementary excitations. *Rev. Mod. Phys.* **2011**, 83, (2), 705-767.
175. Liu, Y.-S.; Glans, P.-A.; Chuang, C.-H.; Kapilashrami, M.; Guo, J., Perspectives of in situ/operando resonant inelastic X-ray scattering in catalytic energy materials science. *J. Electron Spectros. Relat. Phenomena* **2015**, 200, 282-292.
176. Baker, M. L.; Mara, M. W.; Yan, J. J.; Hodgson, K. O.; Hedman, B.; Solomon, E. I., K- and L-edge X-ray Absorption Spectroscopy (XAS) and Resonant Inelastic X-ray Scattering (RIXS) Determination of Differential Orbital Covalency (DOC) of Transition Metal Sites. *Coord. Chem. Rev.* **2017**, 345, 182-208.
177. Yang, W.; Devereaux, T. P., Anionic and cationic redox and interfaces in batteries: Advances from soft X-ray absorption spectroscopy to resonant inelastic scattering. *J. Power Sources* **2018**, 389, 188-197.
178. Ashton, S. J., Differential Electrochemical Mass Spectrometry. In *Design, Construction and Research Application of a Differential Electrochemical Mass Spectrometer (DEMS)*, pp 9-27, Springer Berlin Heidelberg, 2012.
179. McCloskey, B. D.; Bethune, D. S.; Shelby, R. M.; Girishkumar, G.; Luntz, A. C., Solvents' Critical Role in Nonaqueous Lithium–Oxygen Battery Electrochemistry. *J. phys. Chem. Lett.* **2011**, 2, (10), 1161-1166.
180. McCloskey, B. D.; Scheffler, R.; Speidel, A.; Bethune, D. S.; Shelby, R. M.; Luntz, A. C., On the Efficacy of Electrocatalysis in Nonaqueous Li–O₂ Batteries. *J. Am. Chem. Soc.* **2011**, 133, (45), 18038-18041.
181. Renfrew, S. E.; McCloskey, B. D., Residual Lithium Carbonate Predominantly Accounts for First Cycle CO₂ and CO Outgassing of Li-Stoichiometric and Li-Rich Layered Transition-Metal Oxides. *J. Am. Chem. Soc.* **2017**, 139, (49), 17853-17860.
182. McCloskey, B. D.; Valery, A.; Luntz, A. C.; Gowda, S. R.; Wallraff, G. M.; Garcia, J. M.; Mori, T.; Krupp, L. E., Combining Accurate O₂ and Li₂O₂ Assays to Separate Discharge and Charge Stability Limitations in Nonaqueous Li–O₂ Batteries. *J. Phys. Chem. Lett.* **2013**, 4, (17), 2989-2993.

183. Kresse, G.; Furthmüller, J., Efficient iterative schemes for ab initio total-energy calculations using a plane-wave basis set. *Phys. Rev. B* **1996**, 54, (16), 11169-11186.
184. Kresse, G.; Joubert, D., From ultrasoft pseudopotentials to the projector augmented-wave method. *Phys. Rev. B* **1999**, 59, (3), 1758-1775.
185. Blöchl, P. E., Projector augmented-wave method. *Physical Review B* **1994**, 50, (24), 17953-17979.
186. Perdew, J. P.; Burke, K.; Ernzerhof, M., Generalized Gradient Approximation Made Simple. *Phys. Rev. Lett.* **1996**, 77, (18), 3865-3868.
187. Dudarev, S. L.; Botton, G. A.; Savrasov, S. Y.; Humphreys, C. J.; Sutton, A. P., Electron-energy-loss spectra and the structural stability of nickel oxide: An LSDA+U study. *Phys. Rev. B* **1998**, 57, (3), 1505-1509.
188. Becke, A. D.; Edgecombe, K. E., A simple measure of electron localization in atomic and molecular systems. *J. Chem. Phys.* **1990**, 92, (9), 5397-5403.
189. Vinson, J.; Rehr, J. J.; Kas, J. J.; Shirley, E. L., Bethe-Salpeter equation calculations of core excitation spectra. *Phys. Rev. B* **2011**, 83, (11), 115106.
190. Gilmore, K.; Vinson, J.; Shirley, E. L.; Prendergast, D.; Pemmaraju, C. D.; Kas, J. J.; Vila, F. D.; Rehr, J. J., Efficient implementation of core-excitation Bethe-Salpeter equation calculations. *Comput. Phys. Commun.* **2015**, 197, 109-117.
191. Salpeter, E. E.; Bethe, H. A., A Relativistic Equation for Bound-State Problems. *Phys. Rev.* **1951**, 84, (6), 1232-1242.
192. Giannozzi, P.; Baroni, S.; Bonini, N.; Calandra, M.; Car, R.; Cavazzoni, C.; Ceresoli, D.; Chiarotti, G. L.; Cococcioni, M.; Dabo, I.; Dal Corso, A.; de Gironcoli, S.; Fabris, S.; Fratesi, G.; Gebauer, R.; Gerstmann, U.; Gougoussis, C.; Kokalj, A.; Lazzeri, M.; Martin-Samos, L.; Marzari, N.; Mauri, F.; Mazzarello, R.; Paolini, S.; Pasquarello, A.; Paulatto, L.; Sbraccia, C.; Scandolo, S.; Sclauzero, G.; Seitsonen, A. P.; Smogunov, A.; Umari, P.; Wentzcovitch, R. M., QUANTUM ESPRESSO: a modular and open-source software project for quantum simulations of materials. *J. Phys. Condens. Matter* **2009**, 21, (39), 395502.
193. Ceperley, D. M.; Alder, B. J., Ground State of the Electron Gas by a Stochastic Method. *Phys. Rev. Lett.* **1980**, 45, (7), 566-569.
194. Perdew, J. P.; Wang, Y., Accurate and simple analytic representation of the electron-gas correlation energy. *Phys. Rev. B* **1992**, 45, (23), 13244-13249.
195. Troullier, N.; Martins, J. L., Efficient pseudopotentials for plane-wave calculations. *Phys. Rev. B Condens. Matter* **1991**, 43, (3), 1993-2006.
196. Mortemard de Boisse, B.; Liu, G.; Ma, J.; Nishimura, S.-i.; Chung, S.-C.; Kiuchi, H.; Harada, Y.; Kikkawa, J.; Kobayashi, Y.; Okubo, M.; Yamada, A., Intermediate honeycomb ordering to trigger oxygen redox chemistry in layered battery electrode. *Nat. Commun.* **2016**, 7, (1), 11397.
197. Hy, S.; Cheng, J.-H.; Liu, J.-Y.; Pan, C.-J.; Rick, J.; Lee, J.-F.; Chen, J.-M.; Hwang, B. J., Understanding the Role of Ni in Stabilizing the Lithium-Rich High-Capacity Cathode Material $\text{Li}[\text{Ni}_x\text{Li}_{(1-2x)/3}\text{Mn}_{(2-x)/3}]\text{O}_2$ ($0 \leq x \leq 0.5$). *Chem. Mater.* **2014**, 26, (24), 6919-6927.
198. Perez, A. J.; Batuk, D.; Saubanère, M.; Rousse, G.; Foix, D.; McCalla, E.; Berg, E. J.; Dugas, R.; H. W. van den Bos, K.; Doublet, M.-L.; Gonbeau, D.; Abakumov, A. M.; Van Tendeloo, G.;

- Tarascon, J.-M., Strong Oxygen Participation in the Redox Governing the Structural and Electrochemical Properties of Na-Rich Layered Oxide Na_2IrO_3 . *Chem. Mater.* **2016**, 28, (22), 8278-8288.
199. McCalla, E.; Sougrati, M. T.; Rousse, G.; Berg, E. J.; Abakumov, A.; Recham, N.; Ramesha, K.; Sathiya, M.; Dominko, R.; Van Tendeloo, G.; Novak, P.; Tarascon, J. M., Understanding the roles of anionic redox and oxygen release during electrochemical cycling of lithium-rich layered $\text{Li}_4\text{FeSbO}_6$. *J. Am. Chem. Soc.* **2015**, 137, (14), 4804-14.
 200. Jacquet, Q.; Iadecola, A.; Saubanère, M.; Li, H.; Berg, E. J.; Rousse, G.; Cabana, J.; Doublet, M.-L.; Tarascon, J.-M., Charge Transfer Band Gap as an Indicator of Hysteresis in Li-Disordered Rock Salt Cathodes for Li-Ion Batteries. *J. Am. Chem. Soc.* **2019**, 141, (29), 11452-11464.
 201. James, A. C. W. P.; Goodenough, J. B., Structure and bonding in lithium ruthenate, Li_2RuO_3 . *J. Solid State Chem.* **1988**, 74, (2), 287-294.
 202. Kobayashi, H.; Kanno, R.; Kawamoto, Y.; Tabuchi, M.; Nakamura, O.; Takano, M., Structure and lithium deintercalation of $\text{Li}_{2-x}\text{RuO}_3$. *Solid State Ion.* **1995**, 82, (1), 25-31.
 203. Kobayashi, H.; Kanno, R.; Kawamoto, Y.; Tabuchi, M.; Nakamura, O., Physical properties of the de-lithiated $\text{Li}_{2-x}\text{RuO}_3$ with the layered structure. *Solid State Ion.* **1996**, 86-88, 859-863.
 204. Miura, Y.; Yasui, Y.; Sato, M.; Igawa, N.; Kakurai, K., New-Type Phase Transition of Li_2RuO_3 with Honeycomb Structure. *J. Phys. Soc. Japan* **2007**, 76, (3), 033705.
 205. Mori, D.; Kobayashi, H.; Okumura, T.; Nitani, H.; Ogawa, M.; Inaguma, Y., XRD and XAFS study on structure and cation valence state of layered ruthenium oxide electrodes, Li_2RuO_3 and $\text{Li}_2\text{Mn}_{0.4}\text{Ru}_{0.6}\text{O}_3$, upon electrochemical cycling. *Solid State Ion.* **2016**, 285, 66-74.
 206. Reeves, P. J.; Seymour, I. D.; Griffith, K. J.; Grey, C. P., Characterizing the Structure and Phase Transition of Li_2RuO_3 Using Variable-Temperature ^{17}O and ^7Li NMR Spectroscopy. *Chem. Mater.* **2019**, 31, (8), 2814-2821.
 207. Li, H.; Ramakrishnan, S.; Freeland, J. W.; McCloskey, B. D.; Cabana, J., Definition of Redox Centers in Reactions of Lithium Intercalation in Li_3RuO_4 Polymorphs. *J. Am. Chem. Soc.* **2020**, 142, (18), 8160-8173.
 208. Zheng, F.; Zheng, S.; Zhang, P.; Zhang, X.; Wu, S.; Yang, Y.; Zhu, Z.-z., Impact of Structural Transformation on Electrochemical Performances of Li-Rich Cathode Materials: The Case of Li_2RuO_3 . *J. Phys. Chem. C* **2019**, 123, (22), 13491-13499.
 209. Wu, Z.; Saini, N. L.; Agrestini, S.; Castro, D. D.; Bianconi, A.; Marcelli, A.; Battisti, M.; Gozzi, D.; Balducci, G., Ru K-edge absorption study on the $\text{La}_{1-x}\text{Ce}_x\text{Ru}_2$ system. *J. Phys. Condens. Matter* **2000**, 12, (30), 6971-6978.
 210. Lebens-Higgins, Z. W.; Vinckeviciute, J.; Wu, J.; Faenza, N. V.; Li, Y.; Sallis, S.; Pereira, N.; Meng, Y. S.; Amatucci, G. G.; Der Ven, A. V.; Yang, W.; Piper, L. F. J., Distinction between Intrinsic and X-ray-Induced Oxidized Oxygen States in Li-Rich 3d Layered Oxides and LiAlO_2 . *J. Phys. Chem. C* **2019**, 123, (21), 13201-13207.
 211. Yabuuchi, N.; Takeuchi, M.; Nakayama, M.; Shiiba, H.; Ogawa, M.; Nakayama, K.; Ohta, T.; Endo, D.; Ozaki, T.; Inamasu, T.; Sato, K.; Komaba, S., High-capacity electrode materials for rechargeable lithium batteries: Li_3NbO_4 -based system with cation-disordered rocksalt structure. *Proc. Natl. Acad. Sci.* **2015**, 112, (25), 7650-7655.

212. Soma, M.; Sato, H., Lithium Ruthenates: Controlling Dimensionality and Topology of Magnetic-Ion Arrangements. *J. Phys. Soc. Japan* **2006**, 75, (12), 124802.
213. Jacquet, Q.; Rousse, G.; Iadecola, A.; Saubanère, M.; Doublet, M.-L.; Tarascon, J.-M., Electrostatic Interactions versus Second Order Jahn–Teller Distortion as the Source of Structural Diversity in Li_3MO_4 Compounds (M = Ru, Nb, Sb and Ta). *Chem. Mater.* **2018**, 30, (2), 392-402.
214. Yamamoto, T., Assignment of pre-edge peaks in K-edge x-ray absorption spectra of 3d transition metal compounds: electric dipole or quadrupole? *X-Ray Spectrom.* **2008**, 37, (6), 572-584.
215. Shadle, S. E.; Hedman, B.; Hodgson, K. O.; Solomon, E. I., Ligand K-Edge X-ray Absorption Spectroscopy as a Probe of Ligand-Metal Bonding: Charge Donation and Covalency in Copper-Chloride Systems. *Inorg. Chem.* **1994**, 33, (19), 4235-4244.
216. Wasinger, E. C.; de Groot, F. M. F.; Hedman, B.; Hodgson, K. O.; Solomon, E. I., L-edge X-ray Absorption Spectroscopy of Non-Heme Iron Sites: Experimental Determination of Differential Orbital Covalency. *J. Am. Chem. Soc.* **2003**, 125, (42), 12894-12906.
217. Qiao, R.; Chuang, Y. D.; Yan, S.; Yang, W., Soft x-ray irradiation effects of Li_2O_2 , Li_2CO_3 and Li_2O revealed by absorption spectroscopy. *PloS One* **2012**, 7, (11), e49182.
218. Ling, C.; Zhang, R.; Takechi, K.; Mizuno, F., Intrinsic Barrier to Electrochemically Decompose Li_2CO_3 and LiOH . *J. Phys. Chem. C* **2014**, 118, (46), 26591-26598.
219. Mahne, N.; Renfrew, S. E.; McCloskey, B. D.; Freunberger, S. A., Electrochemical Oxidation of Lithium Carbonate Generates Singlet Oxygen. *Angew. Chem. Int. Ed.* **2018**, 57, (19), 5529-5533.
220. Moreau, P.; Guyomard, D.; Gaubicher, J.; Boucher, F., Structure and Stability of Sodium Intercalated Phases in Olivine FePO_4 . *Chem. Mater.* **2010**, 22, (14), 4126-4128.
221. Shadle, S. E.; Hedman, B.; Hodgson, K. O.; Solomon, E. I., Ligand K-edge x-ray absorption spectroscopic studies: metal-ligand covalency in a series of transition metal tetrachlorides. *J. Am. Chem. Soc.* **1995**, 117, (8), 2259-2272.
222. Grimaud, A.; Iadecola, A.; Batuk, D.; Saubanère, M.; Abakumov, A. M.; Freeland, J. W.; Cabana, J.; Li, H.; Doublet, M.-L.; Rousse, G.; Tarascon, J.-M., Chemical Activity of the Peroxide/Oxide Redox Couple: Case Study of $\text{Ba}_5\text{Ru}_2\text{O}_{11}$ in Aqueous and Organic Solvents. *Chem. Mater.* **2018**, 30, (11), 3882-3893.
223. Ohzuku, T., Electrochemistry of Manganese Dioxide in Lithium Nonaqueous Cell. *J. Electrochem. Soc.* **1990**, 137, (3), 769.
224. Johnson, C. S.; Kim, J. S.; Lefief, C.; Li, N.; Vaughey, J. T.; Thackeray, M. M., The significance of the Li_2MnO_3 component in ‘composite’ $x\text{Li}_2\text{MnO}_3 \cdot (1-x)\text{LiMn}_{0.5}\text{Ni}_{0.5}\text{O}_2$ electrodes. *Electrochem. Commun.* **2004**, 6, (10), 1085-1091.
225. Thackeray, M. M.; Kang, S. H.; Johnson, C. S.; Vaughey, J. T.; Hackney, S. A., Comments on the structural complexity of lithium-rich $\text{Li}_{1+x}\text{M}_{1-x}\text{O}_2$ electrodes (M = Mn, Ni, Co) for lithium batteries. *Electrochem. Commun.* **2006**, 8, (9), 1531-1538.
226. Johnson, C. S.; Li, N.; Lefief, C.; Vaughey, J. T.; Thackeray, M. M., Synthesis, Characterization and Electrochemistry of Lithium Battery Electrodes: $x\text{Li}_2\text{MnO}_3 \cdot (1-x)\text{LiMn}_{0.333}\text{Ni}_{0.333}\text{Co}_{0.333}\text{O}_2$ ($0 \leq x \leq 0.7$). *Chem. Mater.* **2008**, 20, (19), 6095-6106.

227. Rozier, P.; Tarascon, J. M., Review—Li-Rich Layered Oxide Cathodes for Next-Generation Li-Ion Batteries: Chances and Challenges. *J. Electrochem. Soc.* **2015**, 162, (14), A2490-A2499.
228. Ben Yahia, M.; Vergnet, J.; Saubanère, M.; Doublet, M.-L., Unified picture of anionic redox in Li/Na-ion batteries. *Nat. Mater* **2019**, 18, (5), 496-502.
229. Hy, S.; Su, W.-N.; Chen, J.-M.; Hwang, B.-J., Soft X-ray Absorption Spectroscopic and Raman Studies on $\text{Li}_{1.2}\text{Ni}_{0.2}\text{Mn}_{0.6}\text{O}_2$ for Lithium-Ion Batteries. *J. Phys. Chem. C* **2012**, 116, (48), 25242-25247.
230. Mortemard de Boisse, B.; Liu, G.; Ma, J.; Nishimura, S.; Chung, S. C.; Kiuchi, H.; Harada, Y.; Kikkawa, J.; Kobayashi, Y.; Okubo, M.; Yamada, A., Intermediate honeycomb ordering to trigger oxygen redox chemistry in layered battery electrode. *Nat. Commun.* **2016**, 7, 11397.
231. Cao, G.; Qi, T. F.; Li, L.; Terzic, J.; Yuan, S. J.; DeLong, L. E.; Murthy, G.; Kaul, R. K., Novel Magnetism of Ir^{5+} ($5d^4$) Ions in the Double Perovskite Sr_2YIrO_6 . *Phys. Rev. Lett.* **2014**, 112, (5), 056402.
232. Terzic, J.; Zheng, H.; Ye, F.; Zhao, H. D.; Schlottmann, P.; De Long, L. E.; Yuan, S. J.; Cao, G., Evidence for a low-temperature magnetic ground state in double-perovskite iridates with Ir^{5+} ($5d^4$) ions. *Phys. Rev. B* **2017**, 96, (6), 064436.
233. Solomon, E. I.; Hedman, B.; Hodgson, K. O.; Dey, A.; Szilagy, R. K., Ligand K-edge X-ray absorption spectroscopy: covalency of ligand–metal bonds. *Coord. Chem. Rev.* **2005**, 249, (1), 97-129.
234. Hu, E.; Yu, X.; Lin, R.; Bi, X.; Lu, J.; Bak, S.; Nam, K.-W.; Xin, H. L.; Jaye, C.; Fischer, D. A.; Amine, K.; Yang, X.-Q., Evolution of redox couples in Li- and Mn-rich cathode materials and mitigation of voltage fade by reducing oxygen release. *Nat. Energy* **2018**, 3, (8), 690-698.
235. Li, L.; Castro, F. C.; Park, J. S.; Li, H.; Lee, E.; Boyko, T.; Freeland, J. W.; Yao, Z.; Fister, T. T.; Vinson, J.; Shirley, E. L.; Wolverton, C.; Cabana, J.; Dravid, V. P.; Thackeray, M. M.; Chan, M. K. Y., Probing Electrochemically-Induced Structural Evolution and Oxygen Redox Reactions in Layered Lithium Iridate. *Chem. Mater.* **2019**.
236. Gent, W. E.; Abate, I. I.; Yang, W.; Nazar, L. F.; Chueh, W. C., Design Rules for High-Valent Redox in Intercalation Electrodes. *Joule* **2020**, 4, (7), 1369-1397.
237. Kobayashi, H.; Tabuchi, M.; Shikano, M.; Kageyama, H.; Kanno, R., Structure, and magnetic and electrochemical properties of layered oxides, Li_2IrO_3 . *J. Mater. Chem.* **2003**, 13, (4), 957-962.
238. Mühle, C.; Dinnebier, R. E.; van Wüllen, L.; Schwering, G.; Jansen, M., New Insights into the Structural and Dynamical Features of Lithium Hexaoxometalates Li_7MO_6 ($\text{M} = \text{Nb}, \text{Ta}, \text{Sb}, \text{Bi}$). *Inorg. Chem.* **2004**, 43, (3), 874-881.
239. Mühle, C.; Karpov, A.; Verhoeven, A.; Jansen, M., Crystal Structures, Dimorphism and Lithium Mobility of Li_7MO_6 ($\text{M} = \text{Bi}, \text{Ru}, \text{Os}$). *Z. Anorg. Allg. Chem.* **2005**, 631, (12), 2321-2327.

VITA

EDUCATION

University of Illinois at Chicago, Chicago, Illinois, USA

Aug. 2015 – Nov. 2020

Ph.D. in Inorganic Chemistry, GPA 3.23/4.0

Dissertation: Insights into Ligand-centered Redox Mechanisms in Li-rich Metal Oxides during Battery Reactions

Advisor: Prof. Jordi Cabana

University of Chinese Academy of Sciences, Beijing, China

Sep. 2011 – Jun. 2015

Graduate study in Inorganic Chemistry, GPA 3.70/4.0

Thesis: Synthesis and Optical Properties of Novel Red-emitting Phosphors for WLEDs

Advisor: Prof. Chengyu Li

Qingdao University of Science & Technology, Qingdao, China

Sep. 2007 – Jun. 2011

B.E. in Packaging Engineering, GPA 3.66/4.0

Thesis: Synthesis and Electrochemical Properties of Polybenzo-coated LiFePO₄ Cathode Material for Li-ion Batteries

Advisor: Prof. Cunguo Wang

RESEARCH EXPERIENCE

University of Illinois at Chicago, Chicago, Illinois, USA

Jan. 2016 – Nov. 2020

Position: Graduate Research Assistant

Goals: Investigation of the mechanism of ligand-centered redox in compensating charges equivalent to extracted/reinserted Li in Li-rich positive electrodes via electrochemical characterization, crystal and electronic structure analysis and density functional theory calculation

- Synthesized Li-rich transition metal oxides using solid state and mechanochemical methods
- Assembled coin cell batteries for an array of electrochemical testing including galvanostatic cycling, rate capability studies, cyclic voltammetry, and impedance measurements
- Utilized an array of analytical techniques including *ex situ/operando* X-ray/neutron diffraction and pair distribution function, X-ray photoelectron spectroscopy, *ex situ/operando* X-ray absorption spectroscopy, X-ray emission spectroscopy, resonant inelastic X-ray scattering spectroscopy, differential electrochemical mass spectroscopy, and electrochemistry to study the nature of ligand-centered redox in charge compensation mechanism of Li-rich positive electrode materials for Li-ion batteries
- Authored proposals to conduct experiments at state-of-the-art facilities at the Advanced Photon Source, Spallation Neutron Source and Canadian Light Source

University of Chinese Academy of Sciences, Beijing, China

Sep. 2012 – Jun. 2015

Position: Graduate Research Assistant

Goals: Synthesis and optical measurement of various elements, like Eu²⁺, Eu³⁺, and Mn⁴⁺ etc., doped phosphors with red light emission under UV excitation to improve the illumination effect of WLEDs

- Synthesized a series of compounds using solid state and sol-gel processes
- Employed an arsenal of spectroscopic methods including photoluminescence excitation and emission spectroscopy, luminescence decay spectroscopy, 3D thermo-luminescence spectroscopy to investigate the photoluminescence performance

Qingdao University of Science & Technology, Qingdao, China

Jul. 2010 – Jun. 2011

Position: Undergraduate Research Assistant

Goals: Synthesis and electrochemical testing of Polybenzo-coated LiFePO₄ cathode material

- Synthesized polybenzo-coated LiFePO₄ and tested electrochemical performance of the modified LiFePO₄
- Completed undergraduate thesis

WORKSHOPS

Next Generation Electrochemistry (NGenE) initiative, University of Illinois at Chicago **Jun. 2019**

- Understood fundamental and frontier of electrochemistry in fields like biochemistry and electrocatalyst
- Worked collectively to solve an electrochemistry-related issue

Modern Methods in Rietveld refinement for Structural Analysis, Oak Ridge National Laboratory **Jun. 2017**

- Grasped the basics for Rietveld analysis
- Used TOPAS to perform Rietveld refinement of synchrotron and neutron diffraction data collected at different facilities

TEACHING EXPERIENCE

Teaching Assistant in General Chemistry and Inorganic Chemistry **Sep. 2015 – Aug. 2018**

AWARDS

GSC Travel Award, University of Illinois at Chicago **Nov. 2019**

Chemistry Department Graduate PhD Travel Award, University of Illinois at Chicago **Aug. 2019**

Chemistry Department Conference Travel Award, University of Illinois at Chicago **Oct. 2018**

The Bodmer Travel Award, University of Illinois at Chicago **Apr. 2017**

Honor Student, University of Chinese Academy of Sciences **Sep. 2011 – Jun. 2015**

Honor Student, Qingdao University of Science & Technology **Jun. 2011**

National Encouragement Scholarship, Qingdao University of Science & Technology **Oct. 2010**

Undergraduate Scholarships, Qingdao University of Science & Technology **Sep. 2007 – Jun. 2011**

PUBLICATIONS

- Xin Cao[#], **Haifeng Li[#]**, Yu Qiao, Min Jia, Xiang Li, Jordi Cabana, and Haoshen Zhou. Stabilizing Anionic Redox Chemistry in a Mn-Based Layered Oxide Cathode Constructed by Li-Deficient Pristine State, *Adv. Mater.* **2020**, Accepted.
- Min Jia[#], **Haifeng Li[#]**, Yu Qiao, Linlin Wang, Xin Cao, Jordi Cabana, and Haoshen Zhou. Elucidating Anionic Redox Chemistry in P3 Layered Cathode for Na-Ion Batteries, *ACS Appl. Mater. Interfaces* **2020**, 12, 38249.
- **Haifeng Li**, Srinivasan Ramakrishnan, John W. Freeland, Bryan D. McCloskey, and Jordi Cabana. Definition of Redox Centers in Reactions of Lithium Intercalation in Li₃RuO₄ Polymorphs, *J. Am. Chem. Soc.* **2020**, 142, 8160.
- Xin Cao[#], **Haifeng Li[#]**, Yu Qiao, Xiang Li, Min Jia, Jordi Cabana, Haoshen Zhou, Stabilizing Reversible Oxygen Redox Chemistry in Layered Oxides for Sodium-Ion Batteries, *Adv. Energy Mater.* **2020**, 1903785.
- Chenglong Zhao, Zhenpeng Yao, Qidi Wang, **Haifeng Li**, Jianlin Wang, Yaxiang Lu, Jordi Cabana, Baohua Li, Xuedong Bai, Alán Aspuru-Guzik, Marnix Wagemaker, Liquan Chen, and Yong-Sheng Hu. Revealing High Na-Content P2-Type Layered Oxides as Advanced Sodium-Ion Cathodes, *J. Am. Chem. Soc.* **2020**, 142, 12.
- Bob Jin Kwon, Ka-Cheong Lau, Haesun Park, Yimin A. Wu, Krista L. Hawthorne, **Haifeng Li**, Soojeong Kim, Igor L. Bolotin, Timothy T. Fister, Peter Zapol, Robert F. Klie, Jordi Cabana, Chen Liao, Saul H. Lapidus, Baris Key, and John T. Vaughey. Probing Electrochemical Mg-Ion Activity in

- MgCr_{2-x}V_xO₄ Spinel Oxides, *Chem. Mater.* **2020**, 32, 1162.
- Sujoy Saha, Gaurav Assat, Moulay Tahar Sougrati, Dominique Foix, **Haifeng Li**, Soma Turi, Jordi Cabana, Gwenaëlle Rousse, Artem M. Abakumov, Jean-Marie Tarascon. Exploring the Bottlenecks of Anionic Redox in Li-rich Layered Sulfides, *Nat. Energy*, **2019**, 4, 977.
 - Quentin Jacquet, Antonella Iadecola, Mattieu Saubanere, **Haifeng Li**, Erik J. Berg, Gwenaëlle Rousse, Jordi Cabana, Marie-Liesse Doublet, and Jean-Marie Tarascon. Charge Transfer Band Gap as an Indicator of Hysteresis in Li-disordered Rock Salt Cathodes for Li-ion Batteries, *J. Am. Chem. Soc.*, **2019**, 141, 11452.
 - Liang Li, Fernando C. Castro, Joong Sun Park, **Haifeng Li**, Eungje Lee, Teak D. Boyko, John W. Freeland, Zhenpeng Yao, Timothy T. Fister, John Vinson, Eric L. Shirley, Christopher Wolverton, Jordi Cabana, Vinayak P. Dravid, Michale M. Thackeray, and Miria K. Y. Chan. Probing Electrochemically Induced Structural Evolution and Oxygen Redox Reactions in Layered Lithium Iridate, *Chem. Mater.*, **2019**, 31, 4341.
 - Alexis Grimaud, Antonella Iadecola, Dmitry Batuk, Matthieu Saubanere, Artem M. Abakumov, John W. Freeland, Jordi Cabana, **Haifeng Li**, Marie-Liesse Doublet, Gwenaëlle Rousse, and Jean-Marie Tarascon. Chemical Activity of the Peroxide/Oxide Redox Couple: Case Study of Ba₅Ru₂O₁₁ in Aqueous and Organic Solvents, *Chem. Mater.*, **2018**, 30, 3882.
 - **Haifeng Li**, Yonglei Jia, Tengfei Ma, Ran Pang, Wenzhi Sun, Da Li, Jipeng Fu, Su Zhang, Lihong Jiang, Chengyu Li, Ca₉Sc(PO₄)₇:Ce³⁺, Mn²⁺ – A Red-Emitting Phosphor Based on Energy Transfer, *Eur. J. Inorg. Chem.*, **2016**, 2016, 867.
 - **Haifeng Li**, Ran Zhao, Yonglei, Jia, Wenzhi Sun, Jipeng Fu, Lihong Jia, Su Zhang, Ran Pang, and Chengyu, Li. Sr_{1.7}Zn_{0.3}CeO₄:Eu³⁺ Novel Red-emitting Phosphors: Synthesis and Photoluminescence Properties, *ACS Appl. Mater. Interfaces*, **2014**, 6, 3163.

PRESENTATIONS


- **Haifeng Li**, Srinivasan Ramakrishnan, John Freeland, Bryan McCloskey, Jordi Cabana, Definition of Redox Centers in Reactions of Lithium-Intercalation in Li₃RuO₄ Polymorphs. ALS user meeting, Aug. **2020**.
- **Haifeng Li**, Jordi Cabana, Liang Li, Miria K. Y. Chan. Probing Electrochemically Induced Structural Evolution and Oxygen Redox Reactions in Layered Li₂IrO₃. Oral presentation at North American Solid State Chemistry Conference, Golden, Colorado, Aug. **2019**.
- **Haifeng Li**, Srinivasan Ramakrishnan, John Freeland, Bryan McCloskey Jordi Cabana, Definition of Redox Centers in Reactions of Lithium-Intercalation in Li₃RuO₄ Polymorphs. Poster presentation at NGenE at University of Illinois at Chicago, Jun. **2019**.
- **Haifeng Li**, John P. Katsoudas, John Freeland and Jordi Cabana. Li₃RuO₄ – Understanding the Role of Li/M Ordering in Triggering the Oxygen Redox. Poster presentation at Materials Research Society Fall Meeting and Exhibit, Boston, Massachusetts, Dec. **2018**.
- **Haifeng Li**, Jordi Cabana. Oxygen Contribution to Li-ion Intercalation-deintercalation in Li₃RuO₄ system by O K-edge X-ray Absorption Spectroscopy. Poster presentation at Annual Chemistry Symposium, University of Illinois at Chicago, Oct. **2017**.

PROFESSIONAL MEMBERSHIP

Materials Research Society

Appendix

Permission for Figures 1-1:



Issues and challenges facing rechargeable lithium batteries
Author: J.-M. Tarascon et al
Publication: Nature
Publisher: Springer Nature
Date: Nov 15, 2001
Copyright © 2001, Springer Nature

Order Completed

Thank you for your order.

This Agreement between University of Illinois at Chicago -- Haifeng Li ("You") and Springer Nature ("Springer Nature") consists of your license details and the terms and conditions provided by Springer Nature and Copyright Clearance Center.

Your confirmation email will contain your order number for future reference.

License Number 4766560868489 [Printable Details](#)

License date Feb 12, 2020


☒ **Licensed Content**

Licensed Content Publisher	Springer Nature
Licensed Content Publication	Nature
Licensed Content Title	Issues and challenges facing rechargeable lithium batteries
Licensed Content Author	J.-M. Tarascon et al
Licensed Content Date	Nov 15, 2001

☐ **Order Details**

Type of Use	Thesis/Dissertation
Requestor type	academic/university or research institute
Format	print and electronic
Portion	figures/tables/illustrations
Number of figures/tables/illustrations	2
Will you be translating?	no
Circulation/distribution	1 - 29
Author of this Springer Nature content	no

Permission for Figure 1-2:



The Li-Ion Rechargeable Battery: A Perspective
Author: John B. Goodenough, Kyu-Sung Park
Publication: Journal of the American Chemical Society
Publisher: American Chemical Society
Date: Jan 1, 2013
Copyright © 2013, American Chemical Society

PERMISSION/LICENSE IS GRANTED FOR YOUR ORDER AT NO CHARGE

This type of permission/license, instead of the standard Terms & Conditions, is sent to you because no fee is being charged for your order. Please note the following:

- Permission is granted for your request in both print and electronic formats, and translations.
- If figures and/or tables were requested, they may be adapted or used in part.
- Please print this page for your records and send a copy of it to your publisher/graduate school.
- Appropriate credit for the requested material should be given as follows: "Reprinted (adapted) with permission from (COMPLETE REFERENCE CITATION). Copyright (YEAR) American Chemical Society." Insert appropriate information in place of the capitalized words.
- One-time permission is granted only for the use specified in your request. No additional uses are granted (such as derivative works or other editions). For any other uses, please submit a new request.

If credit is given to another source for the material you requested, permission must be obtained from that source.

BACK **CLOSE WINDOW**

Permission for Figure 1-3:



Cathode materials for next generation lithium ion batteries

Author: Jiantie Xu, Shixue Dou, Huakun Liu, Liming Dai

Publication: Nano Energy

Publisher: Elsevier

Date: July 2013

Copyright © 2013 Elsevier Ltd. All rights reserved.

Order Completed

Thank you for your order.

This Agreement between University of Illinois at Chicago -- Haifeng Li ("You") and Elsevier ("Elsevier") consists of your license details and the terms and conditions provided by Elsevier and Copyright Clearance Center.

Your confirmation email will contain your order number for future reference.

License Number 4762050958099

[Printable Details](#)

License date Feb 04, 2020

Permission for Figure 1-4:

Permissions

No special permission is required to reuse all or part of article published by MDPI, including figures and tables. For articles published under an open access Creative Common CC BY license, any part of the article may be reused without permission provided that the original article is clearly cited. Reuse of an article does not imply endorsement by the authors or MDPI.

Permission for Figures 1-5, 1-6c and 1-6d and 1-8:



Molecular Orbital Principles of Oxygen-Redox Battery Electrodes

Author: Masashi Okubo, Atsuo Yamada

Publication: Applied Materials

Publisher: American Chemical Society

Date: Oct 1, 2017

Copyright © 2017, American Chemical Society

PERMISSION/LICENSE IS GRANTED FOR YOUR ORDER AT NO CHARGE


This type of permission/license, instead of the standard Terms & Conditions, is sent to you because no fee is being charged for your order. Please note the following:

- Permission is granted for your request in both print and electronic formats, and translations.
 - If figures and/or tables were requested, they may be adapted or used in part.
 - Please print this page for your records and send a copy of it to your publisher/graduate school.
 - Appropriate credit for the requested material should be given as follows: "Reprinted (adapted) with permission from (COMPLETE REFERENCE CITATION). Copyright (YEAR) American Chemical Society." Insert appropriate information in place of the capitalized words.
 - One-time permission is granted only for the use specified in your request. No additional uses are granted (such as derivative works or other editions). For any other uses, please submit a new request.
- If credit is given to another source for the material you requested, permission must be obtained from that source.

[BACK](#)

[CLOSE WINDOW](#)

Permission for Figure 1-6a and 1-6b:



Visualization of O-O peroxo-like dimers in high-capacity layered oxides for Li-ion batteries

Author:
Eric McCalla,Artem M. Abakumov,Matthieu Saubanière,Dominique Folx,Erik J. Berg,Gwenaëlle Rousse,Marie-Liesse Doublet,Danielle Gonbeau,Petr Novák,Gustaaf Van Tendeloo,Robert Dominko,Jean-Marie Tarascon

Publication: Science

Publisher: The American Association for the Advancement of Science

Date: Dec 18, 2015

Copyright © 2015, Copyright © 2015, American Association for the Advancement of Science

Order Completed


Thank you for your order.

This Agreement between University of Illinois at Chicago -- Haifeng Li ("You") and The American Association for the Advancement of Science ("The American Association for the Advancement of Science") consists of your license details and the terms and conditions provided by The American Association for the Advancement of Science and Copyright Clearance Center.

Your confirmation email will contain your order number for future reference.

License Number	4896780216512	Printable Details
License date	Aug 26, 2020	

Permission for Figure 1-7:



Unlocking the Potential of Cation-Disordered Oxides for Rechargeable Lithium Batteries

Author: Jinhyuk Lee,Alexander Urban,Xin Li,Dong Su,Geoffroy Hautier,Gerbrand Ceder

Publication: Science

Publisher: The American Association for the Advancement of Science

Date: Jan 31, 2014

Copyright © 2014, Copyright © 2014, American Association for the Advancement of Science

Order Completed


Thank you for your order.

This Agreement between University of Illinois at Chicago -- Haifeng Li ("You") and The American Association for the Advancement of Science ("The American Association for the Advancement of Science") consists of your license details and the terms and conditions provided by The American Association for the Advancement of Science and Copyright Clearance Center.

Your confirmation email will contain your order number for future reference.

License Number	4896820419509	Printable Details
License date	Aug 26, 2020	

Permission for Figure 1-9:



Approaching the limits of cationic and anionic electrochemical activity with the Li-rich layered rocksalt Li3IrO4

Author: Arnaud J. Perez et al

Publication: Nature Energy

Publisher: Springer Nature

Date: Dec 8, 2017

Copyright © 2017, Springer Nature

Order Completed

Thank you for your order.

This Agreement between University of Illinois at Chicago -- Haifeng Li ("You") and Springer Nature ("Springer Nature") consists of your license details and the terms and conditions provided by Springer Nature and Copyright Clearance Center.

Your confirmation email will contain your order number for future reference.

License Number	4896780642404	Printable Details
License date	Aug 26, 2020	

Permission for Figure 1-10:

SPRINGER NATURE

The structural and chemical origin of the oxygen redox activity in layered and cation-disordered Li-excess cathode materials

Author: Dong-Hwa Seo et al
Publication: Nature Chemistry
Publisher: Springer Nature
Date: May 30, 2016
Copyright © 2016, Springer Nature

Order Completed

Thank you for your order.

This Agreement between University of Illinois at Chicago – Haifeng Li ("You") and Springer Nature ("Springer Nature") consists of your license details and the terms and conditions provided by Springer Nature and Copyright Clearance Center.

Your confirmation email will contain your order number for future reference.

License Number	4896821333815
License date	Aug 26, 2020

 [Printable Details](#)

Permission for Figures 1-11:

SPRINGER NATURE

Fundamental understanding and practical challenges of anionic redox activity in Li-ion batteries

Author: Gaurav Assat et al
Publication: Nature Energy
Publisher: Springer Nature
Date: Apr 9, 2018
Copyright © 2018, Springer Nature

Order Completed

Thank you for your order.

This Agreement between University of Illinois at Chicago – Haifeng Li ("You") and Springer Nature ("Springer Nature") consists of your license details and the terms and conditions provided by Springer Nature and Copyright Clearance Center.

Your confirmation email will contain your order number for future reference.

License Number	4896781120041
License date	Aug 26, 2020

 [Printable Details](#)

Permission for Figure 1-12:

Payment by invoice: You can cancel your order until the invoice is generated by contacting customer service. X

Billing Address Haifeng Li University of Illinois at Chicago 932 W 31st PL Chicago, IL 60608 United States +1 (773) 733-8135 hli211@uic.edu	Customer Location Haifeng Li University of Illinois at Chicago 932 W 31st PL Chicago, IL 60608 United States
PO Number (optional) N/A	Payment options Invoice

PENDING ORDER CONFIRMATION


Confirmation Number: Pending [Print Friendly Format](#)
 Order Date: 26-Aug-2020 Includes Publisher Terms and Conditions

1. Journal of materials chemistry. A, Materials for energy and sustainability Order license ID: Pending ISSN: 2050-7496 Type of Use: Republish in a thesis/dissertation	Publisher Portion: Royal Society of Chemistry Chart/graph/table/figure	0.00 USD
---	---	----------

[View Details](#) [Print License](#)

Total Items: 1 **Total Due: 0.00 USD**

Permission for Figure 1-13:



Detailed Studies of a High-Capacity Electrode Material for Rechargeable Batteries, Li₂MnO₃-LiCo_{1/3}Ni_{1/3}Mn_{1/3}O₂
 Author: Naoaki Yabuuchi, Kazuhiro Yoshii, Seung-Taek Myung, et al
 Publication: Journal of the American Chemical Society
 Publisher: American Chemical Society
 Date: Mar 1, 2011
 Copyright © 2011, American Chemical Society


PERMISSION/LICENSE IS GRANTED FOR YOUR ORDER AT NO CHARGE

This type of permission/license, instead of the standard Terms & Conditions, is sent to you because no fee is being charged for your order. Please note the following:

- Permission is granted for your request in both print and electronic formats, and translations.
- If figures and/or tables were requested, they may be adapted or used in part.
- Please print this page for your records and send a copy of it to your publisher/graduate school.
- Appropriate credit for the requested material should be given as follows: "Reprinted (adapted) with permission from (COMPLETE REFERENCE CITATION), Copyright (YEAR) American Chemical Society." Insert appropriate information in place of the capitalized words.
- One-time permission is granted only for the use specified in your request. No additional uses are granted (such as derivative works or other editions). For any other uses, please submit a new request.
- If credit is given to another source for the material you requested, permission must be obtained from that source.

[BACK](#)
[CLOSE WINDOW](#)

Permission for Figure 1-14a:



Charge-compensation in 3d-transition-metal-oxide intercalation cathodes through the generation of localized electron holes on oxygen
 Author: Kun Luo et al
 Publication: Nature Chemistry
 Publisher: Springer Nature
 Date: Mar 21, 2016
 Copyright © 2016, Springer Nature

Order Completed


Thank you for your order.

This Agreement between University of Illinois at Chicago -- Haifeng Li ("You") and Springer Nature ("Springer Nature") consists of your license details and the terms and conditions provided by Springer Nature and Copyright Clearance Center.

Your confirmation email will contain your order number for future reference.

License Number	4896830303195	Printable Details
License date	Aug 26, 2020	


Permission for Figure 1-14b:



Coupling between oxygen redox and cation migration explains unusual electrochemistry in lithium-rich layered oxides
Author: William E. Gent et al
Publication: Nature Communications
Publisher: Springer Nature
Date: Dec 12, 2017
Copyright © 2017, Springer Nature

Creative Commons
This is an open access article distributed under the terms of the [Creative Commons CC BY](#) license, which permits unrestricted use, distribution, and reproduction in any medium, provided the original work is properly cited.
You are not required to obtain permission to reuse this article.
To request permission for a type of use not listed, please contact [Springer Nature](#)

Permission for Figures 1-15:



Reversible anionic redox chemistry in high-capacity layered-oxide electrodes
Author: M. Sathiya et al
Publication: Nature Materials
Publisher: Springer Nature
Date: Jul 14, 2013
Copyright © 2013, Springer Nature

Order Completed


Thank you for your order.

This Agreement between University of Illinois at Chicago -- Haifeng Li ("You") and Springer Nature ("Springer Nature") consists of your license details and the terms and conditions provided by Springer Nature and Copyright Clearance Center.

Your confirmation email will contain your order number for future reference.

License Number	4896820022753	Printable Details
License date	Aug 26, 2020	

Permission for Figure 1-16:



Metal-oxygen decoordination stabilizes anion redox in Li-rich oxides
Author: Jihyun Hong et al
Publication: Nature Materials
Publisher: Springer Nature
Date: Feb 4, 2019
Copyright © 2019, Springer Nature

Order Completed

Thank you for your order.

This Agreement between University of Illinois at Chicago -- Haifeng Li ("You") and Springer Nature ("Springer Nature") consists of your license details and the terms and conditions provided by Springer Nature and Copyright Clearance Center.

Your confirmation email will contain your order number for future reference.

License Number	4896831308903	Printable Details
License date	Aug 26, 2020	

Permission for Figure 1-17a:

Order Completed

Thank you for your order.

This Agreement between University of Illinois at Chicago -- Haifeng Li ("You") and Springer Nature ("Springer Nature") consists of your license details and the terms and conditions provided by Springer Nature and Copyright Clearance Center.

Your confirmation email will contain your order number for future reference.

License Number 4896831144817

License date Aug 26, 2020

[Printable Details](#)

Permission for Figure 1-17b:

Order Completed

Thank you for your order.

This Agreement between University of Illinois at Chicago -- Haifeng Li ("You") and Springer Nature ("Springer Nature") consists of your license details and the terms and conditions provided by Springer Nature and Copyright Clearance Center.

Your confirmation email will contain your order number for future reference.

License Number 4913290100811

License date Sep 20, 2020

[Printable Details](#)

Permission for Figure 2-1:

Creative Commons

This is an open access article distributed under the terms of the [Creative Commons CC BY](#) license, which permits unrestricted use, distribution, and reproduction in any medium, provided the original work is properly cited.

You are not required to obtain permission to reuse this article.

To request permission for a type of use not listed, please contact [Springer Nature](#)

Permission for Figure 2-2:

WILEY

Book: Crystals and Crystal Structures, 2nd Edition

Author: Richard J. D. Tilley

Publisher: John Wiley and Sons

Date: Aug 1, 2020

Copyright © 2020, John Wiley and Sons

Order Completed

Thank you for your order.

This Agreement between University of Illinois at Chicago -- Haifeng LI ("You") and John Wiley and Sons ("John Wiley and Sons") consists of your license details and the terms and conditions provided by John Wiley and Sons and Copyright Clearance Center.

Your confirmation email will contain your order number for future reference.

License Number 4913290632528

[Printable Details](#)

License date Sep 20, 2020

Permission for Figure 2-3:

permissions

Reuse permissions

If you wish to quote short passages or to reprint any figures or tables from IUCr Journals in a scientific publication, prior permission is not required, subject to the following conditions:

- Reproduction is intended in a journal, book, thesis or similar publication.
- The original article in which the material appeared is cited.
- IUCr's copyright is indicated by the wording "Reproduced with permission of the International Union of Crystallography". In electronic form, this acknowledgement must be visible at the same time as the reused materials, and must be linked to the original article using its DOI.

As a courtesy, please also try to let the authors of the original article know that you are going to reuse their content. Reproduction or systematic or multiple reproduction of longer passages from IUCr Journals is permitted only under licence from the IUCr; in addition, the IUCr may require that permission be obtained from one of the authors. In such cases, enquiries and requests for permission should be addressed to:

Executive Managing Editor
IUCr Journals
5 Abbey Square
Chester CH1 2HU
UK

Email: med@iucr.org or [click here](#)

Please be sure to include the following information:

- The title, author(s) and page extent of the article you wish to republish, or, in the case where you do not wish to reproduce the whole article, details of the section(s) to be reproduced.
- The journal title, volume/issue number and year of publication in which the article appeared, and the page numbers of the article.
- Details of the publication in which you wish to reprint the Journal material.
- If the material is being edited or amended in any way, a copy of the final material as it will appear in your publication.
- Contact details for yourself, including a postal address.

Photocopying permissions

Teaching institutions with a current paid subscription to the journal may make multiple copies for teaching purposes without charge, provided such copies are not resold or copied. In all other cases, permission should be obtained from a reproduction rights organisation (see below) or directly from the Publisher.

Copyright Licensing Agency

Institutions based in the UK with a valid photocopying and/or digital license with the Copyright Licensing Agency may copy excerpts under the terms of their license. For further information go to CLA.

Copyright Clearance Center

Institutions based in the US with a valid photocopying and/or digital license with the Copyright Clearance Center may copy excerpts under the terms of their license, please go to CCC.

Other Territories:

Please contact your local reproduction rights organisation.

Permission for Figure 2-6:



Anionic and cationic redox and interfaces in batteries: Advances from soft X-ray absorption spectroscopy to resonant inelastic scattering

Author: Wanli Yang, Thomas P. Devereaux

Publication: Journal of Power Sources

Publisher: Elsevier

Date: 15 June 2018

© 2018 Elsevier B.V. All rights reserved.

Order Completed

Thank you for your order.

This Agreement between University of Illinois at Chicago -- Haifeng Li ("You") and Elsevier ("Elsevier") consists of your license details and the terms and conditions provided by Elsevier and Copyright Clearance Center.

Your confirmation email will contain your order number for future reference.

License Number 4913290922900

License date Sep 20, 2020

Printable Details

Permission for Chapter 4:



Definition of Redox Centers in Reactions of Lithium Intercalation in Li₃RuO₄ Polymorphs

Author: Haifeng Li, Srinivasan Ramakrishnan, John W. Freeland, et al

Publication: Journal of the American Chemical Society

Publisher: American Chemical Society

Date: May 1, 2020

Copyright © 2020, American Chemical Society

PERMISSION/LICENSE IS GRANTED FOR YOUR ORDER AT NO CHARGE

This type of permission/license, instead of the standard Terms & Conditions, is sent to you because no fee is being charged for your order. Please note the following:

- Permission is granted for your request in both print and electronic formats, and translations.
- If figures and/or tables were requested, they may be adapted or used in part.
- Please print this page for your records and send a copy of it to your publisher/graduate school.
- Appropriate credit for the requested material should be given as follows: "Reprinted (adapted) with permission from (COMPLETE REFERENCE CITATION). Copyright (YEAR) American Chemical Society." Insert appropriate information in place of the capitalized words.
- One-time permission is granted only for the use specified in your request. No additional uses are granted (such as derivative works or other editions). For any other uses, please submit a new request.

[BACK](#)

[CLOSE WINDOW](#)